ABSTRACT

Title of Document: MICROFABRICATION AND MODELLING
OF DIELECTRIC ELASTOMER
ACTUATORS

Bavani Balakrisnan,
Doctor of Philosophy, 2012

Directed By: Professor Elisabeth Smela
Department of Mechanical Engineering

Dielectric elastomer actuators (DEAs) are a class of polymeric actuators that have gained prominence over the last decade. A DEA is comprised of a polymer sandwiched between two compliant electrodes. When voltage is applied between the two electrodes, electrostatic attraction between the electrodes compresses the elastomer in that direction and stretches it in the other two directions. DEAs produce dimensional changes (strains) up to 300% upon application of an electric field. DEAs have tremendous potential for applications requiring large displacements and have been demonstrated for many macro-scale (centimeter and larger) applications such as

robots, loudspeakers, and motors.

There are potentially many useful applications for micro-scale DEAs (less than millimeter-sized devices with micron-sized actuators) in the fields of micro-robotics, micro-optics, and micro-fluidics. However, miniaturization of DEAs is challenging because many of the materials and DEA fabrication methods used on the macro-scale cannot be adapted for micro-scale fabrication of DEAs. This thesis explores the feasibility of developing fabrication strategies for micro-scale DEAs by adapting micro-electromechanical systems (MEMS) technology. In addition, fabrication protocols for micro-scale DEAs have been developed.

The other aspect of this thesis is the design of bending DEAs. Benders are useful because for a given actuation strain, greater deflection can be observed by controlling the stiffnesses and thicknesses of different layers. A general guideline for designing bending DEA configurations such as unimorph, bimorph, and multilayer stacks was developed using a multilayer analytical model. The design optimization is based on the effect of thickness and stiffness of different layers on curvature, blocked force, and work.

Complaint electrodes and their design are important for DEAs to enable the elastomer to stretch unrestricted. Thus, design criteria for the fabrication of crenellated electrodes and crenellated elastomers with electrodes were investigated. This guideline enabled design of structures with appropriate axial or bending stiffnesses

based on the amplitude, angle, length, and thickness. Simple analytical equations for axial and bending stiffness for crenellated electrodes with different shapes were derived. In addition, numerical simulations of crenellated elastomer with stiff electrode were performed.

MICROFABRICATION AND MODELLING OF DIELECTRIC ELASTOMER

ACTUATORS

By

Bavani Balakrisnan

Dissertation submitted to the Faculty of the Graduate School of the
University of Maryland, College Park, in partial fulfillment
of the requirements for the degree of
Doctor of Philosophy
2012

Advisory Committee:
Professor Elisabeth Smela (Chair)
Associate Professor Pamela Abshire (Dean's Representative)
Assistant Professor Sarah Bergbreiter
Professor Donald Devoe
Assistant Professor Teng Li

Dedication

To Suresh, Aaryaa, my mom, and new addition to our family Bavesh.

And in memory of my beloved father who would have loved to see this day.

Acknowledgements

Table of Contents

List of Tables

List of Figures

axial and bending displacements are indicated. c) Schematic illustration of the primary deformations of the horizontal and tilted segments of the basic unit during axial elongation induced by an applied force F in the axial direction. 37

Figure 3-2. Schematic of a meander structure with $n = 3$ periods of length λ showing the numbering of the segments as well as the angle and moment arm for segment $i = 9$. 43

Figure 3-3. Illustration of the four contributions to the deflection at the rightmost tip of the structure from a beam segment of length B_i rigidly mounted on its left and attached to a horizontal section of length L_i. a) Before application of the force at the tip. b) Deflection $\delta_{i,F}$ at the tip of the segment due to segment bending caused by the component of force perpendicular to the endpoint of the segment and the resulting deflection $\delta_{i,dF}$ at the endpoint. c) Tilt of the horizontal section due to the bending angle $\theta_{i,F}$ arising from the bending in (b). d) Deflection due to beam bending caused by the moment M on the segment. e) Tilt of the horizontal section due to the bending angle $\theta_{i,M}$. 44

Figure 3-4. a) Axial stiffness relative to that of a straight beam as a function of corrugation angle for an amplitude $A = 25$ found by simulation, analytical estimation, and experimentally. b) The fraction of axial displacement, given by the analytical approach, due to bending of the horizontal (δ_H) and vertical (δ_T) segments, relative to the total axial displacement of the rectangle. 51

Figure 3-5. a) Relative bending stiffness as a function of corrugation angle for an amplitude $A = 25$ found by simulation, analytical estimation, and experimentally, with the stiffness normalized to that of a straight beam. b) The fraction of bending displacement due to bending of the horizontal (δ_H) and vertical (δ_T) segments given by the analytical approach in (a), normalized by the total displacement of the rectangular crenellation. The relative contributions to (c) δ_T and (d) δ_H by each of the four terms again normalized by the total displacement of the rectangular crenellation. 55

Figure 3-6. Bending stiffness (FEM values) verses the total beam length for the different shapes. 56

Figure 3-7. a) Axial stiffness relative to that of a straight beam as a function of crenellation amplitude, where A is normalized by the beam thickness t. Simulation results are shown as points and results from Equation (4) as a line. The red triangular points are experimental data. b) The fraction of axial displacement due to bending of the horizontal (δ_H) and vertical (δ_T) segments, given by the analytical approach. 58

Figure 3-8. a) Bending stiffness relative to that of a straight beam as a function of crenellation amplitude. (Simulation results, round points; results from Equation (4), line; experimental data, triangular points.) b) The fraction of bending displacement due to bending of the horizontal (δ_H) and vertical (δ_T) segments, given by the

Chapter 1: Motivation and Introduction

Actuators are devices that convert various forms of energy such as light, chemical, and electrical into mechanical energy. Muscles are examples of natural actuators that convert chemical energy into mechanical energy. Dielectric elastomer actuators (DEAs) belong to a category of electroactive polymers (EAPs) that convert electrical energy into large displacement. DEAs have tremendous potential for applications requiring large displacements and have been demonstrated for many macro-scale (centimeter and larger) applications. There are potentially many useful applications of DEAs at the micro-scale (<millimeter). This thesis examines DEA device optimization using numerical simulations and the challenges involved in miniaturizing DEAs using standard microfabrication techniques.

1.1   Outline

Chapter 1 describes the motivation behind this thesis work, literature review on existing micro-scale DEAs and general background on the DEA concept.

Chapter 2 discusses the challenges in adapting the macro-scale materials and/or fabrication methods to the micro-scale DEA fabrication. The chapter outlines the standard micromachining methods (bulk vs. surface) and their advantages, the electrode and elastomer materials that could be used in the micro-scale device fabrication, and illustrates four possible micro-scale DEA actuation modes.

In **Chapter 3,** the design of crenellated electrodes is discussed based on how the amplitude, angle, length, and thickness affect both the axial and bending stiffnesses. Simple analytical equations for the axial and bending stiffnesses of a cantilever configuration for different crenellated shapes are derived, and they are compared with numerical and experimental results. In addition, the more complex case of a stiff film overlying a crenellated elastomer is also simulated.

Chapter 4 examines the behavior of bending DEAs, first using analytical models and then using a coupled electrostatic-mechanical finite element model to provide guidelines for optimizing their design. Specifically, the effect of thickness and moduli of the elastomer on the curvature, block force, and work is explored. In addition, interactions of DEAs with external grounds are explored.

In the micro-scale patterning of the elastomer is important to achieve higher strain. *Chapter 5* shows a quick method of patterning elastomer (PDMS) using a combination of wet and dry etching techniques. This method synergistically combines the advantages of the wet and dry etching methods.

Chapter 6 examines the details on how some of the microfabrication challenges are overcome and the proof-of-concept microfabrication of surface micromachined miniature device is attempted.

Chapter 7 covers the conclusion and discussion of future work.

Chapter 8 lists the contributions of this dissertation.

Appendix A discusses the bending behavior of the bilayers. In this study, microfabrication of another type of EAP (polypyyrole actuators) was used to validate model prediction.

1.2 Motivation

A dielectric elastomer actuator consists of a polymeric elastomer sandwiched between two compliant (does not restrict the movement of the elastomer) electrodes in a capacitor-like configuration (Figure 1-1). When an electric field is applied between these electrodes, electrostatic attraction between the opposite electrodes causes them to squeeze in the direction of the applied field and expand in the other two orthogonal directions. The overall displacement, or mechanical strain, is proportional to the square of the applied voltage or electric field.

DEAs were discovered in the early 1990s and most of the work on DEAs has since been limited to macro-scale, length scales greater than a centimeter [1-10]. They have been used in many applications such as robots, loud speakers and motors [6,9,11-13]. The main advantage of DEAs is their ability to show large strains of up to 200 % [14]. Apart from having the ability to exhibit large strains, DEAs have high

energy density (3 J/g [15]), low power consumption (10 µW [15]), and good efficiency (up to 65% [15]).
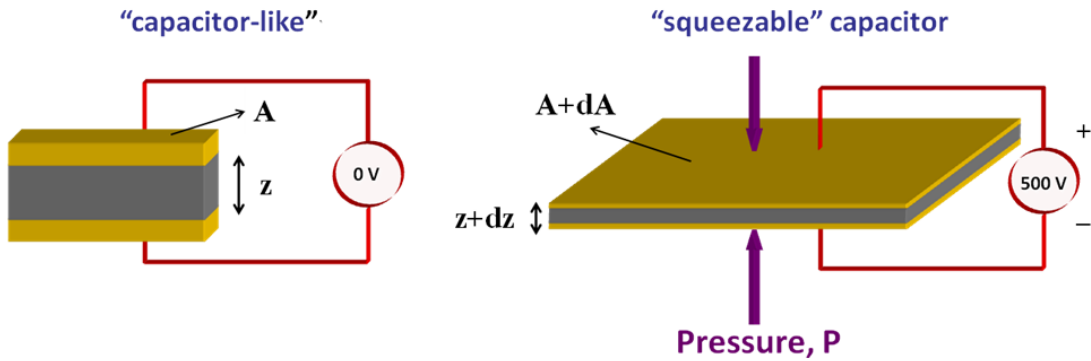
Figure 1-1. Working principle of a DEA.

Macro-scale DEAs require large voltages (>kV range) to show measurable actuations. However, by reducing the thickness of the elastomer, this actuation voltage can be reduced, for example, if the electric field needed to actuate an elastomer is 30 V/µm. If 100 µm thick elastomer is used, the voltage needed will be 3000 V. Meanwhile, if the thickness is reduced to 10 µm and below, less than 300 V will be needed. This is one of the primary motivations moving towards the micro-scale DEA devices.

While macro-scale DEAs have been well studied over the last two decades, the field of micro-scale DEAs is relatively unexplored. With the ubiquitous impact of microelectronics technology in everyday life, the advantages of a miniaturized device are obvious: low power consumption, ability to multiplex with a variety of devices in a small area, and potentially improved performance. One of the primary goals of this research is to develop microfabrication approaches for DEAs using the mature microfabrication processes from the microelectronics field.

Another motivation of this research is to be able to make these actuators in a batch fabrication manner using micro-electromechanical systems (MEMS) technology so that it will be easily applied in a multitude of applications such as microfluidics, micro-optics, and micro-robotics (Figure 1-2).
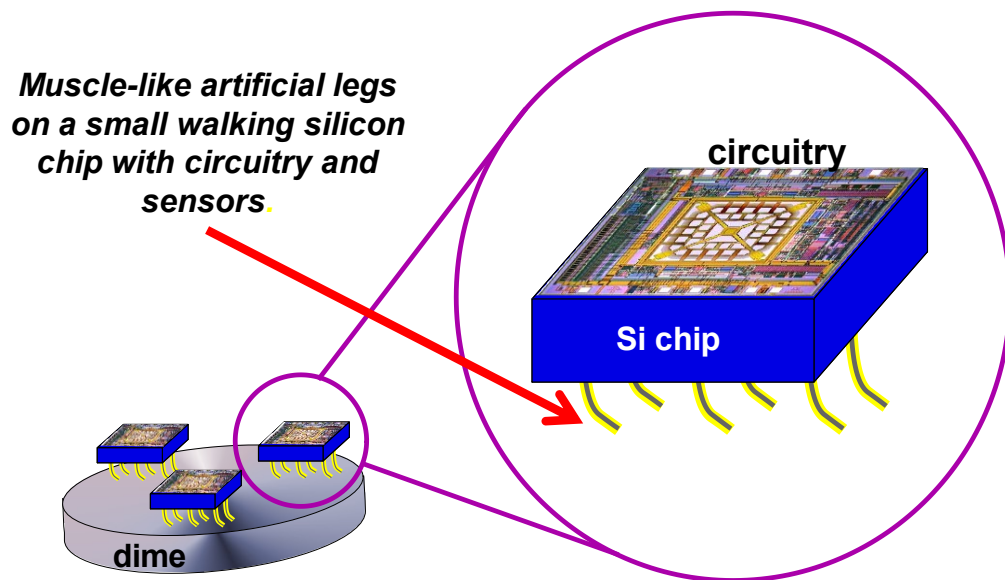
Figure 1-2. Schematic of an autonomous ant-sized micro-robot.

To make an autonomous micro-robot, actuators that have large strains, consume low power, and are highly efficient in turning electrical energy into mechanical work are needed. Micro-scale DEA devices could potentially provide all these attributes. In addition to these performance attributes, the micro-scale DEAs should also be compatible with existing CMOS fabrication processes such as surface micromachining, which enables them to be integrated into a fully functional device with electrical circuitry. However, there are challenges to overcome before micro-

scale DEAs can be realized. Addressing these challenges is one of the primary focuses of this dissertation.

1.3   DEA Theory

For a DEA, the capacitance is defined by

(1) $C = \dfrac{\varepsilon_0 \varepsilon_r A}{z}$,

where ε_o is the permittivity of free space and ε_r is the dielectric constant of the elastomer. The electrical energy of a capacitor, U, is defined as [16]

(2) $U = \dfrac{1}{2}CV^2 = \dfrac{Q^2}{2C} = \dfrac{Q^2 z}{2\varepsilon_o \varepsilon_r A}$,

where Q is the charge and V is the applied voltage. If we assume that the deformation change of the DEA is infinitesimally small, the total change in the electrical energy, dU, will be equal to the change in electrical energy given by the power supply plus the change in mechanical energy due to the decrease in thickness and increase in area. This is given by

$$dU = \frac{Qz}{\varepsilon_o \varepsilon_r A}dQ + \frac{Q^2}{2\varepsilon_o \varepsilon_r A}dz - \frac{Q^2 z}{2\varepsilon_o \varepsilon_r A^2}dA$$

(3) $= \dfrac{Q}{C}dQ + \dfrac{Q^2}{2C}(\dfrac{1}{z})dz - \dfrac{Q^2}{2C}(\dfrac{1}{A})dA$

$= \dfrac{Q}{C}dQ + U[(\dfrac{1}{z})dz - (\dfrac{1}{A})dA]$.

Elastomers are assumed incompressible (Poisson's ratio, $v = 0.5$), and thus, their volume will be conserved ($A \cdot z$ = constant). For an infinitesimal volume change [16],

(4) $Adz + zdA = 0$,

and

(5) $\dfrac{1}{z}dz = -\dfrac{1}{A}dA$.

Substituting this into Equation (5) yields

(6) $dU = \dfrac{Q}{C}dQ + 2U(\dfrac{1}{z})dz$

To find the force acting on the actuator, the energy has to be differentiated with respect to the thickness,

(7) $F = \dfrac{dU}{dz} = \dfrac{Q}{C}\dfrac{dQ}{dz} + 2U(\dfrac{1}{z})$.

If we assume charge is constant in the system then $dQ = 0$ and Equation (7) simplifies to

(8) $F = 2U(\dfrac{1}{z})$.

Combining Equation (8) with Equation (1) gives the pressure applied, P, as

(9) $P = \dfrac{F}{A} = \varepsilon_o\varepsilon_r(\dfrac{V}{z})^2$.

This pressure, sometimes known as Pelrine's pressure on a DEA [17], is twice that of the Maxwell's pressure ($P_{\text{Maxwell}} = 1/2\varepsilon_o\varepsilon_r(V/z)^2$ [15].

The actuation strain in the thickness direction, S_z of the elastomer can be found by [14]

(10) $S_z = -E_{polymer}P$,

7

where E is the elastic modulus of the polymer. The negative sign symbolizes the strain is compressive and the thickness decreases in this direction. To find strain in the other two orthogonal directions, the following equation can be used (based on conservation of volume),

$$(11) \quad (1+S_x)(1+S_y)(1+S_z) = 1$$

It is important to note the assumptions involved in this derivation:

- The electrodes are compliant, meaning the electrode does not restrict the movement of the elastomer during actuation.

- The electrodes have negligible resistance, and the resistance of the electrode does not change during actuation.

- The elastomer has infinite electrical resistance and is perfectly elastic with no mechanical losses.

- The elastomer is considered isotropic and incompressible (volume is conserved).

- Charge in the system remains constant.

Pelrine's pressure equation is widely used for computing force and strain of a DEA; however, there are configurations in which Maxwell's pressure has been used directly [17-20]. Wissler *et al.* have used Maxwell's equations for spherical ball structures since the boundary condition was considered hydrostatic.

1.4   DEA Components

The primary components in a DEA are the elastomers and the electrodes. Elastomers are a class of amorphous polymeric materials that can undergo large recoverable deformation. They contain long chain molecules that are highly twisted and tangled together. When a load is applied, these twisted and tangled chains uncoil, increasing the entropy of the material [21]. When the load is released, they coil back to the original condition, decreasing the entropy of the material. The amount of cross-linking determines the stiffness of the elastomer. A highly cross-linked elastomer would not show much extension [21].

1.4.1 Elastomer

Some of the important characteristics of a desirable elastomer material for DEA applications are given below.

- *Dielectric constant or relative permittivity* – An elastomer with higher dielectric constant shows higher actuation pressure since the actuation pressure is proportional to the dielectric constant (Equation (9)). Typical dielectric constant values for elastomers are between 2 and 8, though there are examples of composites with higher dielectric constant obtained by addition of inorganic and organic fillers [22-27]. Addition of fillers would generally increase the Young's modulus of the elastomer, making them stiffer and reducing their overall strain (exception [28])

- *Young's modulus* - A lower Young's modulus means that the material can be readily squeezed by the electric field (V/z) and exhibit larger strain (Equation

(9)). The effect of modulus on the DEA deformation for bending DEAs is discussed in Chapter 4.

In macro-scale DEAs, the elastomers are typically pre-strained and fixed to a rigid frame. (Note: there are DEAs that do not use frames, e.g., contractile DEAs [29] and multilayer stacked benders [30]). The strain-strain relationship is non-linear after pre-straining [31]. The advantage of pre-straining is that it helps align the elastomer in the direction of the preferred actuation, enabling greater actuation strains. Pre-straining also enhances the actuation strain up to a certain stretch ratio [31]. In addition, it reduces the thickness, which in turn reduces the actuation voltage. However, pre-straining is not practical in micro-scale DEAs. There have been attempts to pre-strain the elastomer without external frames (interpenetration of polymer networks); however, further work is needed before they can be used in the micro-scale [32,33].

1.4.2 Electrodes

The electrodes are another important component of a DEA. The important quality of an electrode is the ability to stretch as much as the elastomer strains during actuation, while maintaining a good electrical contact. If the electrode does not elongate with the elastomer, the overall observed elastomer strain would be lower than the theoretical value. Therefore, selection of a suitable electrode material is a major research topic in the field of DEAs [1,28,34-37]. Carbon/conductive grease electrodes or conductive powders with or without silicone oils are commonly used in

the macro-scale [1,38-40]. These are not compatible with microfabrication processes, which are usually performed in cleanrooms and, thus, would not be feasible to use in micro-scale DEAs. The challenges faced with electrode materials and the design approaches for the micro-scale are discussed in Chapters 2 and 3, respectively.

1.5   Literature Review on Existing Micro-scale DEAs

As discussed earlier, the field of micro-scale DEAs is relatively new and the literature is limited. Within this limited literature, many authors only concentrate on patterning the electrodes and not the elastomer. Uma *et al*. has used DEAs as an electro-optical modulator where the bottom electrode was patterned into a grating structure; however, the elastomers and the top electrode were not patterned [41]. Upon application of the voltage between the electrodes, the elastomer actuated and formed a corrugated structure mimicking the underlying electrode grating structure. The light reflected from this grating structure formed a diffraction pattern. The order of the diffraction pattern was controlled by the elastomer grating structure, which in turn was modulated by the applied voltage (see Figure 1-3).
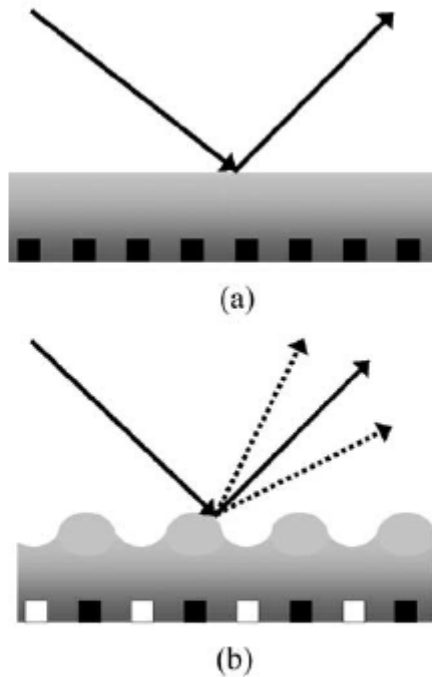
Figure 1-3. Elastomer forms grating structure upon application of the voltage and the reflected light forms a diffraction pattern. [41]

The electro-optical modulator device reported by Uma *et al*. can be called a micro-scale device because of the small elastomer thickness (~ 6 μm) and the device dimension (2 mm x 2 mm); however, was not patterned. Galler *et al*. demonstrated the first surface micromachined out-of-plane or squeezing DEA for optical modulation [42] by using TEM grid as a mask to etch the device (Figure 1-4). Both the top and bottom electrodes were made of metals and were patterned along with the elastomer. This paper showed that patterning both the elastomer and electrodes increased the achievable actuation strain compared to when only the electrodes were patterned. In micro-scale, where pre-straining of the elastomer is not an option, patterning can help improve the actuation strain. Galler's etching method can be

readily adapted to standard batch microfabrication processes using metal thin film mask instead of using a TEM grid. This approach is discussed in Chapter 6.
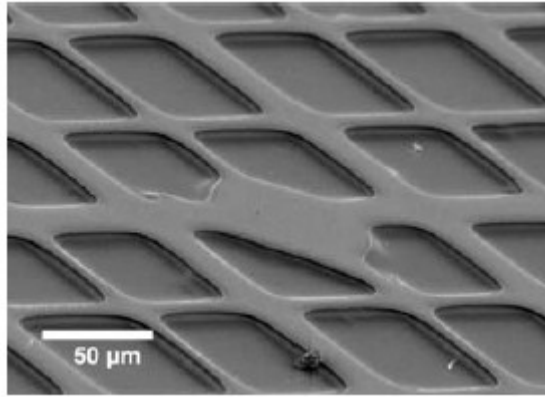
Figure 1-4. Both electrodes and the elastomer are etched using a TEM grid as etch mask. [42]

In addition to surface micromachining, bulk micromachining has been explored in literature. For example, Shea *et al.* and Pimpin *et al.* demonstrated DEA membranes using bulk micromachining. In this process, silicon substrate with elastomer film was deposited and etched from the backside until the elastomer film was released and suspended (Figure 1-5). In this process, the elastomer itself was not etched. Shea *et al.* used metal ion-implanted but the electrode was not patterned. Pimpin *et al.* demonstrated that the higher deformation achieved by patterning electrodes (Cr/Au), about 6 times larger than without patterning electrodes, thus making a case for the benefits of microfabrication. However, the disadvantage of bulk micromachining is that much of the substrate material is lost, making their integration onto devices challenging [20,35].

Si ■ **Oxide** □ **Chromium/Gold** ■ **SYLGARD186**
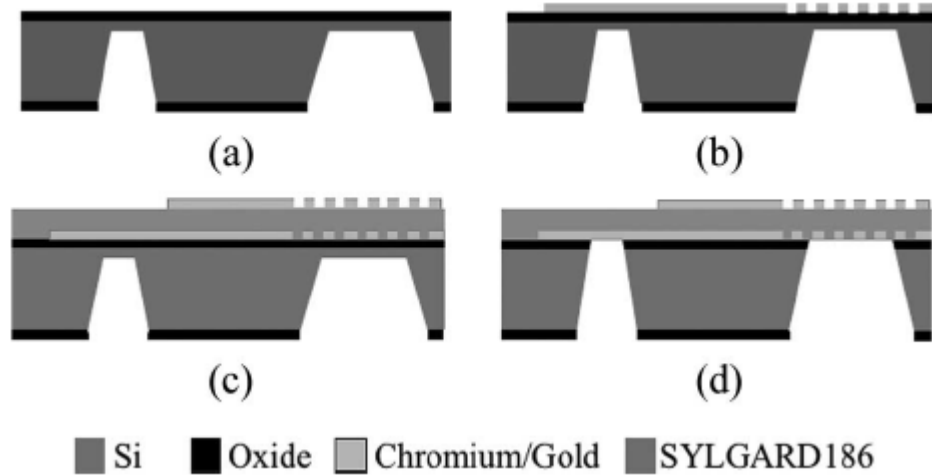
Figure 1-5. Buckling DEA membranes fabricated by bulk micromachining [20]

The idea behind making vertically stacked bulk micromachined DEA benders was first proposed by Lau *et al.* [18], though it was not experimentally demonstrated. Sarah Bergbreiter and her co-workers have shown how bulk silicon micromachining can be used to make stacked bending DEAs [43]. The modeling of stacked DEAs will be discussed in Chapter 4.

Wilson *et al.* used crenellated molded elastomer sandwiched between stiff ITO coated glass electrodes for making a tunable and compressible grating [44]. Since the actuation strain was small, the devices were squeezed by hand to show proof-of concept for this application.

There are other micro-scale structures that are not microfabricated using standard silicon microfabrication processes; Batch-fabricated, laser micro-machined bending DEAs have been made [45,46]. However, carbon grease, which is not clean room

compatible, was used as the compliant electrode. Loverich *et al.* made an all polymer micro-pump with pre-stretched elastomer (VHB) and conductive grease electrodes [47]. As discussed earlier, pre-stretching is not feasible using standard microfabrication.

Microfabrication of DEA devices is relatively new. However, it is an actively researched area as evidenced by several interesting articles over the last few years. While the motivation for micro-scale DEA devices is clear, there are a number of challenges that need to be addressed. One of the primary challenges is to develop efficient and viable microfabrication procedures while considering the materials and process limitations. This thesis aims to address some of these challenges.

1.6   Simulation and Mathematical Modeling in DEA Research

There have been analytical and numerical simulations of framed or stretched macro-scale DEA structures [48-60]. The field of micro-scale DEAs, however, is relatively new and the contribution of the mathematical modeling and simulation to micro-scale DEAs is negligible. Mathematical modeling can play a valuable role in design optimization and performance simulation and, therefore, can play a significant role in the development of micro-scale DEAs.

There are several significant differences in the materials and processes used for fabrication of macro-scale and micro-scale DEA devices. Numerical simulations can play a vital role in understanding the effects of these changes in microscale devices.

15

For example, the macro-scale DEAs typically use electrodes such as grease or carbon powder, while the micro-scale devices use metallic thin films, which are not as compliant with elastomer as grease or carbon powder. Therefore, the electrode configuration, shape, and material can have a significant effect on the overall elastomer deformation. These effects should be modeled prior to fabricating the actual devices.

The elastomer in the macro-scale devices is typically pre-strained to large deformations and is fixed to a frame. This is necessary to achieve measureable actuation. The existing numerical and analytical models for predicting the actuation in macro-scale devices cannot be easily adapted for micro-scale devices because pre-straining is not possible. Therefore, new models for micro-scale devices need to be developed.

Kluge *et al*. has modeled three different types of squeezing out-of-plane DEAs for optical modulation [61]. Their simulation showed that patterning the elastomer as well as the electrodes gave the highest strain because patterning allowed the elastomer to freely squeeze out-of-plane. However, because of the stress concentrations at the edges of the electrodes, the elastomer deformation was large at the edges. This information was used to develop an electrode configuration involving extended electrodes that gave a more uniform elastomer deformation. This demonstrated the benefits of modeling and simulation for DEA device development.
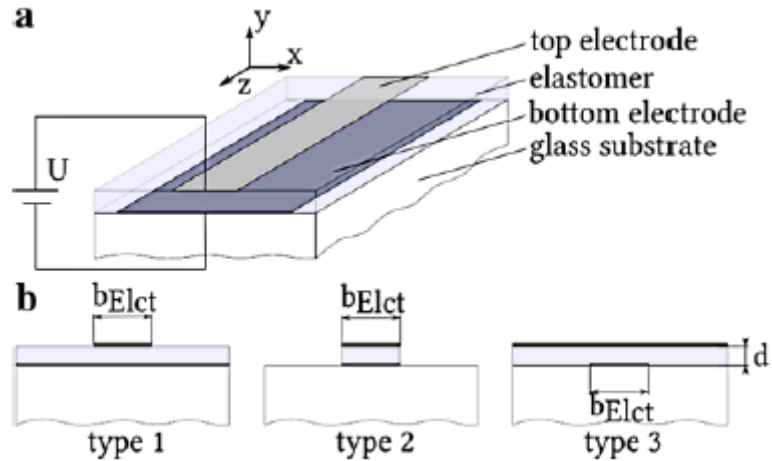
Figure 1-6. Simulation of three different types of electrode and elastomer configurations showed that the model with patterned electrodes and elastomer shows the largest elastomer deformation [61].

While Kluge *et al.* have modeled squeezing structures, other configurations with potentially larger deformations including bending actuators have not been modeled. A bending actuator is similar to a cantilevered beam of elastomer and electrodes that deforms out-of-plane when voltage is applied. These have potential applications as micro-robotic legs. The overall bending level in a bending actuator can be optimized by changing the electrode design, thicknesses of elastomer and electrodes, and the moduli. Numerical and analytical modeling can be a valuable tool for optimization and design of bending actuators. The numerical modeling can also be used to study the minimum interaction distance between adjacent micro-scale DEA devices. These aspects of modeling are covered in Chapter 4.

Chapter 2: Challenges in the Microfabrication of Dielectric Elastomer Actuators

Bavani Balakrisnan and Elisabeth Smela
University of Maryland, Department of Mechanical Engineering
2176 Glenn L. Martin Hall, College Park, Maryland 20742

Abstract

Dielectric elastomer actuators (DEAs) have been demonstrated for meso- and macro-scale applications, but only a few devices have been shown at the micro-scale, the most common of which have been diaphragms that bulge out of the plane of the wafer. Microscale DEAs would be of value in a wide range of small devices, including micro-robots, micro-pumps, and micro-optical systems. An additional advantage of miniaturizing is a reduction in the required driving voltage from kilovolts to tens of volts because the layers are thinner. However, fabrication of micro-scale DEAs remains challenging due in part to the fact that the vast majority of macro-scale materials and/or fabrication methods cannot be adapted to the micro-scale. On the micro-scale, the DEAs must be patternable as well as compatible with other materials used during fabrication, such as sacrificial layers. Another practical issue in fabricating micro-scale devices concerns making connections to the top electrodes. It would also be desirable to develop fabrication procedures for integrating the micro-scale DEAs with complementary metal-oxide-semiconductor (CMOS) driver circuits and other micro-electro-mechanical systems (MEMS). This

article addresses the progress that has been made thus far in making microfabricated DEAs, as well as the challenges and the key areas in which additional research needs to be pursued.

2.1   Introduction

Dielectric elastomer actuators (DEAs) came into prominence two decades ago, and they have been demonstrated for many macro-scale (cm and larger) applications such as robots, loudspeakers, and motors [6,11-13].   On the other hand, many of the technological innovations over the last few decades involved miniaturization.   The main driving factors towards miniaturization have been lower power consumption, higher density per unit area, integration of multiple devices in a given footprint (multiplexing), and improved performance.   There are many useful potential applications for micro-scale (< mm) DEAs in the fields of micro-robotics, micro-optics, and micro-fluidics.   Because of their large strains, low power consumption, high efficiency, and resilience, microscale DEAs will compliment other existing micro-scale actuators, such as piezoelectric, thermal, and electrostatic actuators [62]. In addition, microscale DEAs also possess practical advantages over their macro-scale counterparts, such as lower operating voltages (< 1 kV) and higher breakdown strength [63].   Other factors that scale advantageously include force density, bandwidth, and power density [62].

19

Microfabrication technology has enabled monolithic integration of micro-scale actuators and sensors with electronics on the same substrate [64]. The integration can be done at either the wafer level or the chip level using techniques such as thin film deposition, photolithography, and etching (discussed below).

Moving DEAs to the micro-scale involves modifying the methods and materials used to make devices at the macro-scale. Figure 2-1 shows some methods and materials that cannot be used in microfabrication. For example, grease and carbon powder electrodes, which are widely used for macro-scale devices, are incompatible with MEMS processing, which is performed in a clean room environment. As a second example, pre-straining is a common procedure used with macro-scale DEAs in order to achieve large strains, and is a requirement for some materials to actuate. However, this is incompatible with spin-coating the elastomer onto a substrate, such as is done with batch-processing. Therefore, in addition to developing new fabrication procedures, micro-DEAs may require the use of new elastomers that can achieve high strains without pre-strain.

.
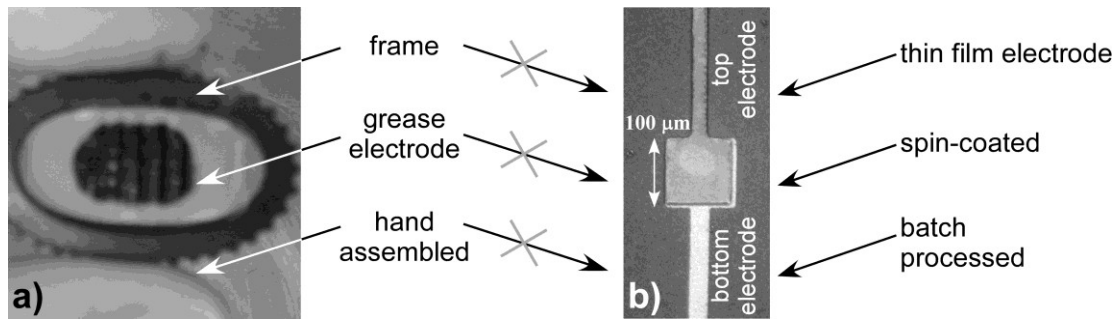
Figure 2-1. a) A DEA fabricated by pre-straining the elastomer onto a frame and hand-applying carbon grease electrodes. b) Microfabricated structures made by spin-coating the elastomer and applying electrodes by evaporation.

This paper focuses on the challenges involved in fabricating micro-scale DEAs using conventional surface micromachining methods. This involves depositing layers on top of a substrate and patterning them using lithography and either etching or lift-off, as shown in Figure 2-2. Film deposition is performed by methods such as spin-coating, evaporation, and chemical vapor deposition. Lithography involves spinning a polymeric resist onto the layer and exposing the resist through a mask to UV light, followed by developing to remove the exposed resist. Etching or lift-off are two methods used to pattern the layer. With etching, the resist is deposited on top of the layer, and with lift-off the layer is applied over ther resist. The deposition and patterning steps are repeated with multple layers to form the device

Etching   **Lift-Off**

1) Deposit layer, then spin-coat photoresist over it.   1) Spin-coat photoresist onto the substrate.

2) Expose the resist to UV through a mask; develop.   2) Expose the resist to UV through a mask; develop.

3) Etch layer.   3) Deposit layer.

4) Remove resist.
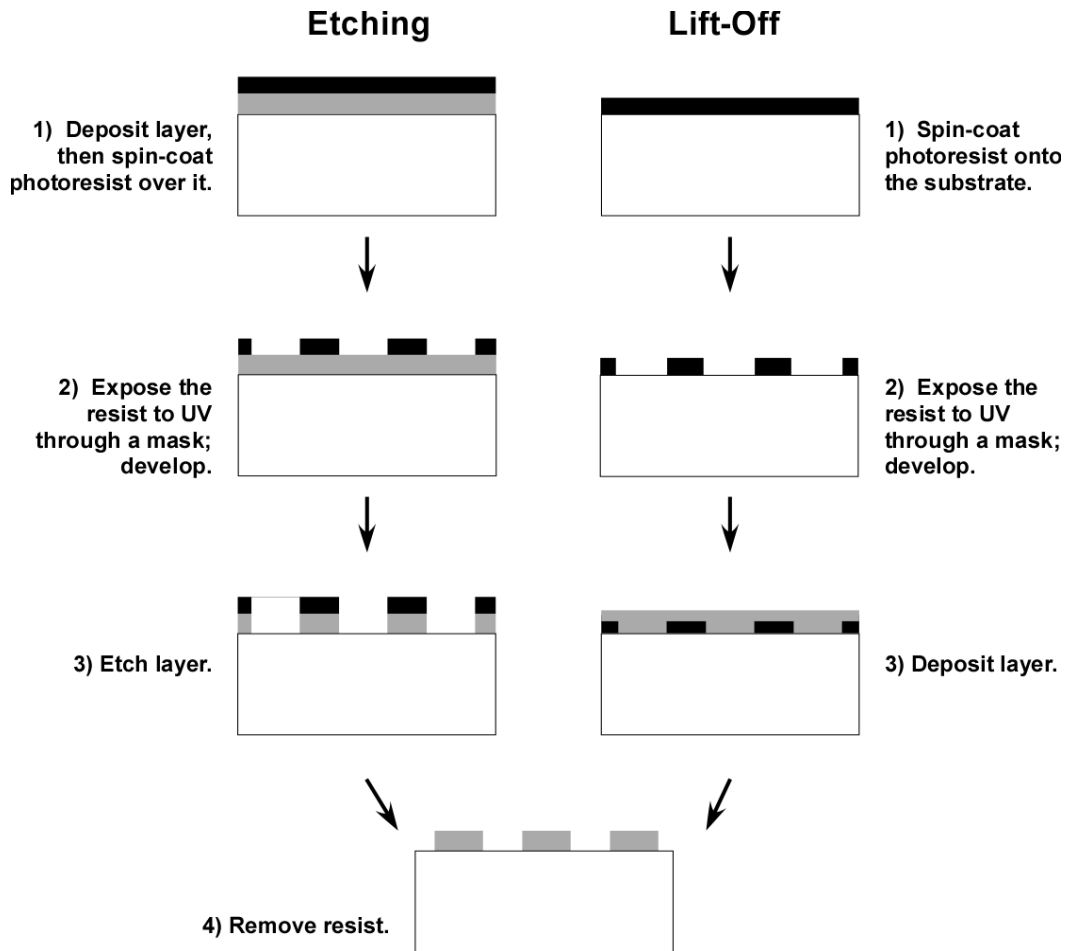
Figure 2-2. Schematic showing the deposition and patterning of a thin film by etching and lift-off.

2.2   Existing Micro-scale DEAs

There are two types of micro-scale devices: those made by bulk micromachining and those made by surface micromachining [65,66]. In bulk micromachining, part of the substrate is removed, as shown in Figure 2-3. In surface micromachining, the device is built up entirely on the surface of the substrate. To partially free a surface micromachined actuator so that it can move in some places but remain attached in

other places, a sacrificial layer is typically used. This is a layer that is added during the formation of the device but removed in the last step, as shown in Figure 2-4.
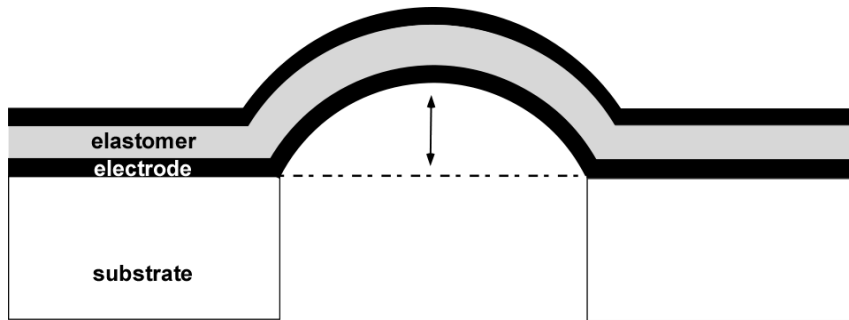
Figure 2-3. Schematic of a bulk micromachined DEA. Part of the substrate is removed to free the device. (Dashed line represents position before actuation.)
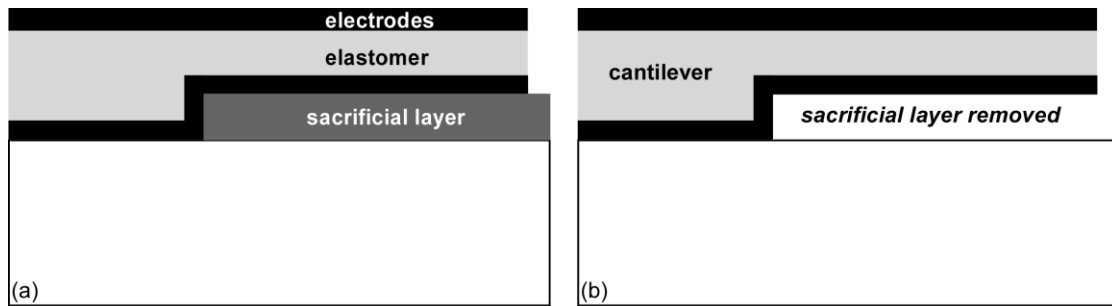
Figure 2-4. Schematic of a surface micromachined DEA. (a) A sacrificial layer supports parts of the device during fabrication. (b) The sacrificial layer is removed to release the moving part.

Figure 2-5 schematically shows four different possible actuation modes for surface micromachined DEAs. Figure 2-5 (a) shows an out-of-plane actuator, (b) an in-plane actuator, (c) a buckling actuator, and (d) a bending actuator. (Note that the actuators in Figure 2-5 (a) and (b) do not require a sacrificial layer, whereas actuators (c) and (d) do). For monolithic integration, surface micromachining is preferred over bulk micromachining because it leaves the substrate intact, allowing more space for the electronics.

Shea *et al*. have demonstrated membrane-style DEAs (such as shown in Figure 2-3) [35]. In most of those devices, through-holes were bulk micromachined into a silicon (Si) substrate, and the elastomer was then transferred manually onto the surface. To form the electrodes, metal ions were ion-implanted into both sides of the elastomer, either before or after the elastomer was attached to the substrate. The membrane dimensions were large, ranging between 1 and 4 mm, making it possible to perform the manual positioning onto the substrate. This fabrication process could not be used for smaller devices.

Pimpin *et al*. have made a synthetic jet utilizing a 2 to 4 mm diameter DEA membrane that was fabricated entirely using bulk micromachining [20]. To form the hole, the back side of the Si wafer was first partially etched. The DEA was fabricated on top of the wafer by first depositing the bottom electrode, which was a patterned metal. The elastomer precursor was deposited by spin coating and then cured. Lastly, the top metal electrode was deposited and patterned. The Si that remained under the membrane was subsequently removed by dry etching to free the membrane.

In both of these membrane DEA devices, the elastomer was neither etched nor patterned. The ability to pattern the elastomer would provide a greater number of actuation modes (Figure 2-5).

Galler *et al*. fabricated micro-scale out-of-plane DEAs (Figure 2-5a) for electro-optical applications by surface micromachining [42]. The DEA was fabricated by patterning the bottom electrode, spin coating and curing the elastomer, and depositing

the top electrode. A transmission electron microscope (TEM) grid was used as an etch mask during the subsequent dry etch of both the top electrode and the underlying elastomer. (Dry etching could be also carried out using a deposited metal mask). This work was the first demonstration of surface micromachined DEAs. The authors noted that if the elastomer was not etched, the out-of-plane deflection was 2.5 times smaller, showing the benefits of patterning this layer.
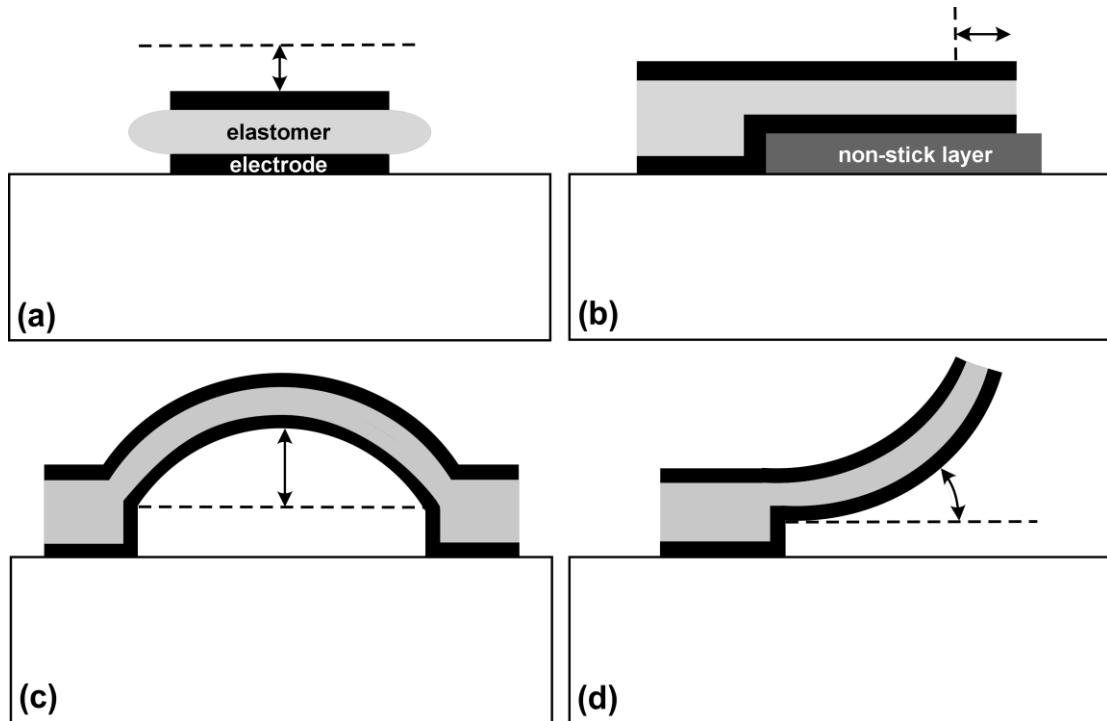
Figure 2-5. Schematic of surface micromachined DEAs showing different actuation modes: a) out-of-plane actuator, b) inplane actuator, c) membrane actuator, and d) bending actuator. (Dashed lines show positions before actuation).

2.3   Elastomers

As discussed above, pre-straining the elastomer is impractical at the micro-scale, and alternative materials are needed that do not require pre-strain to actuate. Possible

candidates reported in the literature include polydimethylsiloxane (PDMS) and electroactive nanostructured elastomers [2,67]. The first is commercially available (for example as Sylgard 184 by Dow Corning [68]) in a two-part precursor form, but the second has to be copolymerized in an involved process.

The elastomer must also be patterned in order to create surface micromachined DEAs. Elastomers can be patterned by non-lithographic methods such as molding [69]. However, these methods are more challenging in terms of surface micromachining. The most convenient method of patterning would be photopatterning: exposing a spin-coatable precursor to UV light through a mask to crosslink it. There are a few photopatternable polymers available, but they generally have high Young's modulus, which reduces the strain. For example, photopatternable silicone WL5130 has a modulus of 160 MPa, 90 times greater than the 1.8 MPa of PDMS [68,70]. It would benefit miniaturization considerably if a photopatternable elastomer is available.

Other lithographic patterning techniques, as described above (Figure 2-2), involve wet or dry (gas phase) etching. For PDMS, fluorine based chemistry is typically used to etch the elastomer. Thus, for dry etching, tetrafluoromethane (CF_4) gas is used and for wet etching, tetrabutyl ammonium fluoride solution is used [71,72]. Our earlier work demonstrated that the combination of wet and dry etching produces the most favorable results, as shown in Figure 2-6.
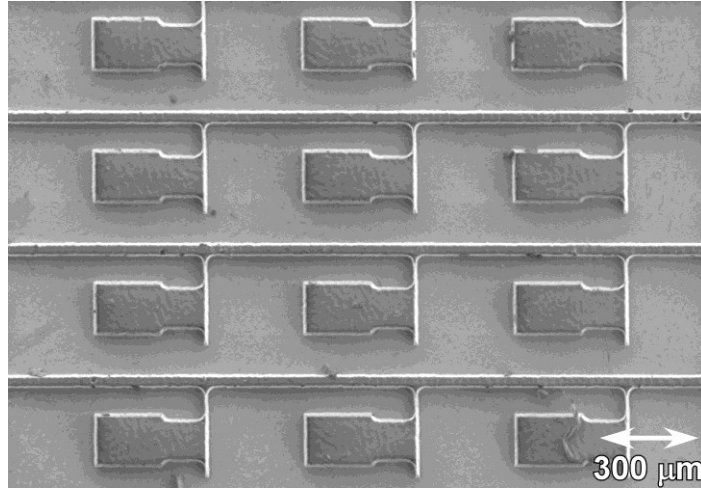
Figure 2-6. PDMS film, 16 μm thick, on an oxidized Si wafer patterned using a combination of wet and dry etching.

2.4   Electrodes

The electrodes of a DEA should have a lower stiffness than the elastomer so that they do not restrict the elastomer motion; in other words, the electrodes must be *compliant*. They must also stay electrically conductive when stretched. Moreover, the adhesion between the elastomer and the electrode must be good. Different types of electrodes have been used in macro-scale DEAs, primarily graphite or metal powders and carbon or silver grease. However, these materials cannot be used on the micro-scale for several reasons. First, the electrode material must not contaminate the clean room. Second, the electrodes should be patternable at high resolution, and the patterning process should be compatible with standard surface micromachining processes. Third, the electrodes should not smear or spread over time or when additional layers are added.

One possible approach to realizing compliant electrodes is to form conductive regions by implanting metal ions (to a depth of ~50 nm) into the elastomer surface [35]. Such electrodes are very compliant: the stiffness of the elastomer is unaffected by the incorporation of the metal ions at the doses of interest. Furthermore, there are no adhesion issues with these electrodes. However, special equipment that is not readily available in most clean rooms is necessary to prepare these electrodes.

Another class of electrodes with good adhesion to the elastomer are composites of the elastomer and a conductive filler, such as graphite, carbon nanotubes (CNTs), or metal nanoparticles. Furthermore, low resolution photopatterning of an elastomer/silver composite was achieved by Cong *et al.* by the addition of light-sensitive additives [73]. However, large amounts (high *loadings*), i.e., tens of percent, of the conductive particles are typically needed before they become conductive, which almost always results in stiffening of the elastomer. The challenge is thus to achieve high conductivity at low loadings. This has been accomplished using exfoliated graphite in PDMS [74]. This composite became conductive (0.4 S/cm) at only 3 wt% loading. In addition, the stiffness of the elastomer was unaffected at loadings up to 25 wt%. This composite could be patterned using the same wet + dry etching techniques discussed earlier or by the photopatterning method of Cong *et al.*

Metal films can also be used as compliant electrodes. Although metal thin films rupture at 1-2% strain [75], patterning the film into zig-zag, serpentine, or horse-shoe

shapes onto an elastomer substrate can enable the metal to undergo strains up to 100% without rupture [76-79]. Horseshoe structures were found to strain 100% with only a 3% change in resistance [79]. The greater the radius: width ratio, *R/W* (Figure 2-7), the better the stretchability. Similarly, the greater the angle of joining, θ, the better the stretchability (a serpentine structure has $\theta = 0°$). The advantage of patterned metal electrodes is that they can be easily incorporated into the microfabrication process. However, the adhesion of the metal to the elastomer can be challenging, and if the elastomer surface is not properly treated, delamination may result. Furthermore, depending on how the metal is deposited, wrinkles can appear on the surface of the elastomer due to residual stress or mismatched coefficients of thermal expansion (CTE). For example, the CTE of PDMS is 10-20 times larger than that of most metals.
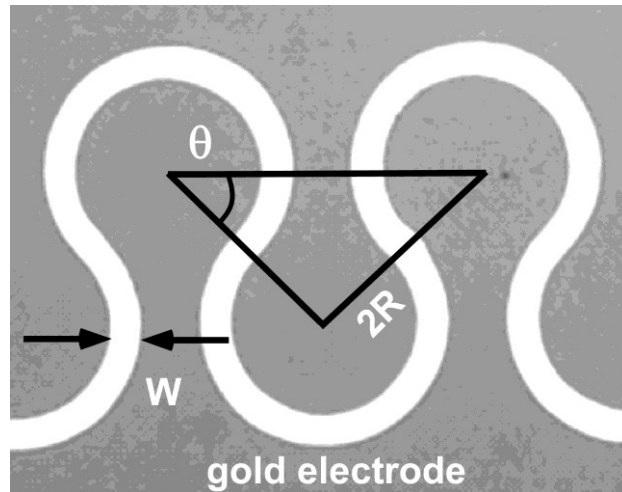
Figure 2-7. Example of a gold film patterned in a horseshoe geometry.

2.5   Additional Challenges

As mentioned previously, surface micromachining typically involves the use of a sacrificial layer. This layer must withstand all of the DEA fabrication steps and be removable when devices are ready for release.

Careful selection of the etchants and solvents used in the fabrication process is critical in preventing damage to the DEA. For example, if a PDMS/metal electrode DEA is fabricated, care must be taken not to expose the PDMS to solvents because PDMS easily swells, resulting in potential delamination [80].

Another issue in surface micromachining is stiction. When the sacrificial layer is removed, Van dar Waals and capillary forces cause the devices to stick to the substrate upon contact. This can be avoided by using anti-stiction coatings or by employing critical point drying [81,82].   Anti-stiction coatings incorporate hydrophobic molecules to reduce the adhesion forces. They can be obtained commercially and deposited as self assembled monolayers from precursors such as octadecyltrichlorosilane or 1H, 1H, 2H, 2H-perfluorodecyltrichlorosilane. In critical point drying, the liquid phase (usually water) is substituted with another liquid (usually CO_2), which is taken from the liquid to the gas phase in the supercritical region under controlled pressure and temperature so that there is no surface tension pulling down the structure during evaporation of the solvent. Another variation

involves freezing the solvent (such as tetrabutyl alcohol) and then subliming it under vacuum.
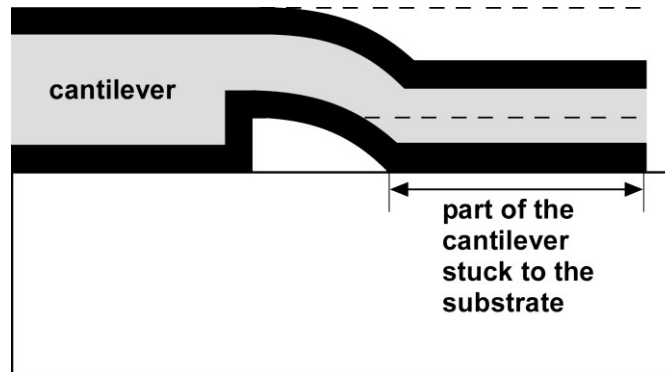
Figure 2-8. Schematic illustration of a cantilever beam stuck to the substrate due to stiction. The dotted line represents the original position.

The other challenge for micro-scale DEAs is to achieve good contact between the external world and the top electrode because the top electrode is resting on the soft elastomer material. Traditional methods like wire bonding cannot be used because the wire would punch through the elastomer or otherwise damage it. It might be possible to use low-temperature soldering.

2.6   Summary

Microscale DEAs have possible applications in many fields. They would compliment existing micro-actuators with a unique set of properties, such as robustness, high strain, and high efficiency. However, additional developments are still required in compliant electrodes, elastomer materials, and fabrication protocols to advance DEAs toward becoming a standard micro-actuator technology.

Acknowledgements

Chapter 3:   Design of Compliant Meanders for Applications in MEMS, Actuators, and Flexible Electronics

Submitted to Smart Materials and Structures

Bavani Balakrisnan[1], Aleksandar Nacev[2], Jeffery Burke[2], Abhijit Dasgupta[1], Elisabeth Smela[1]
[1]Department of Mechanical Engineering, 2176 Glenn L. Martin Hall
[2]Department of Bioengineering, 2314 Kim Building,
University of Maryland, College Park, Maryland 20742

Abstract

Meandering beams, crenellated surfaces, and zigzag-shaped electrodes are employed as compliant elements in micro-scale applications ranging from springs attached to proof masses in micro-electro-mechanical systems (MEMS) to stretchable electrodes in flexible electronics and dielectric elastomer actuators. An understanding of how the meander shape affects the stiffness of these structures would permit preliminary design without the necessity of fabricating or running simulations on each case. In this paper, we present general guidelines for designing meandering cantilevers, showing how the amplitude, angle, length, and thickness affect both the axial and bending stiffnesses. Simple analytical expressions are derived, and the results are compared with those from numerical simulations and experimental measurements. The more complex case of a stiff thin film overlying a crenellated elastomer is also simulated.

Keywords: axial stiffness, bending stiffness, stretchable electrode, corrugated, crenellated, analytical model, FEM, design

3.1 Introduction

Meandering paths are widely used to decrease the stiffness of mechanical structures, including inplane zigzags or serpentines and out-of-plane crenellation or corrugation. This allows one to retain desired properties, such as the high conductivity of a metal or high strength of silicon, without having to employ another material of substantially lower modulus that may not have the same performance or compatibility with standard fabrication methods. For example, meandering polysilicon paths have been used to create springs to tether proof masses in microresonators [83], tunable capacitors[84], and RF switches [85].

Meander paths and crenellation are also often used to form stretchable electrodes from metal films, which are required in flexible displays [86], stretchable circuits [87], flexible antennas [88], and dielectric elastomer actuators (DEAs) [15]. (Patterned metals, unlike some other compliant electrodes, have the advantage of compatibility with standard microfabrication processes). The metal is typically deposited onto a supporting compliant substrate. The rupture strain (ductility) of metals is less than 1% [75], and thin metal films supported on an elastomeric substrate can be strained up to 2.7% before failure [89]. However, patterning the

34

metal inplane allows it to undergo strains of up to 100% without rupture [76-79,90] and with minimal change in conductivity [79]. Patterning in-plane is typically achieved by photolithography [64], while out-of-plane deformation has been produced by molding the surface [91] or by depositing a metal onto a stretched substrate that is later relaxed to form wrinkles [92].

The stiffness of crenellated structures has previously been obtained by summing up, in parallel or in series, the stiffness of each individual segment, obtained using the expression for the stiffness of a cantilever [84,93]. This can, however, under- or over-estimate the stiffness [85] because the interaction among segments is not considered. A closed-form analytical solution for the specific case of a rectangular crenellated cantilever with guided-end boundary conditions has been derived [83]. Numerical simulations have been performed for specific shapes (rectangular, trapezoidal, sinusoidal) under specific boundary conditions (such as both ends fixed, or one end fixed and the other end guided) [83,85,94]. However, extrapolation to other geometries requires new simulations. Thus, while the stiffness of a limited number of crenellated shapes has been studied analytically [83], numerically [94,95], and experimentally [83], a design guide exploring the effects of the meander shape has not been presented.

In order to facilitate the evaluation of the effects of the design parameters, this paper determines the axial and bending stiffness of meandering cantilevered structures (one end fixed and the other free) as a function of their geometry (Figure 3-1), where

35

stiffness (given by the spring constant k) was found from the force required to achieve a unit displacement (or vice versa). The basic unit making up the beam structures (Figure 3-1b) considered in this study comprises two sides of a trapezoid, as shown in Figure 3-1. The key parameters varied in this investigation were the tilt angle α measured from the horizontal, the amplitude A, and the length of the horizontal segment H. When $\alpha = 90°$ a square wave results from concatenating these basic units, and for $H = 0$, a triangle wave is formed. Other shapes considered in this study were sinusoidal and sawtooth.

To permit rapid estimation of the axial and bending stiffnesses and to understand how the various parameters affect them, simple analytical expressions have been derived. The stiffness was also determined using 2D numerical simulations, and we show that the results are within 10% of each other. In addition, the values for several of the shapes were validated experimentally.
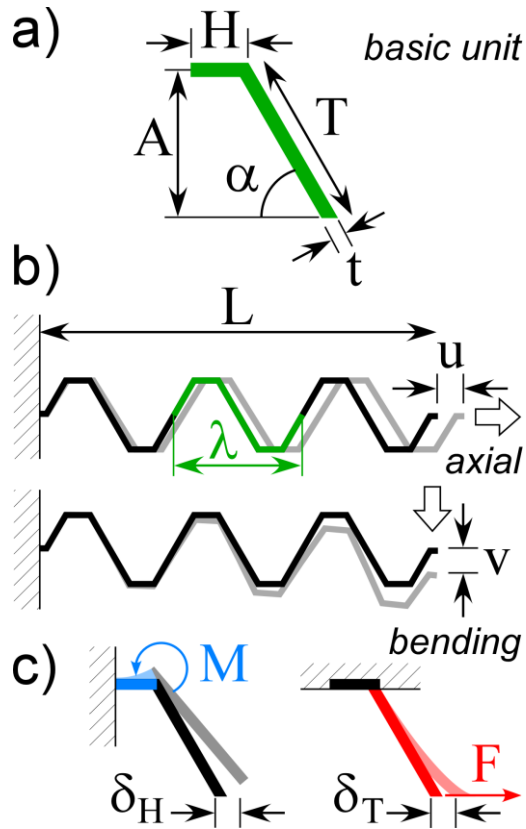
Figure 3-1. a) Parameters defining the beam geometry. b) A trapezoidal example of the 3-period beams used in this work. The fixed-free boundary conditions and the axial and bending displacements are indicated. c) Schematic illustration of the primary deformations of the horizontal and tilted segments of the basic unit during axial elongation induced by an applied force F in the axial direction.

The first key parameter that was varied was the tilt angle α. We show that the axial and bending stiffness both decrease with α: the axial stiffness k_x dropping by a factor of 4 and the bending stiffness k_y by a factor of 2 as α increases from 45° to 120°. Secondly, the amplitude A was varied for a rectangular crenellation ($\alpha = 90°$). The axial stiffness decreases strongly with crenellation height, being proportional to $1/A^3$, while k_y is less affected, being proportional to $1/A$. We also find that axial stiffness is unaffected by the addition of horizontal segments at the vertical center, but

their addition off the vertical center lowers k_x (Section 3.3.5). Bending stiffness depends instead on the overall length of the structure, not the vertical position of additional horizontal segments.

Lastly, using numerical simulations we examined the more complex case of a thin film overlying an out-of-plane-corrugated elastomer of varying thickness (Section 3.3.6). Such structures are found in compliant electrodes [91] and dielectric elastomer actuators [45,91]. We show that for this "filled" structure, at $2A = 0$ (no crenellation) the axial stiffness of the filled structure is approximately equal to that of the metal film. Increasing the crenellation amplitude reduces the axial stiffness by orders of magnitude until it reaches the elastomer stiffness. The bending stiffness for the filled structure with $2A = 0$ is already close to that of the elastomer alone. It initially increases somewhat with crenellation amplitude, reaches a maximum, and then decreases until it levels off at the elastomer stiffness. Crenellation therefore has only a minor effect on bending stiffness, but if it is to be used, care must be taken in designing the crenellation to achieve the desired value.

3.2   Methods

In the simulations, the stiffness was determined by subjecting each structure to a known displacement (axial displacement u or bending displacement v, Figure 3-1b) and calculating the reactive force, F. For the analytical estimates, a force, $F,$ was

applied to the structure and the total displacement, δ, due to deformations of the vertical and horizontal segments was found using basic beam theory.

3.2.1 Numerical Simulations

The numerical simulations were developed using COMSOL Multiphysics version 3.5a, a finite element modeling tool. The 2D structural mechanics plane-stress application mode was used with free triangular meshing and assuming small static prescribed deflections. In the plane-stress mode, the z-components of the stress tensor are assumed to be zero and the loads are constant throughout the width of the material. More detailed information about the model can be found in the Supplementary Information.

The left end boundary of the structure was fixed, and a small prescribed displacement (well below the elastic limit) was applied at the right end of the corrugated beam (Figure 3-1b). For determining axial stiffness, the displacement u was 1 μm. The reaction force in the x-direction was determined by integrating the reaction force at the right hand boundary. The reaction force divided by the prescribed displacement gave the axial stiffness. (The boundary condition was such that the reaction force in the y-direction was zero, so the beam could deflect freely in the y-direction.) Similarly, the bending stiffness was determined by applying a 1 μm displacement v perpendicular to the tip of the cantilever and determining the reaction force in the y-direction. (The boundary condition was such that the reaction force in the x-direction was zero, allowing the cantilever to deflect freely in x-direction). Model validation

was conducted on a straight cantilever beam (see Supplementary Information). The axial and bending stiffnesses, k_x and k_y, were normalized by the width of the beam and the elastic modulus of the material, so they are dimensionless ($\frac{N/m}{m \cdot Pa}$).

For crenellated elastomeric (low modulus) structures with an overlying high-modulus thin film, the modulus of the elastomer was kept constant at 1 MPa and the modulus of the electrode was varied from 5 to 100 GPa. The clamped left side of the structure was kept fixed, and on the free right side equal displacement was applied to both materials. The stiffness was obtained as described above. Because two materials were used in these structures, it was not possible to normalize by the modulus, so the combined beam stiffness was instead normalized by the width of the beam and the stiffness units are N/m^2.

3.2.2   Experimental Methods

A 0.8 mm diameter (giving thickness t = width w = 800 μm) copper (Cu) wire was manually bent to the desired angles to give a structure of three periods, as shown in Figure 3-1a and as used in the simulations. Each period λ was 8 cm long, making L = 24 cm. The length to thickness ratio was L/t = 300 to allow the results to be readily compared to the simulations. Bulk Cu has a modulus E = 120 GPa [96].

For axial stiffness testing, the Cu wire was fixed vertically at the top, weights (5, 10, 20, 30, 40 g) were hung at the bottom, and the deflections were recorded. The wire

was unloaded between tests to confirm the absence of permanent deformation (that the loading was within the elastic regime). The stiffness was found from the slope of the load-deflection plot. For bending stiffness testing, the Cu wire was fixed horizontally on the left side and weights were hung on the right side. Because larger deflections were observed, smaller weights were used (0.28, 0.56, 0.84, 1.12, 1.4 g). (For a picture of the experimental setup, further details, and the displacement data, see Supplementary Information)

3.3 Results

3.3.1 Analytical Estimation of Axial Stiffness

To estimate the axial stiffness of the trapezoidal beams, the deflection of a single unit (Figure 3-1a) was found using beam theory, and the total deflection was obtained by multiplying the deflection of the unit by the number of units. (A more detailed derivation is given in the Supplementary Information.) Briefly, the applied force F produces a moment $M = A \times F$ on the horizontal segment of the unit, H, where A is the amplitude, or distance of segment H above the center line, and is the length of the moment arm. This causes H to bend, angling the vertex connected to the tilted segment, T, by θ_H [97]:

$$\sin \theta_H = \frac{MH}{EI} = \frac{FAH}{EI},$$

(1)

where θ_H is given in radians, H is the length of horizontal segment H, E is the Young's modulus of the material, and I is the moment of inertia of the segment. Thereby, the tilted segment T is rotated, deflecting the tip of T by δ_H (Figure 3-1c):

41

$$\delta_H = A \sin \theta_H = \frac{FA^2 H}{EI} .$$

(2)

The tilted segment T is treated as a cantilever beam fixed at the top end. A force F applied at the tip of a cantilever generates a deflection δ_T given by [97]:

$$\delta_T = \frac{FT^3}{3EI} = \sin\alpha \frac{F\cos\left(\theta_H + 90 - \alpha\right)\left(\dfrac{A}{\sin\alpha}\right)^3}{3EI} ,$$

(3)

where T is the length of segment T.

Summing the two deflections, $\delta = \delta_H + \delta_T$, taking the stiffness $k_x = F/n\delta$, where n is the number of periods in the beam, and using $I = wt^3/12$ for a rectangular cross section, the axial stiffness of the beam is given approximately by:

$$k_x = \frac{Ewt^3}{12nA^2\left(H + \dfrac{A\cos\left(\theta_H + 90 - \alpha\right)}{3\left(\sin\alpha\right)^2}\right)} .$$

(4)

3.3.2 Analytical Estimation of Bending Stiffness

A reasonable analytical estimate of the bending stiffness requires a more complex treatment than the one for the axial stiffness because the moment arm is not constant throughout the beam but depends on the distance of the segment from the end and because terms that were neglected above are not insignificant here. Deflections and rotations caused by both force and moment must be considered. Figure 3-2 shows the various segments and dimensions in the meander.
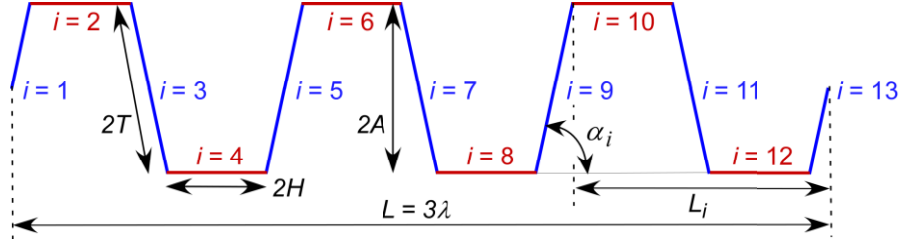
**Figure 3-2. Schematic of a meander structure with *n* = 3 periods of length
λ showing the numbering of the segments as well as the angle and moment
arm for segment *i* = 9.**

Before the structure is subjected to a force at the tip, the length of the moment arm for

the ith horizontal segment is:

(5) $L_i = L + \left[\dfrac{A}{\tan \alpha_i} - \dfrac{i}{2} \dfrac{L}{2n} \right]$, i = even (horizontal segments)

where *n* is the number of periods and the length of the first segment is

$T\cos\alpha_1 = A/\tan\alpha_1$ since $A = T\cos(\alpha_1\text{-}90) = T\sin\alpha_1$.   In what follows, the L_i are

assumed not to change significantly during bending, which is valid for small

deflections. The length of the moment arm for the ith vertical or tilted segment is:

(6) $L_i = L - \left[\dfrac{A}{\tan \alpha_i} + \dfrac{(i-1)}{2} \dfrac{L}{2n} \right]$, i = odd (vertical segments)

except for i = 13, for which it is zero because the moment at the end of the beam is

zero.

Each segment contributes four components to the deflection (Figure 3-3). This is

illustrated for an arbitrary segment i of length B_i at an angle α_i. The segment is

treated as if it is rigidly attached on the left side. For simplicity, the portion of the

meander to the right of the segment is represented as a horizontal line. Figure 3-3a

43

shows the position before the force is applied. The total deflection at the tip is found by summing the four contributions.

Figure 3-3. Illustration of the four contributions to the deflection at the rightmost tip of the structure from a beam segment of length B_i rigidly mounted on its left and attached to a horizontal section of length L_i. a) Before application of the force at the tip. b) Deflection $\delta_{i,F}$ at the tip of the segment due to segment bending caused by the component of force perpendicular to the endpoint of the segment and the resulting deflection $\delta_{i,dF}$ at the endpoint. c) Tilt of the horizontal section due to the bending angle $\theta_{i,F}$ arising from the bending in (b). d) Deflection due to beam bending caused by the moment M on the segment. e) Tilt of the horizontal section due to the bending angle $\theta_{i,M}$.

In response to a force perpendicular to the tip of the meander (Figure 3-3b), the segment will deflect as if it experienced a force $F\cos\alpha_i$ perpendicular to its endpoint, leading it to deflect an amount $\delta_{i,F}$ in that direction. This produces a deflection at the endpoint of the meander of

(7) $\delta_{i,dF} = \delta_{i,F}\cos\alpha_i,$

where the subscript i indicates the segment number, d a contribution due to deflection, and F a contribution due to the force. The tip of the segment is rotated, as a result of the deflection, by an angle $\theta_{i,F}$, tilting the portion of the meander to its right by this angle (Figure 3-3c). The tilt results in a deflection at the meander endpoint of

(8) $\delta_{i,\theta F} = L_i\sin\theta_{i,F},$

where the subscript θ indicates a tip deflection due to tilt.

The force at the tip of the meander furthermore results in a moment $M_i = F \times L_i$ on the segment. The moment also leads to a deflection of the segment (Figure 3-3d), this deflection having a magnitude $\delta_{i,M}$, where the subscript M indicates that the deflection is due to the moment. This appears at the meander endpoint as a deflection of magnitude

(9) $\delta_{i,dM} = \delta_{i,M}\cos\alpha_i.$

This beam bending again causes the portion of the meander to the right of the segment to tilt (Figure 3-3e), and the meander endpoint to displace by

(10) $\delta_{i,\theta M} = L_i\sin\theta_{i,M}.$

Beam theory was used to evaluate the four contributions [97]. The deflection due to force is given by

$$\delta_{i,F} = \frac{(F\cos\alpha_i)B_i^3}{3EI}$$
(11)
,

and the angle $\theta_{i,F}$ is given by

$$\theta_{i,F} = \frac{(F\cos\alpha_i)B_i^2}{2EI}$$
(12)
.

The displacement $\delta_{i,M}$ is given by

$$\delta_{i,M} = \frac{M_iB_i^2}{2EI} = \frac{FL_iB_i^2}{2EI}$$
(13)
,

and, finally, the rotation due to moment is given by

$$\theta_{i,M} = \frac{M_iB_i^2}{EI} = \frac{FL_iB_i}{EI}$$
(14)
.

The deflection at the tip of the meander due to segment i is found by summing the

four terms.

$$\delta_i = \delta_{i,dF} + \delta_{i,\theta F} + \delta_{i,dM} + \delta_{i,\theta M}$$
$$= \frac{(F\cos\alpha_i)B_i^3}{3EI}\cos\alpha_i + L_i\sin\left(\frac{(F\cos\alpha_i)B_i^2}{2EI}\right) + \frac{FL_iB_i^2}{2EI}\cos\alpha_i + L_i\sin\left(\frac{FL_iB_i}{EI}\right)$$

(15)
For small rotations, $\sin\theta_{i,F} \approx \theta_{i,F}$ and $\sin\theta_{i,M} \approx \theta_{i,M}$, allowing Equation (15) to be

simplified as follows.

$$\delta_i \approx \frac{(F\cos\alpha_i)B_i^3}{3EI}\cos\alpha_i + L_i\left(\frac{(F\cos\alpha_i)B_i^2}{2EI}\right) + \frac{FL_iB_i^2}{2EI}\cos\alpha_i + L_i\left(\frac{FL_iB_i}{EI}\right)$$
$$= \frac{FB_i}{EI}\left[\frac{B_i^2\cos^2\alpha_i}{3} + L_iB_i\cos\alpha_i + L_i^2\right]$$
(16)

The total deflection at the tip of the cantilever is the sum over all the segments except

the last ($i = 13$):

$$\delta = \delta_1 + \sum_{i=2}^{4n}\delta_i = \delta_1 + \sum_{i=odd,i=3}^{4n-1}\delta_{iT} + \sum_{i=even,i=2}^{4n}\delta_{iH}$$
(17)
,

where the subscripts H and T indicate the horizontal and vertical segments. The total

number of segments is 4n: 2n horizontal segments and 2n vertical segments.

If one takes into account changes in the angles α_i due to the tilt of segments to their left, then for $i > 1$:

$$\alpha_i = \alpha + \sum_{j=1}^{i-1}\left(\theta_{j,F} + \theta_{j,M}\right)$$

(18)

However, a reasonable estimate can be obtained by treating α as constant. In that case, for $i = $ odd (tilted or vertical segments), $\alpha_i = \alpha$, and for $i = $ even (horizontal segments) $\alpha_i = 0$ and $\cos\alpha_i = 1$. For $i = 1$, $B_i = T$; for $i = $ odd, $B_i = 2T$, and for $i = $ even, $B_i = 2H$. In this case, we can write:

$$\delta = \frac{FT}{EI}\left\{\left[\frac{T^2\cos^2\alpha_1}{3} + L_i T\cos\alpha_1 + L_i^2\right] + 2\sum_{i=odd,i=3}^{4n-1}\left[\frac{(2T)^2\cos^2\alpha_i}{3} + 2L_i T\cos\alpha_i + L_i^2\right]\right\}$$
$$+ \frac{F(2H)}{EI}\sum_{i=even,i=2}^{4n}\left[\frac{(2H)^2}{3} + 2L_i H + L_i^2\right]$$

(19)

The bending stiffness k_y is then given by:

$$k_y = \frac{F}{\delta}$$

(20)

3.3.3 Beam Shape

The effect of beam shape for various trapezoidal configurations was investigated, varying α (and thereby simultaneously H); sinusoid and sawtooth shapes were also examined. The amplitude was fixed at $A = 25t$, where t is the beam thickness, and for each beam, three periods of 100 μm length were used. (In the simulations, to ensure that the displacement was applied at the vertical midline, additional short horizontal sections 2.25 μm in length were affixed at each end making the total length of the

47

beam $L = 304.5$ μm.) The smallest angle allowing that combination of A and L is

$\alpha = 45°$, and the largest angle that gives a shape for which the line does not cross

itself is 130°; we stopped at 120°. (Although not shown here, while the stiffness

values vary with t, the dependence of stiffness on α is unvarying with t.) It should be

noted that axial tension in the x-direction causes a comparable size displacement in

the y-direction.

Table 3-1. Stiffness of beams with a length of three periods, amplitude $A = 25$, and varying shapes, normalized to the stiffness of a straight beam of the same length.

Shape				Relative k_x			Relative k_y		
Type	α (deg)	H (μm)	Schematic	FEM	Estimate	† Expt.	FEM	Estimate	Expt.
Straight Beam	0	---	————————	1.00	1.00	---	1.00	1.00	1.00
				below, x10^{-4}			below, x1		
Trap (triangle)	45	0.0		2.90	2.87	2.45	0.72	0.71	0.62
Trap	49	6.5		2.37	2.36		0.70	0.71	
Trap	56.5	16.7		1.85	1.84		0.66	0.67	
Sawtooth	90, 45	0.0		1.80	1.68		0.43		
Sinusoid	---	---		1.72	---		0.64		
Trap	63.4	25.0		1.56	1.55		0.63	0.63	
Trap	76	37.5		1.24	1.24		0.57	0.57	
Trap (rectangle)	90	50.0		1.00	1.01	1.00	0.51	0.50	0.41
Trap	104	62.5		0.86	0.85		0.46	0.43	
Trap	110	68.2		0.80	0.79	0.75	0.42	0.40	0.34
Trap	120	78.9		0.70	0.69		0.37	0.34	

† Experimental axial values are normalized to the rectangle value, which was set to 1x10^{-4}.

Note: For the dimensions used in the simulations ($L = 300$ μm, $t = 1$ μm), the axial stiffness (per unit modulus and unit width) of the rectangular trapezoid was 3.3x10^{-7} (N/m)/(m·Pa), and its bending stiffness was 4.5x10^{-9}, a factor of 75 smaller. The experimental axial stiffness of this shape was 17.7 N/m and the bending stiffness was 0.23 N/m, smaller by the same

The results of the simulations, analytical estimates, and experimental measurements are presented in Table 3-1 in order of decreasing axial stiffness, normalized by the stiffness of the straight beam to give a relative stiffness. For this amplitude, crenellation reduces the axial stiffness by four orders of magnitude. (The effect of varying amplitude is examined in the next section.) Bending is much less affected, being reduced in the best case by 63%.

3.3.3.1 Axial Stiffness

The agreement between the simulation, analytical, and experimental results for the axial stiffness k_x in Table 3-1 was good, as illustrated in Figure 3-4a. The difference between the FEM result and the analytical estimate was at most 1.5% except for the sawtooth, for which it was 6%. The difference between the experimental and analytical results was at most 3% except for the triangle, for which it was 15%.
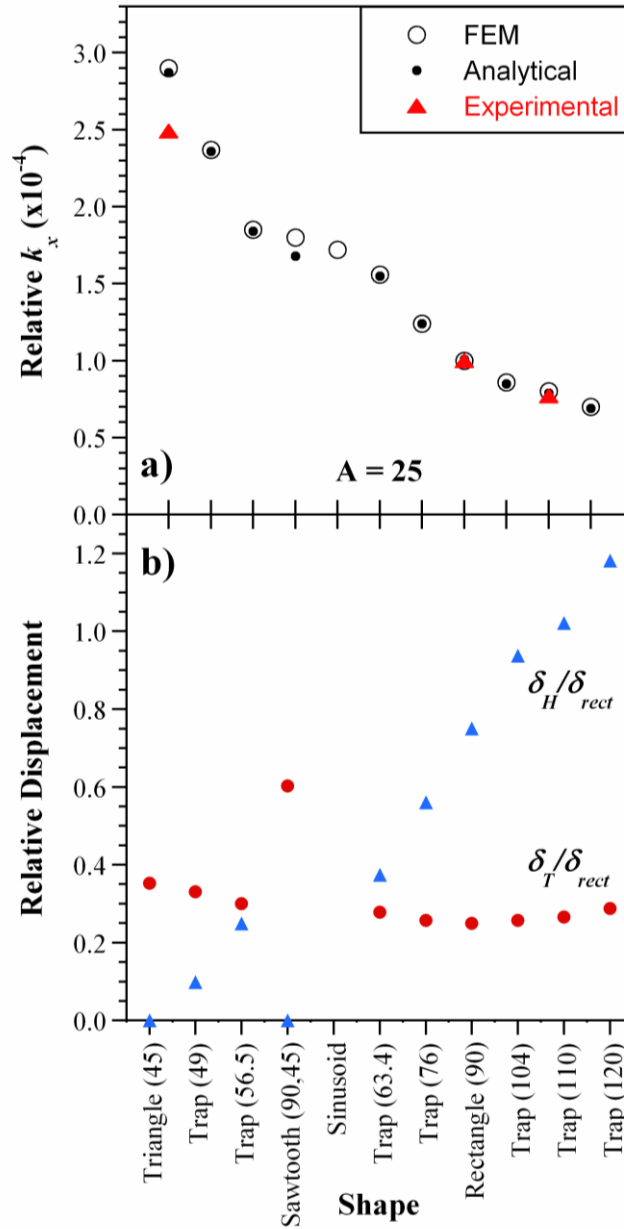
Figure 3-4. a) Axial stiffness relative to that of a straight beam as a function of corrugation angle for an amplitude *A* = 25 found by simulation, analytical estimation, and experimentally. b) The fraction of axial displacement, given by the analytical approach, due to bending of the horizontal (δ_H) and vertical (δ_T) segments, relative to the total axial displacement of the rectangle.

The relative stiffness decreases monotonically with angle α. The triangular shape ($\alpha = 45°$) has the highest relative axial stiffness (2.9×10^{-4}), while the trapezoid with $\alpha = 120°$ has the lowest (0.7×10^{-4}), a factor of four smaller. In comparison with the 10^{-4} drop in stiffness due to crenellation of this amplitude, this difference is relatively small. The rectangular shape is a good choice because it has one of the lowest stiffnesses and is typically the easiest to fabricate.

The reason for the dependence on α is elucidated in Figure 3-4b, which shows the contributions of the displacements δ_H and δ_T due to the horizontal and tilted segments relative to the total displacement of the rectangular shape. The bending of the tilted segment is almost constant across the different shapes, but because of the increasing length of the horizontal segments for the shapes with larger α (δ_H depends linearly on H by Equation (2), and H depends linearly on α), the relative contribution of δ_H to the total displacement increases with α. (Recall that a larger displacement under the same force means a lower stiffness.)

The axial stiffnesses of the sinusoidal and sawtooth beams lies between the trapezoids with α 56.5° and 63.5°. The sinusoidal case cannot be solved with our analytical model, but the sawtooth result was found by summing the contributions of the tilted and vertical components (for this shape, $H = 0$). The sawtooth is softer than the triangle, although both have $H = 0$, because it has greater number of segments (12 versus 6), giving a greater total length.

3.3.3.2 Bending Stiffness

There was also good agreement between the simulations, analytical results, and experiments for the bending stiffness k_y, as illustrated in Figure 3-5a. The difference between the FEM results and the analytical estimates was at most 10%. The difference between the experimental and analytical values was at most 18%. This discrepancy was primarily due to a systematic offset of the experimental values, which were uniformly lower by $15 \pm 2.5\%$. The trend, however, followed exactly as expected. The specimens for meander beam experiments were made by hand-bending the shapes, so the corners were rounded. This offset was more prominent in bending than in axial loading (compare Figure 3-4a) because the change in stiffness was smaller.

As for the axial stiffness, the bending stiffness relative to that of a straight beam decreases with α, from 0.72 at 45° to 0.37 at 120°. The decrease in stiffness is caused by the increase in deflection of the horizontal segments (Figure 3-5b), just as for the axial stiffness. The bending stiffness of the sinusoidal structure follows the same trend, but the bending stiffness of the sawtooth is comparable to that of the rectangle.

Figure 3-5(c) shows the fraction of bending displacement contributed by each of the terms in Equation (15) for the vertical segments. The main contributing factor for the tilted segment is $\delta_{T,\theta M}$, the tilting of the cantilever due to the moment, and the contribution of this term increases with α. Although this term looks large and the

other 3 terms small, ignoring the other 3 terms gives large percentage of error when comparing different shapes. The terms $\delta_{T,dM}$ and $\delta_{T,\theta F}$ are the same magnitude, and they decrease with α, going to zero for the rectangle ($\alpha = 90°$) and then going negative (i.e., causing a deflection in the $-y$ direction). The term $\delta_{T,dF}$ decreases with α and also goes to zero for a rectangle, but then it slightly increases again for $\alpha > 90°$. Since only the $\delta_{T,\theta M}$ contributes to the bending deflection for the rectangle, this simplifies the bending stiffness equation for that shape (see Equation (19)).
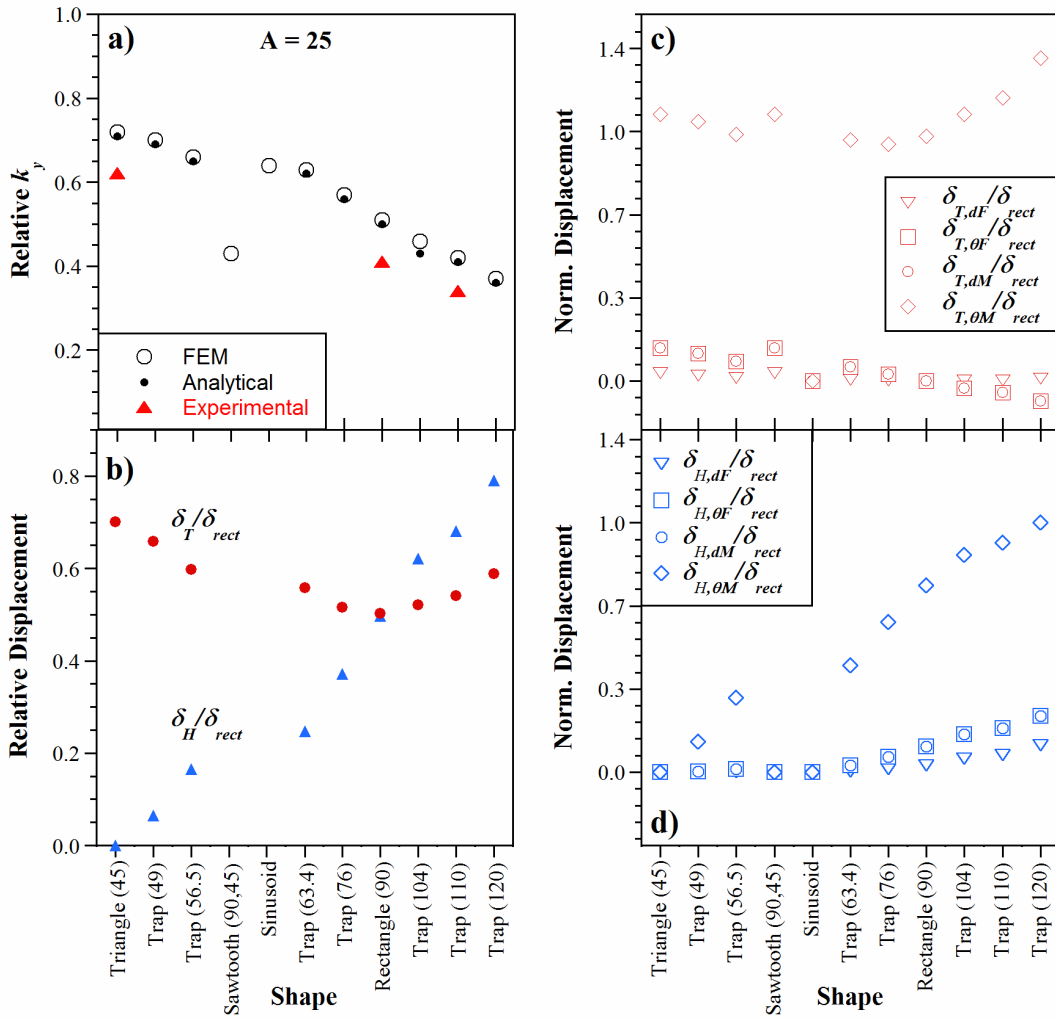
Figure 3-5. a) Relative bending stiffness as a function of corrugation angle for an amplitude $A = 25$ found by simulation, analytical estimation, and experimentally, with the stiffness normalized to that of a straight beam. b) The fraction of bending displacement due to bending of the horizontal (δ_H) and vertical (δ_T) segments given by the analytical approach in (a), normalized by the total displacement of the rectangular crenellation. The relative contributions to (c) δ_T and (d) δ_H by each of the four terms again normalized by the total displacement of the rectangular crenellation.

Figure 3-5(d) shows the fraction of bending displacement contributed by each of the terms in Equation (15) for the horizontal segments. Since the triangle does not have the horizontal segment, all four terms are zero. Just as for the vertical segments, the

main contribution is from $\delta_{H,\theta M}$, the tilting of the cantilever due to the moment. The terms $\delta_{T,dM}$ and $\delta_{T,\theta F}$ are again of comparable magnitudes. The term $\delta_{H,dF}$ contributes the least. Looking at this another way, increasing α increases H, and Equation (14), the largest contributor, increases linearly with H. This results in the bending stiffness actually being proportional to the total length of the structure (for a given A), as shown in Figure 3-6.
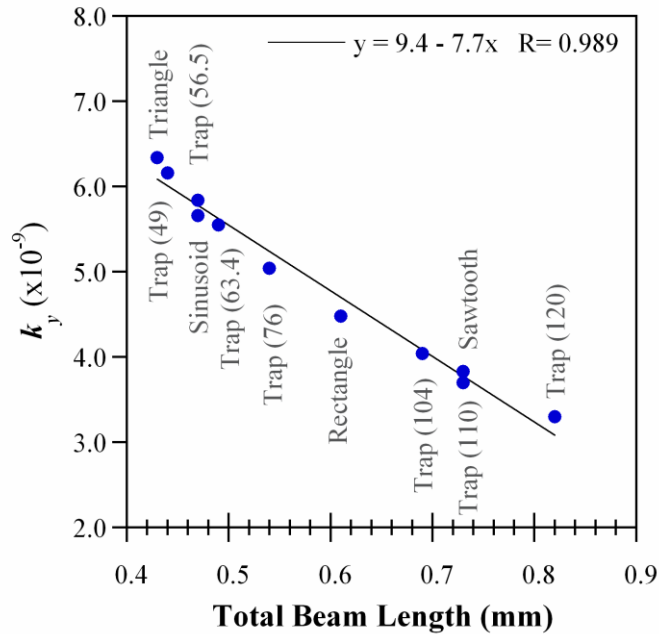
Figure 3-6. Bending stiffness (FEM values) verses the total beam length for the different shapes.

3.3.4 Effect of Amplitude

For $\alpha \neq 90°$, the amplitude A will be limited by the period length. Only for a rectangular crenellation can A be increased without modifying the period. Here we consider, for the rectangular crenellation, the effect of amplitude on the bending and axial stiffness.

56

3.3.4.1 Axial Stiffness

By Equation (4), the most effective way to reduce the axial stiffness of the beam is to decrease its thickness t, since that comes in as the cube. For a given thickness, however, the most effective way to achieve a more compliant beam is to increase the amplitude of the meander or corrugation, A. Figure 3-7a shows the effect on the axial stiffness k_x of varying A for a rectangular crenellated beam ($\alpha = 90$, $H = 25$). The simulation results are shown together with the analytical estimate. For this case, the normalized axial stiffness is:

$$\frac{k_x}{Ew} = \frac{t^3}{144 A^2 \left(H + \dfrac{A\cos(\theta_H)}{3} \right)} \approx \frac{t^3}{144 A^2 \left(H + \dfrac{A}{3} \right)}$$

(21)

As usual, the amplitude is given in units of thickness and the stiffness is reported relative to that of an uncorrugated (straight) beam.
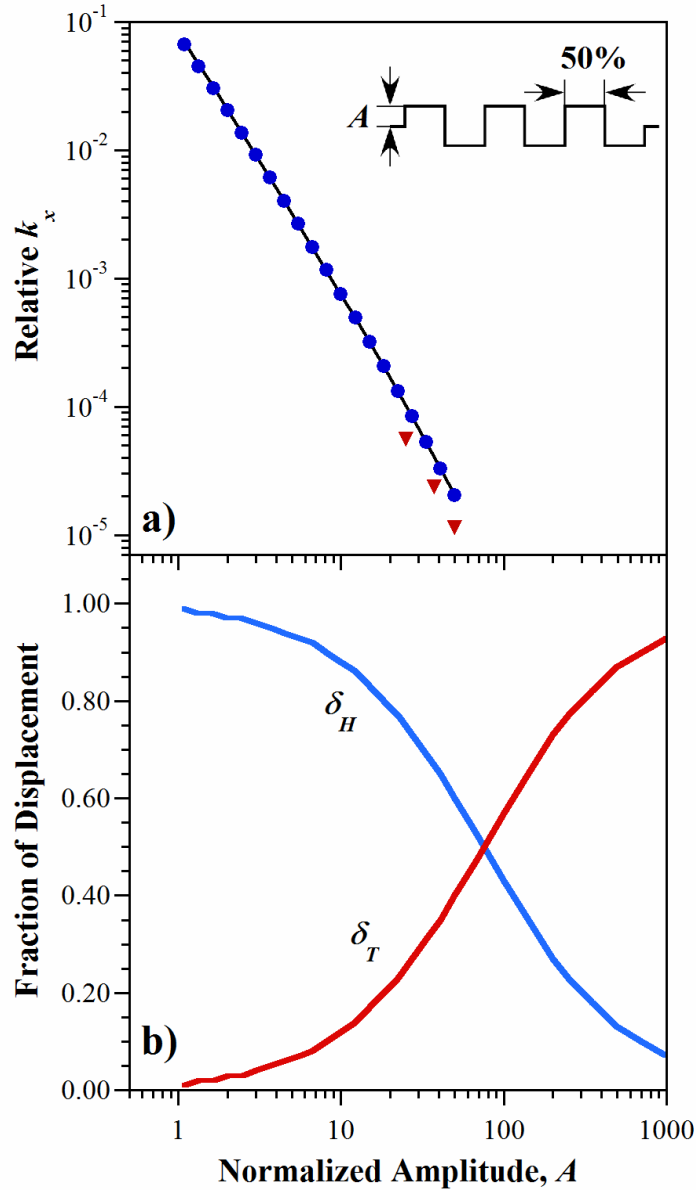
Figure 3-7. a) Axial stiffness relative to that of a straight beam as a function of crenellation amplitude, where A is normalized by the beam thickness t. Simulation results are shown as points and results from Equation (4) as a line. The red triangular points are experimental data. b) The fraction of axial displacement due to bending of the horizontal (δ_H) and vertical (δ_T) segments, given by the analytical approach.

Values from the FEM simulations and the analytical estimate were once again close.

For $A = 1$ (a crenellation amplitude equal to the beam thickness), the difference was

58

5.5%, and the difference dropped rapidly to $< 1\%$ for $A > 3$ (for a plot, see Supplementary Information). This is a remarkably good match, within the 1-3% error of the FEM simulations. The experimental results followed the same trend but were once again systematically lower by 10%.

The axial stiffness falls rapidly with increasing A. For a metal film 1000 Å thick, a crenellation height of 1 μm ($A = 10$) reduces the stiffness by three orders of magnitude, and for $A = 2.5$ μm, four orders of magnitude. These amplitudes are readily achievable with standard microfabrication approaches, both inplane (by photolithographic patterning) and out-of-plane (by etching, molding).

Figure 3-7b gives the fraction of axial beam displacement due to the bending of the horizontal and vertical segments. For small A, the dominant contribution to the lowering of the stiffness comes from the bending of the horizontal segment (Figure 3-7b), which has a length of 25 μm (Figure 3-1a). The bending of the vertical segment becomes more significant when $A = 75t$ ($= 0.75\lambda = 3H$), as expected from Equation (21).

3.3.4.2 Bending Stiffness

According to the analytical model, the bending stiffness of the rectangle is (Supplementary Information for the derivation):

(22)
$$\frac{k_y}{Ew} = \frac{3t^3}{2(6L^3 + 73AL^2)}$$

59

This expression has a linear dependence on $1/A$, whereas the axial stiffness depends on $1/A^3$, accounting for the much smaller effect of crenellation. The bending stiffness drops by less than 50% for a crenellation amplitude of 10, compared to a factor of greater than 1000 for the axial stiffness.

Figure 3-8a shows the bending stiffness from the analytical model, FEM simulations, and experiments. Differences between the FEM simulations and the analytical estimate are less than 2.7% (for a plot of the differences, see Supplementary Information). The experimental values follow the same trend, but with the usual offset.

The relative contributions to the deflection from the horizontal and vertical segments are shown in Figure 3-8b. Again, as expected, for small A the dominant contribution to the lowering of the stiffness comes from the bending of the horizontal segments. From Equation (22), the vertical segments become of equal importance when $A = L/12 = 300/12 = 25$. Thereafter, the moments acting on the vertical segments become more significant.
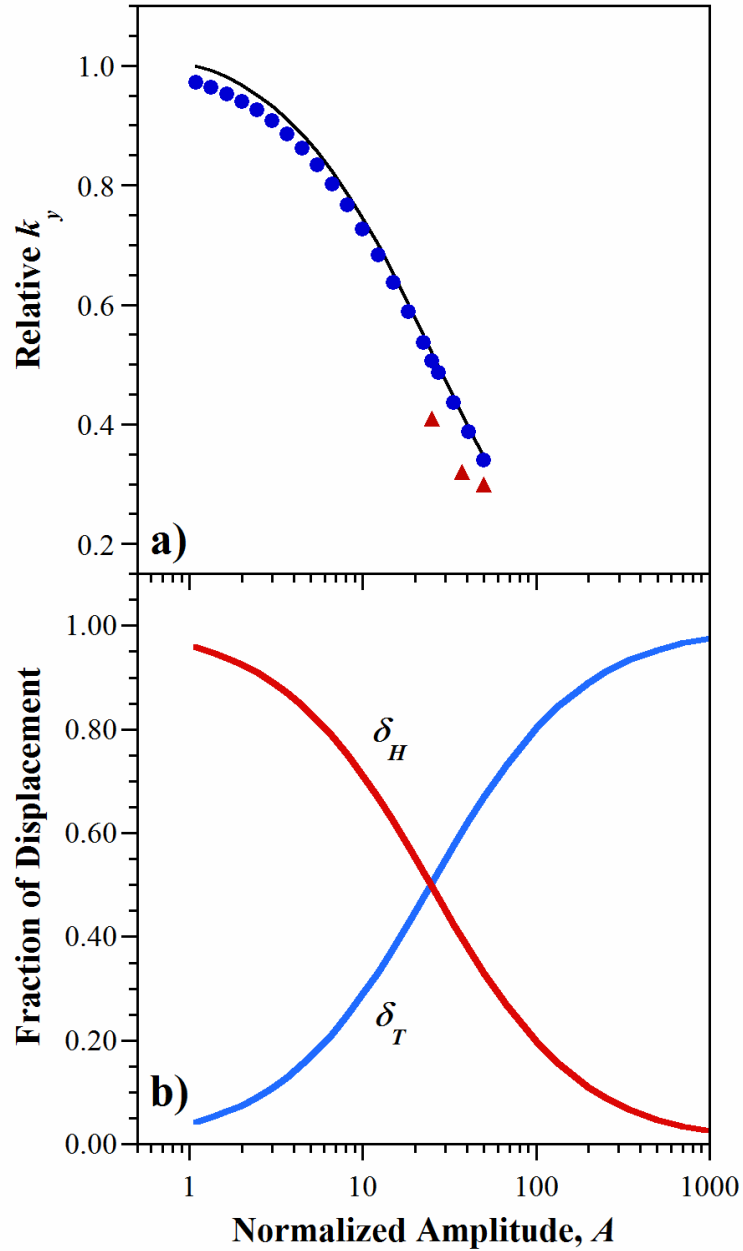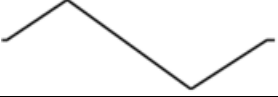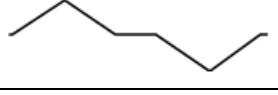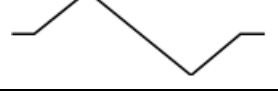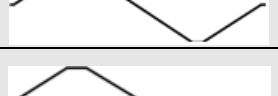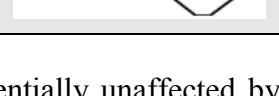
Figure 3-8. a) Bending stiffness relative to that of a straight beam as a function of crenellation amplitude. (Simulation results, round points; results from Equation (4), line; experimental data, triangular points.) b) The fraction of bending displacement due to bending of the horizontal (δ_H) and vertical (δ_T) segments, given by the analytical approach.

3.3.5   Straight Regions at the Horizontal Center of Symmetry

Straight horizontal sections placed at the vertical center of the structure do not bend upon the application of a force in the x-direction, and so were not expected to contribute to lowering the axial stiffness. To confirm this hypothesis, FEM simulations were performed on triangular beams ($\alpha = 45°$, $A = 25t$, one period length, 2 μm long end-attachments) upon changes in the lengths and positions of additional horizontal segments. The structures therefore differed in length. Table 3-2 shows the results.

Table 3-2. Axial and bending stiffness found by FEM for a triangular beam with added straight regions of varying length and vertical position, normalized by the triangular shape.

Straight Regions, Length	Straight Region, Locations	Length	Schematic	Relative Axial Stiffness	Relative Bending Stiffness
0	–	100		1.00	1.00
20	center	120		1.02	0.62
10	both ends	120		1.00	0.63
10, 5	center, both ends	120		1.02	0.63
5	peaks	110		0.81	0.77
10	peaks	120		0.69	0.62
5, 10	peaks, center	120		0.82	0.62

As expected, the axial stiffness is essentially unaffected by the addition of straight sections at the vertical center of symmetry, either in the middle of the beam or at the ends. The addition of small straight sections off the vertical center, however, lowers the stiffness, as was also seen in Figure 3-4.

As shown above, the bending stiffness is proportional to the total length of the structure. This remains true upon the addition of horizontal segments anywhere, which serve to increase the length: the bending stiffness again decreases linearly with total length.

3.3.6 Elastomer under a Crenellated Beam

Metal out-of-plane crenellations and inplane meanders have been used to form compliant electrodes on elastomeric substrates. To fabricate the former, a metal film can be deposited onto an elastomer having a corrugated surface, as demonstrated by Benslimane and Gravesen [91] and subsequently patented and used by Danfoss PolyPower A/S in their commercial DEA material [98]. The corrugation can be formed by techniques such as molding or etching, producing angled corners. Alternatively, the metal can be deposited onto a stretched elastomer, spontaneously forming smooth sinusoid-like wrinkles when the elastomer is relaxed [92]. To form inplane meanders, a metal film is deposited onto a flat elastomer substrate and patterned photolithographically into a meander line. Extensive modeling and experimental work has been done on the second type [77-79,87,89,99-106], so it will not be discussed here.

An elastomer with one rectangular crenellated surface coated by an electrode (Figure 3-9) was modeled by FEM to find the structure's axial and bending stiffness. The thickness $t_{elast.}$ is the thickness of the elastomer underneath the crenellated part, from the flat bottom surface of the elastomer to the trough of the crenellated electrode. The amplitude $2A$, electrode thickness t, structure length L, and period λ are defined the same way as above.
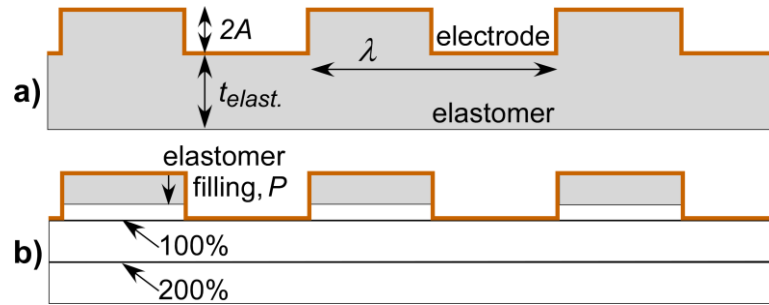
Figure 3-9. Schematic of an elastomer with a crenellated, electrode-covered top surface and a flat uncoated bottom surface. (a) In one set of FEM simulations, 2A was varied and the other dimensions were kept fixed at $t_{elast.}$ = 50 μm, λ = 100 μm, L = 305 μm, t = 1 μm. (b) In a second set of simulations, the percentage of elastomer filling was increased with the electrode dimensions fixed. The lines show the levels at which 100% and 200% of the crenellation are filled.

The effect on stiffness from filling the crenellated shape with an elastomer is shown in Figure 3-10. The filling percentage P is measured from the top of the electrode and given as a fraction of 2A: at 100% the crenellation is completely filled (Figure 3-9b). In these simulations, the Poisson's ratio, ν for the electrode was 0.34, which is a typical value for a metal [96], and for the elastomer it was ν = 0.49, the value for PDMS [61].

The axial stiffness k_{fx} of the filled structure is sigmoidal with P (Figure 3-10a), showing little change up to 50% filling. Above 50%, k_{fx} increases quasi-linearly with P until 200%, and then it flattens out to approximately twice the unfilled stiffness. The axial stiffness of the filled structure is thus dominated by the electrode stiffness, as is confirmed below.
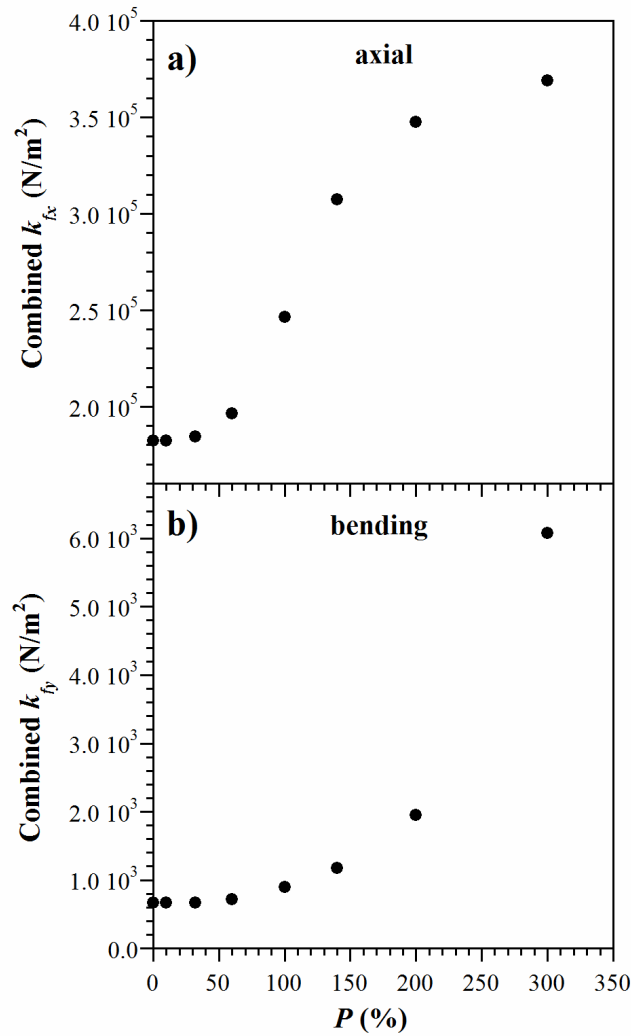
Figure 3-10. The (a) axial and (b) bending stiffness of a rectangular crenellated beam as a function of elastomer filling amount ($t = 1$ μm, $2A = 25$ μm, $E_{electrode} = 120$ GPa, and $E_{elastomer} = 10^{-3}$ GPa).

The bending stiffness k_{fy} follows an x^3 relationship with thickness added to the original structure (Figure 3-10b). Thus, filling to 100% does not significantly change the bending stiffness, but thereafter the stiffness increases as P^3. (Thicknesses greater than 300% were not explored in our study). Unlike for the axial case, the bending stiffness becomes dominated by the elastomer.

66

To gain insight into the shape of the curves in Figure 3-10, the electrode modulus $E_{electrode}$ was varied between 5 and 120 GPa while keeping the elastomer modulus $E_{elastomer}$ constant at 10^{-3} GPa. Six different crenellation amplitudes were studied between $2A = 2$ and 200 μm for a metal film thickness of $t = 1$ μm. The crenellated area was in all the combined cases completely filled, and under the crenellation was an elastomer of thickness $t_{elast.} = 50$ μm (as illustrated in Figure 3-9a). The stiffness is plotted versus the ratio of the moduli $E_{electrode}/E_{elastomer}$ and versus the crenellation height ($2A$) in Figure 3-11. Crenellated electrodes alone are shown for comparison, and for these $E_{electrode}$ was divided by the 10^{-3} GPa modulus of elastomer. The crenellated elastomer alone is also included (as for the combined structure, 50 μm of elastomer plus a $2A$ crenellation height above that), $E_{electrode} = 0$. This is therefore drawn as a horizontal line for visualization. (The elastomer stiffnesses for the different $2A$ overlap and so cannot be distinguished.) Adding the $2A = 25$ crenellated electrode (open black triangles) and the $2A = 25$ elastomer (horizontal gray line) yields the dashed gray line. The axial stiffness of the straight beam ($2A = 0$) with underlying elastomer thickness 50 μm is too large to be included in Figure 3-11a (it is 4 orders of magnitude greater than the crenellated structures, as presented in Table 3-1), but the bending stiffness of the straight beam is shown as the red line in Figure 3-11b. (The k_{fx} for $2A = 2$ μm and 6 μm are also much larger and lie beyond the scale of Figure 3-11a.)
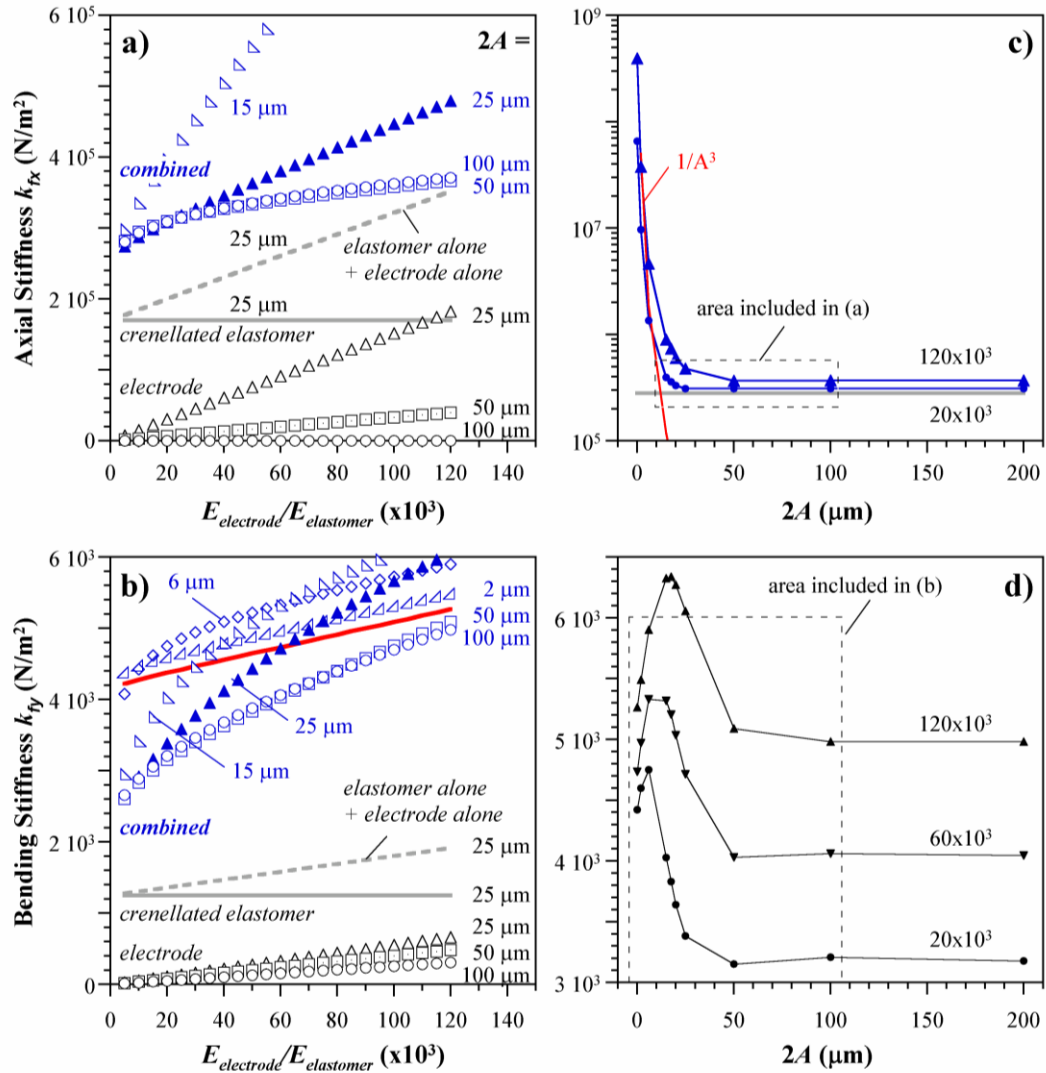
Figure 3-11. a) Axial and b) bending stiffness of the combined elastomer + metal structure shown in Figure 3-9 as a function of the electrode:elastomer stiffness ratio for different crenellation amplitudes 2A and a 50 μm thickness of elastomer under the crenellation (blue symbols, top). Filled triangles indicate the structure of Figure 3-10 with P = 200%. Also shown are the stiffnesses of the crenellated electrodes alone (black symbols, bottom), the crenellated elastomer alone (50 μm + 2A, solid gray line), and the sum of these two (dashed gray line). The red line in (b) shows the bending stiffness of a 50 μm thick layer of PDMS with an overlying flat metal film (2A = 0). c) Axial and d) bending stiffness of the structure as a function of 2A for three values of $E_{electrode}/E_{elastomer}$ (solid lines are guides to the eye).

68

Looking at the axial stiffness of the combined structures (blue symbols) in Figure 3-11a, the axial stiffness increases with $E_{electrode}/E_{elastomer}$ for all values of $2A$, as expected. Also, the expected lowering of stiffness with crenellation height is seen, just as for the electrode alone (black symbols). One might, however, have assumed that the combined axial stiffness k_{fx} would be close to that found by the simple addition of the individual electrode and crenellated elastomer stiffnesses, but that is not the case. Comparing the 25 µm combined structure (solid blue triangles) with the sum (dashed line) of the electrode alone (open triangles) and the elastomer alone (solid line), the combined structure is offset upward by a constant 10^5 N/m^2. The interaction between the electrode and the elastomer arising from bonding the two constrains the axial motion, raising k_{fx}. Another thing to note in Figure 3-11a is that when $2A$ is large, unlike for the electrode alone, the combined structure's axial stiffness increases sublinearly with the modulus of the electrode.

Figure 3-11c shows the dependence of k_{fx} on $2A$ for two values of the relative electrode stiffness. (The range of values in Figure 3-11a is indicated to allow comparison of the two plots.) There are two distinct regimes of behavior: (1) electrode stiffness dominated and (2) elastomer stiffness dominated. The initial slope at small $2A$ is consistent with the results of Figure 3-7, where the axial stiffness of the crenellated electrode decreases as $1/A^3$; for illustration, the red line in Figure 3-11c decreases as $1/A^3$. For larger $2A$, above 50 µm, the stiffness approaches that of the crenellated elastomer alone, shown by the gray line. This plot illuminates the curves in Figure 3-11a: for $2A < 50$ µm, where the crenellated electrode dominates, there is

a linear relationship between k_{fx} and $E_{electrode}/E_{elastomer}$. For $2A \geq 50$, where the elastomer dominates, there is a nonlinear relationship between k_{fx} and $E_{electrode}/E_{elastomer}$ because k_{fx} approaches a constant value.

Figure 3-11b shows the variation of bending stiffness k_{fy} with $E_{electrode}/E_{elastomer}$. As in the case of the axial stiffness, k_{fy} is not a simple addition of the individual electrode and crenellated elastomer stiffnesses. Furthermore, the combined structure is in some cases stiffer than the straight beam (red line), and in other cases less stiff. Looking first at the smallest corrugation, $2A = 2$ μm, the stiffness is close to that for the uncrenellated beam, being offset slightly upward. This is as expected. For $2A = 6$ μm, the slope is greater, but for the smallest $E_{electrode}/E_{elastomer}$ values, the structure is actually less stiff than the straight beam. This curve, and the later ones, are also nonlinear. This trend continues for $2A = 15$ μm, which is almost half as stiff as the straight beam for small $E_{electrode}/E_{elastomer}$, equally stiff at $E_{electrode}/E_{elastomer} = 30 \times 10^3$, and thereafter increasing even more strongly with $E_{electrode}/E_{elastomer}$ than $2A = 6$ μm did. For larger values of $2A$, the curves all have the same stiffness at small $E_{electrode}/E_{elastomer}$. However, the slopes reverse trend and become less steep with increasing $2A$. In fact, with further increases in crenellation amplitude, the stiffness decreases.

Showing the data as a function of $2A$ in Figure 3-11d for three values of $E_{electrode}/E_{elastomer}$ again helps to explain the behavior. At $2A = 0$ the beam is uncrenellated. Unlike for axial stiffness, adding a small crenellation actually initially

70

increases the bending stiffness k_{fy}. It reaches a peak at $2A \approx 15$ μm, then decreases and levels off above $2A \approx 50$ μm to a value that is lower than that of the flat beam. (The $2A = 50$ μm point with $t_{elast.} = 50$ μm corresponds to $P = 200\%$ in Figure 3-10.) Like in Figure 3-11c, for large crenellations the stiffness becomes independent of $2A$. Increasing values of $E_{electrode}/E_{elastomer,}$ result in an overall upshift in stiffness as well as a shift in peak position to higher values of $2A$. These results mean that for bending structures, both $2A$ and $E_{electrode}/E_{elastomer}$ must be chosen to ensure the desired behavior, with both lesser and greater stiffness than a straight beam possible, depending on the parameters. A bending dielectric elastomer actuator with one straight electrode and one crenellated electrode could bend either toward or away from the straight side by changing the design. It should be noted, however, that changes in bending stiffness with crenellation are relatively small (the *y*-axis is linear) compared with changes in the axial stiffness (for which the *y*-axis has a log scale).

3.4   Discussion and Conclusions

We have presented design guidelines based on analytic models derived from beam theory for using out-of-plane crenellation or inplane meandering to reduce the stiffness of a beam. We have derived relatively simple analytical expressions that can be readily applied and that accurately predict the axial and bending stiffness.

The effect of crenellation on axial stiffness is substantially larger than it is on bending stiffness. For both, decreasing the beam thickness and increasing the angle of the

71

vertical-going segments lowers stiffness.   Increasing α affects axial stiffness primarily by increasing the length of the off-midline horizontal segments, while it affects bending stiffness primarily by increasing the total length of the beam. However, the most effective way to reduce the axial stiffness is by increasing the height of the crenellations, which can lower it by orders of magnitude.

Curved meanders are preferred over those with sharp corners because the latter experience larger stress concentrations that can lead to premature failure upon repeated extension. However, from a microfabrication point of view, out-of-plane sinusoidal curves are more challenging to fabricate than trapezoidal structures. (One can produce any desired shape inplane by creation of an appropriate mask.) Instead, one can readily produce out-of-plane rectangular crenellation by anisotropic dry etching of the substrate, trapezoidal crenellation with $\alpha = 54.7°$ by Si anisotropic wet etching, and partially curved structures by isotropic wet etching.   With other fabrication methods, corrugated shapes are produced by bending or folding sheets, strips, or wires, and weaving results in sinusoidal-like corrugation.

When fabricating axial devices, appropriated space for extension must be provided. Thus, it is important to note that axial tension in the x-direction leads not only to displacement in the x-direction, but also to displacement in the y-direction because of out-of-plane deformation of the crenellated shapes [107]. For a 1 μm prescribed displacement in x, a more than 1 μm displacement occurs in y. For bending, on the

other hand, displacement in the *y*-direction is not coupled to significant *x*-displacement.

Elastomer-filled, metal-film-coated structures with moderate crenellation amplitudes are a thousand times less stiff when stretched in the axial direction than uncrenellated beams, approaching the stiffness of the elastomer alone. Even a small crenellation decreases the axial stiffness dramatically. However, the situation is quite different for bending, which is weakly affected by crenellation. While for large crenellations the bending stiffness drops somewhat, at low crenellation amplitude the stiffness is actually higher than that of a straight beam. Thus, when designing crenellated bending structures, appropriate values of the electrode stiffness and crenellation height must be chosen to achieve the desired behavior.

Acknowledgements

Supplementary Description

The supplementary information includes information about the COMSOL simulation, model validation, and experimental data. In addition, the axial stiffness derivation and the simplification of bending stiffness to rectangular crenellation are given.

73

Finally, the difference between the analytical and FEM for various amplitudes of rectangular crenellation is also illustrated.

Supplementary Information

Simulation: Implementation and Computational Parameters

Governing Equations

The software package COMSOL Multiphysics (version 3.5a) was used for implementing the numerical simulations. COMSOL solved the following discretized structural mechanics partial differential equation (PDE):

$$(\text{SI-1}) \quad \vec{F} = -\nabla \cdot \sigma \, ,$$

where F is the force vector and ∇ is the differential operator [108]. The stress tensor σ was classically defined as:

$$(\text{SI-2}) \quad \sigma = \begin{bmatrix} \sigma_x & \tau_{xy} & \tau_{xz} \\ \tau_{yx} & \sigma_y & \tau_{yz} \\ \tau_{zx} & \tau_{zy} & \sigma_z \end{bmatrix}, \quad \tau_{xy} = \tau_{yx}, \quad \tau_{xz} = \tau_{zx}, \quad \tau_{yz} = \tau_{zy} \, ,$$

where σ_x, σ_y, and σ_z are the normal stresses acting in the x, y, and z directions, respectively, and τ_{xy}, τ_{xz}, and τ_{yz} are the shear stresses. The notation τ_{xy} denotes that the shear stress acts on face x in the y-direction. Similarly, the classical strain tensor [97] was defined as:

$$(\text{SI-3}) \quad \varepsilon = \begin{bmatrix} \varepsilon_x & \varepsilon_{xy} & \varepsilon_{xz} \\ \varepsilon_{xy} & \varepsilon_y & \varepsilon_{yz} \\ \varepsilon_{xz} & \varepsilon_{yz} & \varepsilon_z \end{bmatrix},$$

where

$$\text{(SI-4)} \quad \begin{aligned} \varepsilon_x &= \frac{\partial u}{\partial x} & \varepsilon_{xy} &= \frac{\gamma_{xy}}{2} = \frac{1}{2}\left(\frac{\partial u}{\partial y} + \frac{\partial v}{\partial x}\right) \\ \varepsilon_y &= \frac{\partial v}{\partial y} & \varepsilon_{yz} &= \frac{\gamma_{yz}}{2} = \frac{1}{2}\left(\frac{\partial v}{\partial z} + \frac{\partial w}{\partial y}\right) \\ \varepsilon_z &= \frac{\partial w}{\partial z} & \varepsilon_{xz} &= \frac{\gamma_{xz}}{2} = \frac{1}{2}\left(\frac{\partial u}{\partial z} + \frac{\partial w}{\partial x}\right) \end{aligned}$$

with u, v, and w defined as the displacements in the x, y and z directions, respectively,

ε_x, ε_y, and ε_z as the normal strains, and γ_{xy}, γ_{yz}, and γ_{xz} as the shear strains.

Using classical structural mechanics, the relationship between the strain and stress tensors is obtained by reorganizing the strain and stress tensors into a six-element vector form, which simplifies the numerical simulation. The relationship between the stress and strain vectors is

$$\text{(SI-5)} \quad \sigma = D\varepsilon \,,$$

where D is the elasticity matrix. By observing that three elements in the stress tensor are equivalent to three others (see equation (SI-2)), one can write

$$\text{(SI-6)} \quad \sigma = \begin{bmatrix} \sigma_x \\ \sigma_y \\ \sigma_z \\ \tau_{xy} \\ \tau_{yz} \\ \tau_{xz} \end{bmatrix}, \quad \varepsilon = \begin{bmatrix} \varepsilon_x \\ \varepsilon_y \\ \varepsilon_z \\ \gamma_{xy} \\ \gamma_{yz} \\ \gamma_{xz} \end{bmatrix}.$$

The elasticity matrix is then a 6 x 6 matrix defined as:

$$\text{(SI-7)} \quad D = \frac{E}{(1+v)(1-2v)} \begin{bmatrix} 1-v & v & v & 0 & 0 & 0 \\ v & 1-v & v & 0 & 0 & 0 \\ v & v & 1-v & 0 & 0 & 0 \\ 0 & 0 & 0 & \dfrac{1-2v}{2} & 0 & 0 \\ 0 & 0 & 0 & 0 & \dfrac{1-2v}{2} & 0 \\ 0 & 0 & 0 & 0 & 0 & \dfrac{1-2v}{2} \end{bmatrix},$$

where E is the Young's modulus and v is Poisson's ratio. The above equations can be solved to give the displacement (or strain shown in equation (SI-5)) of an object from the induced stresses (calculated from the applied forces in equation (SI-1)) and the material properties described by the displacement matrix (equation (SI-7)).

Boundary Conditions and Constraints

Discretization involves breaking the geometry into small volume elements (mesh elements). The stresses, strains, and resultant deflections are calculated for each element based on its mechanical properties (in this case, the Young's modulus and Poisson ratio) and the specified boundary conditions.

The simulation was two-dimensional (2D), meaning that it looked at the cantilever cross section and did not consider changes in the width direction (z direction). This saved computation time without loss of accuracy. To simplify to two dimensions, the third dimension was accounted for by specifying that it held no stress (σ_z, τ_{xz}, and τ_{yz} are zero). This assumption is reasonable for structures whose out-of-plane width is much greater than their length. Agreement between the full 3D and the 2D model

76

was checked for the case rectangular crenellation with $A = 25$; results were within 7%.

The boundary conditions for the 2D model are summarized in SI_Table 1, completing the definition of the model. The reaction forces acting upon the entire structure are determined by solving the model. The structure's reaction forces are computed by integrating over the right-hand boundary (determined using equation (SI-1)) subject to the requirement that the sum of all forces acting upon a structure is zero.

SI_Table 1. Boundary conditions used in the simulations.

Boundary	Physical Interpretation	Definition
Left hand boundary	No horizontal or vertical movement.	$u = 0$, $v = 0$
Right hand boundary	Prescribed physical displacement	$u = u_{prescribed}$ or $v = v_{prescribed}$
All other boundaries	Continuity	Solved by Equations (SI-1) - (SI-7)

Meshing

With any finite element modeling (FEM), the mesh size must be sufficiently small to capture the physics, including any steep gradients in the solutions that might occur at edges, corners, and interfaces. Mesh refinement, a technique in which the mesh element size is systematically reduced, was enacted until the solution converged to a stable value (a variation of $\leq 1\%$); in most instances 2 to 3 mesh refinements were sufficient. The shape of the mesh is also a consideration. We used a free (not fixed or uniformly sized) triangular (not quad) mesh because it ensured that the physics

were accurately captured for any geometry: curves can be modeled more accurately using triangular meshes compared to square or quad meshes [108].

Solving

The COMSOL solver UMFPACK, an unsymmetric multifrontal method designed to solve asymmetric sparse linear systems [109], was used to solve the system of equations, and it was sufficient to generate a converged solution. Issues with convergence arose when the model was displaced by large values (on the order of the length of the model, $A = 100$); this problem was resolved by fixing the structure at a single point instead of along a boundary.

Post-Processing

In order to obtain accurate values for the reaction force under a prescribed displacement, the displacement in the perpendicular direction must be free to change, meaning that the right-hand boundary only contains a prescribed physical displacement in the x-direction (or y-direction) for axial (bending) stiffness. This ensures that the force exerted upon the structure is in only a single direction while allowing the structure to freely deform, and thereby to compensate for that geometric change. As mentioned previously, the model's reaction forces due to the prescribed displacement are determined by integrating the reaction forces (equation (SI-1) from the solved model) at the right hand boundary.

Model Validation with Cantilevered Rectangular Beam

The axial stiffness of a rectangular cantilevered beam is given by [97],

$$k_x = \frac{Ewt}{L}$$
(SI-8)

and its bending stiffness is given by

$$k_y = \frac{Ewt^3}{4L^3}$$
(SI-9)

where E is the Young's modulus, w is the width of the beam, t is its thickness, and L is its length.

As a control to check that the COMSOL simulations were working properly, the stiffness of a straight cantilevered beam was found. The beam was 1 μm thick and had a length L varying from 100 to 500 μm. Since this was a 2D simulation, the width w was set to be essentially infinite so that the stress is the width direction could be considered zero; in practice this was done by setting $w = 1$ m. A displacement of 1 μm in the $+x$ direction (along the long axis of the beam) was prescribed, and the x-direction reaction force was determined. This strain was small compared to the length and smaller than the plastic strain limit of the material. The axial stiffness was determined by dividing the reaction force by the displacement: $k_x = F_x/x$. Similarly, to determine the bending stiffness a 1 μm displacement was applied perpendicular to the tip of the cantilever, and the y-direction reaction force was determined: $k_y = F_y/y$. As described above, it was necessary to *not* set the displacement in the other direction equal to zero.
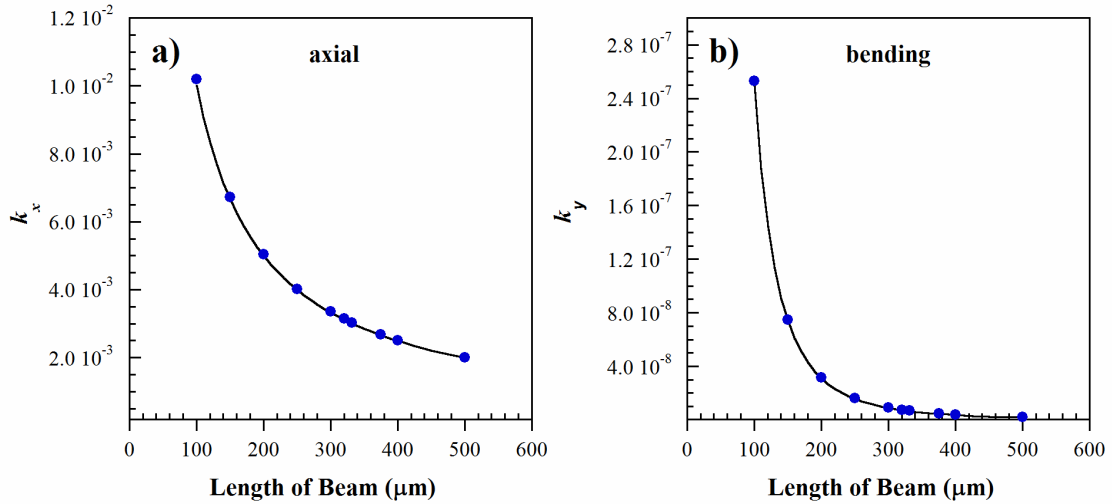
SI_Figure 1. Stiffness versus cantilever length. The blue symbols are the FEM results while the black lines are the analytical solutions using Equations (SI-8) and (SI-9) for (a) axial stiffness and (b) bending stiffness.

There was close agreement between the FEM and analytical results for both axial (SI_Figure 1a) and bending (SI_Figure 1b) stiffness. This validates the correct implementation of the FEM and allows us to proceed with some confidence to modeling more complicated structures.

Experimental Data

SI_Figure 2 shows the experimental configuration that was used to measure axial and bending stiffnesses. Copper (Cu) wire of 0.8 mm diameter was bent into one of the simulated shapes and fixed at one end with a clamp. There were 3 periods, and each period was 8 cm long.

To measure the axial stiffness, the Cu beam was placed vertically and increasing loads between 5 and 45 g were applied at the bottom (SI_Figure 2a). For bending

tests, the Cu beam was placed horizontally and increasing loads were applied at the tip (SI_Figure 2b). A printed grid with line spacings of 1 mm was placed behind the wire cantilever to allow measurement of the displacement. Close-up images of the tip of the beam were recorded using a digital camera (Sony SLT-A33), from which the deflections were obtained. Readings were taken to the nearest 1 mm. The slope of the load-deflection curve gave the stiffness. Between measurements, the position of the beam tip was measured to ensure that there had been no permanent deformation.
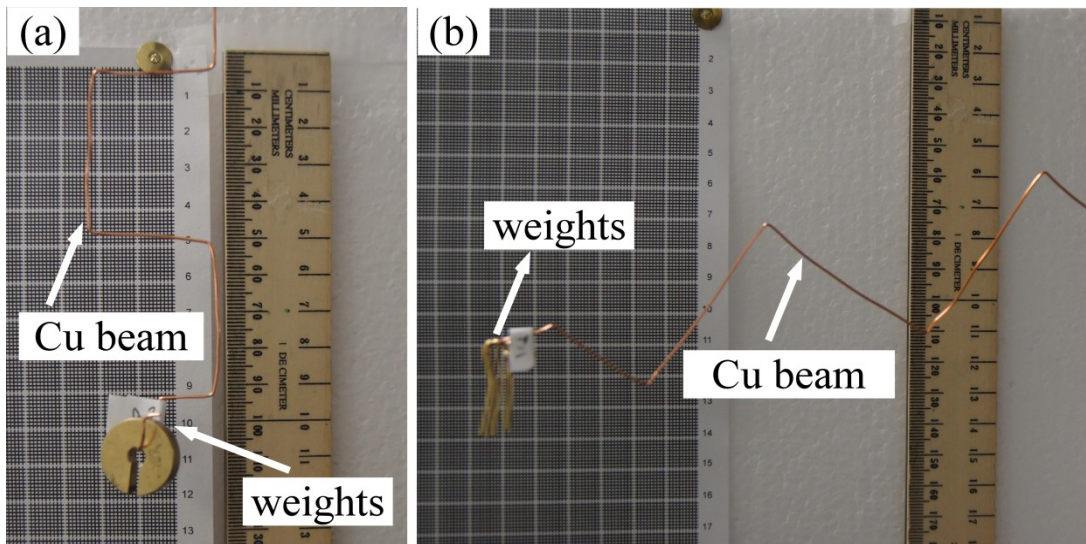
SI_Figure 2. Configuration for the experimental measurement of (a) axial and (b) bending stiffness. The ruler shows the scale.

SI_Table 2 shows the measured displacement for the five shapes and the plain beam. Four nominally identical shapes with rectangular crenellation ($\alpha = 90°$, $A = 25$) were fabricated and tested to determine the variability due to fabrication differences. Two identical triangular beams were also tested, and a single structure was made for the other shapes. Variability due to mounting and unmounting was investigated by measuring on different days (Rect #1 and Trap (110,68)). A small mass (5 g for axial

and 0.12 g or 0.28 g for bending) was applied to ensure that the structures were straight before further loads were added, and this point was treated as the zero deflection point. The structures were systematically loaded and then unloaded to confirm that there was no difference in the loading and unloading events.

SI_Table 2. Experimental displacements for loads applied axially and perpendicularly to the beams.

Beam	Load (g)	Axial Displacement (mm)	Load (g)	Bending Displacement (mm)
Straight Beam			0.18	3, 3, 3
			0.43	8, 8, 8
			0.70	12,12,12
Triangular (A = 25) Beam #1	5	1, 2	0.28	9, 8
	15	3, 4	0.56	17, 16
	25	5, -	0.84	25, 25
	35	7, 8	1.12	34, 32
	45	9, 10		
Triangular (A = 25) Beam #2	5	1, 2	0.28	8, 7
	15	4, 4	0.56	16, 15
	25	6, 7	0.84	24, 22
	35	8, 8	1.12	31, 29
	45	10, 10		
Rectangular (A = 25) Beam #1 Day 1	5	3, 3, 3, 3, 3	0.18	10, 9, 9, 9
			0.43	22, 21, 21, 21
	15	9, 9, 9, 9, 9	0.70	34, 32, 32, 32
	25	14, 14, 15, 15, 15		
Rectangular (A = 25) Beam #1 Day 2	5	3, 4	0.28	14, 15
	10	7, 7	0.56	27, 28
	15	9, 9	0.84	39, 39
	25	15, 15	1.12	52, 52
	35	20, 20		
Rectangular (A = 25) Beam #2	5	2	0.28	13, 13, 12, 12
	10	5	0.56	25, 24, 25, 24
	15	8	0.84	34, 34, 35, 35
	25	16	1.12	46, 45, 45, 45
	35	23		
Rectangular (A = 25) Beam #3	5	3, 3, 3	0.28	13, 11
	10	6, -, 5	0.56	23, 22
	15	8, 5, 7	0.84	33, 31
	25	14, 11, 12	1.12	43, 41
	35	16, 16, 17		
Rectangular (A = 25) Beam #4	5	2, 3	0.28	15, 14
	10	5, 5	0.56	26, 27
	15	10, 8	0.84	40, 38
	25	15, 13	1.12	53, 50
	35	16, 17		
Rectangular (A = 37.5)	5	8, 9, 8, 8	0.28	14, 14, 19, 20
	15	21, 22, 20, 22	0.56	34, 30, 36, 34
	25	34, 33, 33, 34	0.84	47, 45, -, 47
	35	47, 45, 45, 45	1.12	59, 55, 62, 60
Rectangular (A = 50)	5	13, 14, 15	0.28	19, 16, 19, 16, 17,18, 18, 18
	10	25, 28, -	0.56	36, 34, 34, 33, 34, 34, 31, 34
	15	44, 39, 41	0.84	53, 50, 49, 47, 48, 48, 50, 50
	25	66, 66, 67	1.12	66, 61, 66, 63, 65, 65, 61, 60
Trap (110, 68) (A = 25) Day 1	5	4, 4, 4, 5	0.18	10, 9, 9, 10
			0.43	23, 22, 22, 22
	15	12, 11, 11, 12	0.70	35, 34, 34, 34
	25	18, 17, 18, 19		
Trap (110, 68) (A = 25) Day 2	5	4, 4	0.28	19, 14
	10	7, 7	0.56	32, 27
	15	12, -	0.84	48, 42
	25	19, 18	1.12	64, 57
	35	27, 27		

SI_Figure 3 shows bending displacement under consecutive loading and unloading cycles. There was no sign of hysteresis, and the slopes of the eight lines varied by at most 3%. Thus, we remained in the elastic regime, and increasing or decreasing loads can be treated as equal in performing further analysis.
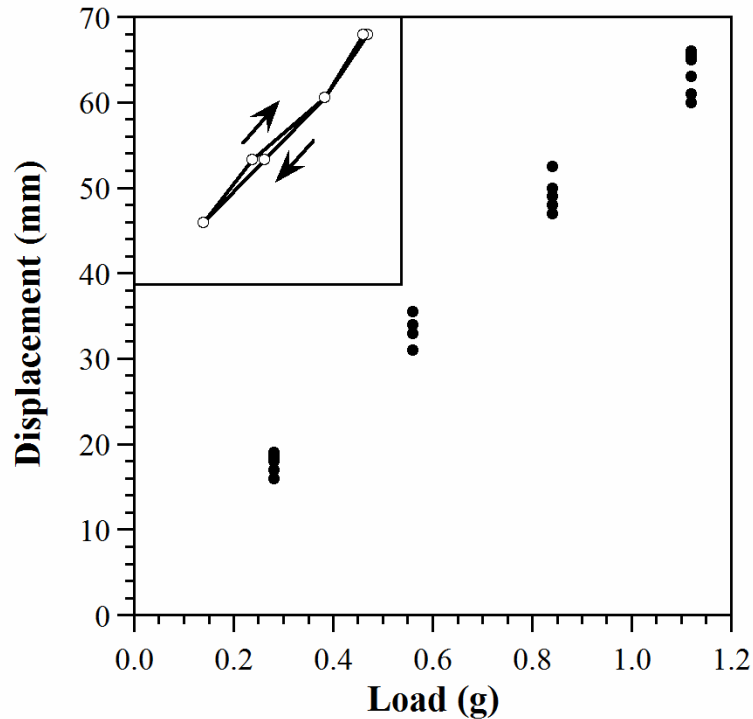
SI_Figure 3. Displacement versus bending load for a rectangular crenellated beam with $A = 50$ during loading and unloading. Inset: one loading-unloading cycle, with the directions indicated by arrows.

SI_Figure 4 shows the average displacement (averages of the displacements for each load for each beam from SI_Table 2) for four nominally identical rectangular crenellated structures ($A = 25$) in axial and bending loading. Beam # 1 (dotted line – linear fit) was tested on two separate days to measure repeatability after unmounting and re-mounting. The two linear fit lines overlap for axial loading and are close for bending. The stiffness of the beam is given by the inverse of the slope of the linear

fit. Stiffnesses determined for beam #1 on the two different dates were within 0.04% for axial and 1.35% for bending. Thus, variation due to mounting was small.
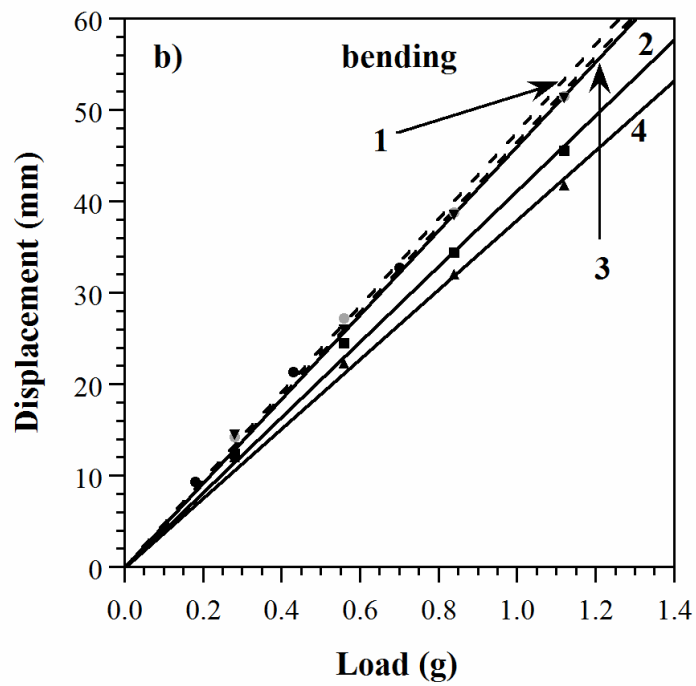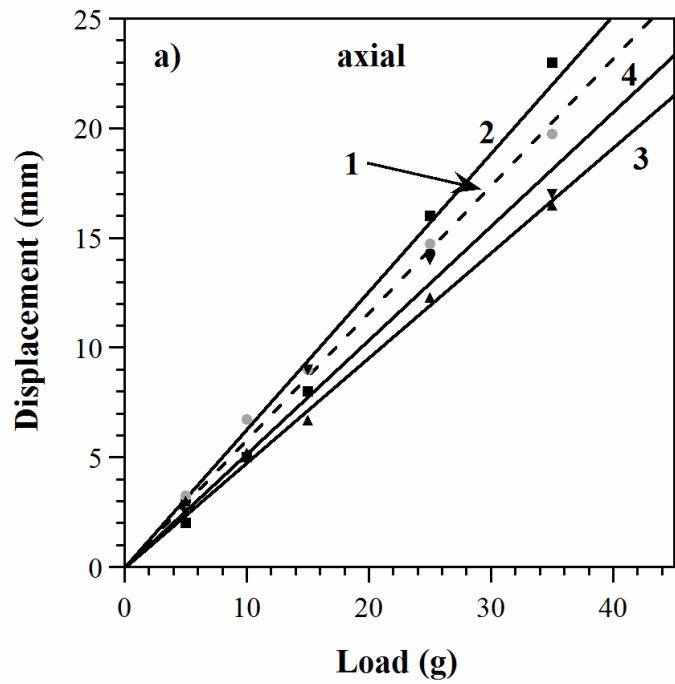
SI_Figure 4. (a) Axial and (b) bending displacement vs. applied load for four rectangular crenellations with $A = 25$.

The standard deviations of the slopes of the four nominally identical rectangular beams were at most 12% for axial extension (SI_Figure 4a) and 10% for bending (SI_Figure 4b). Even though the structures were hand made, the data showed good reproducibility in fabrication. However, in comparison to repeated testing of the same beam on two separate days or repeated testing of a beam several times, this error was much higher, as would be expected. Thus, the dominant error in these experiments is from the fabrication process.

SI_Table 3 shows the axial and bending stiffness values that were used the main text. Bending stiffness was normalized to the experimentally determined stiffness of the straight beam; axial stiffness values were normalized to the rectangular crenellation with $A = 25$, set to 1×10^{-4} based on the analytically-obtained ratio of this to the straight beam (see section 3.3 in the main text).

SI_Table 3. Axial and bending stiffness values calculated from the data in SI_Table 2. Standard deviations are given if multiple measurements were performed.

	k_x (N/m)	k_y (N/m)	*Normalized k_x (x10^{-4})*	*Normalized k_y*
Beam	-	0.562		1.00
Triangular ($A = 25$)	44.05 ± 3.00	0.347 ± 0.022	2.45	0.62
Rectangular ($A = 25$)	17.98 ± 2.19	0.223 ± 0.023	1.00	0.41
Trap (110,68) ($A = 25$)	13.32 ± 0.13	0.190 ± 0.011	0.75	0.34
Rectangular ($A = 37.5$)	7.46	0.179	0.42	0.32
Rectangular ($A = 50$)	3.67	0.170	0.20	0.30

Axial Stiffness Derivation, Detailed

The stiffness of a crenellated structure can be estimated with beam theory. The following assumptions were made in these derivations.

- The applied force is small and does not cause plastic deformation.
- The deflections are small, so the small-angle approximation, $\sin\theta \approx \theta$, can be used. (The largest deflection that the beams experienced was 10°, and even at 14° the error from using this approximation is still only 1%.)
- The beam has a uniform thickness t, a uniform width w, and an isotropic, uniform modulus E.
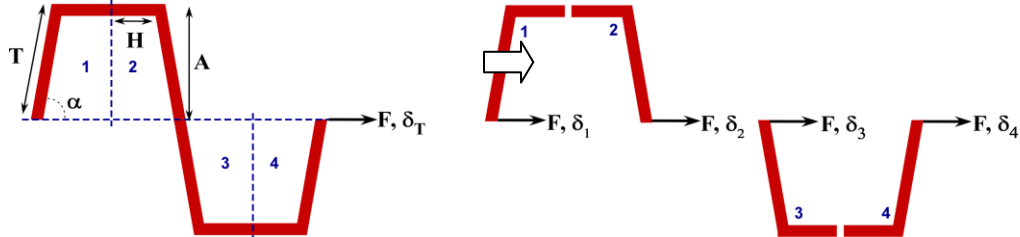
SI_Figure 5. Schematic of a cantilever structure with one period split into four parts.

The structure can be divided into constituent parts (SI_Figure 5), each comprising a horizontal segment H and a tilted or vertical segment T. Each unit (spring) experiences the same applied force F. The total deflection of the structure is estimated to be equal to the sum of the deflections of these parts. The stiffness of the structure is given by the force divided by the total displacement, and the displacements of all the unit parts are assumed to be equal. If there are 3 periods each made up of 4 unit parts, then

$$(\text{SI-10}) \quad k_x = \frac{F}{\delta} = \frac{F}{\delta_1 + \delta_2 + ... + \delta_{12}} = \frac{F}{12\delta}.$$

The displacement of the unit part is found by summing the displacements due to the motions of H and T.

Contribution of H

Consider first the deformation of the horizontal segment H (SI_Figure 6a). The force produces a moment $M = F$ x A that causes H to bend, where A, the amplitude, is the distance that the horizontal segment is vertically offset from the parallel line of force. The *decrease* in the x-position of the rightmost tip of this unit due to this bending of H is relatively small and is neglected. However, the change in angle θ_H (SI_Figure 6b) at the point where H and T meet causes segment T to tilt and, thereby, to deflect in the $+x$ direction by δ_H.
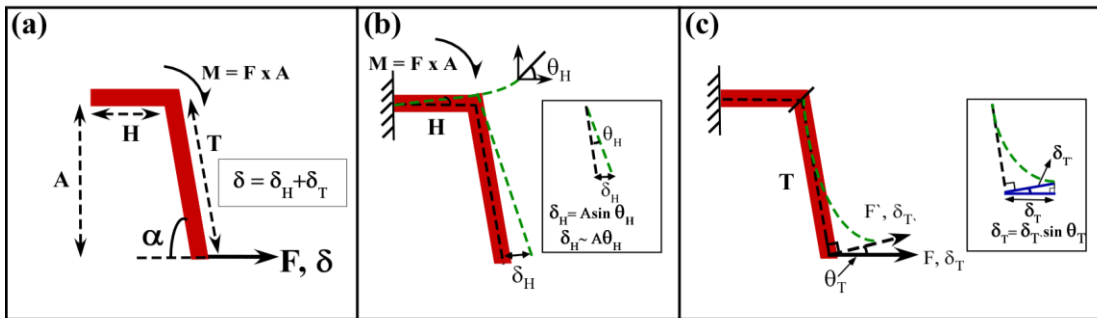
SI_Figure 6. (a) The unit part under consideration. (b) Rigid body rotation of segment T due to the deformation of segment H. The axial force creates a moment M acting on H (force x offset, $M = F$ x A), and this causes a rigid body rotation of T, producing a deflection δ_H. (c) T is treated as a cantilever beam experiencing a point load at the tip. The axial force causes a deflection δ_T. The total deflection is the sum of deflections δ_H and δ_T.

The rotation θ_H is given by [97]:

$$\text{(SI-11)} \quad sin\,\theta_H \approx \theta_H = \frac{MH}{EI} = \frac{FAH}{EI} \ ,$$

where θ_H is given in radians, H is the length of the horizontal section, E is the Young's modulus of the material, and I is the moment of inertia. The deflection δ_H is then found using

$$\text{(SI-12)} \quad \delta_H = A\,sin\,\theta_H \approx A\theta_H = \frac{FA^2H}{EI} \ .$$

Contribution of T

Consider next the bending of the tilted segment T caused by a force F at the tip (SI_Figure 6c). If a force F' is applied perpendicular to a beam of length T then the deflection is given by [97]:

$$\text{(SI-13)} \quad \delta_T = \frac{F'T^3}{3EI} \ .$$

The length of the tilted segment T is equal to $A/sin\alpha$, and the force is applied not perpendicular but at an angle $\theta + 90 - \alpha$ from the perpendicular. The displacement in x is therefore the displacement perpendicular to the beam multiplied by $sin\alpha$. The equation becomes:

$$\text{(SI-14)} \quad \delta_T = sin\,\alpha\,\frac{F\,cos\left(\theta_H +90-\alpha\right)\left(\dfrac{A}{sin\,\alpha}\right)^3}{3EI} \ ,$$

since $F' = F\,cos(\theta_H + 90 - \alpha)$.

Obtaining the Axial Stiffness

The axial stiffness is found by summing the two deflections (SI_Figure 6):

$$\delta = \delta_H + \delta_T = \frac{FA^2 H}{EI} + \sin\alpha\, \frac{F\cos\left(\theta_H + 90 - \alpha\right)\left(\dfrac{A}{\sin\alpha}\right)^3}{3EI} = \frac{FA^2}{EI}\left(H + \frac{A\cos\left(\theta_H + 90 - \alpha\right)}{3\left(\sin\alpha\right)^2}\right)$$

(SI-15)
.

If the device has a rectangular cross-section, then $I = wt^3/12$, where w is the width and

t is the thickness. Then k_p for the unit part equals

$$k_p = \frac{Ewt^3}{12A^2\left(H + \dfrac{A\cos\left(\theta_H + 90 - \alpha\right)}{3\left(\sin\alpha\right)^2}\right)}$$

(SI-16)
,

and k_x for a structure of 12 parts is

$$\text{(SI-17)}\quad k_x = \frac{Ewt^3}{144A^2\left(H + \dfrac{A\cos\left(\theta_H + 90 - \alpha\right)}{3\left(\sin\alpha\right)^2}\right)}.$$

Note: because $sin(180 - \alpha) = sin(\alpha)$, the following two geometries (SI_Figure 7) have

equivalent stiffness *if* all the horizontal segments have the same length.
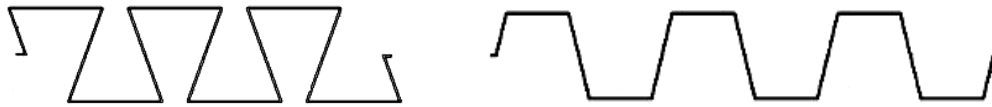
SI_Figure 7. Two geometries with equivalent stiffness.

Simplification of Bending Stiffness for Rectangular Crenellation

For a rectangular crenellation $\cos \alpha_i = 0$ for the odd-numbered terms since $\alpha_l = 90°$.

Equation (19) in the main paper then simplifies to:

(SI-18)

$$\delta = \frac{FT}{EI}\left\{\left[\frac{T^2 \cos^2 \alpha_1}{3} + L_i T \cos \alpha_1 + L_i^2\right] + 2 \sum_{i=odd,i=3}^{4n-1}\left[\frac{(2T)^2 \cos^2 \alpha_i}{3} + 2L_i T \cos \alpha_i + L_i^2\right]\right\}$$

$$+ \frac{F(2H)}{EI} \sum_{i=even,i=2}^{4n}\left[\frac{(2H)^2}{3} + 2L_i H + L_i^2\right]$$

$$= \frac{FT}{EI}\left\{\left[L_i^2\right] + 2 \sum_{i=odd,i=3}^{4n-1}\left[L_i^2\right]\right\} + \frac{F(2H)}{EI} \sum_{i=even,i=2}^{4n}\left[\frac{(2H)^2}{3} + 2L_i H + L_i^2\right]$$

For $n = 3$,

(SI-19) $\quad L_i = L - \dfrac{iL}{12}$ $\qquad$ (i = even terms) and

(SI-20) $\quad L_i = L - \dfrac{(i-1)L}{12}$ $\quad$ (i = odd terms).

Substituting L_i for the odd and the even terms into Equation (SI-18) yields:

(SI-21)

$$\delta = \frac{FT}{EI}\left\{\left[L_i^2\right] + 2 \sum_{i=odd,i=3}^{11}\left[L_i^2\right]\right\} + \frac{F(2H)}{EI} \sum_{i=even,i=2}^{12}\left[\frac{(2H)^2}{3} + 2L_i H + L_i^2\right]$$

$$= \frac{FT}{EI}\left\{\left[L^2\right] + 2\left[(L - \frac{2L}{12})^2 + (L - \frac{4L}{12})^2 + (L - \frac{6L}{12})^2 + (L - \frac{8L}{12})^2 + (L - \frac{10L}{12})^2\right]\right\} +$$

$$\frac{F(2H)}{EI}\left[\begin{array}{l} 6 * \dfrac{(2H)^2}{3} + 2H\left[(L - \frac{2L}{12}) + (L - \frac{4L}{12}) + (L - \frac{6L}{12}) + (L - \frac{8L}{12}) + (L - \frac{10L}{12})\right] \\ + (L - \frac{10L}{12})^2 + (L - \frac{2L}{12})^2 + (L - \frac{4L}{12})^2 + (L - \frac{6L}{12})^2 + (L - \frac{8L}{12})^2 + (L - \frac{10L}{12})^2 \end{array}\right]$$

.

Further rearrangement and combination gives:

$$\delta = \frac{FT}{EI}\left\{[L^2]+2\left[\frac{100L^2}{144}+\frac{64L^2}{144}+\frac{36L^2}{144}+\frac{16L^2}{144}+\frac{4L^2}{144}\right]\right\}$$

(SI-22) $+\dfrac{F(2H)}{EI}\begin{bmatrix}8H^2+2H\left[\dfrac{10L}{12}+\dfrac{8L}{12}+\dfrac{6L}{12}+\dfrac{4L}{12}+\dfrac{2L}{12}\right]+\\[2mm]\left[\dfrac{100L^2}{144}+\dfrac{64L^2}{144}+\dfrac{36L^2}{144}+\dfrac{16L^2}{144}+\dfrac{4L^2}{144}\right]\end{bmatrix}$,

and the total deflection becomes:

(SI-23) $\delta = \dfrac{FT}{EI}\left\{L^2+\dfrac{440L^2}{144}\right\}+\dfrac{F(2H)}{EI}\left[8H^2+\dfrac{60L}{12}H+\dfrac{220L^2}{144}\right].$

Since, for a rectangular crenellation, $T = A$ and $L = 6$ $(2H)$, Equation (SI-23) can be simplified as follows:

$$\delta = \frac{FA}{EI}\left\{\frac{584L^2}{144}\right\}+\frac{F(2L)}{12EI}\left[\frac{8L^2}{144}+\frac{60L^2}{144}+\frac{220L^2}{144}\right]$$

(SI-24) $= \dfrac{FA}{EI}\left\{\dfrac{584L^2}{144}\right\}+\dfrac{FL}{6EI}\left[\dfrac{288L^2}{144}\right]$.

$= \dfrac{FA}{EI}\left\{\dfrac{73L^2}{18}\right\}+\dfrac{FL^3}{3EI}$

$= \dfrac{F}{18EI}\left[73AL^2+6L^3\right]$

For a rectangular cross-section, $I = wt^3/12$ and $k_y = \dfrac{F}{\delta}$. Substituting into Equation (SI-24) yields:

(SI-25) $\begin{aligned}k_y &= \frac{18EI}{6L^3+73AL^3}\\[2mm] &= \frac{3Ewt^3}{2(6L^3+73AL^2)}\end{aligned}$.

93

FEM Results vs. Analytical Estimates

The values from the FEM simulations and the analytical estimates for the axial and bending stiffnesses of the rectangular crenellated beam were shown in Figure 7a and Figure 8a of the main text. The difference in the values, $\dfrac{FEM - Analytical}{FEM}$, is shown as a function of amplitude in SI_Figure 8, normalized by thickness. The difference was at most 5.5% for the axial stiffness and 3% for the bending stiffness, being greatest at small amplitudes when $A \approx t$.
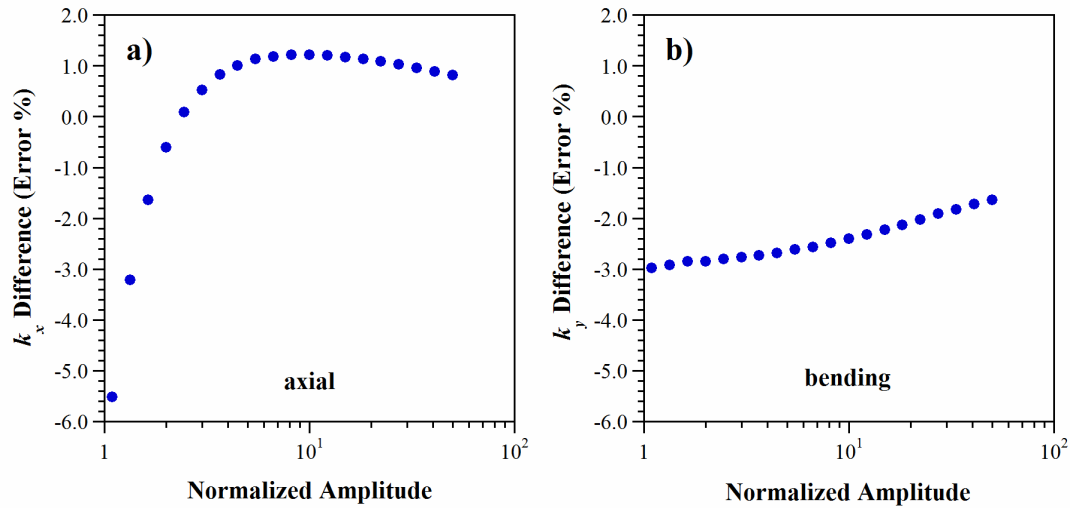
SI_Figure 8. For the rectangular beam in Figure 7a and Figure 8a of the main text, the difference between the FEM and analytical a) axial stiffness b) bending stiffness values.

Chapter 4:   Design of Bending Dielectric Elastomer Actuators

Bavani Balakrisnan[1], Alek Nacev[2], and Elisabeth Smela[1]
[1]Department of Mechanical Engineering, 2176 Glenn L. Martin Hall
[2]Department of Bioengineering, 2314 Kim Building,

Abstract

This paper examines the design of bending dielectric elastomer actuators (DEAs). An analytical multilayer model is used to investigate the effect of thickness and stiffness of the different layers involved in the design of these actuators. Unimorph, bimorph, and multilayer stacking configurations are analyzed. Design is based on curvature, blocked force, and work. Other electroactive polymers (EAPs) such as ionic polymer metal composites (IPMCs) and conjugated polymer (CP) structures are also analyzed.

Keywords: multilayer model, DEA, bending

4.1   Introduction

Dielectric elastomer actuators (DEAs) are comprised of an elastomer sandwiched between two stretchable electrodes. Upon application of a voltage, the electrodes are attracted together by electrostatic forces, causing an in-plane expansion and out-of-plane contraction of the elastomer. The in-plane expansion has been utilized in configurations such as stretched sheets, membranes, and rolled tubes [9,15,110] to

perform mechanical work, while the out-of-plane contraction has been harnessed in folded stacks [2]. A bending configuration first introduced over ten years ago [8,15] has recently received more attention [30,36,43,46,111]. It is produced by introducing a difference in stiffness on one side of the actuator relative to the other, for example, by making one electrode less compliant or by adding a passive layer to one side of the DEA [8, Maleki, 2011 #1369]. These bending actuators have also been made in multi-layer stacks [30,36,111]. Multilayer DEAs are advantageous because the thickness of each layer can be reduced, which reduces the operating voltage, and because multiple layers add rigidity, which increases the actuation force.

In this paper, we examine the behavior of bending DEAs by using analytical multilayer model and provide guidelines for DEA design. We have used the trilayer model developed Benslimane [112] and multilayer developed by DeVoe[113]. The multilayer model developed by DeVoe et al. has been widely used in the field of piezoelectric actuators where the active layer is usually of same or higher stiffness than the electrodes [114-122], however, this sort of analysis has not be demonstrated for a DEA. Unimorph, bimorph, and multilayer stacking configurations for a DEA are analyzed. Specifically, we show that for a given number and placement of electrode, elastomer, and passive layers how the curvature, blocked force, and work can be optimized by adjusting the thicknesses and moduli. We also include configurations that are relevant for two other types of electroactive polymer (EAP) actuators: ionic polymer metal composites (IPMCs) and conjugated polymer (CP) sandwich structures

96

4.2   Analytical Models

The curvature of bending bilayers, with one layer having an inplane strain α, can be described by the Timoshenko equation [123]. An analytical trilayer model was developed by Benslimane et al. [112], and Devoe et al. derived an *m*-layer model [113]. We begin by introducing these models, and then we provide the *m*-layer expressions for blocked force.

4.2.1 Tri-Layer Curvature Model

A trilayer DEA configuration is illustrated in Figure 4-1. (In the results section, an inplane strain of α% was specified for the EAP layers.) The Benslimane et al. trilayer model gives the curvature κ under zero load as [Benslimane, 1999 #85]:

(23)
$$\frac{-2\alpha_{12}E_2t_2\left[6E_1t_1\left(t_1+t_2\right)-E_3t_3\left(6t_2+t_3\right)\right]-2\alpha_{13}E_3t_3\left[E_2t_2\left(6t_2+t_3\right)-E_1t_1\left(6t_1+12t_2+12t_3\right)\right]}{2E_1^2t_1^4+2E_2^2t_2^4+2E_3^2t_3^4+E_2E_3t_2t_3\left(8t_2^2+7t_2t_3+3t_3^2\right)+E_1t_1\left\{4E_2t_2\left[2t_1^2+3t_1t_2+t_2^2\right]+E_3t_3\left[8t_1^2+24t_1t_2+24t_2^2+7t_1t_3+14t_2t_3+3t_3^2\right]\right\}}$$

where α_{1i} are the differences in strains between layers 1 and i, t_i are the layer thicknesses, and E_i are the Young's moduli. The E_i in Equation (23) are the effective moduli: the Young's moduli divided by $1-\nu_i^2$, where ν_i is the Poisson's ratio for the layer. This model assumes that the thicknesses of the layers are much smaller than the length and width of the device. As it should, Equation (23) reduces to the Timoshenko equation as the thickness and/or modulus of the third layer go to zero. This expression can readily be used to calculate curvatures using a hand calculator or

software packages such as Excel; we used Matlab to generate maps over ranges of modulus and thickness values.
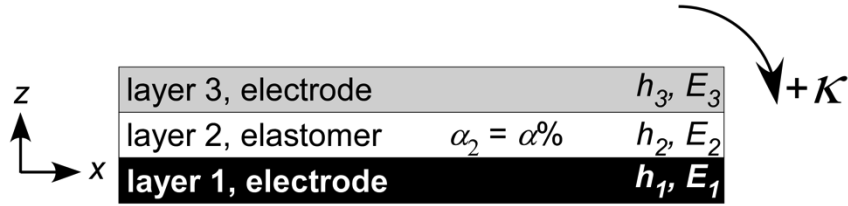
Figure 4-1. Trilayer configuration for a typical bending DEA, also applicable to other EAP bending actuators. If the moduli and/or thicknesses of the electrodes differ, the structure will bend with curvature κ.

4.2.2 m-Layer Curvature Model

DeVoe et al. showed that for an *m*-layer bending actuator, the curvature κ under zero external load is given by [113]:

$$(24) \quad \frac{1}{R} = \kappa = \frac{2DA^{-1}C}{2 - DA^{-1}B},$$

where **A**, **B**, **C**, and **D** are matrices. The matrix **D** is associated with the requirement that the moments at any cross-section of the actuator sum to zero at equilibrium, $\sum_{i=1}^{m} M_i = 0$. It can be written as the product of two components. The first is the inverse of the sum over the products $E_i I_i$, the flexural rigidities of the layers. The second is a vector giving the center positions of each layer, having thickness t_i, relative to the bottom of the multilayer stack. For the bottom-most layer, $i = 1$, as in Figure 4-1.

$$(25) \quad \mathbf{D} = \frac{1}{\sum_{i=1}^{m} E_i I_i} \left[\frac{t_1}{2} \quad t_1 + \frac{t_2}{2} \quad \cdots \quad \sum_{i=1}^{m-1} t_i + \frac{t_m}{2} \right]$$

The matrix **A** contains the inverse products of the cross-sectional areas A_i and the Young's moduli E_i for each layer and for the layer immediately above it. These terms are related to the axial components of the strain. The cross sectional area A_i is given by $t_i w_i$, where w_i is the width of the layer (perpendicular to the plane of the page in Figure 4-1). The E_i in Equation (26) are again the effective moduli: the Young's moduli divided by $1 - v_i^2$. The last row of 1s in the matrix arises from the requirement for axial force equilibrium, $\sum_{i=1}^{m} F_i = 0$.

$$(26) \quad \mathbf{A} = \begin{bmatrix} \dfrac{1}{A_1 E_1} & -\dfrac{1}{A_2 E_2} & 0 & \cdots & 0 \\ 0 & \dfrac{1}{A_2 E_2} & -\dfrac{1}{A_3 E_3} & 0 & \cdots \\ \cdots & \cdots & \cdots & \cdots & \cdots \\ 0 & \cdots & 0 & \dfrac{1}{A_{m-1} E_{m-1}} & -\dfrac{1}{A_m E_m} \\ 1 & 1 & 1 & 1 & 1 \end{bmatrix}$$

The column vector **C** contains the differences in the actuation strains α_i between each layer and the one above it and originates from equating the strains at the m-1 interfaces. The last row is zero.

$$(27) \quad \mathbf{C} = \begin{bmatrix} \alpha_2 - \alpha_1 \\ \alpha_3 - \alpha_2 \\ \cdots \\ \alpha_m - \alpha_{m-1} \\ 0 \end{bmatrix}$$

Finally, the column vector **B** contains the sum of the thicknesses of adjacent layers, $t_{i-1} + t_i$, and it also originates from equating the strains at the interfaces. The last row is again zero.

99

$$(28) \quad \mathbf{B} = \begin{bmatrix} t_1 + t_2 \\ t_2 + t_3 \\ ... \\ t_{m-1} + t_m \\ 0 \end{bmatrix}$$

This model gives the same results as the Benslimane et al. model for three layers, and the same results as the Timoshenko equation for two layers.

4.2.3 m-Layer Blocked Force Model

Blocked force is a key actuator parameter: it is the maximum force that the actuator can exert when held in the zero deflection position while actuated, or alternatively, the amount of force required to flatten the beam from its bent state. The actuator can lift loads smaller than this value, but not larger. The analysis in this paper assumes that the materials have linear stress-strain curves, the slopes of which yield the Young's moduli, and that they are ideal (the analysis does not take into account creep, changing dielectric constants, etc.).

To determine the blocked force, the composite beam was first transformed into an equivalent single-material beam. The ratio of the Young's modulus of layer i relative to that of layer 1 is:

$(29) \quad n_i = E_i/E_1.$

The layer widths w_i were then expressed in terms of the modulus ratios:

$(30) \quad w_i = n_i w_1 .$

This transforms the description of the beam to one with each layer having a varying width but the same modulus as layer 1; this beam behaves equivalently to the original composite beam. The distance d_i, in the thickness direction, from the bottom of layer 1 to the middle of each layer is given by:

$$(31) \quad d_i = \frac{1}{2}t_i + \sum_{j=1}^{i-1} t_j .$$

The neutral axis of a beam with m layers can then be found by:

$$(32) \quad t_{neutral} = \frac{\sum_{i=1}^{m} w_i t_i d_i}{\sum_{i=1}^{m} w_i t_i} .$$

To calculate the blocked force, the parallel-axis theorem was used to compute the combined moment of inertia I_c for the equivalent beam [97]. This was possible because the neutral axis is parallel to all the center of mass axes of the individual layers. By this theorem, I_c is the sum of the individual layer moments I_i plus terms that depend on the square of the distance between each layer and the neutral axis.

$$(33) \quad I_i = w_i t_i^3 / 12$$

$$(34) \quad I_c = \sum_{i=1}^{m} [I_i + w_i t_i (d_i - t_{neutral})^2]$$

The blocked force can then be described as the load applied to the end of the deflected beam necessary to push it back to the original undeflected position. Therefore, the deflection of a beam due to an applied point load was found starting with the differential equation for beam deflection [97],

(35) $EI_c \dfrac{d^3 \delta(x)}{dx^3} = -F_b$,

and using the following boundary conditions. These state that the moment at the end of the beam is zero and the slope and deflection at the fixed point is zero:

(36) $\dfrac{d^2 \delta(L)}{dx^2} = 0, \quad \dfrac{d\,\delta(0)}{dx} = 0, \quad \delta(0) = 0$,

where δ is the deflection of the beam, x is the position along the beam, and F_b is the blocked force. The displacement along the beam can then be written as follows by integrating Equation (35) three times and using the boundary conditions of Equation (36) to determine the unique solution.

(37) $\delta(x) = \dfrac{1}{EI_c} \left(\dfrac{F_b L x^2}{2} - \dfrac{F_b x^3}{6} \right)$.

At the end of the beam, $x = L$, and

(38) $\delta(L) = \dfrac{F_b L^3}{3EI_c}$.

By using the following curvature approximation [97], for small deflections,

(39) $\kappa = \dfrac{2\delta}{L^2}$,

the blocked force can be written as:

(40) $F_b = 3EI_c \kappa / 2L$.

4.3   Analytical Model Results

Several EAP-relevant cases were examined using Matlab. In all the results presented in this section, the Young's moduli of the layers are given *relative to those of the*

elastomer, which was taken as $E_{elastomer} = 1$ (in real numbers, this might be 1 MPa). (In other words, a modulus of 100 for an electrode layer means a modulus 100 times greater than that of the elastomer.) Likewise, thicknesses are given relative to those of the elastomer, taken as $t_{elastomer} = 1$. All layers were set to be incompressible ($v_i = 0.5$). (This is a good assumption for the elastomer polydimethylsiloxane (PDMS), which has a Poisson's ratio of 0.49 [61], but for metals v is typically 0.34 [96]. This will introduce an error, so for accurate modes of particular configurations, the actual Poisson's ratio of the materials should be used.) An inplane (x-direction) actuation strain of $\alpha\%$ was specified for the elastomer (or other electroactive) layers, and the electrode/passive layers had zero actuation strain. Curvature is in all cases linear with actuation strain (Equations (25), (27)). Changes in layer thickness (out-of-plane, or z-direction) were neglected. The length of the structure was set to $L = 1$, and the width of every layer was set to $w = 1$. These are arbitrary values and these choices are useful for converting the unitless values in the plots of this section to values with units for a particular device geometry. The Supplementary Information includes how values limits of thicknesses and moduli were chosen.

A variety of materials is used in the construction of bending actuators. (1) The electrode may be thinner than the elastomer and have lower modulus, such as is the case for carbon nanotube powder electrodes. (2) The electrode may be as thick or thicker than the elastomer but have a lower modulus, as is the case for carbon grease electrodes. (3) The electrode may be thinner than the elastomer but have a higher modulus, such as when metal thin films are used. (4) The structure may include a

passive layer to induce bending, such as Kapton or Mylar, which has a higher

modulus and is of comparable thickness. Given that there are numerous scenarios of

interest, in this section we examine the roles of modulus and thickness systematically

over a wide range (in fact, over a wider range than may be physically practical).

4.3.1 3-Layer Actuators

The trilayer configuration is shown in Figure 4-1. First we examine the effect on

curvature of varying the stiffness of the outer two layers when all three layers have

the same thickness, $t_1 = t_2 = t_3$. The result is shown in Figure 4-2.
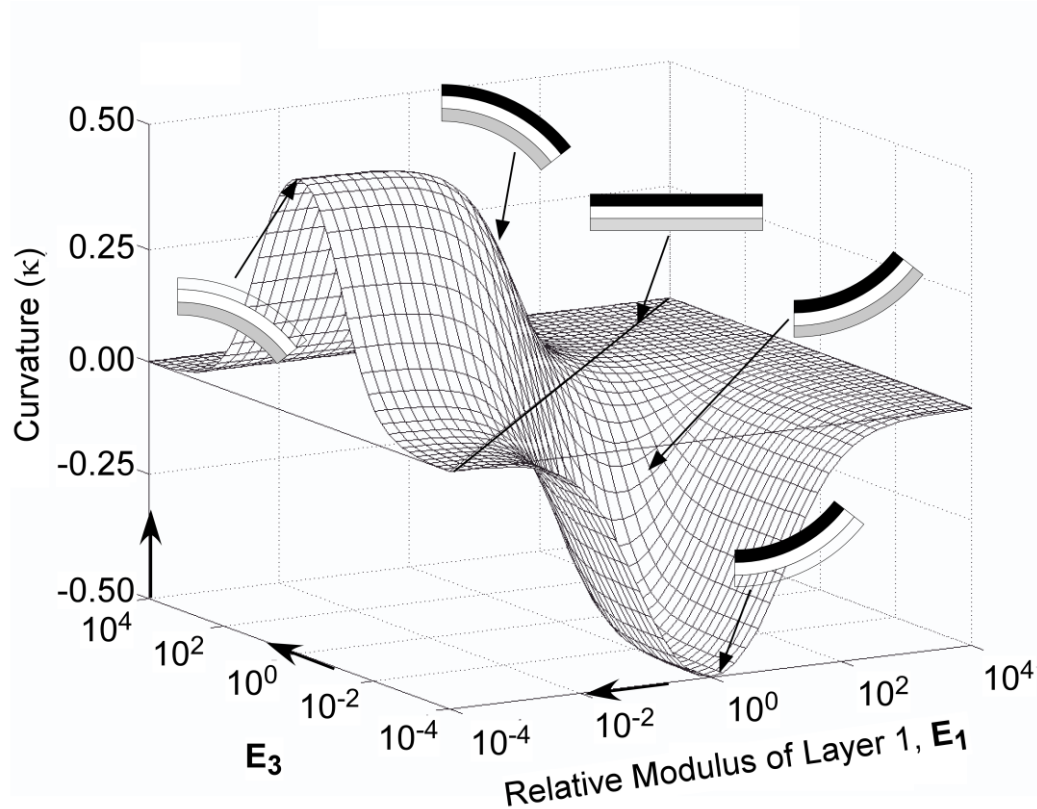
**Figure 4-2. Curvature as a function of the moduli of the outer two layers
when $\alpha_2 = \alpha\%$, $t_1 = t_2 = t_3 = 1$ and $E_2 = 1$. The trilayer bending directions
are indicated in the sketches. For either E_1 or E_3 very small, the layer**

becomes mechanically "invisible" in comparison with the other two, as indicated in the sketches, and the trilayer behaves as a bilayer. Arrows indicate the directions of increasing values.

Figure 4-2 reveals that for the case $t_1 = t_2 = t_3$, maximum bending is achieved when one of the two outer layers has a negligible stiffness compared to the other two; in other words, when the third layer is mechanically invisible and system behaves as a bilayer. When E_3 is very small, the maximum curvature occurs when $E_1 = E_2$. As expected, there is a line of symmetry around the line $E_1 = E_3$, along which there is no curvature: when the structure is symmetric, an expansion of the elastomer in the x-direction does not lead to bending. The bending direction changes from positive to negative around the line of symmetry. A plot of κ as a function of t_1 and t_3 for $E_1 = E_2 = E_3$ looks very similar. The trilayer solutions are the same as those obtained from the Timoshenko bilayer equation, as they should be, when $t_3 = 0$ or $E_3 = 0$ or 1.

Is this the maximum curvature that can be achieved? To explore the interplay between thickness and modulus, Figure 4-3a shows the curvature versus the relative modulus E_1 and thickness t_1 in the maximum bending case (i.e., essentially a bilayer), in which layer 3 has a negligible modulus ($E_3 = 10^{-4}$). Physically, this might be realized in a DEA by using one metal electrode and one carbon grease electrode. When layer 2 (elastomer) and layer 1(electrode) have equal moduli (green line, $E_2 = E_1 = 10^0$), greatest bending is achieved not when they have the same thickness but when the electrode is half as thick as the elastomer ($t_1 = 0.5 \times 10^{-1}$) The curvature can be doubled from the maximum in the $t_1 = t_2$ case of Figure 4-2 (shown in Figure

4-3 by the intersection of the green and cyan lines) by reducing the thickness of t_1 to be less than 10^{-2} of the elastomer thickness t_2 and simultaneously increasing the modulus E_1 to be greater than 10^2 of the elastomer modulus. Curvature is overall highest approximately when

$$\frac{\log E_1}{\log t_1} = -2$$
(41)

This is illustrated in Figure 4-3 for the case when $E_1 = 10^6$ and $t_1 = 10^{-3}$ by the red and purple lines. There is a maximum curvature plateau of $\kappa = 1$ that broadens with further decreases in t_1 and increases in E_1.

As mentioned earlier, these plots are unitless and are applicable to every trilayer structure. The highest curvature for a trilayer will always be given by Equation (41), but this curvature has been normalized to the elastomer thickness and modulus. To obtain a dimensional value for a given structure, the curvature value read from the plot is transformed as follows

$$(42) \qquad \kappa_{dimensional} = (1.5 \times 10^{-2}) \alpha \frac{\kappa}{t_2},$$

where the dimensional curvature is obtained by dividing the unitless curvature by the thickness of the elastomer and multiplying it by the strain α and the coefficient 1.5×10^{-2} (corresponding to a unit percent strain). This additional material strain multiplier is a coefficient that incorporates a material's breakdown voltage and relative permittivity to express the maximum strain that a bender can produce. It is described simply as the axial strain at the breakdown voltage using Pelrine's formula

$$(43) \qquad \alpha = \frac{\varepsilon_0 \varepsilon_r}{2E_2} \left(\frac{V_{breakdown}}{t_2} \right)^2 \times 100\%,$$

where $V_{breakdown}$ is the breakdown voltage of the material. Using Equation (42) and (43) the curvature for any trilayer device can be determined from the values on Figure 4-2. If the thickness of the elastomer for meso-scale applications is on the order of 100 μm and the expected elastomer strain is 5% at the maximum breakdown voltage, the curvature in the figure shows $\kappa = 0.5$ on the plot will correspond to $\kappa = 375$ m^{-1} in real numbers (radius of curvature, R, which is the inverse of κ is 2.667 mm).
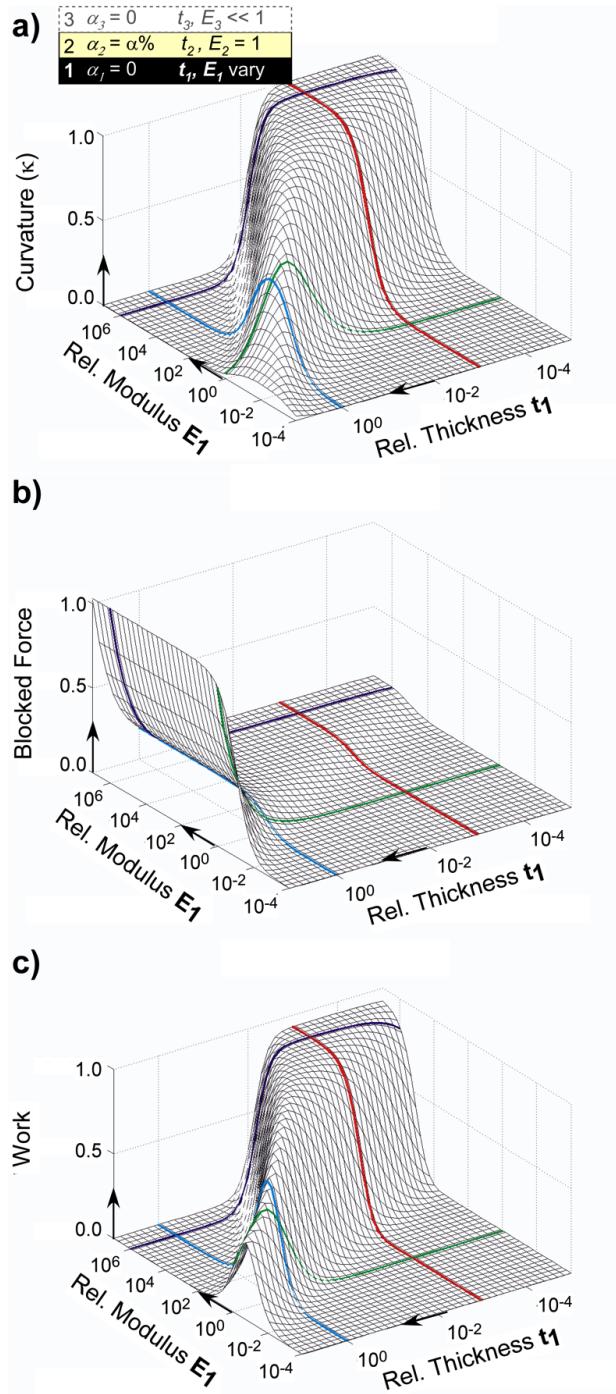
Figure 4-3. A 3-layer model with $t_2 = t_3 = 1$, $E_2 = 1$, and $E_3 = 10^{-4}$ (mechanically negligible layer 3, so the trilayer behaves as a bilayer). (a) Curvature, (b) blocked force, and (c) work as a function of the relative modulus and thickness of layer 1. Arrows indicate the directions of increasing values.

Figure 4-3b shows the blocked force over the same range of t_1 and E_1. The blocked force increases strongly with t_1 (by Equation (36) , $F_b \sim t^2$) and is almost independent of E_1. (In the frontmost corner, at $t_1 = 10^4$ and $E_1 = 10^{-4}$, the blocked force is 0.5. It doubles at $E_1 = 10^{-2}$ to 1 and is thereafter constant.) Below $t_1 = 10^2$, the blocked force is small, on this linear scale, for all E_1. As with the curvature plots, the blocked force plot is also unitless and therefore must be transformed to obtain a dimensional blocked force. The following transformation must be used:

$$(44) \qquad F_{b,\text{dimensional}} = 8.25x10^{-4} \alpha F_b \frac{E_2 w t_2}{L} ,$$

Here again the coefficient 8.25×10^{-4} is the coefficient representing a unit percent strain and α is the strain from Equation (44). This shows that the blocked force depends linearly with the Young's modulus, and inversely with the length, and to the second power with the thickness. Therefore for an elastomer thickness t_2 of 100 μm and a E_2 of 1 MPa with 5% strain and the length L is $10w$, a blocked force value of 1 on the figure corresponds to 0.4125 mN, while for a elastomer thickness of 1 μm it would be 41.25 μN.

The curvature and blocked force maxima occur at different positions on the t_1, E_1 plane; there is no region with both high κ and high F_b. In real applications, it is often the work W done by the actuator that is instead of more interest. Work is defined as the product of force and displacement. Since κ was found under zero load and F_b for zero displacement, to generate the work curve in Figure 4-3c we assumed a linear load curve and used the point at which the curvature was half the maximum value and

the corresponding force was also half its maximum value. The shape of the work surface in Figure 4-3c resembles that for the curvature in Figure 4-3a, but without the fall-off at small t_1 and E_1. The work is again maximum at backmost corner, at the intersection of the red and purple lines, where $W = 1$. To obtain a dimensional work, use

$$(45) \quad W_{\text{dimensional}} = (1.405 \times 10^{-1})\alpha^2 WE_2 wLt_2,$$

where the coefficient, 1.405×10^{-1}, corresponds to a unit percent strain. For $t_2 = 100$ µm ($\alpha = 5\%$, $L = 10w$), so 1 on the plot corresponds to 3.5×10^{-9} J, whereas for $t_2 = 1$ µm, corresponds to 3.5×10^{-15} J. The maximum occurs in an area of the E_1-t_1 plane where F_b is small, but in this case the trade-off between smaller force but larger curvature is most favorable. The work decreases to only approximately half that value moving along the line given in Equation (41) toward the frontmost corner, at which the curvature is small but the work is large. (At the point $E_1 = 10^{-4}$ and $t_1 = 10^4$, $W = 1$). In the other two corners, W is much smaller.

4.3.2 4-Layer Actuators

The single-elastomer DEA bending actuator results of the previous section provide a starting point for a more general exploration of the behavior of multi-layer bending actuators. Now we asked the question, how do two laminated bilayers behave, compared to a single bilayer? There are two ways to laminate bilayers: as a stack and face to face. For a DEA stack configuration is only feasible and the back to back is common for other electroactive polymer like IPMC

4.3.2.1 Stacks of Two Bilayers

Figure 4-4 shows the bending of a 2-bilayer stack having the same total elastomer thickness as the bilayer in Figure 4-3 with $t_2 = t_4 = 0.5$; t_1 and t_3 were varied together. In this configuration, the strain in both elastomer layers was $\alpha\%$ relative to layer 1. Such a configuration of layers would correspond to a 2-elastomer DEA having a mechanically invisible 5th electrode layer.
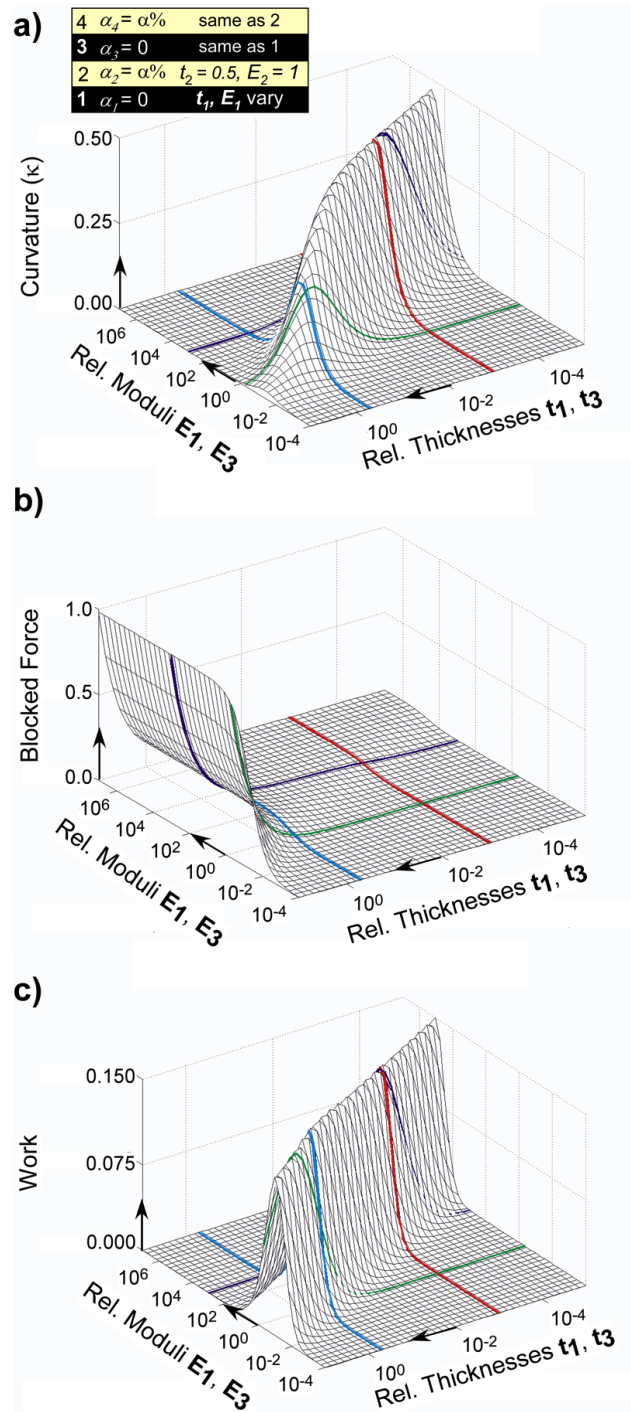
Figure 4-4. A 2-bilayer stack with $t_2 = t_4 = 0.5$ and $E_2 = E_4 = 1$ (a) curvature (b) blocked force (c) work a as a function of the relative modulus and thickness of the passive layers relative to the EAP layers with a strain in the latter of $\alpha\%$.

The maximum bending (Figure 4-4a) is $\kappa = 0.5$, half as much as for the bilayer, but it occurs at the same combination of E_1 and t_1 (equal to E_3 and t_3) as for the bilayer, with $t_1 \leq 0.01 t_2$ and $\log(E_1) = -2\log(t_1)$. (The curvature does not increase further if E_1 is increased or t_1 is decreased beyond the values shown in the plot. The maximum is constant along the ridge, although it may appear by the perspective to be increasing.) However, the peak lacks the broad plateau seen in the bilayer. The curvature is linear with the inverse of the total thickness, so for $t_2 = t_4 = 1$ instead of 0.5, it halves to $\kappa = 0.25$, and for $t_2 = t_4 = 0.25$, it increases to $\kappa = 2$, nearly that of the bilayer. This configuration has the same total thickness as the bilayer, so this arrangement of layers is less favorable for bending than the bilayer, behaving as a bilayer with half the strain. If the moduli E_3 and E_4 are reduced by a factor of 10,000, then the bilayer behavior is completely recovered, including the plateau.

For a 3-bilayer stack (not shown) having $t_2 = t_4 = t_6 = 0.33$, the surface plot looks identical to the one for the 2-bilayer stack, but with the smaller maximum curvature of $\kappa = 0.34$. Likewise, for a 4-bilayer stack having $t_2 = t_4 = t_6 = t_8 = 0.25$, the surface plot looks the same but with a maximum curvature of $\kappa = 0.25$. The loss of curvature slows for each added bilayer.

Figure 4-4b shows the blocked force for the 2-bilayer stack. It has the same shape and magnitude (with a maximum at 1) as the single bilayer in Figure 4-3b. This is because the blocked force depends on total thicknesses, which is the same in both cases.

The work is shown in Figure 4-4c. The maximum work is constant along the ridge, although it may appear by the perspective to be increasing, $W_{max} = 0.15$. Except this ridge decreases slight above $t_1 = t_3 > 1$ and $E_1 = E_3 < 1$ and then becomes constant again. This W_{max} is a factor of 6 smaller than for the bilayer since the κ is much half as small as the bilayer (even though the blocked force is the same for both). In fact, the combination $t_1 = t_3 = E_1 = E_3 = 0.5$ (shown by cyan and green lines) may represent a reasonable compromise between curvature, blocked force, and work. This could be realized physically by using carbon nanotube (CNT) or exfoliated graphite (EG) loaded elastomers with slightly lower modulus than the dielectric elastomer.

Figure 4-5a shows the curvature for different 2-bilayer stack having only one active elastomer layer, layer 2, with the other elastomer, layer 4, having zero strain. This corresponds to a DEA made with identical electrodes but with a passive layer added on one side to provide bending. This causes a dramatic change in the shape of the κ surface: unlike either Figure 4-3 or Figure 4-4, a broad plateau appears in the entire lower-right quadrant, not the upper-right diagonal. Furthermore, the maximum bending amplitude is $\kappa = 1$. Making layer 4 passive results in *higher* curvature than when it is active because in the lower-right quadrant, layers 1 and 3 are mechanically negligible, so in fact the configuration reverts to a bilayer (between layers 2 and 4). (As before, since the curvature is linear with the inverse of the total thickness, for $t_2 = t_4 = 1$ it halves to $\kappa = 0.5$, and for $t_2 = t_4 = 2$, $\kappa = 0.25$.) This configuration is advantageous because the broad plateau provides flexibility in the fabrication of

devices using a range of different materials for the electrodes, the only requirement being to make them much less stiff than the elastomer. The stiffness of the passive layer can be optimized using Figure 4-3.

Figure 4-5b shows the blocked force of this DEA plus passive layer configuration. The maximum is in the front-most corner (high t_1, low E_1), reaching 1 within the studied range of thickness and modulus values, which is 0.48. When $E_1 = 1$ ($t_2 = 10$) the blocked force decreases to zero. In comparison bilayer was high all along the line $t_1 = 10$ (Figure 4-3c), while here the force decreases rapidly with increasing modulus E_1.

Figure 4-5c shows the work that can be done by this stack. When t_1 ($= t_3$) = 5, a small peak is observed (work = 0.33) at E_1 ($= E_3$) = 10^{-4}; this decreases slightly (to 0.25 and plateaus as t_1 decreases. This is about 3 times smaller than for the previous 2-bilayer stack. In addition, when E_1 increases the work decreases dramatically. There is a reasonable overlap in curvature and blocked force in the region $t_1 = 10^0$ to 10^1 and $E_1 = 10^{-4}$ to 10^{-2}. This region is therefore optimum for this device, having a reasonable compromise between curvature, blocked force, and work.
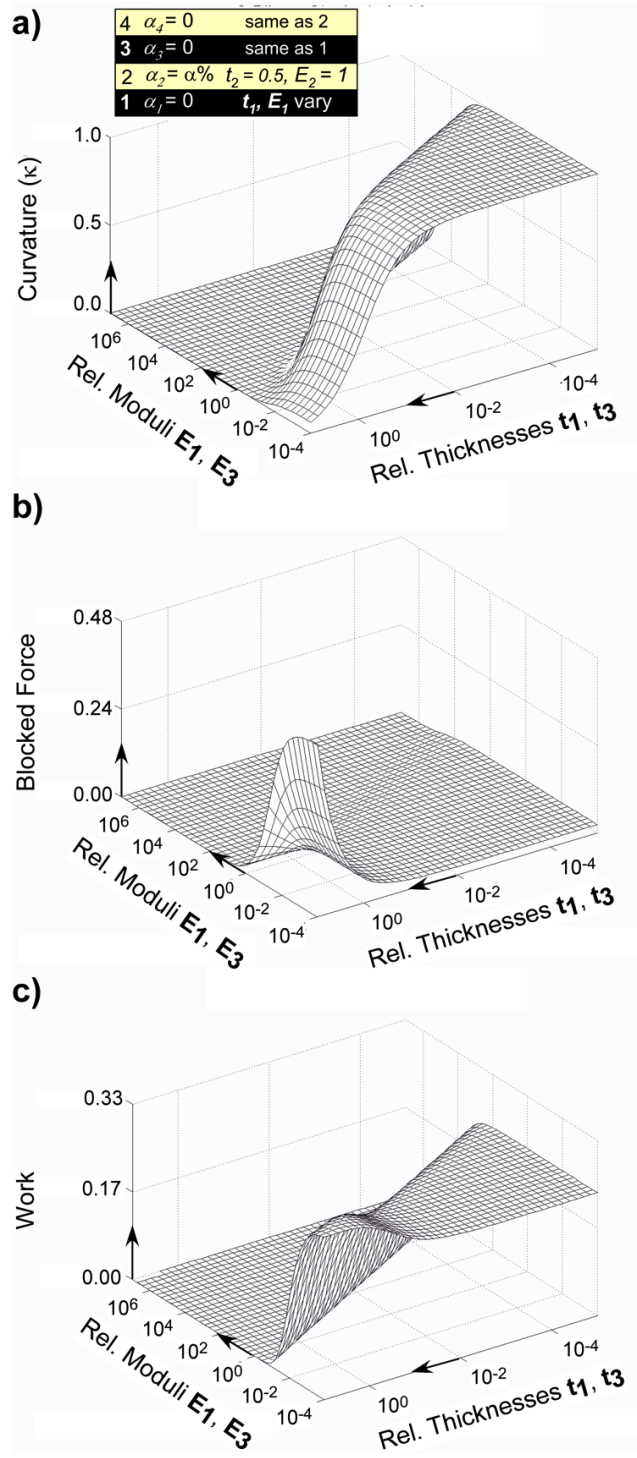
Figure 4-5. A 2-bilayer stack with $t_2 = t_4 = 0.5$, $E_2 = E_4 = 1$, $\alpha_2 = \alpha\%$, and $\alpha_4 = 0$, corresponding to an inplane DEA with a passive layer on one side. (a) Curvature, (b) blocked force, and (c) work a as a function of the relative modulus and thickness of the passive layers relative to the elastomer layers.

4.3.2.2 Face-to-Face Bilayers

Bilayers can also be placed face to face. This configuration is not relevant for DEAs, but it is for ion-transporting EAP actuators. If the volume-changing layers are on the inside and mass moves between layers 2 and 3, causing one to expand and the other to shrink, then this corresponds approximately to an IPMC configuration. If the volume-changing layers are instead on the outside, then this corresponds to a conjugated polymer (CP) / solid polymer electrolyte (SPE) configuration.

The IPMC configuration has the same surface for curvature (Figure 4-6a) as the DEA+passive layer configuration of Figure 4-5. The maximum in the lower-right quadrant again tells us that the outer two electrode layers should be mechanically invisible for greatest bending, since that reduces the structure to a bilayer. The blocked force surface (Figure 4-6b) is quite different, however: it is constant across all outer electrode layer moduli and thicknesses (the variation in the upper-left corner is due to computational noise). The blocked force is dominated by the elastomer, rather than the electrodes: the force is 20x smaller than for the other 4–layer stack at 0.045 (instead of 1). The work plot (Figure 4-6c) therefore just follows the curvature plot.

We now consider a face-to-face stack in which the outer two layers change volume, which corresponds to a CP/SPE/CP configuration. Figure 4-7 shows the curvature, which can be optimized simply: the modulus of the inner SPE layer is almost irrelevant (for $E_2 > 1$ the required thickness decreases gradually), but it should made

thin, less than 0.01 that of the outer CP layers. The CP layers should be as close together as possible to get maximum curvature, again approaching the optimal bilayer case, which gives $\kappa = 2$, the same as for the IPMC and half of that for a bilayer.

Blocked force is also unaffected by the SPE modulus E_2 ($= E_3$) and depends only on its thickness t_2 ($= t_3$), which, as in Figure 4-3 (a single bilayer) and Figure 4-4 (a 2-bilayer stack), increases with the square of t_2. Because it has two active layers, the blocked force is about twice as great ($F_b = 1.88$) as for a single bilayer.

The highest work can be achieved when $t_2 = 10^2$ and E_2 is minimized, but the work remains almost as high for any value of E_2 as long as $t_2 < 10^{-2}$. The work tops out at $W = 1.33$, which is 1.33x as high as for a single bilayer partly because there were two layers with a strain of $\alpha\%$ instead of one.
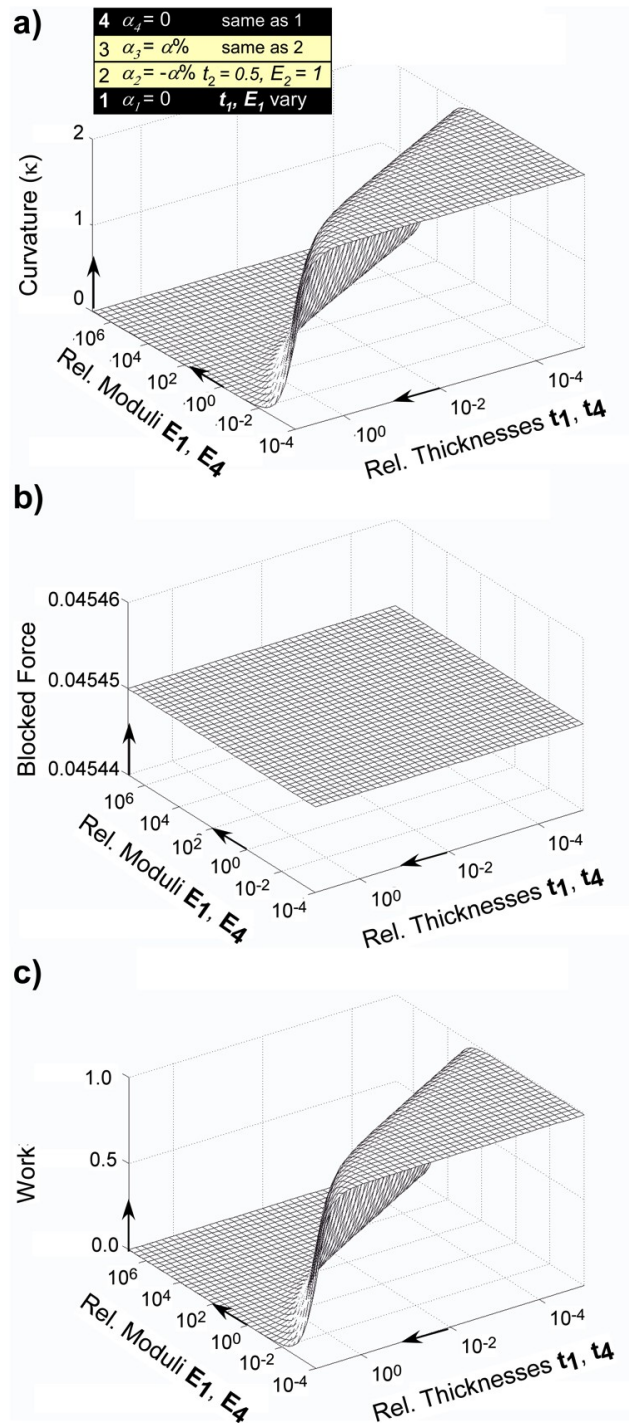
Figure 4-6. Face to face bilayers ($t_2 = t_3 = 0.5$, $E_2 = E_3 = 1$, $\alpha_2 = \alpha\%$, and $\alpha_3 = -\alpha\%$), with an ion-transporting EAP on the inside that increases in volume on one side and decreases by the same amount on the other, analogous to an IPMC. (a) Curvature, (b) blocked force, and (c) work as a function of the relative modulus and thickness of the passive layers relative to the elastomer layers.
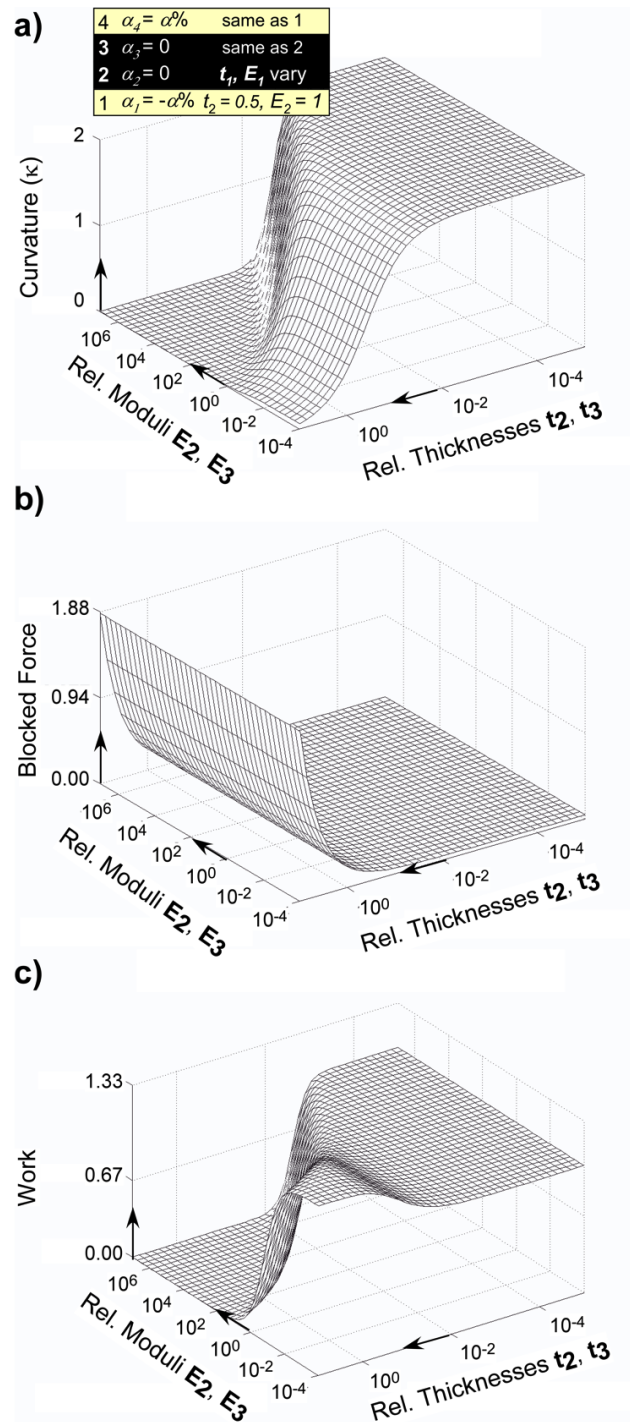
Figure 4-7 Face to face bilayers ($t_1 = t_4 = 0.5$, $E_1 = E_4 = 1$, $\alpha_1 = \alpha\%$, and $\alpha_4 = -\alpha\%$), with EAP on the outside, as for a CP/SPE/CP sandwich. (a) Curvature (b) blocked force (c) work as a function of the relative modulus and thickness of the mechanically passive layers relative to the EAP layers.

4.3.3 5-Layer Actuators

A 5-layer DEA stack can be used as a bimorph, bending in either direction depending on where the voltage is applied. Figure 4-8a shows the curvature for a 2-bilayer DEA stack with only one active layer (similar to Figure 4-5, but the fifth electrode layer is not considered negligible). The strain magnitude remains at $\alpha\%$ in layer 2 but it is set to zero in layer 4. If the strain is applied in layer 4 instead of layer 2 the stack will bend in the other direction. The curvature plot is almost identical to Figure 4-5a, with a same maximum plateau at $\kappa = 1$.

The blocked force (Figure 4-8b vs. Figure 4-5b), however, looks completely different, resembling instead that of a bilayer (Figure 4-3b), but with half the magnitude. In Figure 4-8b the blocked force is independent of the relative moduli of the three electrodes layers, depending only on their thicknesses. The maximum blocked force is 1. Thus by adding a non-mechanically-invisible fifth layer, the blocked force could be improved. The work curve (Figure 4-8c) is similar to that in Figure 4-5c, and the maximum work that can be performed is the same (at $t_1 (= t_3 = t_5) = 5$ and $E_1 (= E_3 = E_5) = 10^{-4}$, $W = 0.33$).
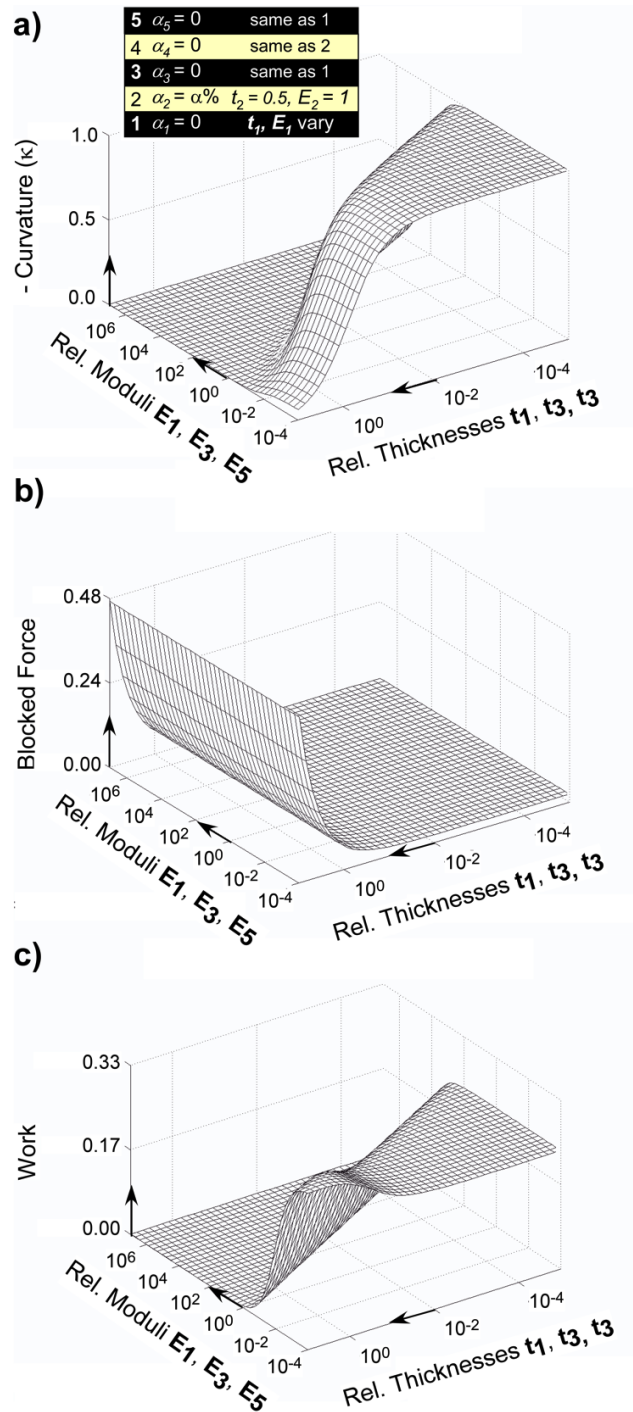
Figure 4-8. 5-layer device (a bimorph comprising 2 stacked DEAs) with $t_2 = t_4 = 0.5$, $E_2 = E_4 = 1$, $\alpha_2 = \alpha\%$, **and** $\alpha_4 = 0$. **(a) Curvature, (b) blocked force, and (c) work a as a function of the relative modulus and thickness of the electrodes relative to the elastomer layers. If the strain is applied in** α_4 **instead of** α_2, **the stack will bend in the opposite direction.**

4.4   Summary

Since the configuration with maximum curvature is the bilayer, in multi-layer structures bending is optimized by making selected electrode or mechanically passive layers "disappear," relative to the electroactive layers, by decreasing their thickness and/or modulus below some threshold. The results of the four cases that were run are shown in Table 4-1. In one case, the CP/SPE/CP, maximum curvature κ could be achieved entirely by reducing the SPE thickness below a critical value, for any modulus. Within an optimal region in the plane of thickness and modulus values, the curvature may have a maximum value plateau, allowing a range of combinations that work equally well. This is beneficial from a device design standpoint.

On the other hand, the blocked force F_b is optimized by *increasing* the thickness of the passive layers, since this increases the thickness of the structure overall. The required greater thickness to achieve high F_b is in direct conflict with the requirement for lower thickness to achieve high κ. One exception was the IPMC-like configuration, which had no dependence at all on either thickness or modulus of the electrode layers. Typically, the modulus of the mechanically passive layers does not matter to the force, except in the instance when a passive layer is added to one side of a planar DEA, and then the modulus of the electrodes must be small to recover a bilayer-like configuration because it is the passive layer and electroactive layer that participates in this bilayer.

123

Work W is optimized by choosing those coordinates in the thickness-modulus plane at which neither curvature or blocked force are too small so that their product can be maximized, and this is often far from the optimum for either. There are, however, distinct areas in the thickness-modulus plane to avoid, in which κ, ℓ and W are all low, and this area differs depending on which layers are participating in the bilayer and which layers need to vanish.

Table 4-1. Summary of multi-layer bending results. The electroactive layers (yellow) had a strain α %, modulus $E_{EAP} = 1$, and thickness $t_{EAP} = 0.5$, except for the effective bilayer which had $t_{EAP} = 1$. The passive and/or electrode layer (black) relative thicknesses and moduli were varied from 10^{-5} to 10^{-1} and 10^{-7} to 10^{4} respectively; maximum values are given *within this range*, and units are found as explained in the text.

	Effective Bilayer		2-Bilayer Stack		DEA + Passive	
Structure	3 $\alpha_3 = 0$ $t_3, E_3 \ll 1$ 2 $\alpha_2 = \alpha\%$ $t_2, E_2 = 1$ 1 $\alpha_1 = 0$ t_1, E_1 vary		4 $\alpha_4 = \alpha\%$ same as 2 3 $\alpha_3 = 0$ same as 1 2 $\alpha_2 = \alpha\%$ $t_2 = 0.5, E_2 = 1$ 1 $\alpha_1 = 0$ t_1, E_1 vary		4 $\alpha_4 = 0$ same as 2 3 $\alpha_3 = 0$ same as 1 2 $\alpha_2 = \alpha\%$ $t_2 = 0.5, E_2 = 1$ 1 $\alpha_1 = 0$ t_1, E_1 vary	
	Max.	Optimal	Max.	Max.	Optimal	Max.
Curvature κ	1	$E_1 > 10^2$ & $t_1 < 10^{-2}$ & $\dfrac{\log E_1}{\log t_1} = -2$	0.5	1	$E_1 > 10^2$ & $t_1 < 10^{-2}$ & $\dfrac{\log E_1}{\log t_1} = -2$	0.5
Blocked Force F_b	1	any E_1, increases as $t_1{}^3$	1	1	any E_1, increases as $t_1{}^3$	1
Work W	1	$E_1 = 10^4$ & $t_1 = 10^{-2}$	0.15	1	$E_1 = 10^4$ & $t_1 = 10^{-2}$	0.15

	IPMC		CP/SPE/CP		5-layer Bimorph	
Structure	4 $\alpha_4 = 0$ same as 1 3 $\alpha_3 = \alpha\%$ same as 2 2 $\alpha_2 = -\alpha\%$ $t_2 = 0.5, E_2 = 1$ 1 $\alpha_1 = 0$ t_1, E_1 vary		4 $\alpha_4 = \alpha\%$ same as 1 3 $\alpha_3 = 0$ same as 2 2 $\alpha_2 = 0$ t_1, E_1 vary 1 $\alpha_1 = -\alpha\%$ $t_2 = 0.5, E_2 = 1$		5 $\alpha_5 = 0$ same as 1 4 $\alpha_4 = 0$ same as 2 3 $\alpha_3 = 0$ same as 1 2 $\alpha_2 = \alpha\%$ $t_2 = 0.5, E_2 = 1$ 1 $\alpha_1 = 0$ t_1, E_1 vary	
	Max.	Optimal	Max.	Max.	Optimal	Max.
Curvature κ	2	$E_2 < 10^{-2}$ & $t_1 < 10^0$	2	2	$E_2 < 10^{-2}$ & $t_1 < 10^0$	2
Blocked Force F_b	0.045	no dependence	1.88	0.045	no dependence	1.88
Work W	1	$E_2 < 10^{-2}$ & $t_1 < 10^0$	1.33	1	$E_2 < 10^{-2}$ & $t_1 < 10^0$	1.33

4.5　Conclusions

The multilayer analytical model is a convenient method for design optimization of bending DEA structures.　The DEA configurations discussed in this paper are unimorph (effective bilayer, DEA+Passive), unimorph stack (2-bilayer stack), and bimorph.　The 2-bilayer stack has half the curvature compared to the remaining 3 configurations.　Thus, straining two layers like in the 2-layer stack second layer is not good for systems that require large deflection.　However, the blocked force for this configuration is the highest (same as effective bilayer).　The curvature and blocked force do not significantly overlap for the 2-bilayer stack, and thus, the work is the smallest.　The highest work was found for the effective bilayer followed by DEA+Passive and 5-layer bimorph, which have the same values.　In these systems there is a reasonable compromise between curvature and blocked force.

In the case of DEA device fabrication using standard micro-scale techniques, the electrode material would have to be metal (soft electrode materials are not readily available).　However, elastic moduli does vary greatly between different metal materials.　Thus, for design optimization, the only parameter one can vary is the thickness.　Thinner devices would give higher curvatures; however, the blocked force would decrease.

Acknowledgements

Supplementary Description

The supplementary information includes how the limits of the various plots are chosen. In addition, comparison of the multilayer model with a published result is shown.

Supplementary Information

Plot limits

The limits of the plot in the main paper are based on the range of values of thicknesses and typical moduli for a DEA (SI_Table 4). The X_{min} is the ratio of electrode thickness minimum and elastomer thickness maximum. The X_{max} is the ratio of electrode thickness maximum and elastomer thickness minimum. The Y_{min} is the ratio of electrode modulus minimum and elastomer thickness maximum. The Y_{max} is the ratio of electrode modulus maximum and elastomer thickness minimum.

SI_Table 4. Thickness and modulus of electrode and elastomer

	Thickness		Modulus	
Electrode	t_{elec} *min*	1E-08	E_{elec} *min*	1E+03
	t_{elec} *max*	1E-05	E_{elec} *max*	1E+11
Elastomer	t_{elas} *min*	1E-06	E_{elas} *min*	1E+04
	t_{elas} *max*	1E-03	E_{elas} *max*	1E+07
Limits	$X_{min}=t_{elec}$ *min*/t_{elas} *max*	1E-05	$Y_{min}=E_{elec}$ *min*/E_{elas} *max*	1E-04
	$X_{max}=t_{elec}$ *max*/t_{elas} *min*	1E+01	$Y_{max}=E_{elec}$ *max*/E_{elas} *min*	1E+07

Multilayer Model and Experimental Result Validation

Lau et al.'s experimental result from a multilayer stacked DEA [36] was used to validate the multilayer analytical model. The structure used in the study is an eight layer stack with a top passive layer (VHB tape), two active layers (VHB tape) sandwiched between three electrode layers (electro-less deposited silver), another passive layer of VHB, followed by a bottom passive layer (PDMS). The authors have fitted the curvature of the device to a bilayer model, assuming that the total thickness of the active layer consists of four VHB layers with uniform strain, and the PDMS layer as the passive layer (SI_Figure 1). In our multilayer model, we have varied the moduli of silver from 0 to 10^6 Pa but applied only strain to the two active layers as described in their experiment. The curvature of our multilayer fit did not show much variation with changes to moduli of silver. This is consistent with the authors' assumption that the stiffness of the electrode can be ignored. However, our multilayer fit under predicts their experimental result (SI_Figure 1). It is surprising

that with their assumption of treating the four-layers as a single layer, with constant strain, yielded result (bilayer fit) closer to the experimental value than our multilayer model prediction, which correctly accounts for the strain (present only in two-layers).
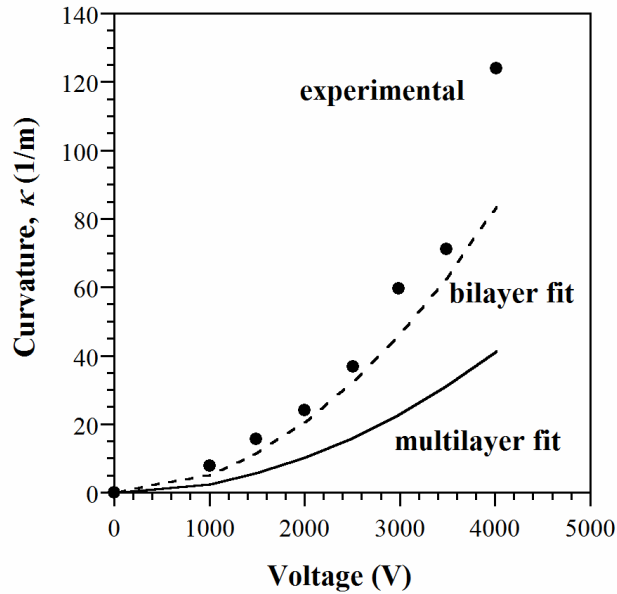
SI_Figure 9. Curvature versus voltage plot for experimental result, bilayer fit [36], and multilayer fit.

One possible reason for the deviation of our analytical multilayer fit with their experimental result is that the materials properties used in the modeling were assumed and no experimental data is available. Especially, in the case of the VHB tape which could have undergone some chemical exposure during electrode deposition that could possibly affect its properties. For example, the dielectric constant is taken to be 4.7. However, during the electro-less silver deposition, conductive particles could be trapped within the elastomer. This could change the dielectric constant of the VHB. Only if materials properties are known accurately can the analytical model predict the

129

experimental result.

Chapter 5: Patterning PDMS Using a Combination of Wet and Dry Etching

Bavani Balakrisnan, Sheetal Patil, Elisebeth Smela
University of Maryland, Department of Mechanical Engineering
2176 Glenn L. Martin Hall, College Park, Maryland 20742

Abstract

PDMS films 10 μm thick can be patterned within 30 minutes by combining dry etching to achieve substantially vertical sidewalls with wet etching to achieve high etch rates and to protect the underlying substrate from attack. Dry etching alone would have taken 5 hours, and wet etching alone would produce severe undercutting. In addition, using either technique alone produces undesirable surface morphologies. The mask used during etching is critical to a successful patterning outcome. E-beam evaporated Al was found to work well, adhering strongly to oxygen plasma treated PDMS, and holding up well during both dry and wet etching. To prevent wrinkling of the PDMS, a fast deposition rate should be used.

Keywords: PDMS, wet etching, dry etching, dielectric elastomer, surface morphology

5.1   Introduction

Polydimethylsiloxane (PDMS) is an elastomeric material that has good chemical resistance [124], biocompatibility [125], as well as ease of processibility [126], making it one of the widely-used materials for microfabrication of devices in a wide spectrum of fields ranging from microfluidics [127] to microelectronics [90]. PDMS is usually patterned by molding, or soft lithography [126].   A number of micromolding techniques, such as replica molding [71], microtransfer molding [128], and micromolding in capillaries [129], have been used for making PDMS-based microdevices. It would be advantageous in some cases, however, to be able to pattern PDMS not only by molding but also by etching. Unfortunately, both dry [130] and wet [72] etching have thus far given poor results, other than for removal of post-molding PDMS residues [128,131,132].

Dry etching produces substantial surface roughness, making it difficult to produce either smooth-bottomed channels or smooth features etched partway into the PDMS [133]. To produce smooth bottoms, the PDMS needs to be removed right down to the substrate, without etching the substrate. However, the dry etch recipes for PDMS are similar to recipes for silicon (Si) and silicon dioxide (SiO_2) [72,134]. Thus, if the PDMS is on a silicon substrate, the plasma will begin to etch the substrate after it etches through the PDMS, propagating the roughness. This can be avoided by using

an etch-stop layer such as Al [135] or Au [136], which adds to process complexity. Another approach to avoiding damage is to use a two-step process: a high etch rate recipe to remove up to the last micron followed by a lower etch rate recipe to remove the final micron. The etch rate is changed by changing the ratio of the two etchant gases, CF_4 and O_2 [136]. The main disadvantage of this two-step process is the long etch time required. For example, the process described in ref. [136] would require ~5 hours to etch a 10 μm thick PDMS film.

Wet etching is also possible, but it results in severe undercutting [72]. Furthermore, wet etching of PDMS can adversely affect the bonding of PDMS to substrates such as glass and to other PDMS layers [132]. Bonding can, however, be restored by following the wet etch with a dry etch protocol.

We required a method of patterning PDMS films on SiO_2-coated Si substrates in the effort to produce surface micromachined dielectric elastomer actuators, in which the PDMS elastomer is sandwiched between metal electrodes. The PDMS was 10 μm thick and had been spin-coated over Au electrodes on oxidized Si. The etching was therefore required not to attack either SiO_2 or Au. It also needed to completely remove the PDMS in the etched locations with minimal undercutting and without leaving residue. Further, it was necessary to identify a mask material that was compatible with the etch process.

In this paper, we demonstrate a combination of wet and dry etching steps to effectively pattern PDMS on Si or SiO$_2$ substrates. PDMS films 10 µm thick can be patterned in under 30 minutes while retaining a smooth substrate surface.

5.2   Experimental

Substrates were 4" p-type silicon wafers, some of which had a 1 µm thick layer of thermal oxide and several of which had chromium/gold electrodes (Cr 5 nm thick, Au 100 nm). The wafers were cleaved into quarters. The Au and Cr were deposited by thermal evaporation (1x10^{-6} Torr; Cr deposition rate 2 Å/s, Au 10 Å/s) and patterned photolithographically. Photoresist (Shipley 1813, MicroChem Corp, Newton, MA) was spin-coated at 3000 rpm for 60 seconds, exposed to 365 nm light for 8 seconds. (9 W/m^2, Karl Suss MJB-3 mask aligner), and developed for 25 seconds. (Microposit 352, MicroChem Corp, Newton, MA). The metals were wet etched (Transene Inc., Danvers, MA, TFA Au etchant, Type 1020 Cr etchant).

Sylgard 184 (Dow Corning Corp, Midland, MI) base compound and curing agent were mixed in a 20:1 ratio by weight and degassed in a vacuum desiccator for 30 minutes. The mixture was spun onto the substrates at 1000-5000 rpm for 60 seconds, and the samples were cured on a hotplate at 95 °C for 40 minutes. The PDMS surface is smooth but a has thickness variation due to spin coating of up to 1-2 µm.

134

Unless otherwise noted, aluminum films were used as hard masks for etching the PDMS. The Al was deposited over the PDMS to a thickness of 370-1000 nm by e-beam evaporation (Airco Temescal, 2×10^{-6} Torr, deposition rates of 3, 20, or 50 Å/s) and patterned by wet etching (Transene Type A Al etchant). (Thermally evaporated Al 1 μm thick only stood up to dry etching for 600 seconds). E-beam deposited hard masks of Cr (5 nm) and Au (360 nm) were also tested (5×10^{-6} Torr, deposition rate: Cr 2 Å/s, Au 15 Å/s).

Deposition and patterning of the metal hard mask was carried out in the following sequence. (1) Treat PDMS surface with O_2 plasma (150 mTorr, 50 W for 30 seconds). (2) Deposit metal film. (3) Spin-coat photoresist and let dry for 10 minutes at room temperature. (4) Expose resist for 15 seconds and develop in Microposit 352. (5) Wet etch metal. (6) Remove resist by rinsing sequentially in acetone, methanol, and isopropanol.

Dry etching of PDMS was performed by reactive ion etching (RIE) in CF_4:O_2 (Trion RIE, 37:13 sccm, 150 W, 150 mTorr). Wet etching of PDMS was done at room temperature and under continuous stirring (500 rpm) in a solution of N-methyl pyrrolidinone (NMP) and tetra-butyl ammonium fluoride (TBAF) (75 wt.% in H_2O, Sigma-Aldrich, St.Louis, Mo). The ratio of NMP to TBAF/water was 3 to 1.

Scanning electron microscopy (SEM) was done using a Hitachi SU-70 with a field emission gun at 1 kV. Elemental analysis was performed in the SEM using energy dispersive x-ray spectroscopy (EDS) at 5 kV (Bruker AXS Microanalysis, Ewing, NJ, equipped with silicon drift detector, SDD, Bruker XFlash).

Thickness was characterized by mechanical profilometry (Dektak 3ST, **Veeco Metrology Inc.**, Santa Barbara, CA). The stylus force was 1 mg. Average surface roughness (S_a) was measured optically with a Polytec Topography Measurement System (TMS-1200 TopMop µLab, Tustin, CA).

5.3   Results and Discussion

This section is organized as follows. First, results of dry etching alone are presented, second are the results of wet etching alone, and third are the results of combining the two. The last section concerns the qualities required of the hard mask.

Dry Etching Alone

The structures used in the work described in this section were fabricated as follows. (1) Cr/Au was thermally evaporated, then patterned by wet etching. (2) PDMS was spin coated and cured. It was then exposed to an O_2 plasma for 30 seconds (30 sccm, 150 mTorr, 50 W) so that the next metal layer would adhere. (3) An Al hard mask was deposited by e-beam evaporation and patterned by wet etching. This hard mask

overlapped the bottom Au electrode in some regions. (4) The unprotected PDMS was dry etched, and the surface morphology was examined. (5) To examine damage to the underlying substrate, residual etched PDMS was removed with PDMS wet etchant and the masked, unetched PDMS was removed with a razor blade. Figure 5-1a shows the process sequence. Figure 5-1b shows an optical image of the surface after removal of the PDMS.

Dry etching of PDMS was pioneered by Garra et al. [72]. The fastest etch rate, 20 μm/hr, was obtained in a mixture of CF_4 and O_2 at a 3:1 ratio (47 mTorr, 270 W). In CF_4 alone, the etch rate was only 12 μm/hr, and in O_2 alone, PDMS was not etched.

In our system, using Garra's recipe (CF_4:O_2 37:13 sccm, 50 mTorr, RF 270 W) resulted in high etch rates (32 μm/hr), but also extensive etching of the underlying SiO_2. The damage was still significant upon decreasing the power by half (150 W, etch rate to 18 μm/hr), as is evident in the optical images of the sample in Figure 5-1. In Figure 5-1b, on the right (appearing green and labeled 2) is the region where the PDMS was protected by the hard mask during etching (and from which the PDMS was subsequently removed). Therefore, the underlying substrate was unetched and appears optically smooth. In region 3, the SiO_2 substrate was exposed to the plasma during the etching cycle and therefore appears rough. Similarly, the gold (region 1) that was exposed to plasma during the etching cycle was also etched, while the portion that was protected by PDMS was smooth.

137
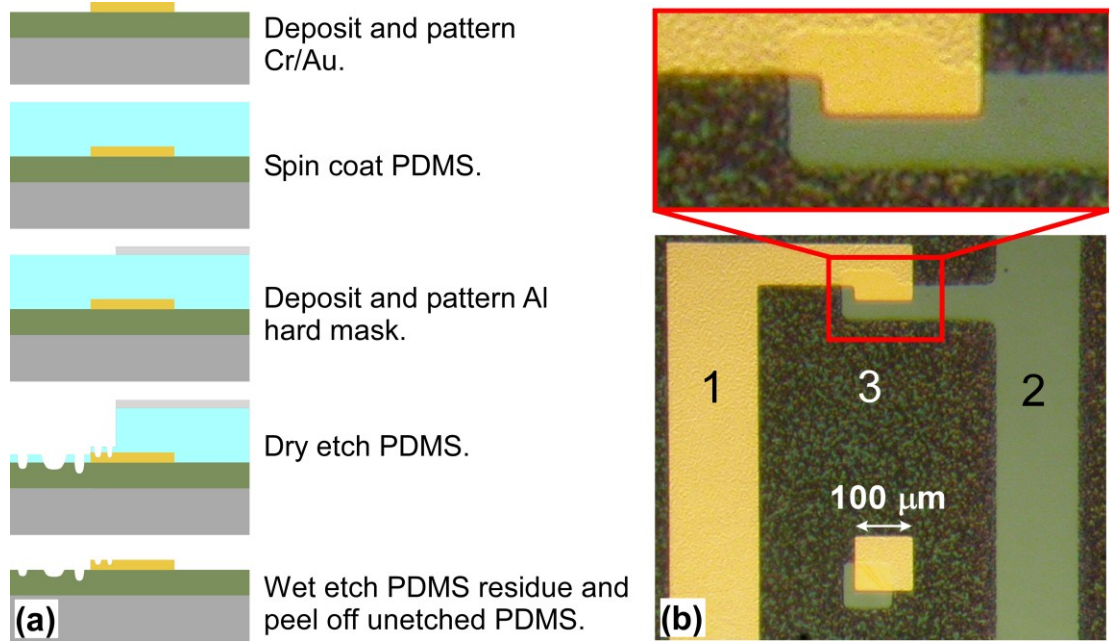
**Figure 5-1. a) Cross-sectional schematic of fabrication steps.
b) Photograph of a sample after PDMS removal.**

Optical profilometry showed that the average surface roughness of the etched Au in region 1 was 60 nm, while the protected Au had a roughness of 30 nm. The roughness of the etched SiO_2 (region 3) was 200 nm, while that of the unetched SiO_2 (region 2) was 50 nm. The differences in the roughness values of the SiO_2 and Au reflect the selectivity of the etch.

It should be noted that upon the start of dry etching, after the first 100 seconds under the conditions used here, the PDMS turned from colorless and transparent to translucent white. This translucence remained the same as etching continued, regardless of etch time.

138

Figure 5-2 shows typical surface morphologies of dry etched PDMS samples. In Figure 5-2a, the smooth, square middle region is the hard mask, with unetched PDMS below it; the surrounding region was etched. Etch products appear to be redeposited over the entire surface. Figure 5-2b and c are higher magnification images of the same sample, showing a rippled area and an area covered by structures that have the appearance of shavings.
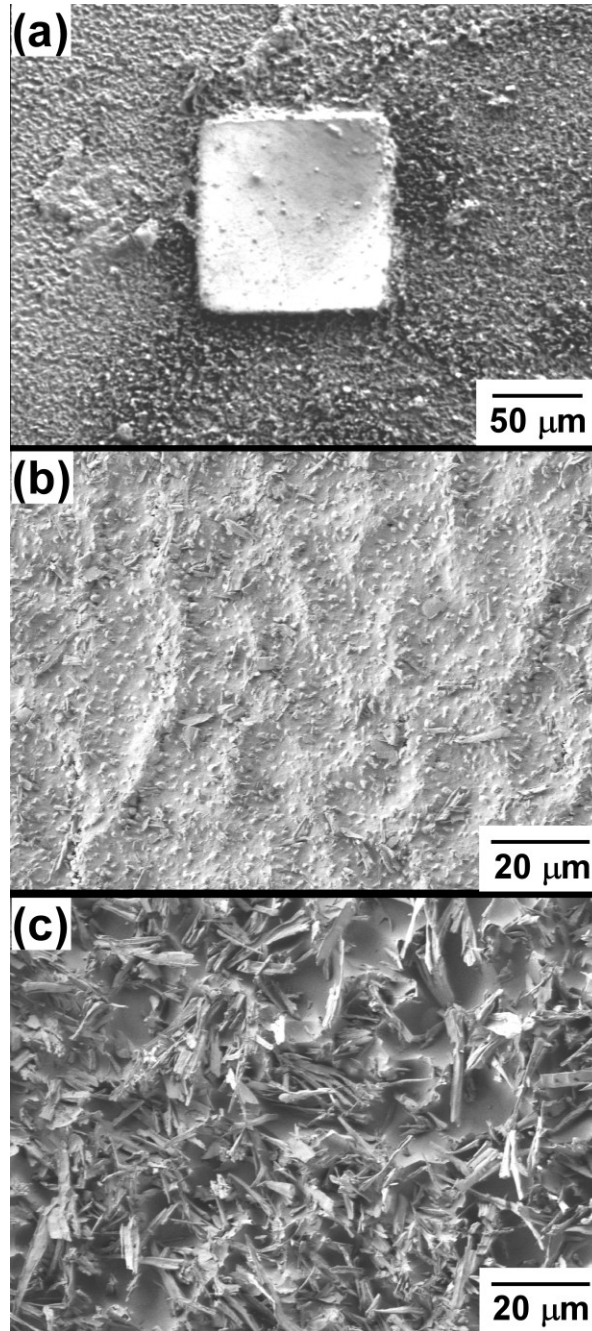
Figure 5-2. Surfaces of PDMS etched for 800 seconds. a) The center region was protected by an Al hard mask. b,c) Higher magnification images of the same etched PDMS surface. Both images were taken at the same magnification.

Another challenge in dry etching PDMS is reliably detecting the end-point. This is

critical because when the film is etched down by 10 μm, continued etching results in a residual porous layer. The gas permeability of PDMS results in severe substrate attack [136] when the residual layer forms. This porous PDMS could not be removed mechanically using a blade (PDMS peels off smoothly prior to forming the residual layer), nor chemically by using solvents (such as acetone, ethanol, or isopropanol) or wet etchant.

A critical parameter in dry etching PDMS is the time for which the PDMS is etched continuously. A sample with a PDMS thickness of 30 μm was diced into three pieces and dry etched for 300, 600, and 900 seconds. The samples were then placed into wet etchant to remove the remaining PDMS. It took 18 minutes to remove the PDMS from the 300 second sample and 30 minutes for the 600 second sample, but the PDMS on the 900 second sample was still there after 60 minutes. One would have instead expected the films that were dry etched longer to be removed faster. This indicates that PDMS changes during dry etching. Another indication was that continuously etched PDMS could not be easily removed using a blade, and left a sticky residue. This issue can be addressed by performing the dry etching in short-duration steps of 150-200 seconds, separated by 30-60 second resting periods during which the plasma and gas flow are turned off.

To summarize these results: dry etching alone leads to substantial substrate surface roughness, and it is difficult to determine when the PDMS has been completely

removed. The PDMS changes during the dry etch process, most likely due to heating, so it is best to etch it by pulsing, with approximately 150 seconds on, 30 seconds off.

Wet Etching Alone

Wet etching was done in a solution of TBAF in NMP. TBAF etches PDMS, and NMP dissolves the etched material [130]. The etch rate was 1.5 μm/min. The etchant should be replaced by fresh solution every 10-15 minutes to prevent the etch rate from decreasing over time.

Wet etching of PDMS did not proceed uniformly, but yielded a rough surface. Figure 5-3a shows an optical image of a partially etched sample. After etching a 10 μm film down to 2 μm, the peak-to-peak surface roughness was 0.7 μm.

Figure 5-3b shows the sample near the end of etching, when the PDMS had been almost completely removed: the remaining PDMS took the form of globular islands. These islands were 400 to 600 nm high and took longer to remove from the substrate than the PDMS bulk, with the etch rate dropping to 0.3 μm/min. Such a drop in etch rates has been reported previously, causing high aspect ratio structures to undergo substantial undercutting [72].

In summary, wet etching gives higher etch rates than dry etching: 1.5 μm/min versus

18 μm/hr, or 5 times faster, and the wet etchant does not attack Si, SiO$_2$, or Au. However, wet etching produces higher surface roughness, 0.7 μm compared to 0.2 μm, which eliminates this method from being appropriate for many applications. Furthermore, the etch rate slows near the end-point, which leads to undercutting [72], a particular concern when patterning high aspect ratio structures.
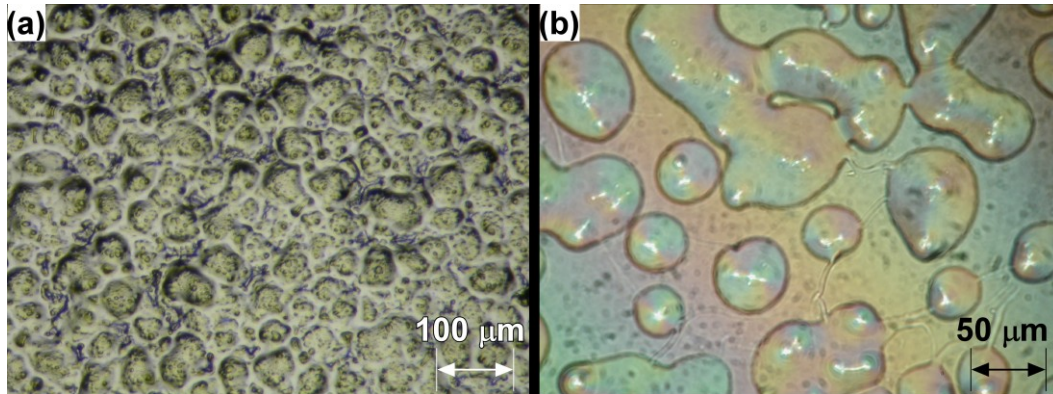
Figure 5-3. a) PDMS film after wet etching for 8 minutes. b) Globular islands seen just prior to complete removal of the PDMS.

Combining Wet and Dry Etching

To obtain the advantages of both dry etching (directionality for achieving high aspect ratio structures) and wet etching (no surface attack, fast etch rates), we combined the two methods. Figure 5-4 shows SEM micrographs of a PDMS film 16 μm thick patterned using the combined etching protocol. Figure 5-4a shows the Al hard mask after the Al was patterned but before carrying out any PDMS etching. Figure 5-4b shows the surface after dry etching the PDMS for 30 minutes to a thickness of 7 μm (CF$_4$:O$_2$ 37:13 sccm, 50 mTorr, RF 150 W). Figure 5-4c was taken after wet etching the PDMS for 8 minutes, followed by removing the Al by wet etching. Figure 5-4d

143

shows an enlarged image of Figure 5-4c, showing the straight sidewalls and smooth substrate.

The smallest features of these structures were below 30 μm, and this technique gave clean edges with negligible undercut.

This method was also used successfully to pattern 10 μm thick PDMS films over Au electrodes on oxidized Si substrates. The PDMS was dry etched to a thickness of 3 μm before wet etching. PDMS patterning was achieved in less than 30 minutes without affecting the substrate. Care must be taken not to dry etch below 2 μm, since this will result in attack of the substrate.
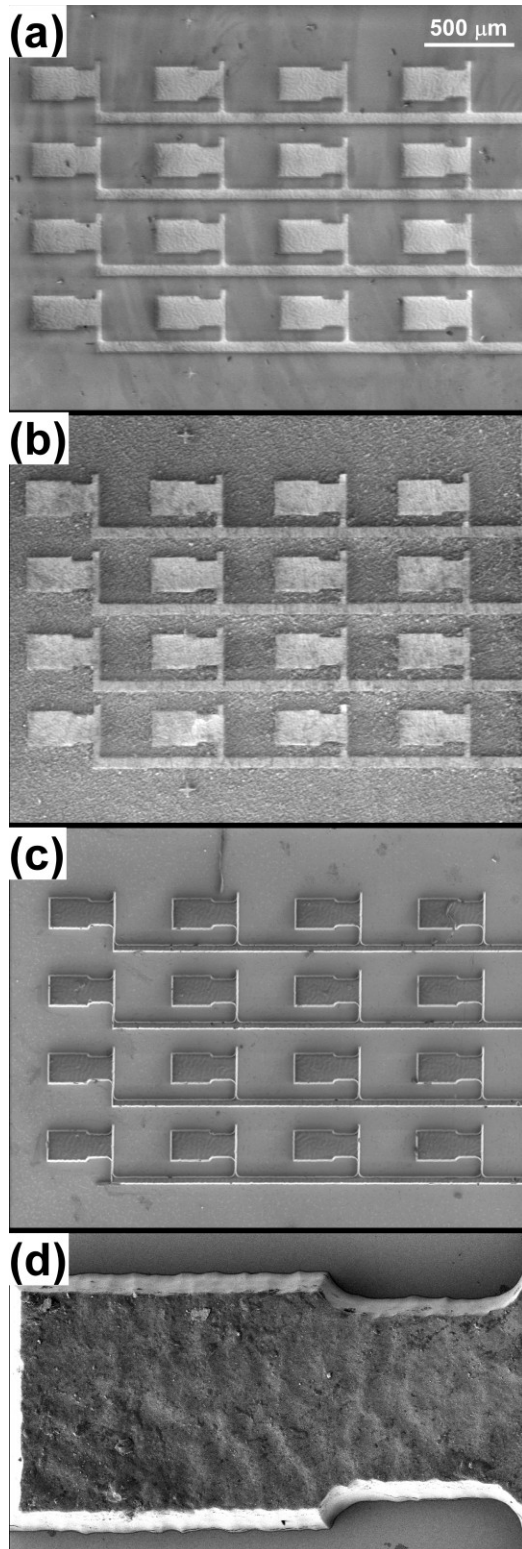
Figure 5-4. a) SEM micrograph of an Al hard mask on an a PDMS film 16 μm thick. b) The same sample after dry etching the PDMS and c) after wet

145

etching the remaining PDMS and removing the Al. d) Close-up of one of the structures in (c).

Masking

A hard mask is essential for etching PDMS using the combined dry+wet method because photoresist, although it stands up to the dry etching step, is removed by the PDMS wet etchant.

The quality of the hard mask, in terms of its ability to withstand both wet and dry etching conditions, is a critical criterion in choosing the material and the patterning method. This is a matter not only of the materials, but also of the deposition method. E-beam evaporated Al 1 μm thick stood up longer to the PDMS dry etch environment than thermally evaporated Al, which was eroded within 10 minutes. E-beam evaporated Al of only 300-400 nm thickness withstood dry etching for more than 30 minutes, and also withstood wet etching for more than 30 minutes.

Another important factor is the effect of the hard mask deposition conditions on the PDMS layer. Severe wrinkles were formed at slow e-beam deposition rates (3-20 Å/second) that extended to a depth of 2 μm below the surface. These wrinkles remained permanently on the surface even after removing the Al. Such wrinkles have been seen previously and were attributed to local heating of the surface and formation of additional crosslinks in the PDMS [92,137]. Figure 5-5a shows a PDMS film after Al had been deposited over the whole surface, and then removed over half of it using

Al wet etchant. The wrinkles could be seen even after dry etching for about 2 μm, as shown in region 1 of Figure 5-5b. Figure 5-5c shows a close-up of region 1. Region 2 has a morphology similar to that shown in Figure 5-2. The deeply wrinkled surface can be avoided by using higher deposition rates. At 50 Å/s, there wrinkles formed only in small patches, and they were shallower (less than 0.5 μm deep).
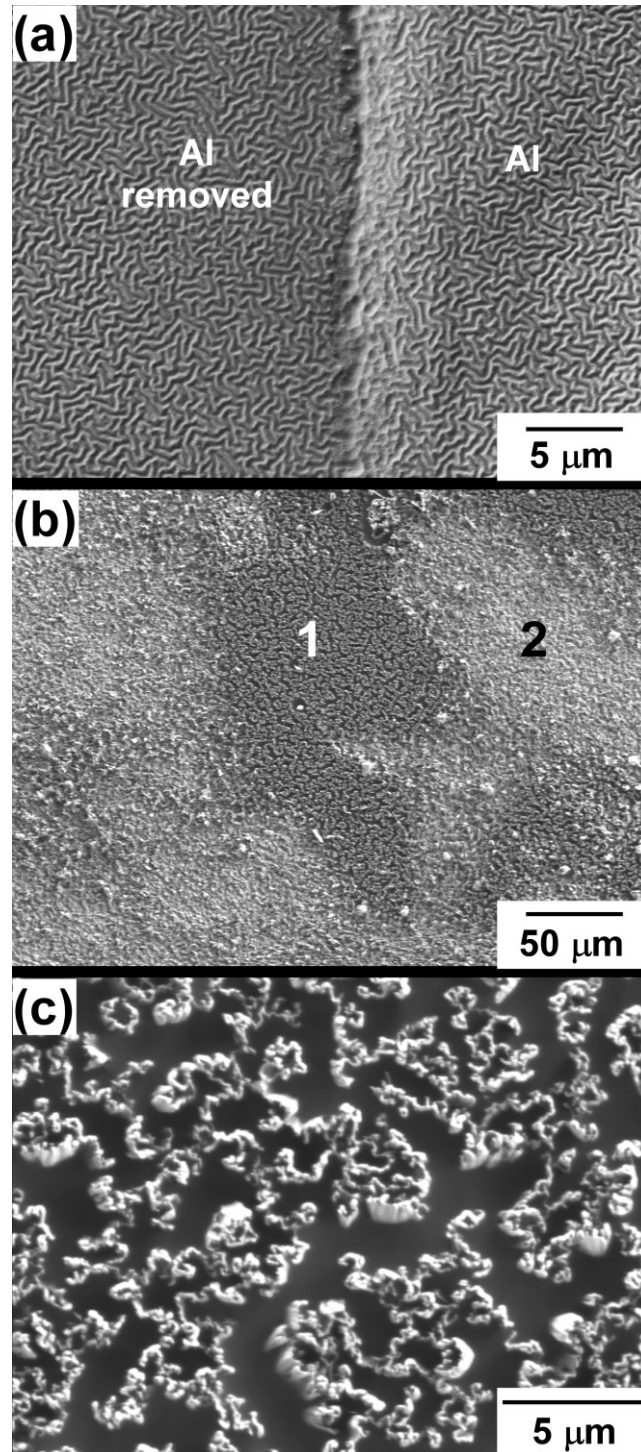
Figure 5-5. a) SEM micrographs of a PDMS film after Al deposition by e-beam evaporation. The Al was subsequently removed on the left half of the figure. b) PDMS surface after removal of the metal and dry etching to a depth of 2 μm. c) Higher magnification view of region 1 in (b).

148

Cr /Au (5 nm/360 nm) was explored as an alternative hard mask, and this had almost no wrinkles even though it was deposited at a lower deposition rate (Cr 2 Å/s, Au 15 Å/s) than the Al. However, the Au did not perform as well as a hard mask: the surface of the Au blackened within 800 seconds during PDMS dry etching. If Au is used as a hard mask, a layer of photoresist (Shipley 1813) could be used as a protective overcoat, since resist is not etched appreciably under these conditions. In addition, the aluminum adhered better to the PDMS and held up longer than the Cr/Au did during wet etching.

Patterning the metal hard mask can also be challenging. The first challenge is to overcome poor adhesion between the metal and the PDMS. Treating the PDMS with oxygen plasma (150 mTorr, 50 W, 30 secs) increased the adhesion sufficiently to allow the successful patterning described in section 0. This same treatment was also used to promote adhesion between photoresist and PDMS during lithography. The second challenge is associated with PDMS swelling if it is exposed to acetone or other organic solvents [80], which causes the metal layer to peel off. In this work, the hard mask was therefore patterned by wet etching rather than by lift-off. Lift-off can, however, be accomplished if the resist is blanket exposed after patterning but prior to metal deposition, and then removed after metal deposition using aqueous developer.

In summary, a hard mask is needed when using the combination of dry and wet

etching, but the material, deposition method, and deposition conditions must be well chosen so that the mask holds up and so that wrinkling is avoided. It may be necessary to treat the PDMS prior to mask deposition to promote adhesion, and during patterning of the hard mask organic solvents should be avoided.

5.4   Conclusions

We have demonstrated an effective PDMS patterning protocol by combining wet and dry etching of PDMS. This protocol exploits the advantages of the wet and dry etching processes while avoiding their disadvantages. Using this protocol, we have demonstrated that it is possible to pattern PDMS with10 μm thickness down to sub-100 μm sized features in under 30 minutes without substrate attack. The concept of this method is to dry etch the PDMS to a thickness of 2-3 μm, producing substantially vertical sidewalls, followed by wet etching to remove the remaining material, which produces a smooth substrate.

A good hard mask is crucial in the successful fabrication of good quality PDMS patterns. E-beam evaporated Al works well for this application. The PDMS surface should be pre-treated with an oxygen plasma to improve the adhesion of the mask material, and a high deposition rate should be used to prevent wrinkle formation.

There are several questions that should be answered in future work. The first is

whether the dry etch step affects the Young's modulus of the PDMS. It has been reported that the surface of PDMS is stiffened by plasma etching: the surface stiffness was found to be an order of magnitude higher than the bulk after 4 minutes in oxygen plasma [138]. Second, it is known that wet etching can adversely affect the bonding of PDMS to glass and other materials [132]. Since our fabrication technique ends with a wet etch, if subsequent bonding is required it may be necessary to follow that with a brief dry etching protocol, as suggested in [132].

Acknowledgements

Chapter 6:   Surface Micromachined Dielectric Elastomer Actuators

Bavani Balakrisnan, Deepa Sritharan, Elisabeth Smela
University of Maryland, Department of Mechanical Engineering
2176 Glenn L. Martin Hall, College Park, Maryland 20742

Abstract

DEAs came into prominence about two decades ago and most of the demonstrated applications involved macro-scale DEA devices.   There are potentially many applications for micro-scale DEAs such as in micro-robots, micro-pumps, and micro-optical systems; however, fabrication challenges have to be overcome before they can be realized.   This paper addresses the challenges faced in fabricating surface micromachined DEAs using standard microfabrication techniques and, in addition, outlines the fabrication of out-of-plane DEAs by surface micromachining.   Surface micromachining was chosen instead bulk micromachining because bulk micromachining involves removal of large portions of the substrate to release the devices, reducing space for integration with driver circuitry.   The fabrication protocol developed in this paper for the fabrication of out-of-plane DEAs can be extended to fabricate devices in other actuation modes such as in-plane, bending, and membrane DEAs.

6.1 Introduction

Dielectric elastomer actuators (DEAs) are a class of electroactive polymers (EAPs) that convert electrical energy into displacement [8]. A DEA is comprised of an elastomer sandwiched between two compliant electrodes. Upon application of voltage (V) between the electrodes, the electrostatic attraction between the oppositely charge electrodes squeezes the elastomer with pressure, p, in the direction of the applied field, causing the elastomer to stretch in the two orthogonal directions [8]. The pressure, p, is calculated from

$$(1) \quad p = \varepsilon_o \varepsilon_r (V/z)^2 = -S_z E \,,$$

where, ε_o is the permittivity of free space, ε_r is the dielectric constant of the elastomer, z is the thickness of the elastomer layer, S_z is the strain in the z-direction, and E is the elastic modulus of the elastomer. The strain in the elastomer is defined by

$$(2) \quad S_z = -\left(\frac{\varepsilon_o \varepsilon_r}{E}\right)\left(\frac{V}{z}\right)^2.$$

Over the last two decades, since DEAs came into prominence, most of the demonstrated applications involved macro-scale DEA devices. DEAs are used in applications requiring large displacements (up to 300% has been reported) [8] and have been demonstrated for many macro-scale (centimeter and larger) applications such as robots, loudspeakers, and motors [6,9,11-13]. Apart from having the ability to exhibit large strains, DEAs have high energy density (3 J/g [15]), low power consumption (10 μW [15]), and good efficiency (above 65% [15]). There are many

153

advantages for miniaturization including higher device density per unit area, multiplexing (multiple devices in a given foot print), and lower costs associated with batch processing [139]. In addition, macro-scale DEAs require large voltages (>kV range) to achieve measurable actuation. By reducing the thickness of the elastomer, the actuation voltage required is reduced. For example, the voltage needed to actuate a 100 μm thick elastomer at 30 V/μm is 3000 V. If the thickness of the elastomer is reduced to 10 μm, only 300 V will be needed. This is one of the primary motivations for development of micro-scale DEA devices. Other factors that scale advantageously include force density, bandwidth, and power density [62].

Micro-scale DEAs can be fabricated by adapting the mature standard silicon microfabrication processes commonly used in microelectronics [64]. This approach integrates micro-scale DEA devices with complementary metal-oxide-semiconductor (CMOS) driver circuitry and other micro-electro-mechanical systems (MEMS). There are two different standard silicon microfabrication approaches: surface micromachining and bulk micromachining. Bulk micromachining involves removal of large portions of the substrate to free the devices. This reduces the space required for integration with the driver circuitry. On the other hand, surface micromachining involves the fabrication of devices on top of the substrate through a series of thin-film deposition and etching steps. The surface micromachining approach is more amenable to multiple device integration with the driver circuitry [64].

154

There are four different modes of actuation for a micro-scale DEA device (Figure 6-1): (1) squeezing mode, (2) stretching mode, (3) buckling mode, and (4) deflection mode. In the squeezing mode, the elastomer is squeezed, and the out-of-plane displacement is utilized, e.g., in electro-optical modulation; whereas, in the stretching mode, the in-plane displacement caused by the out-of-plane squeezing is utilized, e.g., to push objects. In the buckling mode, which could be used for vibration tuning, the edges of the DEA are pinned, and upon actuation, the membrane bulges out-of-plane. In the deflection mode, actuation of the DEA causes out-of-plane bending. The bending actuation is a promising actuation mode for the development of soft robotic legs. Various other motions can be achieved by combining these modes.
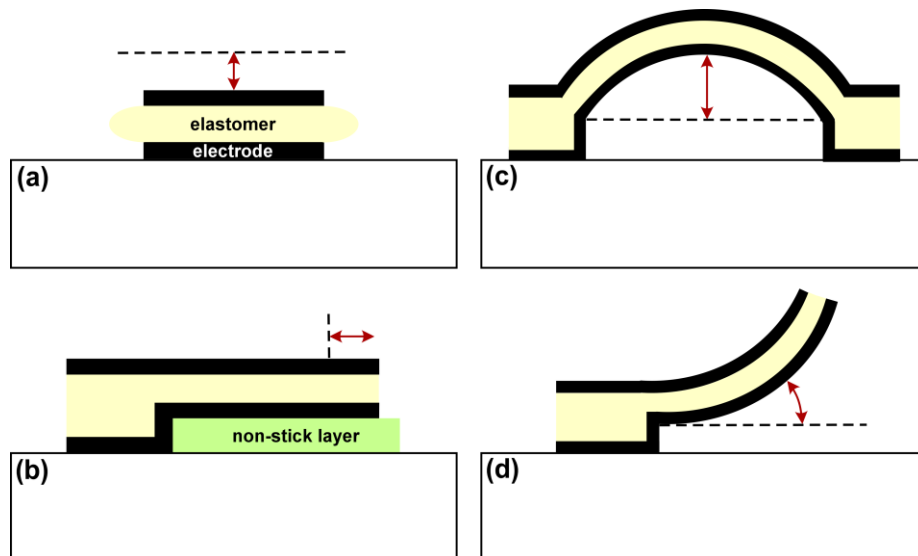
Figure 6-1 Four different modes of actuation in a surface micromachined micro-scale DEA: a) out-of-plane (squeezing) actuator, b) in-plane (stretching) actuator, c) membrane (buckling) actuator, and d) bending (deflection) actuator. (Dashed lines show positions before actuation).

The field of micro-scale DEAs is relatively new and prior work is limited. Within this limited literature, many authors concentrated on patterning the electrodes and not the elastomer. Uma *et al.* demonstrated an electro-optical modulator DEA device using an elastomer deposited on top of a patterned electrode grating structure. In their device, the elastomer and the top electrode were not patterned [41]. Galler *et al.* demonstrated the first surface micromachined squeezing DEA by etching the elastomer [42] using a TEM grid as a hard mask. This paper showed that patterning both, the elastomer and the electrodes, increased the achievable actuation strain as compared to when only the electrodes were patterned. Shea *et al.* [35] and Pimpin *et al.* [20] demonstrated DEA membranes using bulk micromachining. In this process, Si substrate with elastomer film was patterned and etched from the back until the elastomer film was suspended. The elastomer itself was not patterned in this process. It was demonstrated that the deformation achieved by patterning electrodes was about six times larger than without patterning the electrodes [20].

This paper focuses on surface micromachining for fabrication of micro-scale DEAs. Specifically, this paper outlines an optimized microfabrication protocol to develop a workable out-of-plane micro-scale DEA device. Several processing and materials challenges were encountered while developing this protocol. The paper highlights various successful approaches undertaken to address these challenges. It also includes several initial attempts at developing a microfabrication protocol for other modes of DEA such as bending and in-plane DEAs. The knowledge gained while

156

addressing the challenges encountered in optimizing the processes during the fabrication of out-of-plane DEAs provides information for the development of other actuation modes of DEAs.

6.2   Fabrication of Micro-scale Out-of-Plane DEA

This section highlights several challenges encountered during fabrication of the out-of-plane DEA micro-scale device using standard surface micromachining processes. To fabricate a simple out-of-plane DEA, the bottom electrode is first deposited and patterned, followed by spinning and curing of the elastomer. Next, the top electrode is deposited and patterned. The top electrode plays a dual role of the electrode as well as a hard mask for etching the elastomer. This seemingly simple process poses several processing challenges that needed to be successfully resolved in order to fabricate a functioning device.

6.3   Experimental

Silicon substrates (4" p-type, (100)) with 1 μm thermal oxide were used. Three different materials were tested as the bottom electrode: (1)50 nm Cr/100 nm Au, (2) 50 nm Cr/100 nm Au/50 nm Cr, and (3) 200 nm Al/200 nm SiO_2. The Cr/Au electrodes were deposited by thermal evaporation (Metra; $1x10^{-6}$ Torr; Cr deposition rate 2 Å/s, Au 10 Å/s) and Al/SiO_2 electrodes were deposited by e-beam evaporation (Airco Temescal, $2x10^{-6}$ Torr, deposition rates of 25 and 10 Å/s). The electrodes

were patterned by photolithography. Photoresist (Shipley 1813, MicroChem Corp, Newton, MA) was spin coated at 4000 rpm for 60 seconds followed by exposure to 365 nm light for 8 seconds (8 W/m^2, Karl Suss MJB-3 mask aligner) and development for 25 seconds (Microposit developer CD-30, MicroChem Corp, Newton, MA). The metals were then wet etched (Transene Inc., Danvers, MA, TFA Au etchant, Type 1020 Cr etchant, Al etchant). The SiO$_2$ was wet etched in dilute buffered hydrofluoric acid (1 part hydrofluoric acid: 6 part ammonium fluoride with surfactant, J.T. Baker, Phillipsburg, NJ).

After patterning the bottom electrodes, the elastomer was spin-coated onto the substrate. Three different silicone elastomers were tested: Sylgard 184, Sylgard 527 (Dow Corning Corp, Midland, MI) and MRTV-9 (Insulcast, Montgomeryville, PA). Sylgard 184 and Sylgard 527 base compound and curing agent were mixed in a 20:1 and 1:1 ratio by weight, respectively, and degassed in a vacuum desiccator for 15 minutes. MRTV-9 base compound and curing agent were mixed in a 10:1 ratio by weight and degassed in a vacuum desiccator for 15 minutes. The Sylgard silicones were spin-coated onto the substrates at 5000 rpm for 60 seconds followed by curing on a hotplate at 95 °C for 60 minutes yielding a ~10-15 μm thick elastomer layer. The MRTV-9 was more viscous and was spin-coated in a two-step process, first by spinning at 500 rpm for 60 seconds followed by spinning at 5000 rpm for 60 seconds. The samples were subsequently cured on a hotplate at 65 °C for 60 minutes resulting

in a 30-35 μm MRTV-9 elastomer layer. When two layers were spin-coated to achieve thicker layers, the first layer was cured for only 15 mins before the second layer was spin-coated.

After spin-coating the elastomer, the top electrode was patterned by lift-off. First, the elastomer surface was treated with oxygen plasma (O_2 - 50 sccm, 50 W, 100 mtorr for 20 seconds) to enhance adhesion between the elastomer surface and the photoresist. Then, photoresist Shipley 1813 was spin-coated at 1000 rpm for 60 seconds, dried at room temperature for 10 mins, exposed to 365 nm light for 11 seconds at 8 mW/cm^2, and developed for 10 seconds (Microposit developer CD-30, MicroChem Corp, Newton, MA). After developing the resist, the electrode was flood-exposed for 20 seconds at 8 mW/cm^2 and treated with oxygen plasma before loading it into the top electrode deposition chamber. Flood exposure enabled removal of the resist from the electrode without exposing it to acetone, which tended to swell the elastomer. Al and Cu were tested as materials for the top electrode. The top electrode materials have dual functions: as a top electrode as well as a hard mask for etching the elastomers. A 500 nm thick top electrode was deposited by e-beam evaporation over the elastomer previously patterned with resist (Airco Temescal, $2x10^{-6}$ Torr, deposition rates of 3 Å/s). The patterned top electrode was then achieved by removing the resist layer in developer (CD-30).

The patterned top electrode was then used as a hard mask to etch the elastomer.

Elastomer was dry etched using reactive ion etching (Oxford ICP etcher 100) in SF$_4$:O$_2$ (45:5 sccm RF-50 W, ICP-1400W, 7 mtorr) at an etch rate of 2 μm/min. The fabrication process is shown schematically in Figure 6-2.

Scanning electron microscopy (SEM) imaging was done using a Hitachi S-3400 variable pressure SEM at 20 kV accelerating voltage in backscattered imaging mode. Elemental analysis was performed in the SEM using energy dispersive x-ray spectroscopy (EDS) at 20 kV (Bruker AXS Microanalysis, Ewing, NJ, equipped with silicon drift detector, SDD, Bruker XFlash).

The elastomer thickness was characterized by a Dektak 3ST mechanical profilometer. The contact to the electrodes were made with probes and the voltage was applied using a high voltage power supply (UltraVolt). The contraction of thee devices were monitored using white light interference system.

cross-sectional view *top view*

(1) Si wafer

(2) bottom electrode, deposit & pattern by wet etch

(3) elastomer, spin & cure

(4) photoresist, spin expose & develop

(5) top electrode, deposit & pattern by lift off

(6) elastomer, etch by RIE
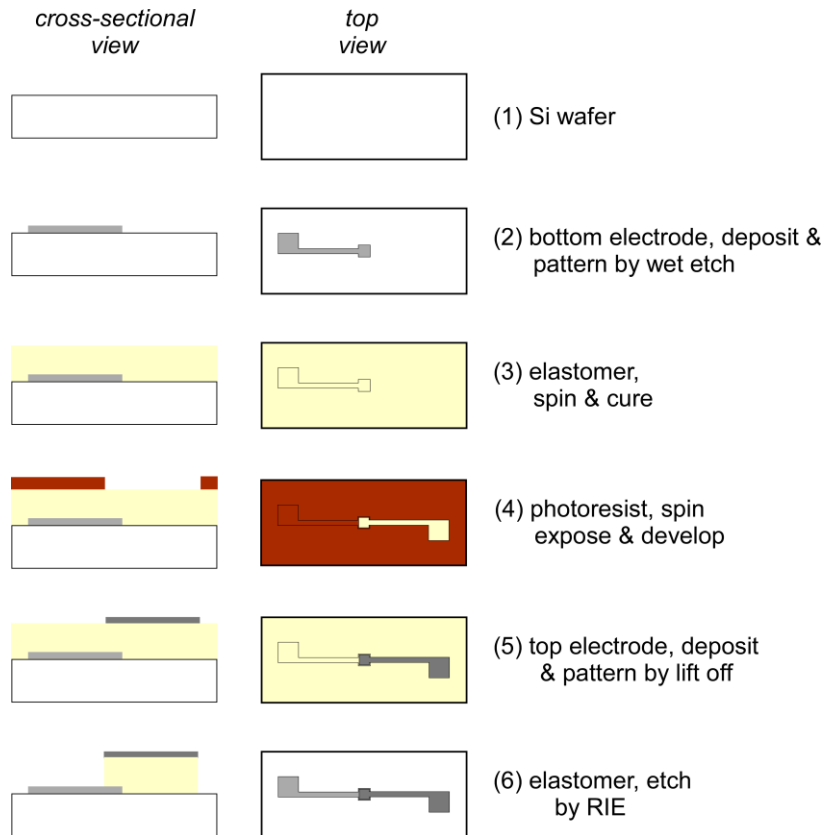
Figure 6-2. Fabrication protocol for out-of-plane DEA.

6.4   Fabrication Challenges

6.4.1   Challenges with Bottom Electrode Fabrication

The material chosen for the bottom electrode is important, because it has to withstand several subsequent processing steps, including exposure to etching chemicals and reactive gases during etching of the elastomer. The resistance of a DEA device should typically be >200 Mohms. However, several initial attempts at fabricating an out-of-plane DEA device with Cr/Au bottom electrode resulted in an electrical short (i.e. a resistance of only 5-15 kohms range for a 20 μm elastomer thickness) between the bottom and top electrode. Consequently, there is high current through the device,

161

resulting in significant heat generation and causing the device to behave as a thermal actuator instead of a DEA actuator. The electrical short was probably caused by resputtering of the bottom electrode during the dry etching of the elastomer. During dry etching, there was no etch-stop to prevent the etching of the bottom electrode below the elastomer. This resulted in Au resputtering onto the surface of the elastomer edges, forming a conductive path between the top and the bottom electrode. Evidence of this phenomenon is shown in Figure 4. The edges of the elastomer directly above the Au bottom electrode (Figure 4b) are bright while it is darker at regions away from the Au bottom electrode. In a backscattered image, brightness is related to the atomic mass: heavier elements (Au in this case) appear brighter than lighter elements (Al). Thus, some re-deposition of the Au (resputtering) onto the elastomer may have occurred during elastomer etching, causing an electrical short between top and bottom electrode. The presence of re-deposited Au on the elastomer edges was also confirmed through EDS analysis.
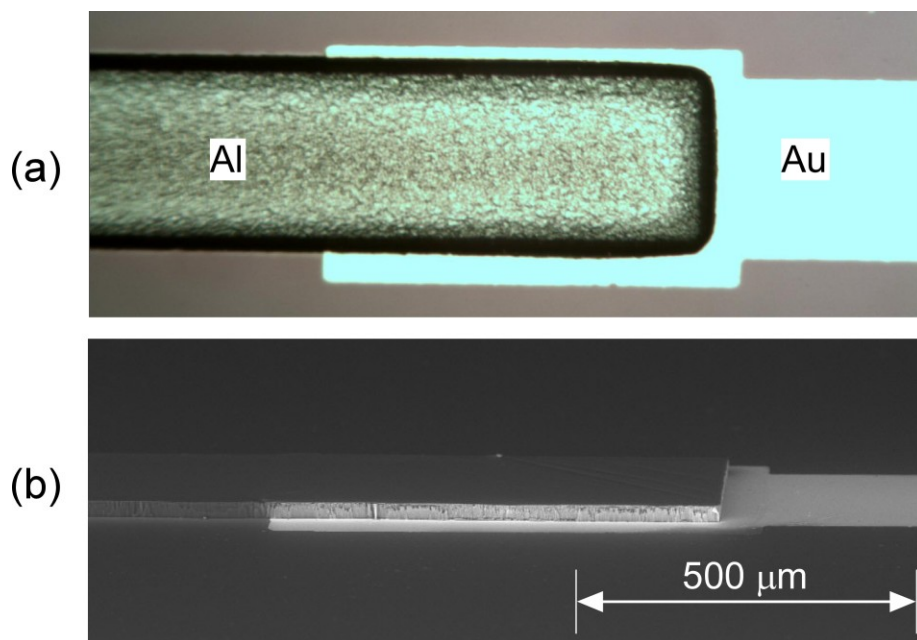
Figure 6-3 a) Optical image of the top view of the fabricated device. b) Tilted backscattered image of the device. Right side is the Au bottom electrode and left side is the Al pad on top elastomer (Sylgard 184). The middle portion is the active area of the device.

Four different approaches were taken to address the resputtering of Au: (1) undercutting elastomer through wet etching, (2) using Cr/Au/Cr as the bottom electrode, (3) using Al/SiO$_2$ as the bottom electrode, and (4) negating the use of a patterned metal bottom electrode by using a heavily doped Si substrate.

(1) *Undercutting elastomer through wet etching*: The devices with the resputtered Au electrode on the elastomer edges were wet etched for three minutes in a solution of N-methyl pyrrolidinone (NMP) and tetra-butyl ammonium fluoride (TBAF) (3:1 ratio) [140]) in an attempt to remove resputtered Au from the edges.   The elastomer etch rate in this solution is about one 1.5 µm/min.   Figure 6-4 shows the device after this wet etching step. While the wet etching

163

step was successful in undercutting the elastomer, the device remained conductive. This is likely due to regions where the resputtered Au was not completely removed. Wet etching also resulted in delamination of the elastomer from the bottom electrode. Therefore, undercutting elastomer with wet etching is not a viable solution to address the Au resputtering problem.
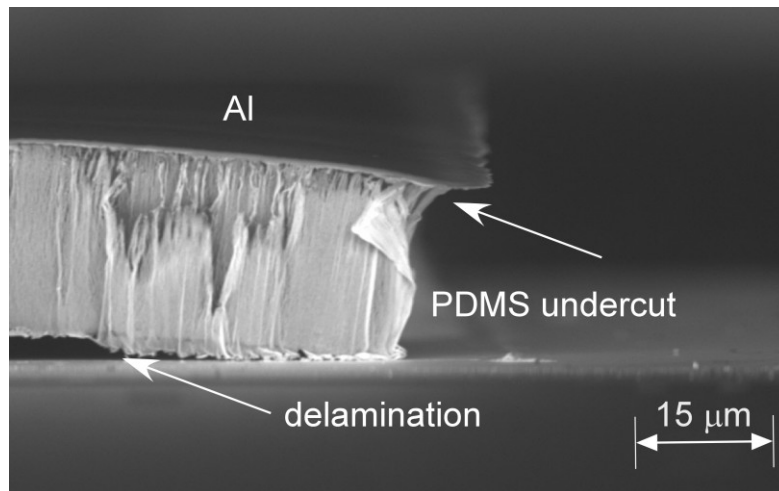
Figure 6-4. Device that was wet etched shows undercut. Resputtered Au is still present at the elastomer edge.

(2) *Cr/Au/Cr as bottom electrode* : A micro-scale out-of-plane DEA device was fabricated using 50 nm Cr/100 nm Au/50 nm Cr trilayer as the bottom electrode (Figure 6-5a). The Cr layer on top of Au layer prevented the resputtering of Au during dry etching of the elastomer. This eliminated the shorting.

(3) *Al/SiO₂ as bottom electrode*: A micro-scale out-of-plane DEA device with 200

nm Al/200 nm SiO_2 bilayer as the bottom electrode was fabricated with other process steps being essentially the same (Figure 6-5b). This was also found to eliminate shorting and the device. Another advantage with this electrode configuration is the comparable dielectric constant values of the SiO_2 and the elastomer, which would not undesirably affect the actuation of the out-of-plane DEA [64]. An added benefit of this approach is that when fabricating thinner elastomer layers the pin-holes present in them could affect conductivity. The SiO_2 could function as a good insulating layer. Furthermore, the adhesion between SiO_2 and the elastomer is significantly better than with Au electrode because of the comparable chemical structures.

(4) *Heavily doped Si substrate as bottom electrode*: The fourth approach to address the shorting was to eliminate the need for a patterned Au bottom electrode. This was achieved by using a heavily doped silicon wafer (resistivity of 0.005 to 0.02 Ωcm) substrate as the bottom electrode (Figure 6-5c). This approach would also reduce the number of steps required for patterning, as the bottom electrode does not need to be patterned. Figure 6-5c shows over-etching of the silicon, but this did not affect the conductivity of the device. However, the disadvantage of this electrode is that it cannot be used for other actuation modes.
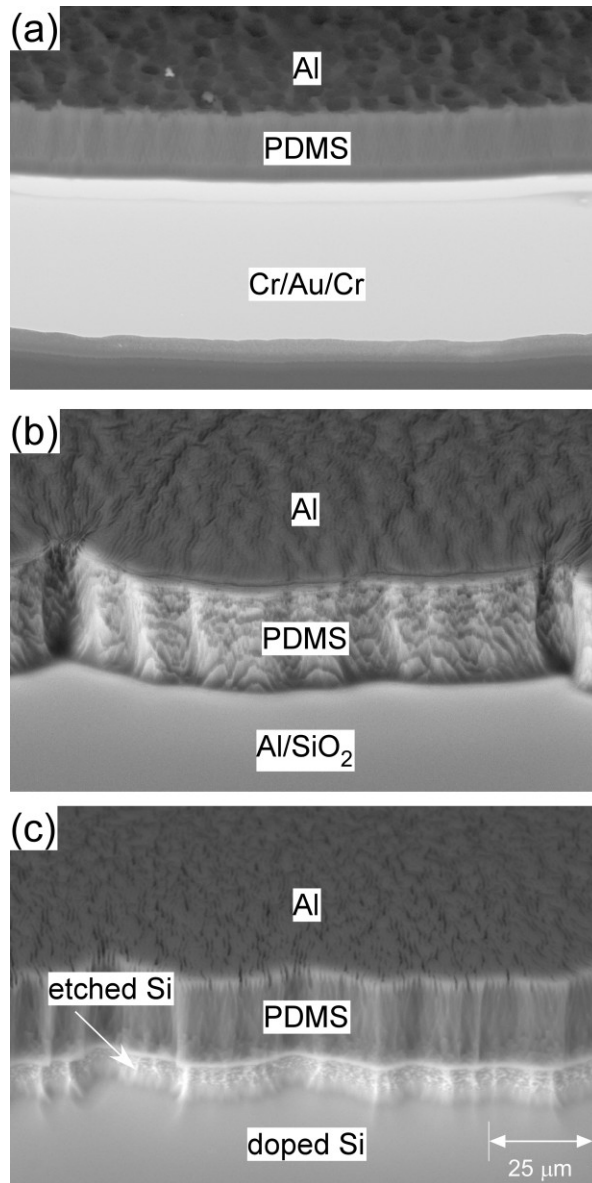
Figure 6-5. Cross-sectional morphology of the etched surface with different bottom electrodes (BSE images). In all cases the top electrode was Al and the elastomer used was Sylgard 184 a) Cr/Au/Cr b) Al/SiO₂ c) Si.

6.4.2 Challenges with Elastomer Patterning

Strain in the elastomer is inversely proportional to modulus and directly proportional

to the dielectric constant as seen from Equation (1). Thus, an elastomer with high dielectric constant (up to 15) and a low modulus (<1MPa) would be ideal for a DEA. In addition to these criteria, for the micro-scale fabrication, the elastomer must be spin-coatable and be able to withstand the microfabrication steps without significant changes in mechanical or electrical properties. Broadly, there are two major challenges involved in patterning the elastomer. First is the adhesion of the photoresist or the electrodes on the surface of elastomer. Second is the compatibility of the elastomer with the materials used in photolithography patterning.

Elastomer adhesion to the electrode layers is critical for device functionality. Furthermore, in the case of the lift-off process for the top electrode, the elastomer must also have good adhesion to a photoresist layer. Adhesion of different layers to the elastomer is challenging because of the hydrophobic nature of the silicone elastomer surface. However, this issue can be solved by surface treatment of the elastomer surface by either using self-assembled monolayers with suitable end groups [141] or by using oxygen plasma treatment [142]. We used the second approach in our process. Oxygen plasma treatment increases the number of dangling bonds on the surface of the elastomer, resulting in better adhesion to other materials [143].

The second challenge in patterning the elastomer is the compatibility of the elastomer with the photolithography process. Typical photolithography patterning using photoresist (Shipley 1813) would involve spinning the resist and soft-baking at 95°C.

This process caused cracks to form in the resist as well as on the elastomer surface (Figure 6-6). In order to avoid cracking, the photoresist was left to dry in air for 10 mins instead of soft-baking at 95°C. The exposure time was 11 seconds at 8 mW/cm^2. Lift-off did not occur properly with shorter exposures. Developing time is critical for the process and is, generally, about 20-25 seconds. However, developing for more than 10 seconds caused cracks in the resist, which were transferred to the elastomer surface. To conduct lift-off of a metal layer using photoresist patterned onto the elastomer, the resist had to be flood exposed before metal deposition. Flood exposure of the resist enabled the lift-off process to be conducted in an aqueous developer instead of an organic solvent. Using organics (e.g. acetone) swelled the elastomer, causing metal delamination, and in some instances, wrinkling of the metal films.
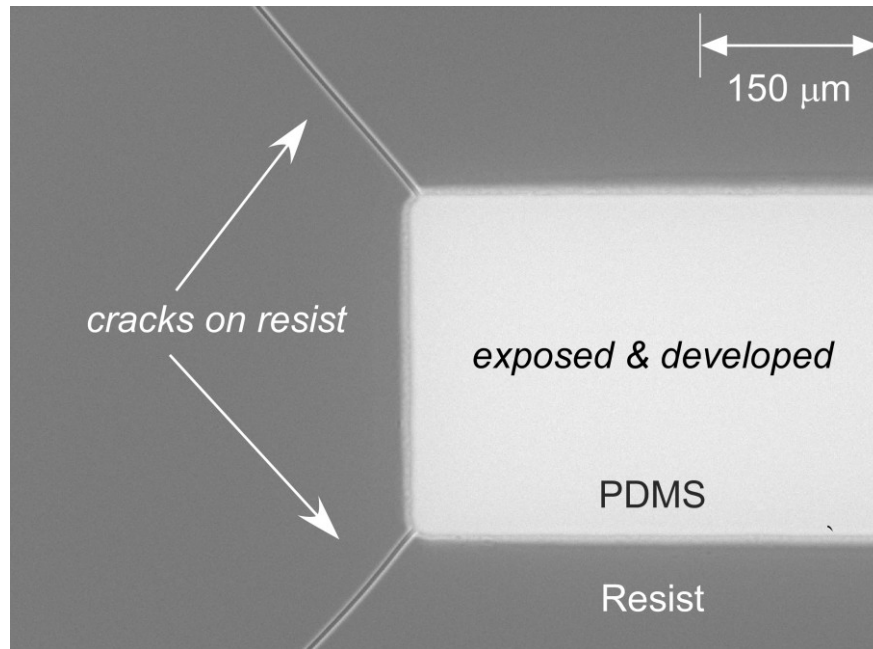
Figure 6-6. BSE image of exposed and developed resist on the surface of PDMS. Cracks are formed during developing.

6.4.3 Challenges with Top Electrode Fabrication

In out-of-plane DEA microfabrication, the top electrode also serves as a hard mask to etch the elastomer. Thus, it must be able to withstand the etching process of the elastomer and yet remain conductive. In addition, the process used to pattern the metal affects the properties of the elastomer beneath it.

The ability of the top electrode to withstand the etching process of the elastomer and function as a hard mask depends on two parameters: the deposition condition for the top electrode and the elastomer etching process. If an ICP dry etching system is available, the top electrode must only withstand the dry etching process. However, if an ICP system is not available, a two-step wet and dry etching process is necessary

169

[140]. When patterning the elastomer with combination of wet and dry etching (see Chapter 5), we found that the e-beam deposited Al electrode was able to withstand the etching process better than thermally deposited Al [140]. E-beam evaporated Cu of only 500 nm thickness withstood dry etching for more than 40 minutes and withstood wet etching for more than 30 minutes. Thus, e-beam deposited Cu and Al are compatible with both wet and dry etching of the elastomer.

The top electrode patterning process also affected the properties of the elastomer. When the Al or Cu was deposited and then patterned by wet etching, it was observed that all three types of elastomers (Sylgard 184, 527, and MRTV-9) were conductive (resistance values ranged from 500 to 5000 Ω for thicknesses around 25 to 35 μm) even before dry etching of the elastomer. Thus, wet etching of the metal makes the elastomer beneath became conductive. This is possibly because residual ions from the wet etching solution remained in the elastomer (a detailed study on the chemistry of the interference was not explored). Thus, patterning of the top electrode by wet etching was avoided and lift-off was used instead. Only MRTV-9 was conductive (500 Ω) after Al lift-off. The photoresist and the developer seemed to affect this elastomer. On a different occasion, Cu was deposited onto MRTV-9 using a physical mask and dry etched. In this case, the MRTV-9 sample was not conductive. Further investigation on this elastomer was not carried out since it was not able to withstand patterning.

6.5 Optimized Fabrication Protocol of the Out-of-Plane DEA

This section summarizes the optimized fabrication process developed for the fabrication of out-of-plane DEAs.

Bottom electrode fabrication -

1) Deposit and pattern bottom electrode by standard photolithography. Al/SiO_2 or Cr/Au/Cr used as bottom electrodes.

Elastomer deposition -

2) Spin PDMS (spin two layers to reduce pinholes) and cure.
3) Treat the PDMS surface with oxygen plasma (O_2 - 50 sccm, 50 W, 100 mtorr for 20 s)

Top electrode fabrication through lift-off -

4) Spin Shipley 1813 at 1000 rpm for 60 s and leave at room temperature for 10 min to dry off the solvent. Do not heat because it will cause cracks and wrinkles on the PDMS.
5) UV exposure for 11 s at 8 mW/cm^2.
6) Develop in CD 30. Developing time should not exceed 10 s.
7) Flood expose the resist for 20 s at 8 mW/cm^2
8) Treat the PDMS surface with oxygen plasma (O_2 - 50 sccm, 50 W, 100 mtorr for 20 s)
9) Load in the e-beam machine to deposit Al at 1-3 nm/s. To etch 20 μm of PDMS, 500 nm of Al is sufficient.
10) In an ultrasonic bath place a beaker containing CD-30. Immerse the sample into the sonicating CD-30 for ~1min.

Patterning elastomer through dry etching -

11) Etch in SF_6:O_2 (45:5 sccm) gas under RF power of 50 W, ICP power of 1400 W, and chamber pressure at 7 mtorr in the ICP. The substrate is helium cooled at 10°C while etching. Etch rate is 2 μm/min.

6.6   Results and Discussion

The actuation of the DEAs was measured using white light interferometry.   The schematic of the experimental setup is shown in Figure 6-7.   An LED (1510-1590 nm) was used as the light source.   Corning SMF-28e single mode optical fibers were used to transmit light.   An SM13 spectrometer (Micron Optics Inc, Altanta, GA) was used to measure the interference spectrum.

The light signal travels through the coupler into the optical fiber and propagates to the device.   The light reflected from the device travels back along the same fiber to recombine with the incoming light signal and reaches to the spectrometer to create an interference pattern.   The measured spectrum is visualized using a LabView program that processes the data using the two-peak tracing technique as described by Qi et al[144].
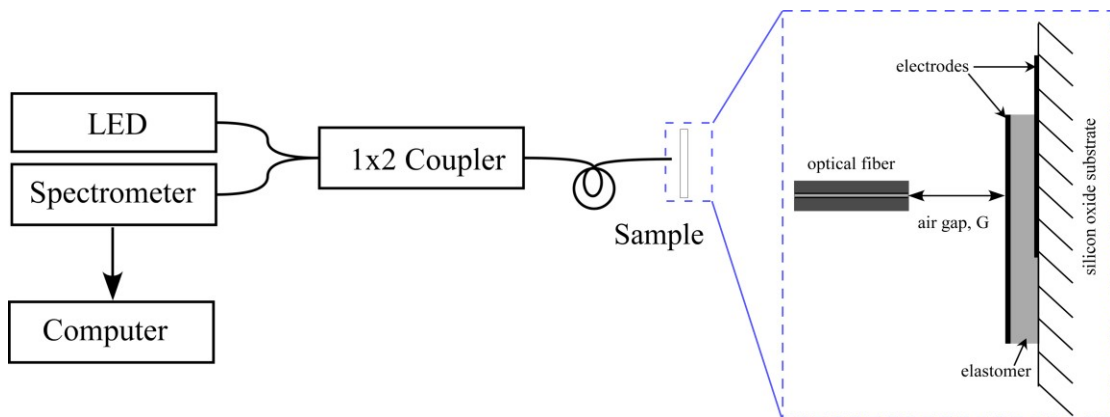
Figure 6-7. Experimental setup of white light interferometric system.

Figure 6-7 inset shows an optical fiber centered above the DEA sample. The lead-in optical fiber is connected with the light source. The top aluminum electrode of the DEA reflects the incident light. The resulting interference spectrum due to the superposition of the two light signals changes as the gap (G) between the sample and lead-in fiber changes. Applying a field between the DEA electrodes causes the squeezing of the elastomer, thus increasing the gap, G. This data was recorded using the LabView program that demodulated G from the interference spectrum using the two-peak tracing method.

Three circular DEAs with radius 300 μm, 450 μm, and 600 μm and thickness of 12 μm each were characterized in this study. The G values at different voltages were measured. Voltage was applied as an on-off step signal for a duration of 15~20 seconds until a steady-state signal was observed. The data shown in Figure 6-8 was obtained from five such repeats at each voltage. An exponential drift of the baseline was present due to the background. This was subtracted from the raw data by using the Butterworth signal processing filter in Matlab to obtain a flat baseline.
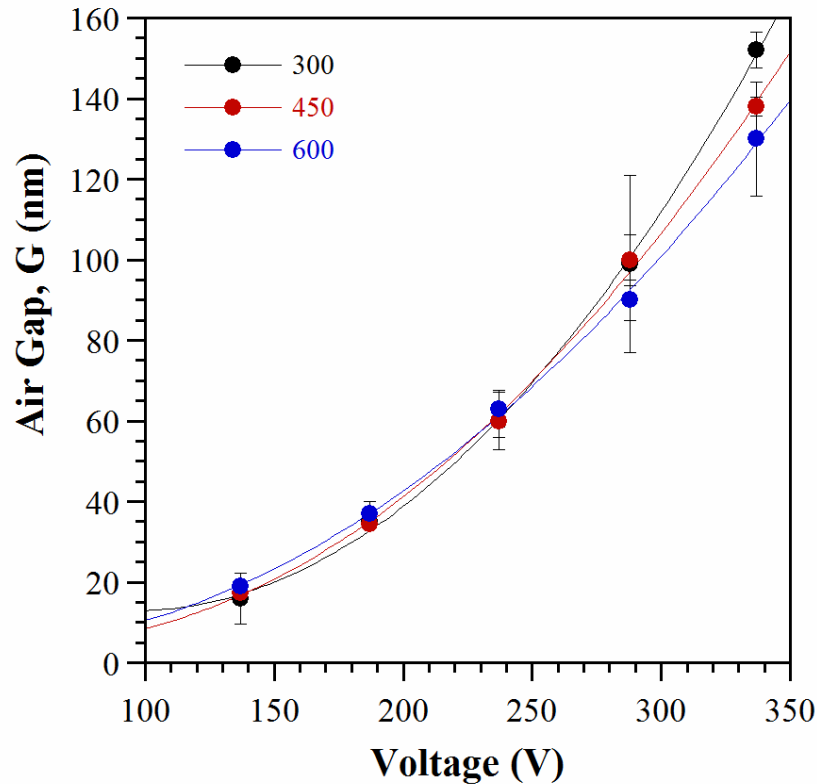
**Figure 6-8.Measurement of air gap distances from the DEA device as a
function of applied electric field.**

Figure 6-8 shows that the *G* values at different applied voltages. An increase in *G*

value corresponds to squeezing of the elastomer between the device electrodes. All

the three devices show similar contraction behavior. The devices show

approximately 1% strain at an applied voltage of 340 V, which is comparable for,

reported values of Sylgard 184 [42].

When high voltages were applied to the device as an on-off step signal, in the regions

where no device was present a pulse signal of about 40 nm was observed. This signal

is approximately 25% of the device contraction and further investigation is necessary to characterize the actuation strain of these devices accurately. Probably a different testing method such as conducting atomic force microscope might be necessary to characterize such small contractions.

6.7   Proposed Design for In-plane and Bending DEAs

Learning from the challenges encountered in the fabrication of out-of-plane DEAs, we have attempted to fabricate the other actuation modes. These additional modes are bending, membrane, and in-plane actuators. Fabrication of micro-scale DEAs with these actuation modes need additional steps compared to the out-of-plane DEA. This introduces new challenges to the fabrication protocol. This section discusses some of the challenges and the general fabrication procedure for these structures.

6.7.1   Bending and Membrane DEAs

The fabrication processes for bending and membrane actuation modes are similar. In bending mode, the actuator is anchored on one end while in membrane mode the actuator is anchored at both the ends.

Bending DEAs are useful because for the same actuation strain greater deflection can be observed by controlling the stiffnesses and thicknesses of different layers (Chapter 4). In addition, the length of the device can be increased to obtain greater deflection (Chapter 4). Even for a small strain, large curvature could be obtained by having a

stiff top electrode and a compliant bottom electrode. Figure 6-9 shows a schematic of the proposed fabrication protocol for bending actuators.

To fabricate benders, the bottom electrode must be more compliant than the top electrode so as to enable upward bending of the actuator. One method of creating a compliant electrode is to use a patterned electrode. We have attempted to use patterned (horse-shoe) metal bottom electrodes to fabricate the benders because the patterned electrode affords greater stretchability (Chapter 2). However, by patterning the bottom electrode, the effective overlap area of the top and the bottom electrode was less than 50%, and thus, the amount squeezing of the elastomer was reduced. As a result, no noticeable bending was observed upon actuation. An alternative to patterned electrode is to use a very thin metal layer or to use a conductive elastomer composite. Reducing the thickness of the metal helps to reduce the stiffness of the layer. Finding a suitable elastomer composite, that is (1) conductive at low percolation length, (2) does not increase moduli, and (3) is easily microfabricatable is challenging.

The other component necessary to fabricate the bender is the sacrificial layer. This layer must be able to withstand all the processing steps before it is released at the last stage. We have used e-beam deposited silicon dioxide, which can be released easy with 1:6 dilute buffered HF with surfactant.

Stiction is another major challenge in microfabrication of the bending DEAs. The elastomer tends to stick to the substrate after the sacrificial layer has been removed. The stiction issue cannot be readily solved by simply varying the height of the sacrificial layer or the length of the device since the work of adhesion of elastomers like the PDMS is high ($47mJ/m^2$) [145]. Critical point drying will be helpful to reduce stiction but the operating parameters need to be optimized in order to prevent the soft elastomer layer from ripping-off. The detailed procedure of patterning the non-stick layer and sacrificial layer in discussed in the Supplementary Information.

cross-sectional
view

top
view

(1) Si wafer

(2) non-stick layer,
     deposit & pattern

(3) sacrificial layer,
     deposit & pattern

(4) bottom electrode,
     deposit & pattern

(5) elastomer,
     spin & cure

(6) top electrode,
     deposit & pattern

(7) elastomer,
     dry etch

(8) sacrificial layer,
     removal
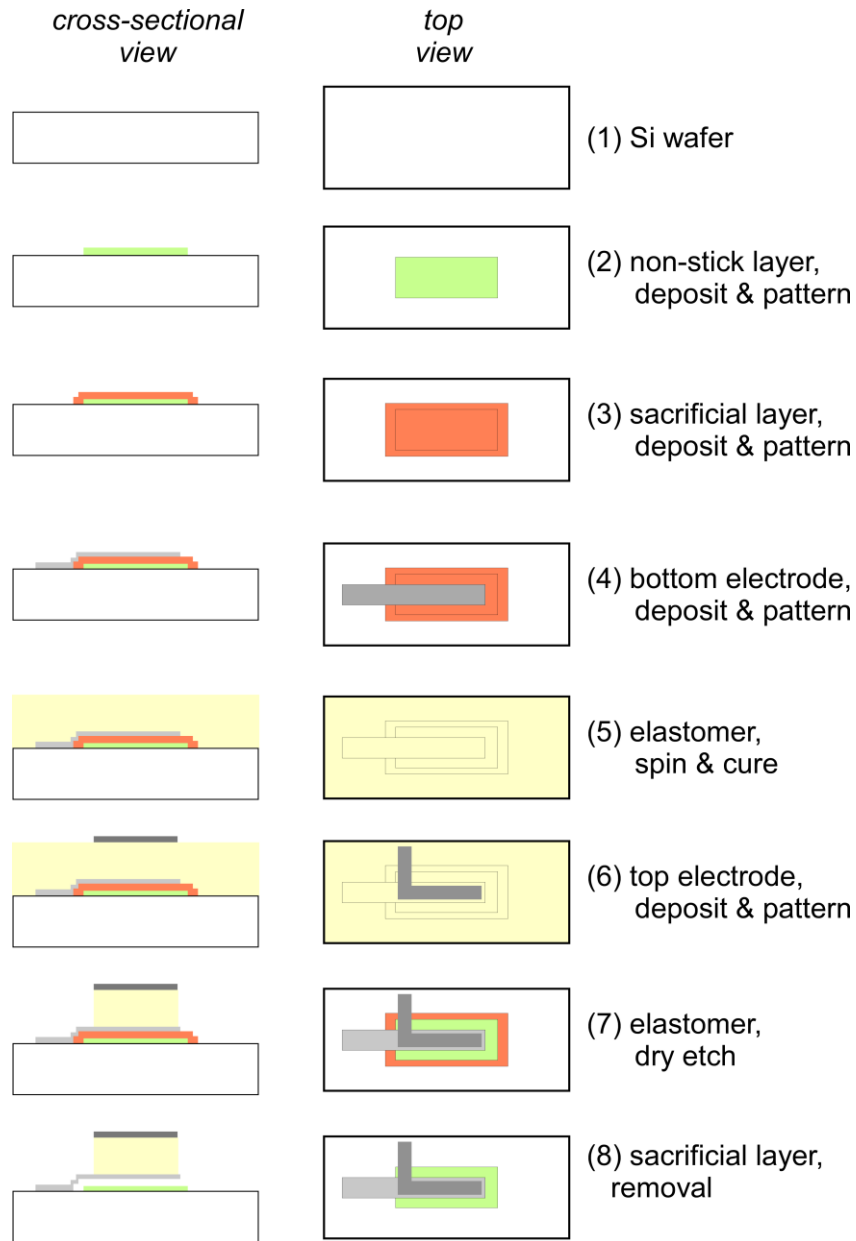
Figure 6-9. Schematic of the fabrication protocol for bending DEAs.

6.7.2   In-plane DEAs

In-plane DEAs are useful because they generate higher linear force compare to

benders.   However, it is a more challenging structure to fabricate and actuate

178

compared to all the other actuator modes. To fabricate in-plane DEAs, a sacrificial release layer as well as a non-stick layer and/or lubricating layer are necessary. While the sacrificial layer is necessary to free the actuator, a lubricating layer is used to reduce the friction during actuation.

Figure 6-10 shows the schematic of a fabrication protocol for the in-plane DEAs. The important difference between the benders/membranes and in-plane DEAs is associated with the process sequence. In in-plane DEA fabrication, the electrode layer is first patterned followed by the non-stick layer and the sacrificial layer. While with benders/membranes, the non-stick layer and the sacrificial layers are patterned before patterning the bottom electrode. Another difference between the benders and in-plane DEAs is related to the electrodes. In the case of benders, the top electrode is usually stiffer compared to the elastomer, while in the case of the in-plane DEAs, the top electrode needs to be compliant with the elastomer otherwise the elastomer strain would be limited by the top electrode.

The main challenge in fabricating an in-plane DEA is associated with the lubricating, non-stick layer. First, it is a challenge to find a suitable lubricating material. Even on a teflon-like layer, the elastomer does not easily slip. Not only does the elastomer have to overcome adhesion, but it also has to overcome shear forces associated with friction. For hard materials like metals, overcoming this lubricating effect has been well understood, e.g., in motors and gears. For soft materials such as PDMS to

179

undergo slipping, the elastomer must overcome an iso-viscous elasto-hydrodynamic (I-EHL) regime or soft-EHL regime [146]. This could limit the use of in-plane DEAs in dry environments because a wet lubricating layer is usually necessary.

On a meso-scale, we have tested different types of lubricating oils, including a type of silicone oil. However, the silicone elastomer absorbs the silicone oil and swells. We have also used paraffin wax, and under high electric field, the wax caught fire. To date, the only suitable coating we have tested is a hydrophilic coating (Ulterion® 140 WD, Ulterion International LLC, Braselton, GA).
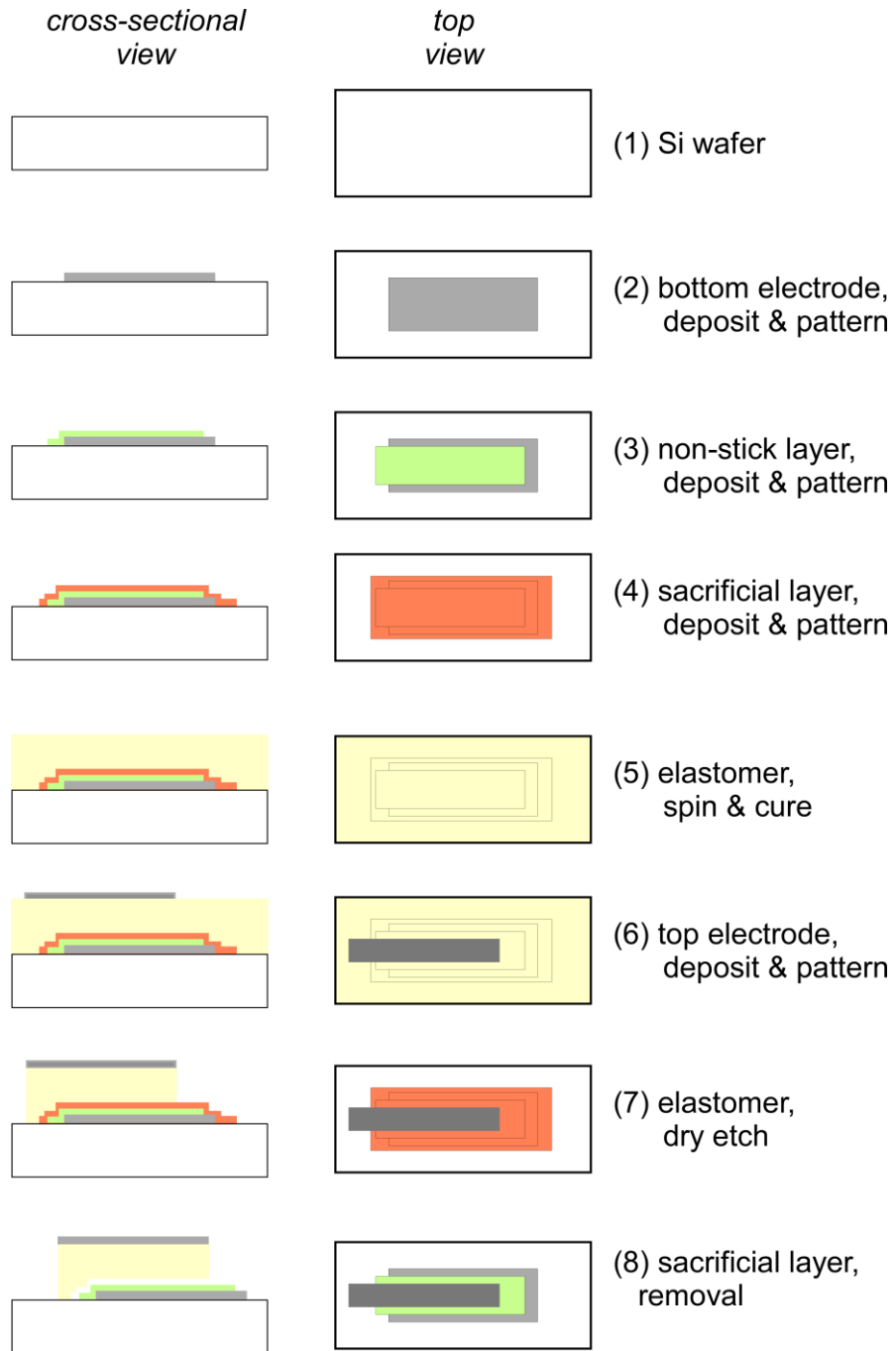
Figure 6-10. Schematic of the fabrication protocol for in-plane DEAs.

6.8   Conclusions

Microfabrication of DEAs using surface micromachining is challenging. We have attempted to make it in a batch processible manner; however, many challenges remain before DEAs can become a standard microactuator technology.

The compatibility of the materials and processes are critical since soft materials are involved in the process. Out-of–plane DEA fabrication challenges and how they can be overcome to produce these out-of-plane devices was shown. A simple out-of-plane DEA device was fabricated and tested. However, new device fabrication and testing is necessary to further fully characterized this actuator. Based on the knowledge gained in fabricating an out-of-plane DEA, some design guidelines were proposed for devices utilizing other modes of actuation such as membrane, bending, and in-plane.

Due to the small strains observed at the micro-scale, it is recommended that other elastomers with potential for larger actuation strains be explored for use in the micro-scale. Since the modulus of the elastomer is inversely proportional to the actuation strain, elastomer modulus may be used as an initial screening criteria to explore newer elastomers. While the selection of other elastomers is important, it is also necessary to understand that these elastomers must be tested for their compatibility with the standard microfabrication methods.

Acknowledgements

Supplementary Description

The supplementary information includes information about patterning of non-stick layer followed by the sacrificial layer.

Supplementary Information

Patterning Non-Stick Layer Followed by Sacrificial Layer

Cytop (Asahi chemical Co., Ltd., Japan) was spun at 4000 rpm for 60 seconds onto a silicon wafer and cured at 150°C for 40 minutes. The thickness of the layer was 0.3 μm. The surface of the Cytop was oxygen plasma treated (150 mtorr, 50 W, 50 sccm, 10 seconds). HMDS followed by photoresist Shipley 1813 was spun (4000 rpm) and soft baked at 95 °C for 1 min. UV exposure (8 mW/cm^2) was carried out for 11 seconds followed by development using CD-30 and hard baking for a minute. Dry etching was performed for a minute (CF$_4$:O$_2$ 10:50, 150 W, 50 mtorr). The photoresist was then removed using acetone, methanol, or IPA.

Before spinning the resist on the he non-stick layer, the surface must be oxygen plasma cleaned to ensure that the resist would adhere. The non-stick layer was oxygen plasma treated (150 mtorr, 50 W, 50 sccm, 10 seconds) before loading into the e-beam chamber. The silicon oxide deposition pressure was 5e-6 torr, and the deposition rate was 50 Å/s. HMDS followed by photoresist Shipley 1813 were spun at 4000 rpm and soft baked at 95 °C for 1 minute. UV exposure (8 mW/cm^2) was carried out for 11 seconds. Development was done using CD-30 followed by a one minute hard bake. The oxide layer was patterned using buffered HF (1:6). The patterned structure can be seen in SI_Figure 10, where the Teflon layer is encapsulated by the SiO$_2$ layer.
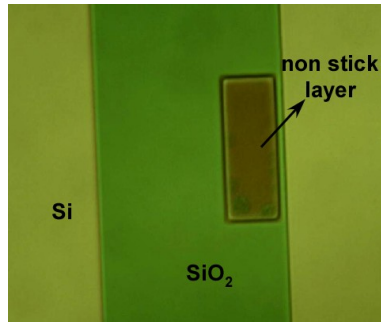
SI_Figure 10. The optical image shows the SiO$_2$ layer patterned on top of a patterned non-stick layer.

Chapter 7: Concluding Remarks and Future Work

7.1 Concluding Remarks

This thesis explored the feasibility of realizing DEAs as standard microactuator technology. This is addressed from design and fabrication standpoints. DEA device design was carried out using analytical method. The challenges involved in miniaturizing DEAs using standard microfabrication techniques were outlined and proof-of-concept microfabrication of surface micromachined devices was demonstrated.

7.2 Suggestions for Future Work

More research is needed in order to make micro-scale DEAs using standard microfabrication techniques. These are some suggestions for future work.

- The elastomer materials tested in this thesis did not exhibit much strain at the micro-scale. The strains were small, and a special setup was needed to characterize the devices. In the meso-scale, the actuator exhibited strains above 3.5% (results from our lab); however, in the micro-scale, the strains were less than 1%. This will limit the use of micro-scale DEAs for large strain actuator applications. Thus, it is important to understand the factors that limit the strain at the micro-scale. Experiments should be designed to address following questions. Does microfabrication processing affect the actuation

property of the elastomer at the micro-scale? Or does the elastomer behave fundamentally different when it is relaxed, as elastomer is not pre-strained in the microscale DEAs?

- This thesis was predominantly limited to investigation of one type of silicone elastomer, PDMS. Due to the small strains observed at the microscale, other elastomers should be tested to determine their potential for larger actuation strains. Since the modulus of the elastomer is inversely proportional to the actuation strain, elastomer modulus may be used as an initial screening criteria to explore newer materials. While the selection of other elastomers is important, it is also necessary to understand that these elastomers must be tested for their compatibility with the standard microfabrication methods.

- Electrodes that are compatible and compliant with the elastomer are crucial for micro-scale DEAs. Developing new electrode materials with low moduli that are compatible with standard microfabrication process is another high impact research area. These electrodes are especially crucial for the top electrode for in-plane DEAs and the bottom electrode for the bending DEAs.

- Lubricating materials are critical for the actuation of the inplane DEAs. Currently, the choice of lubricating materials is limited. Unless we are able to

187

find a truly lubricating layer that is compatible with standard microfabrication processes, the use of inplane DEAs at the micro-scale will be limited.

- Alternative sacrificial layers have to be explored for the fabrication of the in-plane, bending, and buckling DEAs so that there is greater flexibility in the fabrication protocols.

- The protocol developed in this thesis can used to fabricate new devices. In addition, the micro-scale devices performance should be characterized.

- The other challenge for micro-scale DEAs is to achieve good contact between the external world and the top electrode. Traditional methods such as wire bonding cannot be used because the wire bonding process would damage the soft elastomer material. New approaches such as low-temperature soldering may be explored.

- From the design point of view, it will be interesting to combine different actuation modes of DEAs to explore different architectures that have greater degree of freedom than the individual modes.

Chapter 8:   List of Contributions

Below is the list of intellectual contributions that resulted from the work presented in this thesis.

(1)   Developed design criteria for the fabrication of crenellated electrodes and crenellated elastomers with electrodes.

- Developed a general guideline for designing crenellated-cantilevered electrodes. This guideline enables design of structures with appropriate axial or bending stiffnesses based on their amplitude, angle, length, and thickness. The effect of crenellation on axial stiffness is substantially larger than it is on bending stiffness. For both the modes, decreasing the beam thickness and increasing the angle of the vertical-going segments lowers stiffness. Increasing α affects axial stiffness primarily by increasing the length of the off-midline horizontal segments, while it affects bending stiffness primarily by increasing the total length of the beam. However, the most effective way to reduce the axial stiffness is by increasing the height of the crenellations, which can lower it by orders of magnitude.

- Derived simple analytical equations for axial and bending stiffness for crenellated electrodes with different shapes. Although finite element methods can be used to determine the stiffness, they are not easily accessible to everyone. Using the results presented in the thesis, researchers in non-

189

mechanical fields such as materials science can readily design simple meandering cantilevered structures with a specific stiffness.

- Developed the understanding of the effect of crenellation on stiff electrode on a crenellated elastomer. This is important for the application of flexible electrodes as well as for DEA crenellated structures. Even a small crenellation decreases the axial stiffness dramatically. At moderate crenellation amplitudes, the crenellated structures are a thousand times less stiff when stretched in the axial direction than uncrenellated beams. However, the situation is quite different for bending, which is weakly affected by crenellation. While for large crenellations the bending stiffness drops somewhat, at low crenellation amplitude the stiffness is actually higher than that of a straight beam. Thus, when designing crenellated bending structures, appropriate values of the electrode stiffness and crenellation height must be chosen to achieve the desired behavior.

(2) Developed design criteria for the fabrication of bending DEAs

- Developed a general guideline for designing DEA configurations such as unimorph, bimorph, and multilayer stacks using a multilayer analytical model. Design optimization was based on the effect of thickness and stiffness of different layers on curvature, blocked force, and work. There is always a compromise between curvature and blocked force. Thus, based on the need of the specific application the stiffness and thickness have to be chosen. Apart

190

from DEAs, other electroactive polymers (EAPs) such as ionic polymer metal composites (IPMCs) and conjugated polymer (CP) sandwich structures were also analyzed.

(3) Optimized fabrication protocol for etching elastomer

- Developed an etching method that synergistically combines wet and dry etching to reduce etching times to 30 mins for 10 μm PDMS. Dry etching alone would have taken 5 hours, and wet etching alone would produce severe undercutting. The concept of this method is to dry etch the PDMS to a thickness of 2-3 μm, producing vertical sidewalls, followed by wet etching to remove the remaining material, which produces a smooth substrate. This method is essential for labs, which does not have a good dry etching system like the ICP etcher.

(4) Developed surface micromachining protocols for DEAs

- Outlined the challenges involved in fabricating micro-scale DEAs using standard microfabrication methods.
- Developed the fabrication protocol for out-of-plane (squeezing) DEAs using standard microfabrication techniques. Fabricated the first fully batch-fabricated squeezing DEAs.
- Developed fabrication protocols for bending, buckling, and in-plane DEAs.

(5)   Developed fabrication protocols to design devices for understanding the bending behavior of bilayers

- Developed microfabrication protocol for center-mounted polypyrrole actuators. A combination of differential adhesion and sacrificial release methods was used to fabricate these actuators to ensure completely free movement of devices upon actuation.

- Experimentally validated the theoretical findings that the bending direction is determined by double-curvature at the edges of the bilayer with experimental data from the arrays of bilayers that were produced in an unstressed state. The model and the experiments found only two stable equilibria: the spiral and the cigar. The spiral was energetically preferred, and the preference for the spiral increased with aspect ratio.

Journal Publications

1. **B. Balakrisnan,** A. Nacev, J. M. Burke, A. Dasgupta, E. Smela, "Design of compliant meanders for applications in MEMS, actuators, and flexible electronics" – *Submitted to Smart Materials and Structures* (2012).
2. S. Alben, **B. Balakrisnan**, E. Smela, "Edge effects determine the direction of bilayer bending" – *Nano Letters,* 11, 2280 (2011).
3. **B. Balakrisnan**, S. Patil, E. Smela," Patterning PDMS using a combination of wet and dry etching" – *Journal Micromechanics Microengineering* 19, 7 (2009)

Journal Manuscripts in Preparation

4. **B. Balakrisnan,** A. Nacev, E. Smela, "Design of bending dielectric elastomer actuators" – *To be submitted to Smart Materials and Structures*.
5. **B. Balakrisnan**, D. Sritharan, E. Smela, "Surface micromachined dielectric elastomer actuators" – *To be submitted to Journal Micromechanics Microengineering*.

Conference Proceedings

6. A. Gerratt, **B. Balakrisnan**, I. Penskiy, S. Bergbreiter, "Batch microfabricated dielectric elastomer actuators" *International Conference on Solid-State Sensors, Actuators, and Microsystem*, Beijing, China. 2422 (2011).
7. **B. Balakrisnan,** E. Smela, "Challenges in Microfabrication of DEAs", *SPIE Conference on Smart Structures and Materials & Nondestructive Evaluation: Electroactive Polymer Actuators and Devices (EAPAD) XII,* USA (2010).

Poster Presentations

8. **B. Balakrisnan**, E. Smela, "Micro-scale electroactive polymers", *Gordon Research Seminar and Gordon Research Conference on Polymers,* USA (2011)
9. **B. Balakrisnan**, E. Smela," Microfabrication of dielectric elastomer actuators" – *The Mid Atlantic MEMS Alliance 10th Annual Special Topics Symposium "Micro- and Nano- Technology in the Green Revolution: Energy and Environmental Sensing"*, USA (2009). **[Best student poster award]**
10. **B. Balakrisnan**, E. Smela," Effective combination of wet and dry etching in patterning PDMS for DEA devices" - *The Mid Atlantic MEMS Alliance 9th Annual Special Topics Symposium "Technology Pull"*, USA (2008).

Chapter A: Edge Effects Determine the Direction of Bilayer Bending

Silas Alben[1], Bavani Balakrisnan[2], and Elisabeth Smela[2]
[1] School of Mathematics, Georgia Institute of Technology, Atlanta, GA
[2] Department of Mechanical Engineering, University of Maryland, College Park, MD

Abstract

We elucidate the reason for preferential bending along the long edge in thin rectangular bilayers in which one of the layers is isotropically strained. While this preference has been observed previously, the physical basis for this preference has not been understood. We find that the bending direction is determined by the existence of doubly-curved regions at the curled edges, which lower the energy. This energy difference between "spiral" and "cigar" shapes increases with aspect ratio.

Keywords

bilayer, edge effects, bifurcation, doubly curved, self-folding, polypyrrole

There has been considerable recent interest in understanding spontaneous curvature, such as seen in the deformation of bilayers [147-149]. Bilayers are planar membranes or plates with a different material on each face, and they bend or wrinkle into curved three-dimensional structures if one face expands more than the other. Similarly, a single material (unimorph) will bend in response to a strain gradient in the thickness

194

direction. One of the motivations for studying curvature arises because combination of top-down patterning via photolithography with bottom-up design of material structures capable of spontaneous or induced curvature allows the fabrication of structures that cannot readily be created by conventional microfabrication [150], and it is envisioned that these structures will allow new functionalities. Another motivation is that this bending phenomenon is seen on every length scale, from macroscopic bilayer thermostats to nano-scale graphene [149].

Micro-scale bilayers have been constructed from a wide variety of organic and inorganic materials [151]. Recent examples are light-actuated microrobots built from rectangular bilayers that include a liquid crystalline polymer [152], silicon microelectromechanical systems (MEMS) that fold into three dimensional shapes under thermal actuation [153], magnetostrictive-piezoelectric bilayers that undergo giant magnetoelectrostriction for memories and energy conversion [154,155], and piezoelectric MEMS radio-frequency switches for wireless communication [156]. Cho et al. created more complex structures with annular bilayers, the shapes of which depended on the annulus width [148]; wrinkled, saddled, and wedge shaped structures were formed. Often, intrinsic stress is exploited to self-assemble curled structures. For example, spirals have been microfabricated that curl upon release from the substrate due to lattice mismatch strain [157]. Chun et al. formed micro- and nano-scale tubes with controlled sizes by the self-rolling of epitaxially mismatched rectangular bilayers, demonstrating that the bending direction varied depending on

the length to width ratio (the aspect ratio *A*) [147]. They also performed FEM modeling, showing that the strain energy was lower for long-side rolling than short-side rolling, but the reason for the lower energy was unclear. Cendula et al. looked at the rolling of wrinkled, strained rectangular films, finding a preferential rolling direction that depended on the geometry and strain gradient [149]. Despite the extensive prior work, however, a fundamental elucidation of the mechanism that propels rolling in the long direction is still missing.
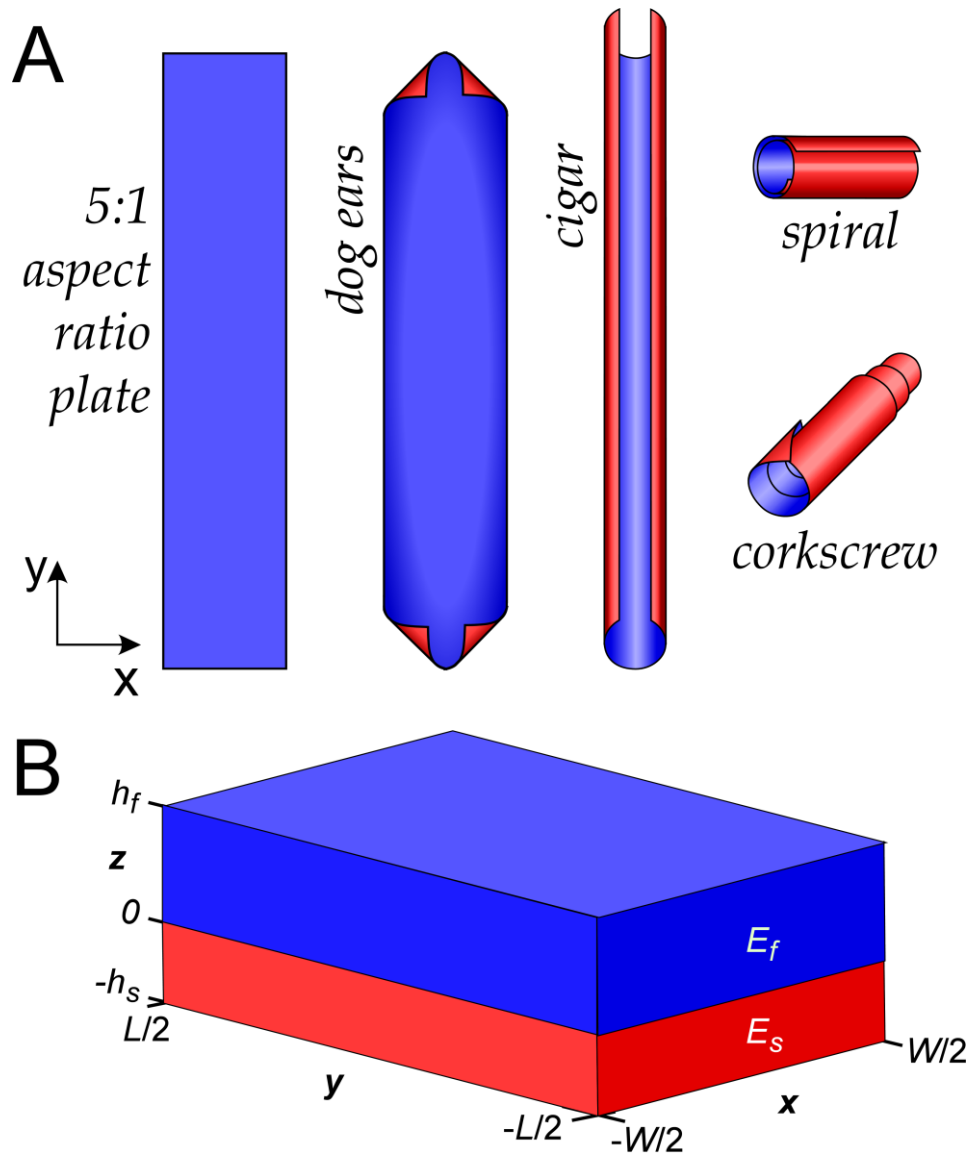
Figure A-1. A) Some of the possible shapes that a thin bending plate can take, illustrated for a length to width ratio A of 5, upon contraction of the upper face (blue). B) Bilayer geometry.

For a bilayer to become curved in two orthogonal directions, like the surface of a sphere, it must undergo stretching, which for large deformations has a significant associated stretching energy [158,159]. So, the plate instead tends to assume shapes

that are locally curved in one direction only (such as cylinders and cones), minimizing regions of double curvature. A few of these bending possibilities are illustrated in Figure A-1A based on experimental observations; other configurations are also possible [147-149]. The plate could bend into a "cigar" (short edge curved), a spiral (long edge curved), or a corkscrew [160] (intermediate angle). These configurations have the same curvature in the direction of bending, so one might expect them to have the same elastic energy. If this were the case, the bending direction would be random, which is not observed experimentally. (Curvature has been shown to depend on the strain, thickness, and moduli of the layers, and not the bilayer dimensions [147].) Alternatively, the plate can develop "dog-ears", with the corners curved inward to the point at which they meet (see for example the Supporting Information).

In this paper, we offer new insight into why a rectangular bilayer will curve along the long direction. We show mathematically that the reason lies in the spatial distribution of curvatures. The bilayer does not bend into a perfect tube, but has narrow regions of *double-curvature* at the curved edges that lower the energy density at those locations. The total length of curled edge is greater for bending in the long direction, so during the transition from a spherical to a singly-curved shape, it is more favorable for the rectangle to adopt the spiral geometry. The edge effects become relatively stronger as the length to thickness ratio increases. The increasing probability of curvature along the long direction with aspect ratio A is confirmed experimentally

198

using isotropic bilayers of polypyrrole and gold, and the slight double-curvature is also shown.

Hou and Chen studied, experimentally, rectangular bilayers that were clamped along one edge, which constrained the direction of bending [161]. They found that at intermediate aspect ratios, much of the bilayer was doubly curved, whereas at large and small ratios it was nearly singly-curved except for a narrow region near the edges. (We have also simulated this problem and obtained results that are essentially identical to theirs, as shown in the Supporting Information.) In this work we consider bilayers that are two orders of magnitude thinner and without the clamp at the edge, removing the bias on the bending direction.

The classical model of bilayer bending, initiated by Timoshenko in 1925 [162] and since extended [163-165], assumes that the bilayer can bend in only one direction and results in a bilayer with uniform curvature. More recent models have considered bilayer bending in two dimensions. Mansfield found analytical solutions for large deflections of circular [166] and elliptical [167] plates having lenticular cross-sections with a temperature gradient through the thickness. For small gradients, the plates formed spherical caps, curved equally in all directions. At a critical gradient, a configuration with greater curvature in one direction became more favorable. Because of the lens-shaped thickness profile, even though the elliptical plate had a major axis it showed no preferred direction for bending even for large deflections.

199

For the uniform thickness typical in experiments (here and [161]), we show that a particular bending direction *is* preferred. For a circular bilayer of uniform thickness, Freund determined the strain at which the spherical cap becomes unstable using low order polynomial solutions and finite element simulations [168]. Our model extends that of Freund to more general bilayer displacements and arbitrary values of layer thicknesses.

We model the bilayer as two rectangular layers of elastic material: a passive *substrate* and an active *film* (Figure A-1B). Each has a length L in the y direction, width W in the x direction, Young's moduli E_f (E_s), thicknesses h_f (h_s), and Poisson ratio ν, and they are bonded together at $z = 0$. In the model, an isotropic *actuation* strain ε_a is applied to the film; this is the strain that the film would experience if it were free, and a simple expansion (or contraction) by ε_a in x, y, and z would result in the film having the lowest energy. However, the film is bonded to the substrate, which is not actuated, and the two layers must have the same *deformation*, u, at their interface. The interfacial strain that minimizes the total elastic energy of the bilayer therefore lies somewhere between ε_a and 0. The total energy can be decreased further if the bilayer bends into the z direction because in a curved plate, the layer at the outer circumference is stretched while the one at the inner circumference is compressed, bringing each layer closer to its individual "preferred" strain.

Our model considers the elastic energy of a bilayer as two plates undergoing moderate out-of-plane deflections, intermediate between the thickness and the width, with continuous deformations at their interface ($z = 0$). This is well described by the Föppl-von-Kármán equations [169]:

$$(46) \quad U = \int_{-L/2}^{L/2} dy \int_{-W/2}^{W/2} dx \int_{-hs}^{hf} dz \frac{E(z)}{2(1+v)} \left(\begin{array}{l} \dfrac{1-v}{1-2v}\bar{u}_{xx}^2(x,y,z) + \dfrac{1-v}{1-2v}\bar{u}_{yy}^2(x,y,z) + 2\bar{u}_{xy}^2(x,y,z) \\ + \dfrac{2v}{1-2v}\bar{u}_{xx}(x,y,z)\bar{u}_{yy}(x,y,z) \end{array} \right).$$

Here u_{xx}, u_{yy}, and u_{xy} are components of in-plane strain in the material: u_{xx}, u_{yy} are normal strains (leading to normal stresses, i.e. tension or compression) in the x and y directions, and u_{xy} is the shear strain. The strains are given in terms of the displacements (u_x, u_y, u_z) of the bilayer in the x, y, and z directions:

$$(47) \quad \bar{u}_{ij}(x,y,z) = -z\frac{\partial^2 u_z}{\partial x_i \partial x_j}(x,y) + \frac{1}{2}\left(\frac{\partial u_i}{\partial x_j}(x,y) + \frac{\partial u_j}{\partial x_i}(x,y)\right) + \frac{1}{2}\left(\frac{\partial u_z(x,y)}{\partial x_i}\frac{\partial u_z(x,y)}{\partial x_j}\right) + \varepsilon(z).$$

In (2), x_i and x_j range over (x,y) while u_i and u_j range over (u_x, u_y), respectively. The first term on the right side of (2) is due to bending and the second is due to in-plane stretching. The third is the leading nonlinear stretching term that occurs for small-to-moderate strains (although the materials obey linear elasticity, strain depends nonlinearly on displacement; see [169]). The fourth term is the equilibrium strain ε (z), which equals ε_a in the film and zero in the substrate. (1) and (2) are well known

201

equations of elasticity, and versions of these equations have been used recently to study single thin plates under forcing [158,159,170].

For a given ε_a, we obtain the bilayer shape by finding the displacements that minimize the elastic energy in (1). We discretize the integrals over x and y using uniform grids, and we compute the z integral analytically. We use Newton's method to find the energy-minimizing shapes, using analytical formulae for the gradients and Hessian matrices. (This approach allows a more direct knowledge and verification of the numerical accuracy and convergence rates of our results than would be obtained using commercial software.) To compare with our experiments, we take $E_s = 83$ GPa, $E_f = 0.2$ GPa, $W = 100$ μm, $h_s = 0.1$ μm, $h_f = 0.45$ μm, and $v = 0.4$ for both layers. (Results are similar for other values.) We vary ε_a and the aspect ratio A.

We increase ε_a from zero in a series of small steps, and at each value the energy in (1) is minimized. Figure A-2 shows the corresponding transition in the bilayer's shape, in terms of the spatially-averaged curvatures in the x (blue) and y (orange) directions. The inset figures show surface and contour plots of displacement corresponding to the indicated points on the plots.
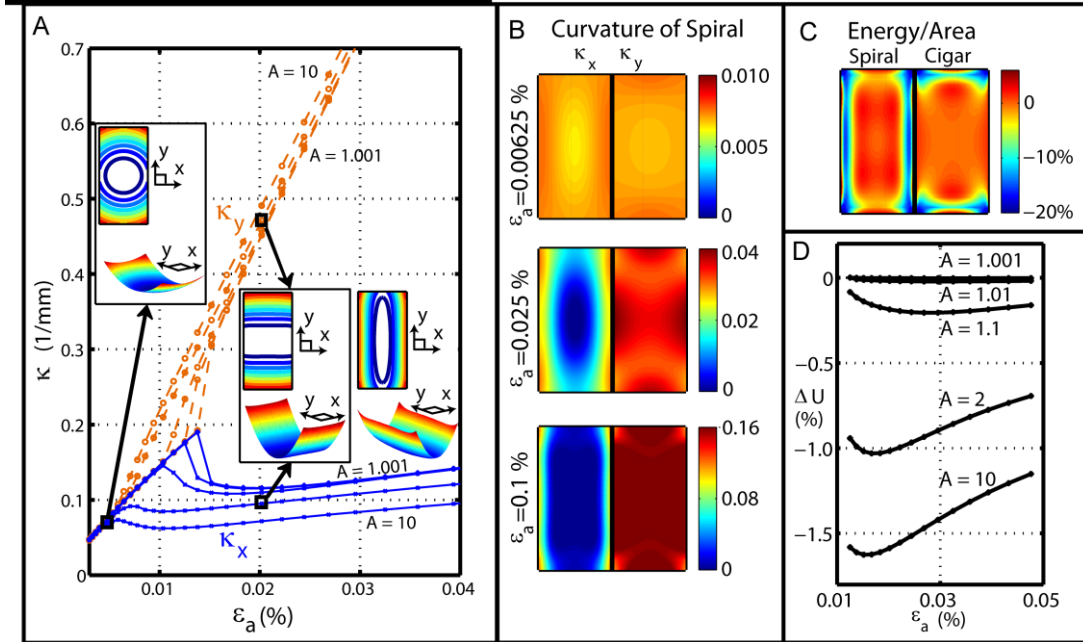
Figure A-2. A) From the simulations, curvature as a function of actuation strain ε_a. The curvatures in the x (blue) and y (orange) directions, averaged over the bilayer, are plotted for $A = 1.001$, 1.01, 1.1, 2, and 10. The insets show shapes for $A = 2$ at the indicated ε_a; the out-of-plane z-axis is greatly exaggerated for illustration. The colors go from blue to red as the z-displacement increases. For comparison, an alternative equilibrium state with higher energy, the cigar (which does not correspond to any of the lines of the plot), is shown at the same ε_a (0.02%) as the adjacent spiral. B) Maps of curvature κ in x and y directions for three ε_a spanning the transition from spherical cap to developable spiral for $A = 2$. The colors go from blue to red as the curvature increases. C) Maps of elastic energy per unit area for the spiral and cigar at $\varepsilon_a = 0.1\%$, as a fraction of the energy density for the Timoshenko solution. D) Total energy difference $U_{spiral} - U_{cigar}$ versus ε_a for different A.

For very small ε_a, the bilayer is a shallow spherical cap, bending with equal curvature in the x and y directions, as shown by the overlapping of the orange and blue curves. At a critical ε_a, the bilayer transitions to a shape with nearly uniaxial bending—a nearly *developable* shape—shown for aspect ratios ranging from 1.001 (nearly

203

square) to 10. The transition occurs because the bilayer trades one elastic energy term for another. For small ε_a, the nonlinear stretching strain in (2) is negligible compared to the other terms. At large ε_a, the nonlinear stretching strain becomes important. The nonlinear term associated with double curvature—simultaneous bending in x and y—can be reduced to zero by making the bilayer flat in one direction. However, the substrate and film then undergo additional stretching in the flat direction, without the curvature in this direction that allows each layer to get closer to its equilibrium strain. Although the shape is nearly developable, stretching energy is comparable to bending energy throughout the bilayer. This transition to a developable shape has been studied extensively [171] and has been analyzed previously in lower-order models of circular and elliptical plates [166-168]. Unlike these cases, however, the rectangular bilayer shows a preferred direction of bending after the transition. The transition occurs where the orange and blue curves separate, with curvature increasing along y and decreasing along x, yielding the spiral shape of Figure A-1. The curves separate sharply at a critical ε_a for a square plate ($A = 1$), but for $A > 1$ they separate more smoothly, reflecting a small bias for a particular direction even in the spherical cap state. The ε_a at which the curves visibly separate decrease with increasing aspect ratio A.

The Föppl-von-Kármán equations are valid for deflections that are much smaller than the length or width of the bilayer. In particular, our model does not represent the

shapes past the point of overlapping, as in Figure A-1. However, the direction of bending is determined well before this point, and well within the range of deflections where the model is valid. Once the bilayer transitions to the spiral shape shown in Figure A-2A, our experiments and model show that it remains a spiral (with increasing curvature) as ε_a increases further.

If the simulations are initialized with the bilayer already bent along the x direction and with ε_a above the transition value, our numerical method finds a second stable equilibrium shape—a cigar, shown adjacent to the spiral shape in Figure A-2A for the same ε_a. This shape remains stable with increasing ε_a. However, for gradual increases of ε_a from zero, our numerical method always finds the spiral because it has lower energy. There are no initializations for which the corkscrew or dog-ears are found.

We now consider the critical question of *why* the spiral has lower elastic energy than the cigar. The answer can be found by examining the spatial distributions of curvatures κ during the transition from spherical to developable shapes. Figure A-2B shows the local curvatures in the x and y directions for three values of ε_a spanning the transition. At the smallest ε_a, the two curvatures are nearly equal, giving a nearly spherical cap. Quadrupling ε_a, κ_y becomes large and nearly uniform while κ_x drops dramatically, producing a spiral, modified by regions of double curvature near the

longer sides (the edges bend slightly inward). Quadrupling ε_a again, the regions of nonzero κ_x become narrower. These regions are similar to other edge layers in solid mechanics [172], which can occur when a control parameter (here, ε_a) becomes sufficiently large. Previous bilayer models [166-168] had insufficient resolution to show the edge layers. However, the experiments of Hou [161] clearly showed their presence for small A. Similar edge layers occur for the cigar, except that they lie on the shorter sides. These edge effects become relatively stronger as the length to thickness ratio increases.

The effect of edge layers on the elastic energy component is shown in Figure A-2C. The color maps give the local elastic energy per unit area, as a percentage of the Timoshenko solution energy density, which was used as a baseline. Away from the edge layers, where the bilayer is curved primarily in one direction, the energy density is within 2.5% of that of the Timoshenko solution, but in the edge layers the energy density is nearly 20% lower. Because the edge layers occur on only two of the four sides, and because they are longer for the spiral than for the cigar, the energy of the spiral is lower.

In Figure A-2D we plot the difference in *total* energy between the spiral and the cigar, relative to that of the Timoshenko solution. The energy difference is largest at ε_a just beyond the transition from spherical cap to developable shape. At larger ε_a, the edge

layers become smaller and contribute proportionately less to the total energy. The energy difference is larger for larger aspect ratios, but is still fairly small (< 1.6%) at $A = 10$.

Because the elastic energy difference between the spiral and cigar configurations are minute, to study the bending question experimentally requires bilayers that are essentially perfectly homogeneous in the plane of the layer, so that no directional bias is introduced that could influence the bending direction. Macro-scale fabrication methods such as roll milling to produce sheet metal or extrusion to produce polymer films introduce a definite anisotropy to the material. For this reason, and because of the significant role of bilayers in micro- and nano-systems, bilayers were produced using surface microfabrication techniques (Figure A-3A). To achieve isotropic mechanical behavior, the films of the bilayer were amorphous or polycrystalline: the active film was polypyrrole (PPy), and the substrate layer was gold (Au) [150,173,174].

PPy is an electroactive polymer that changes volume upon the application of an electrochemical potential, which allows electrical control over the strain. The Au layer served as the constant-volume substrate, as well as the electrode contacting the PPy. The PPy was doped with dodecylbenzenesulfonate (DBS) during electrochemical deposition. The bilayers were actuated in an aqueous solution of NaDBS using a potentiostat [173], contracting upon oxidation and expanding upon

reduction [150]. The actuation strain in PPy depends on its oxidation level via the incorporation of charge-compensating ions, which is determined by the voltage applied to the Au film (working electrode) in intimate contact with the PPy. (The *rate* of oxidation or reduction depends on the rate of arrival of charge-compensating ions [175], which may be higher at the edges.) The in-plane strain in fully actuated PPy(DBS) is on the order of 3% [174].

Another critical factor was ensuring that the bilayers were able to move freely upon first actuation. It has been shown that if bilayers curl during release from the substrate by underetching a sacrificial layer, the final rolled state is influenced by that history of constrained rolling [147]. Constraints also affect the bending behavior of the PPy bilayers (see Supporting Information). Because the as-deposited Au and PPy films were unstressed, these bilayers remained flat during underetching and did not curl until they were actuated, removing constraints and any memory effects.

A series of devices was fabricated (see the Supporting Information for details) having widths of 100 μm and increasing lengths to give aspect ratios between 1 and 3. To apply the electrochemical potentials, the bilayers required an attachment point to the substrate, which was a small square 16 μm wide at the center of the bilayer (Figure A-3A). There were 100 bilayers of each aspect ratio in a 10 x 10 array. As mentioned previously, in this work the layers were unstrained during fabrication, and

so remained completely flat during underetching to remove the sacrificial layer. This is unlike in some prior work in which the membranes began curling during the etching process [147,149,157], which affected the final curled shapes.
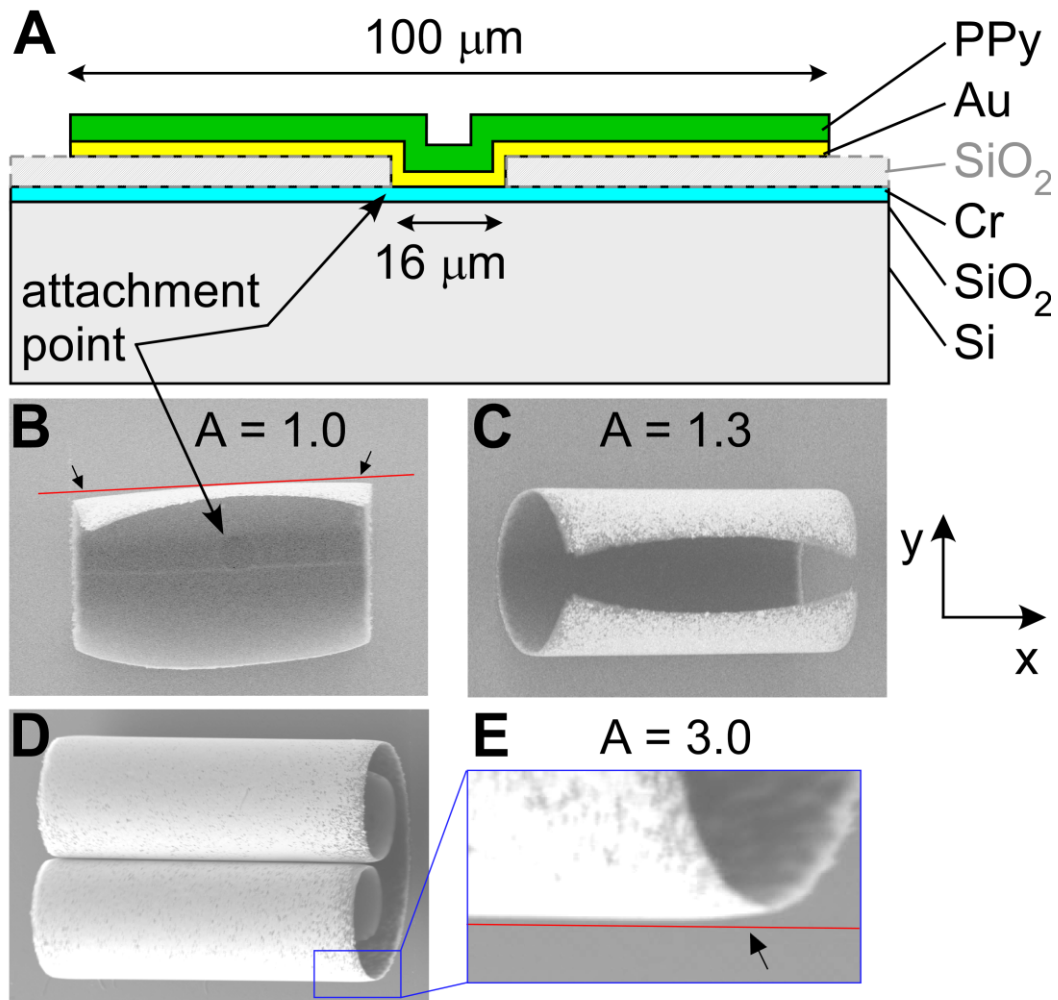
Figure A-3. A) Cross-sectional schematic (not to scale) of one of the bilayer actuators. The upper SiO₂ (gray) is a sacrificial layer that is removed in the final fabrication step to free the bilayer to bend. B-E) SEM images of bilayers after actuation. Arrows indicate regions of double curvature at the long edges.

Upon electrochemical actuation, the bilayers curved upward around the center mount point, as shown in the scanning electron microscope image (SEM) in Figure A-3B. Between these two curved regions, on either side of the center mount, the bilayers remained flat. Figure A-3B and C show double-curvature at the corners, and Figure A-3B-E show double-curvature at the long edges (marked by arrows), as predicted (Figure A-2A). Figure A-3C also shows that the bilayers bent with a uniform curvature into a circle, unaffected by the center mount and showing both that the working electrode provided the same potential to the entire device, resulting in an unvarying oxidation level in the PPy film, and that the fabrication process produced devices with the correct behavior. In Figure A-3D, both sides of the bilayers curled more than 90°, giving a double-roll configuration because of the center mounting.

The bending direction as a function of aspect ratio is shown in Figure A-4. Each point corresponds to one array (100 devices) on the sample and shows the fraction of devices in the array that bent in the y-direction, which for $A > 1$ means that the longer edge is curved. In the array with $A = 3.0$ (see inset), there is a predominance of spirals. For the shorter bilayers with $A = 1.0$, there is a mixture of bending in the x and y directions. The sides of the shorter bilayers were curled ~90°, so they appear dark in the optical micrograph.
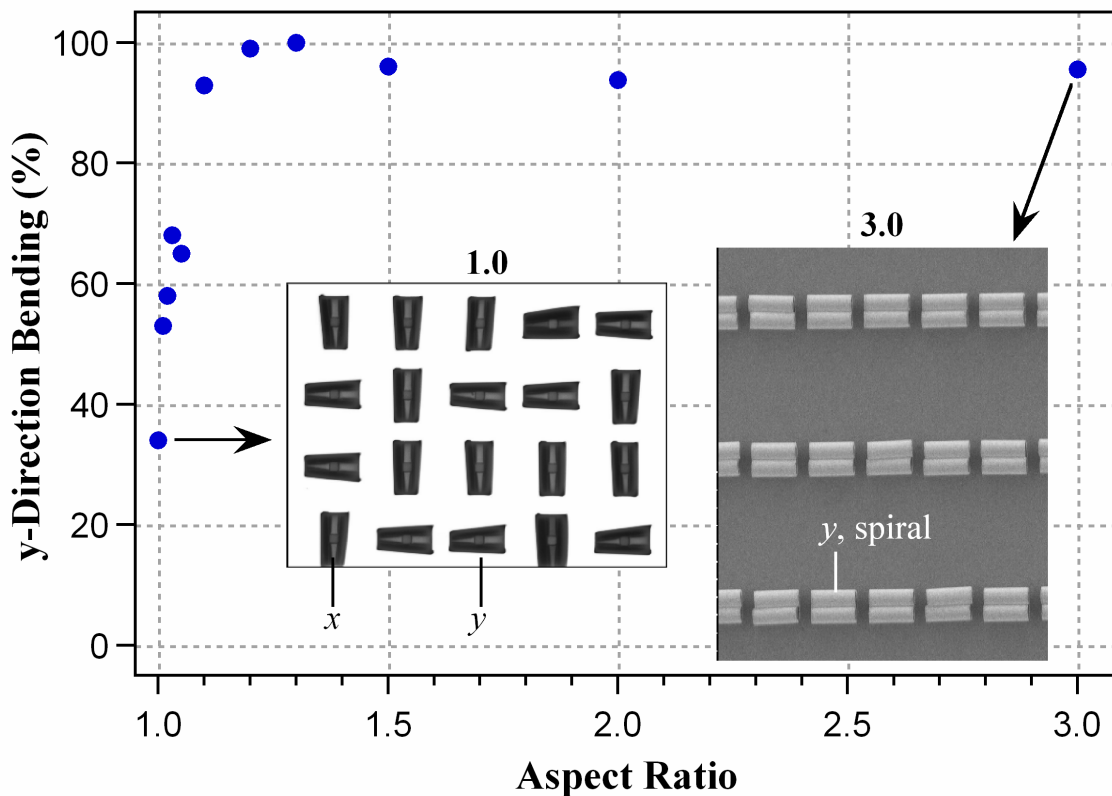
Figure A-4. The fraction of defect-free PPy/Au bilayers that curved in the *y*-direction (i.e. spirals for *A* > 1) as a function of aspect ratio. The insets show close-up images of parts of two arrays in the fully oxidized (bent) state, an optical micrograph for *A* = 1.0 and an SEM for *A* = 3.0.

There are several things to note in Figure A-4. First, the preferred configuration at high aspect ratios was the spiral (i.e., curved along the longer edges). This was expected from the prior experimental and theoretical work discussed above. Second, the aspect ratio had a powerful influence on the fraction of bilayers in the array that bent into a spiral versus a cigar (i.e., curved along the shorter edges). A significant increase in the fraction of *y*-directional bending was seen even for the smallest tested asymmetry, going from *A* = 1.00 to *A* = 1.01 (The energy difference at *A* = 1.01 is

less than 0.03% , Figure A-2D) By $A = 1.1$ (at which the energy difference is still only 0.2%), over 90% of the devices were spirals. Conversely, for $A = 1$ bending along either the x or y directions was random. (There was actually a small bias toward curvature in the x-direction in this particular $A = 1$ array. Other $A = 1$ arrays showed either no bias, a small bias in x, or a small bias in y; see the Supporting Information).

It is also important to note that almost no bilayers bent into corkscrews or dog-ears. (This is not due to the shape of the center mount. The Supporting Information (SI) shows that bilayers with round and square center mounts had the same behavior. The SI also shows that dog-ears form when the bilayers initially adhere slightly to the surface, rather than being completely free.) In samples with a greater number of fabrication non-uniformities and defects, there were tilted spirals, corkscrews, and dog-ears, but with increasing A the spiral still became heavily favored, with the frequency of the other configurations dropping sharply. This finding confirms the model result that there are no stable off-axis configurations.

In conclusion, the model and the experiments found only two stable equilibria: the spiral and the cigar. The spiral was energetically preferred, and the preference for the spiral increased with aspect ratio. The model shows that edge layers are the important feature that differentiates the spiral and cigar from the constant curvature Timoshenko approximation, and which therefore differentiates their elastic energies.

212

This double-curvature at the long edges, observed in the devices, has only rarely been seen because it is a very small effect, and its energy-lowering effect has not previously been known to be responsible for the long direction bending bifurcation. Although we have focused on rectangular bilayers, edge layers are a general phenomenon occurring in other shapes [172,176], and we expect that they will also contribute to the direction of bending for other shapes. Therefore, this approach provides a fundamental basis for thinking about these problems in general.

We present the theoretical finding that the bending direction is determined by double-curvature at the edges. We support these theoretical results with experimental data on arrays of bilayers that were produced in an unstressed state, which removes confounding memory effects that have previously been observed in prior work.

Acknowledgments

Supplementary Description

The supporting information includes full detail on the mathematical model, the fabrication process, data from two additional samples, additional data on $A = 1$ arrays, additional still and SEM images of the PPy/Au bilayers, and images of devices that were made with a different fabrication process leaving the bilayers sticking lightly to the substrate, which resulted in dog-ears. The supporting information also compares the bending behavior of bilayers with round versus square center mounts, and shows that a larger aspect ratio is needed to ensure the spiral geometry in less perfectly fabricated bilayers. In addition, there is a video of the actuators. This material is available free of charge via the Internet at http://pubs.acs.org.

Supplementary Information

Bilayer Fabrication

A combination of differential adhesion [1] and sacrificial release methods [2] was used to fabricate polypyrrole actuators to ensure completely free movement of devices upon actuation. Partial adhesion during the first cycle changes the behavior, since it leads to the corners lifting first. The poor adhesion of SiO_2 to Au was used to advantage in the sacrificial layer removal step. Separation of the Au from the SiO_2 allows the HF wet etchant to etch from the top, rather than just the side, reducing the etch time. This is beneficial for the actuation of the PPy, which is adversely affected

by HF.
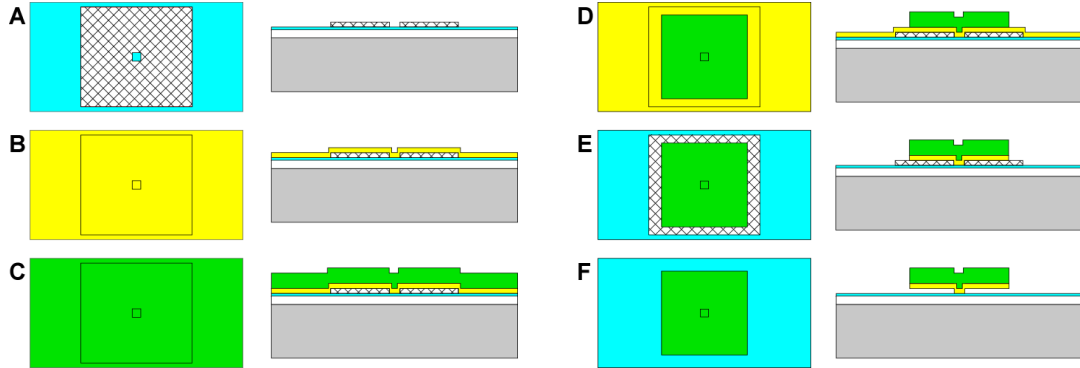
**Figure SI - 1. Fabrication process for the PPy(DBS)/Au bilayer actuators.
A) Onto an oxidized Si wafer, deposit a layer of Cr. Deposit and pattern a
sacrificial layer of SiO$_2$. Deposit B) Au and C) PPy. Pattern the D) PPy
and E) Au. F) Remove the sacrificial layer.**

The fabrication process for the PPy(DBS)/Au bilayer actuators is shown in Figure SI
- 1. A Cr adhesion layer (40 nm) and an SiO$_2$ sacrificial layer (100 nm) were
sequentially deposited onto an oxidized Si wafer by electron beam evaporation.
Positive resist (Shipley 1813) was spin-coated onto the SiO$_2$, exposed to 365 nm UV
light in a mask aligner, and developed (Shipley 352). The SiO$_2$ was wet etched using
buffered HF (JT Baker) diluted by a factor of 66 in deionized (DI) water. This first
mask step defines the rectangular sacrificial layer area, which has 10-16 μm square
openings down to the underlying Cr. The resist was removed via flood exposure and
development to avoid surface residue from exposure to organic solvents.
Immediately after rinsing the surface in DI and drying, the Au was deposited. Further
surface treatments, such as piranha, oxygen plasma, or Cr etching, caused difficulties
in later steps.

The PPy-Au bilayers were fabricated by first depositing an Au layer (100 nm) by thermal evaporation. This was followed immediately by the electrochemical deposition of a first $PPy(ClO_4)$ adhesion layer. This was grown by cyclic voltammetry, ramping the potential between 0 and 0.6 V vs. Ag/AgCl at 50 mV/s for 2 scans in 150 mL of an aqueous solution of 0.1 M pyrrole and 0.1 M $NaClO_4$. Thereafter the actuating PPy(DBS) layer was deposited potentiostatically (EcoChemie AutoLab) to a thickness of 400 nm at 0.46 V vs. Ag/AgCl in 150 mL of an aqueous solution of 0.1 M pyrrole and 0.1 M NaDBS. The counter electrode was an oxidized Si wafer coated with Au (100)/Cr (20 nm) positioned parallel to the sample and 4 cm away. The reference electrode was placed close to the back side of the sample. After deposition, care was taken during rinsing and drying to prevent excessive shear forces that would delaminate the Au.

Photoresist (1813) was patterned onto the surface of the PPy to act as a mask during the dry etching of the PPy by reactive ion etching in an oxygen plasma. The photoresist was removed by continued etching in the oxygen plasma; the etch rates for the resist and the PPy are comparable. The exposed Au was removed by wet etching (Transene Au etchant, diluted 2x) without agitation. Since some of the structures were partially freed during this step, undercutting of the Au occurred with agitation. The devices were kept in DI water after the Au was patterned to prevent stiction until the structures were released by wet etching in the dilute HF (66x) solution. The released bilayers were stored in water to prevent stiction after HF

216

etching. Testing was performed without delay to prevent chemical reactions on the surface of the exposed Cr, which occur over time if the Cr is left in the water.

The devices were actuated in 0.1 M NaDBS (EcoChemie AutoLab). The sample and the counter electrode were both fixed flat at the bottom of an electrochemical cell, with a spacing of 0.5 cm between them. The reference electrode was adjacent to the sample. The PPy was first reduced by ramping the voltage from 0 to -0.85 V vs. Ag/AgCl at 10 mV/sec using a Au (100)/Cr (20 nm) on oxidized Si wafer counter electrode. The oxidation/reduction level was monitored by measuring the consumed current. It was then partially re-oxidized by gradually increasing the voltage in small increments until the bilayers started to curve upward (at approx. -0.63 V). The bilayers were imaged through Leica MZ12.5 stereomicroscope using Bunton 5 MP CMOS digital camera under coaxial illumination.

Arrays Used to Generate the Data in Figure 4 of the Main Text

The eleven arrays from which the data in Figure 4 were obtained (Sample 1) in the main text are shown in Figure SI - 2. In these images, the bilayers are in the oxidized (curled) state. Two kinds of defects that can be seen here and in the following figures: 1) devices that are missing because they sheared off (e.g. during rinsing or moving the wafer into the actuation solution) and 2) devices that did not release but that remained flat on the surface due to stiction. It is likely that stiction also led to the

small number of dog-ears and corkscrews that are present. Also, not all of the devices are fully curled up. The reasons for incomplete actuation may be stiction or a poor electrical connection.   If the bending direction was clear, then these were included in the counts of spirals, cigars, dog-ears, and corkscrews.
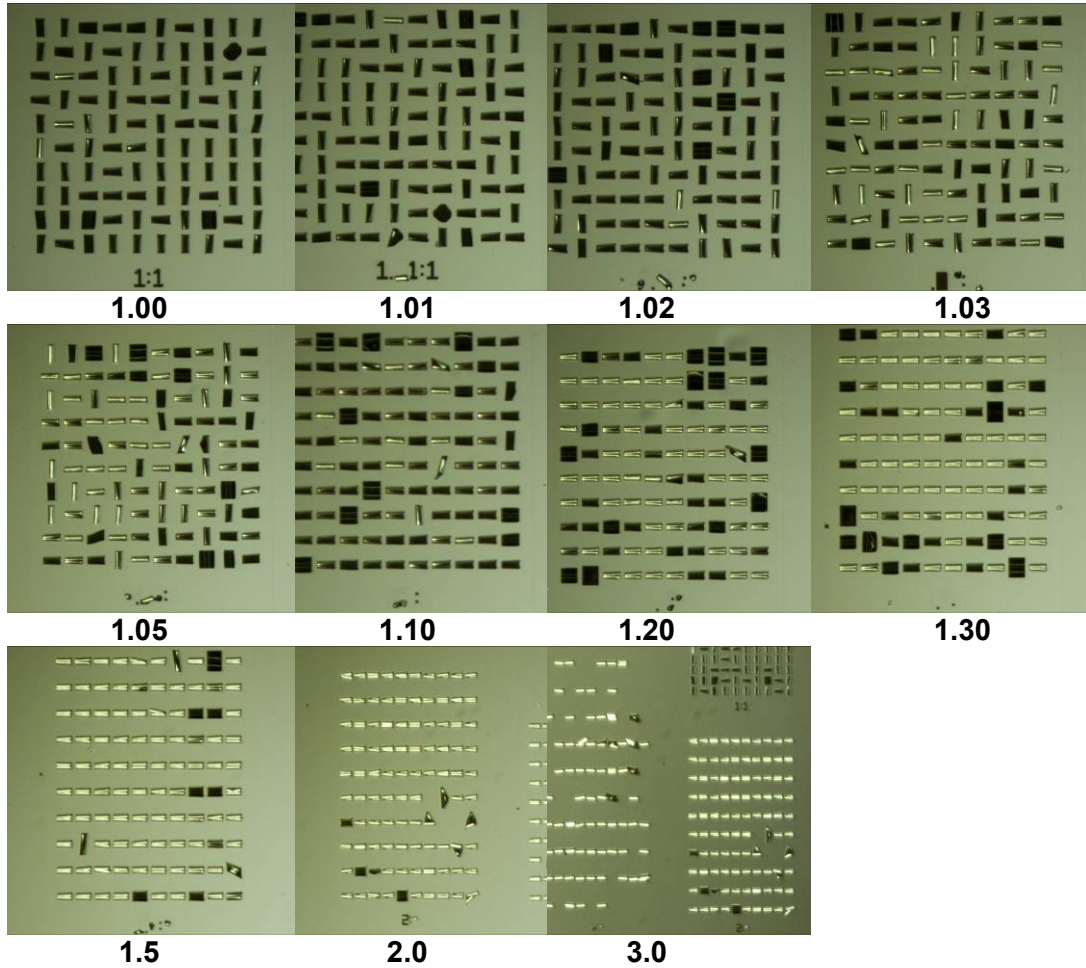
Figure SI - 2. Sample 1 arrays with increasing aspect ratio (used to generate the data in Figure 4 in the main text). Bilayers were considered defective if they came off the surface (such as in A = 2.0 at the position x= 9, y = 7), did not curl (A = 1.2, x = 8, y = 1), or partially adhered to the substrate (A = 1.10, x = 7, y = 2).

Close-ups of three of the arrays showing how the devices were categorized are included in Figure SI - 3 and Figure SI - 4. In Figure SI - 4b there were three defects due to stiction: the bilayers did not pick up (they were flat). In Figure SI - 4c,d it is probable, but not absolutely clear, that stiction caused the dog-eared or corkscrew bilayers, so they were counted as dog-ears or corkscrews rather than defects. Out of the 1100 bilayers in the 11 arrays, the total number of dog-ears was 11, corkscrews 13, and defects 43.
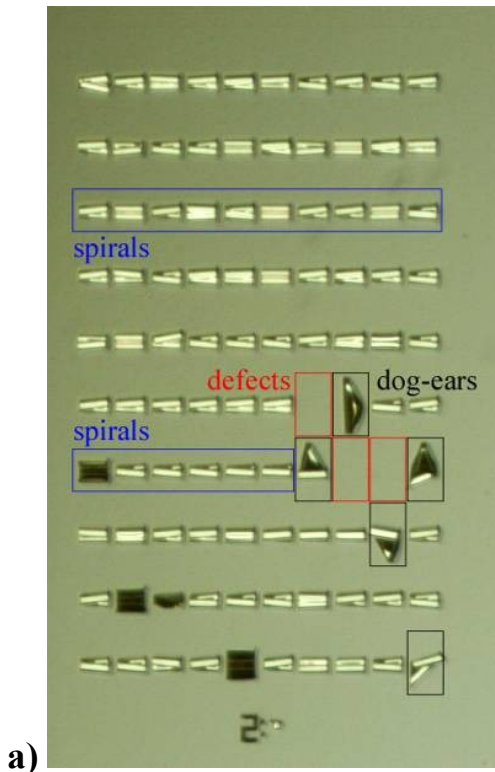
cigars	spirals	dog-ear	cork-screw	defects
0	10			
0	10			
0	10			
0	10			
0	10			
0	8	1		1
0	6	2		2
0	9	1		
0	10	1		
0	9	1		

Figure SI - 3. a) Sample 1, *A* = 2 array showing how the bilayers were categorized. b) The counts for each row of the array. These devices are so long that they curl into a double-spiral (see SEM images in Figure SI - 14c,d).
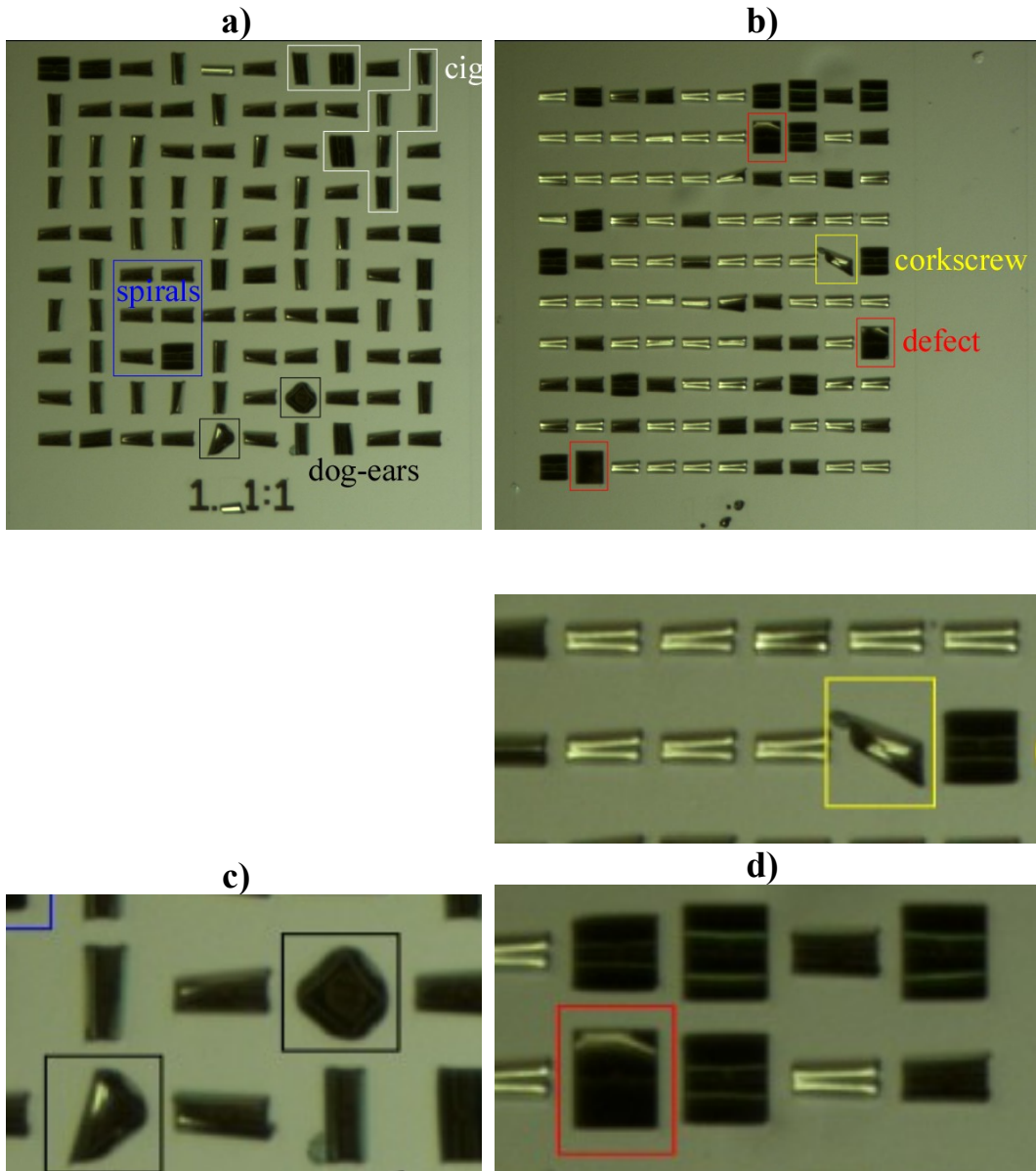
Figure SI - 4. Sample 1, a) A = 1.01 and b) A = 1.2 **arrays showing how the bilayers were categorized.   c) & d) close-ups from a) & b), respectively.**

From the images, one can see that bilayers with larger aspect ratios had a larger number of defects (Figure SI - 5); this is because the shear forces they experienced

during fabrication were larger for the bigger plates, leading to delamination. The number of bilayers with at least one dog-eared corner and those that tilted (corkscrews) are also plotted in Figure SI - 5.

Figure SI - 5. Percentage of defect-free bilayers from Sample 1 (arrays in Figure SI - 2) with one or more corners curled inward (dog-ears) (black diamonds) , spirals (blue circles), and corkscrews (green triangles). Also shown is the percentage of defective/missing bilayers (red Xs).

Results from Other Samples

It must be emphasized that the fabrication of perfect devices is exceedingly challenging. The slightest degree of stickiness to the surface results in dog-ears or

corkscrews (the subject of a future publication). Variations in PPy thickness or a mask in which the dimensions are slightly different from those that were drawn might produce directional bias. Etching the Au too long results in underetching, giving a thinning of the Au, or even a complete loss of the Au, at the bilayer edges. Small particulates give rise to point defects, which destroy the symmetry of the bilayer and cause misfolding. During actuation, small particulates interfere with curling.

In the two additional samples (Samples 2 and 3) shown in this section, the fabrication was not as perfect as in Sample 1(Figure SI - 7, Figure SI - 8). For example, during fabrication these samples were exposed to acetone, which Sample 1, shown in the main text, was not, and this most likely resulted in a small degree of stiction.

The fraction of spirals for Samples 2 and 3 is shown in Figure SI - 6, in comparison with the data from Figure SI - 5. The key thing to note is that even given the defects, the fraction of bilayers bending into the spiral configuration nevertheless still increased strongly with aspect ratio. This is remarkable given the very small energy differences (less than 1%) between spirals and cigars for these aspect ratios at these strains (see Figure 2D in the main text).
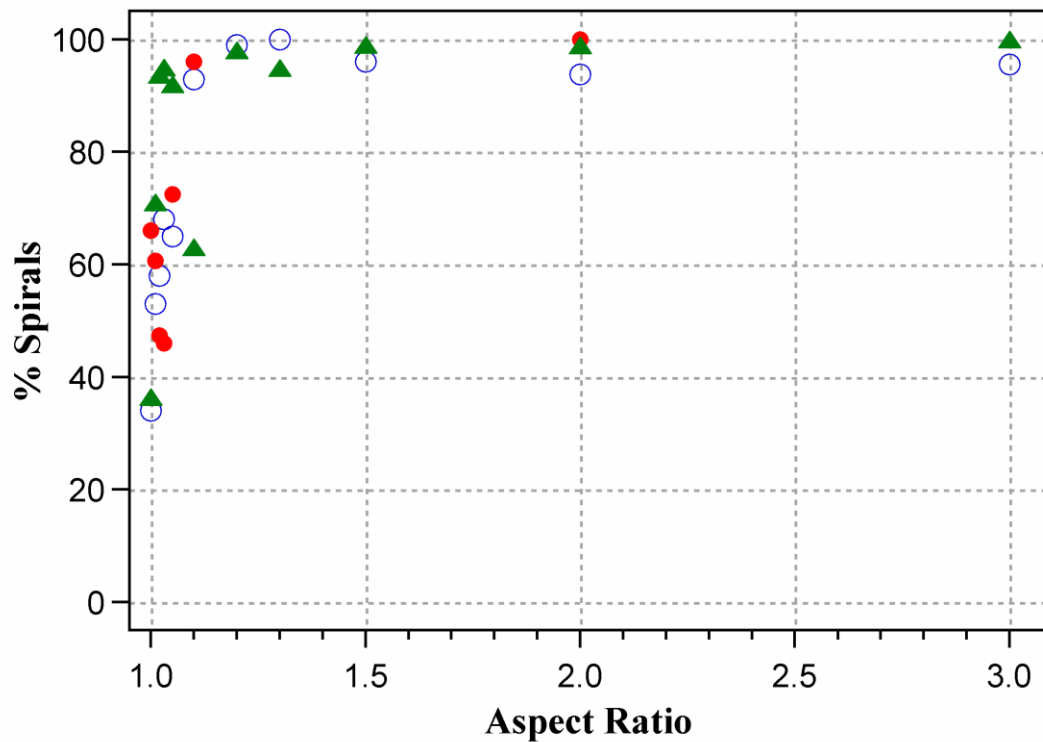
Figure SI - 6. The fraction of defect-free PPy/Au bilayers that curled into spirals as a function of aspect ratio. Open blue circles are from Sample 1, green triangles are from Sample 2, and red circles are from Sample 3.
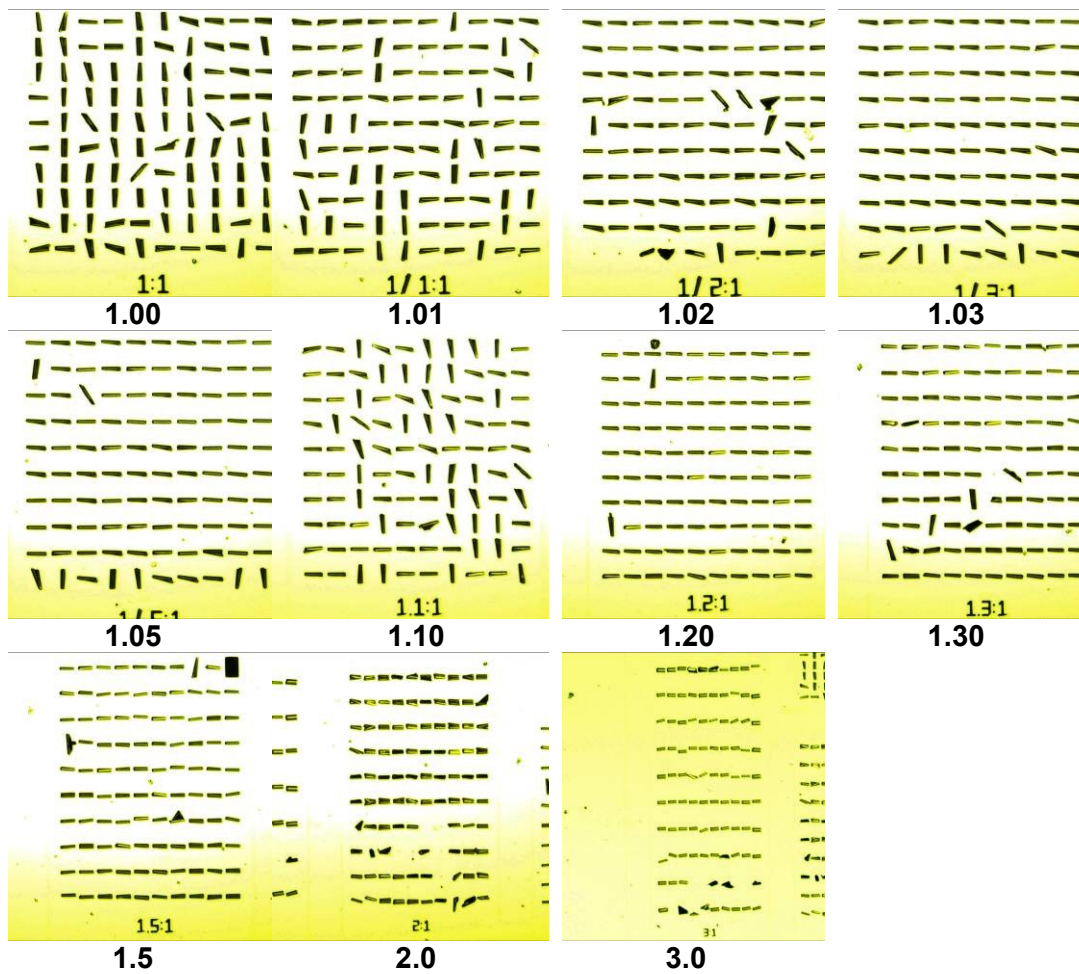
Figure SI - 7. Arrays from Sample 2 (green triangles in Figure SI - 6).
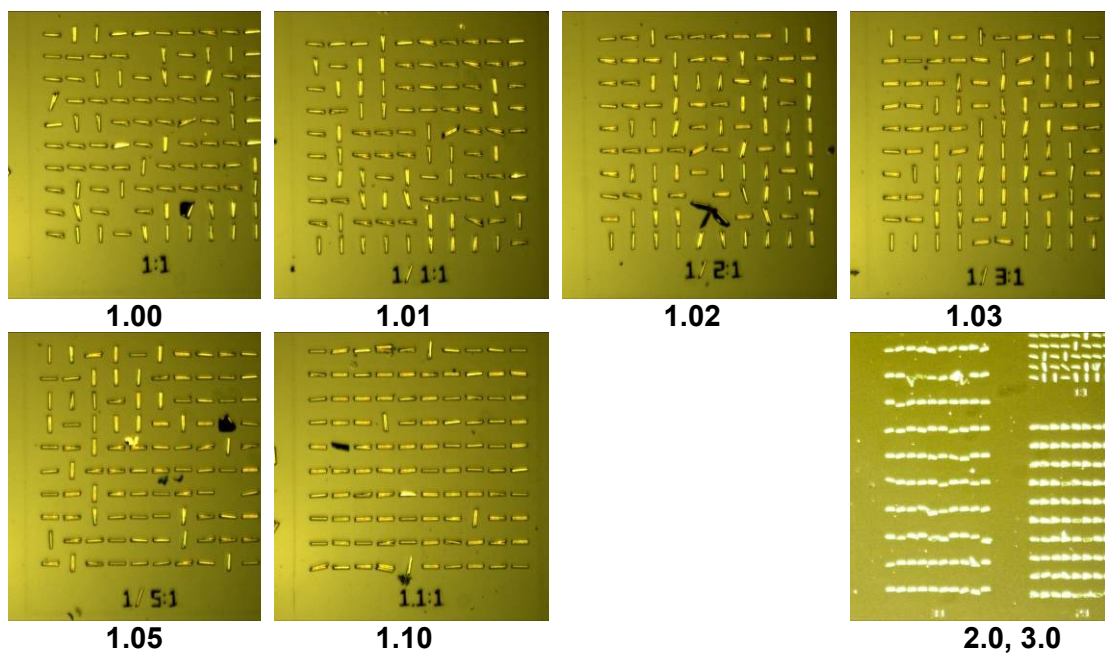
Figure SI - 8. Arrays from Sample 3 (red circles in Figure SI - 6). (The missing devices were accidently damaged during testing.)

Y-Direction Bending < 50% for $A = 1$

Each of the three samples had three arrays with an aspect ratio of 1 (Figure SI - 9). In eight of these arrays, there was a preference for the bilayers to bend along either along the x-direction (samples 2 and 3) or the y-direction (sample 1), with approximately two thirds of the bilayers going one way and one third the other (Table SI - 1). Only one of these arrays showed 50% going both directions, as would be expected if there was no bias.
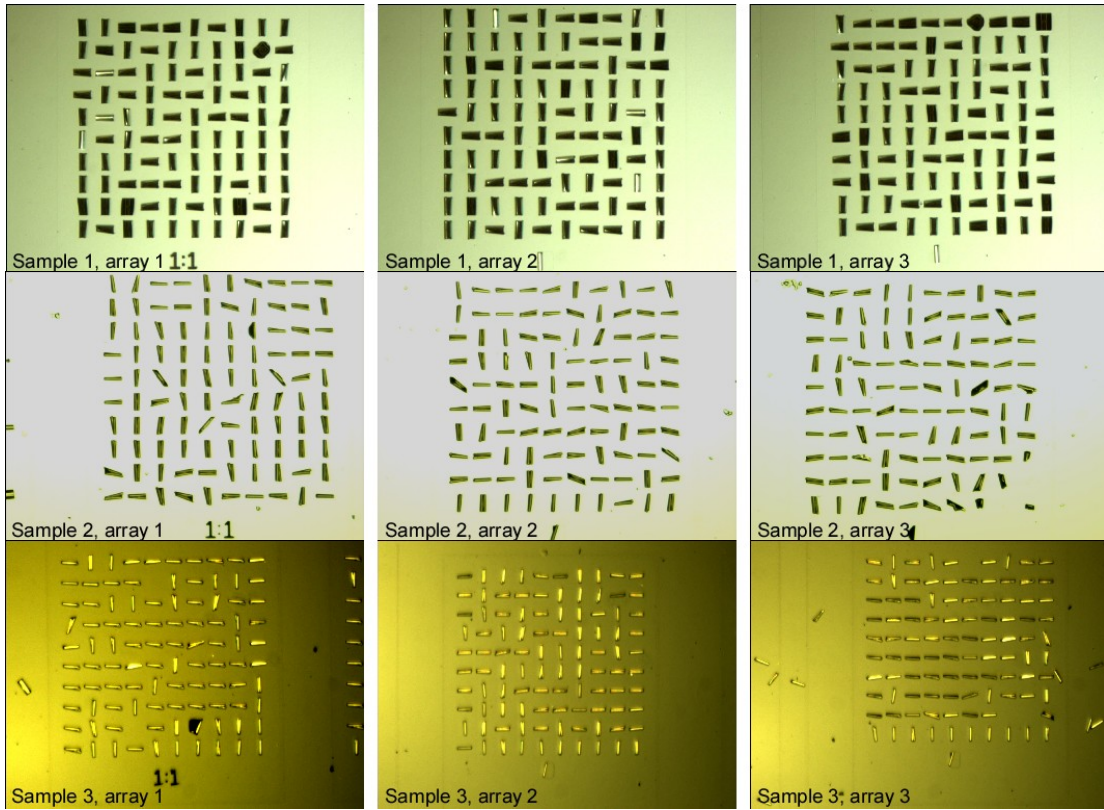
Figure SI - 9. Nine *A* = 1 arrays from three samples.

**Table SI - 1. Fraction of bilayers bent
into the *y*-direction (horizontal tubes)
for *A* = 1 arrays.**

Sample	Array 1	Array 2	Array 3
Sample 1	34%	34%	40%
Sample 2	35%	63%	65%
Sample 3	66%	51%	77%

The reason for the bias in these arrays is unclear. However, sample 1 was from one wafer, and samples 2 and 3 were from another wafer, suggesting that it was a difference in the fabrication process for each wafer. Given that the sample 1 arrays

had a preference for *x* and other two a smaller preference for *y,* one can rule out non-square features on the photolithography mask as being responsible. However, a small tilt of the wafer relative to the mask during exposure may have produced a small foreshortening that made the bilayers not perfectly square, with the tilt being different for the two wafers. The flow of chemicals over the structures during etching may also not have been perfectly symmetric. Both wafers were dry etched at the same position and orientation in the reactive ion etcher, but agitation during the wet etch steps might have added some directionality.

Systematic thickness variations in *x* versus *y* might have been introduced by wafer placement in the evaporator, or by the placement of the counter and reference electrodes during electrochemical deposition or actuation. This seems to be an unlikely explanation for the bias, however, given the inconsistency of the results based on the array number and the difference between the two wafers. The variation in PPy thickness across the wafer was approximately 1000 Å based on film color, with the PPy being thicker at the edges of the sample than the center. This corresponds to a difference of only approximately 5 Å across a single bilayer, with the direction varying depending on the array position.

Square vs. Circular Center Mount

In order to examine the question of whether the shape of the center mount influenced the behavior, a mask was designed in which the top five rows of each array had a circular-shaped center mount and the bottom five rows the usual square mount.

During the fabrication of these devices, during step 1 (Figure SI - 1) the patterning of the sacrificial oxide was done 4 months after the deposition of the Cr and oxide layers, rather than immediately. These bilayers adhered slightly to the surface and didn't curl up completely freely during the first actuation cycle. As a result, a significant number of the bilayers dog-eared. This is the subject of a future paper. While it is not clear why the delay in patterning affected the bilayer release, release is strongly affected by processing procedures. (There also a small mis-alignment on this mask that affected the topmost row of the $A = 3$, in which the bilayers are fixed at the top.) The oxidized (curled) states are shown in Figure SI - 10 (Sample 4) and Figure SI - 11 (Sample 5).
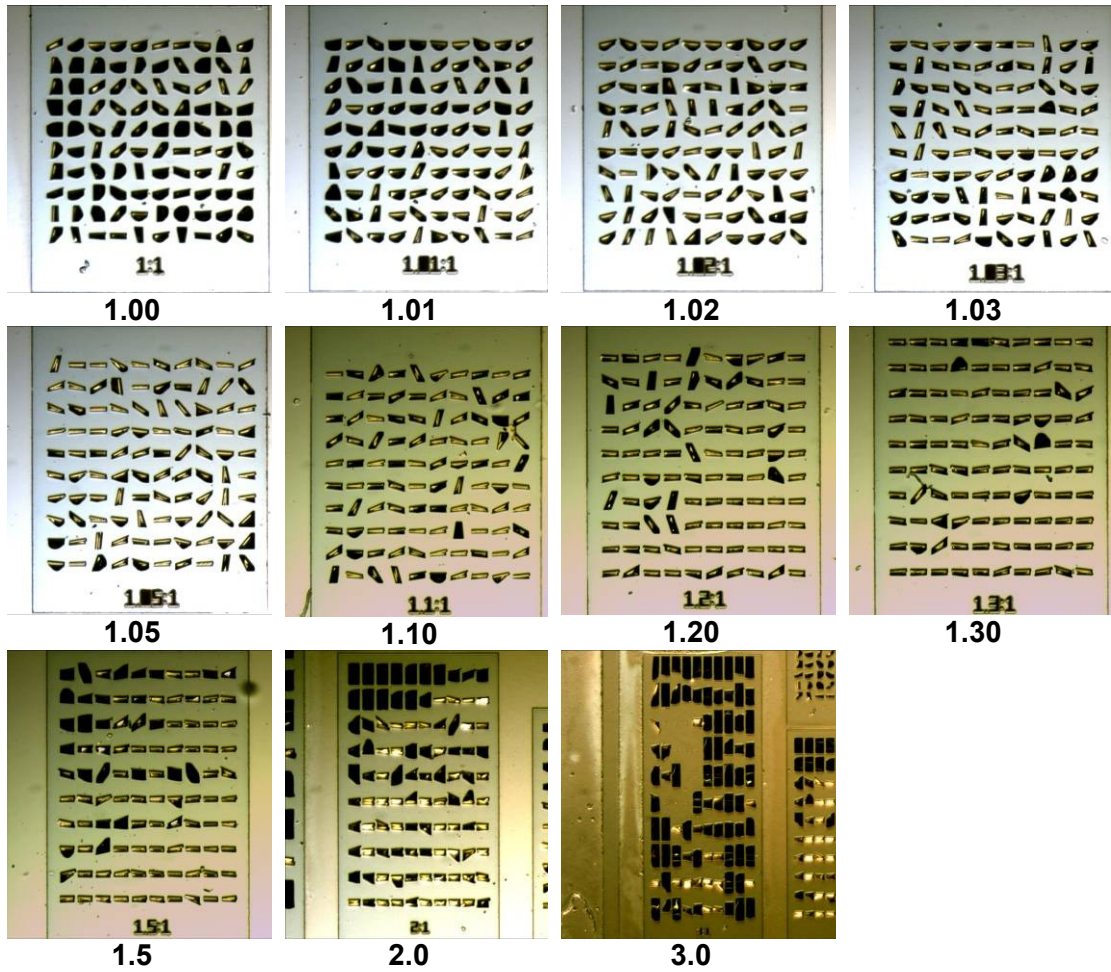
Figure SI - 10. Arrays from Sample 4 with round mounts in the top five rows of each array and square mounts in the bottom five.
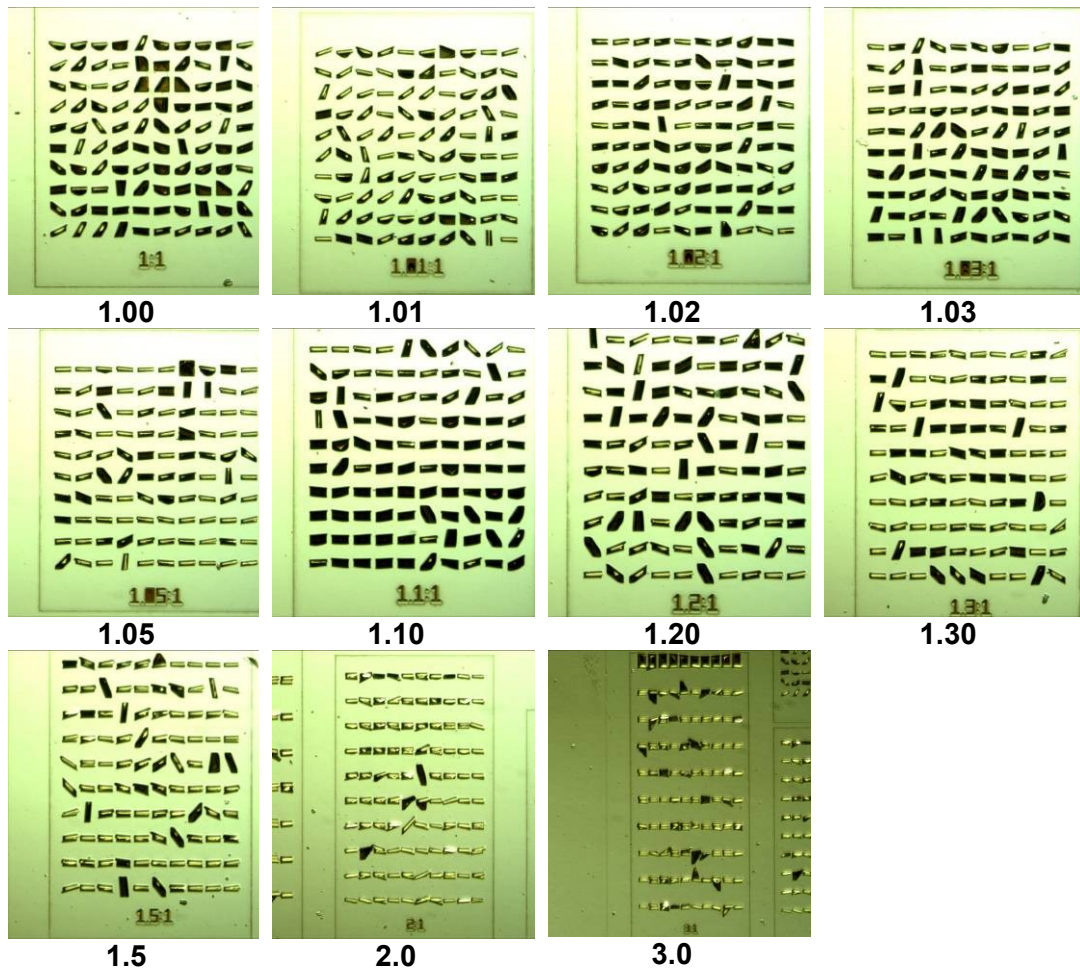
Figure SI - 11. Arrays from Sample 5 with round mounts in the top five rows of each array and square mounts in the bottom five.

The behaviors for the two mounts are compared in Figure SI - 12 and Figure SI - 13. They behaved similarly, with the number of devices curling into a corkscrew being small for both mount shapes on both samples and dropping to zero as the aspect ratio increased. We can therefore conclude that this off-axis bending is *not* due to the shape of the center mount. The fraction of bilayers bending into spirals was essentially the same for the circular and square mounts, and it increased with aspect

ratio *A*. As discussed above, a significant number of the bilayers on Samples 4 and 5 dog-eared. For small *A*, the fraction of spirals was therefore small. However, as *A* increased, the dog-earing behavior was suppressed, in favor of the spiral configuration. These data also again show an increase in the number of defects as the area of bilayers increased.

In general, we learn from Figure SI - 12 and Figure SI - 13 that for the less perfect devices, it requires a higher aspect ratio to enforce the spiral geometry. This is consistent with the increasing energy difference with increasing *A* calculated in the model (Figure 2D in the main text).
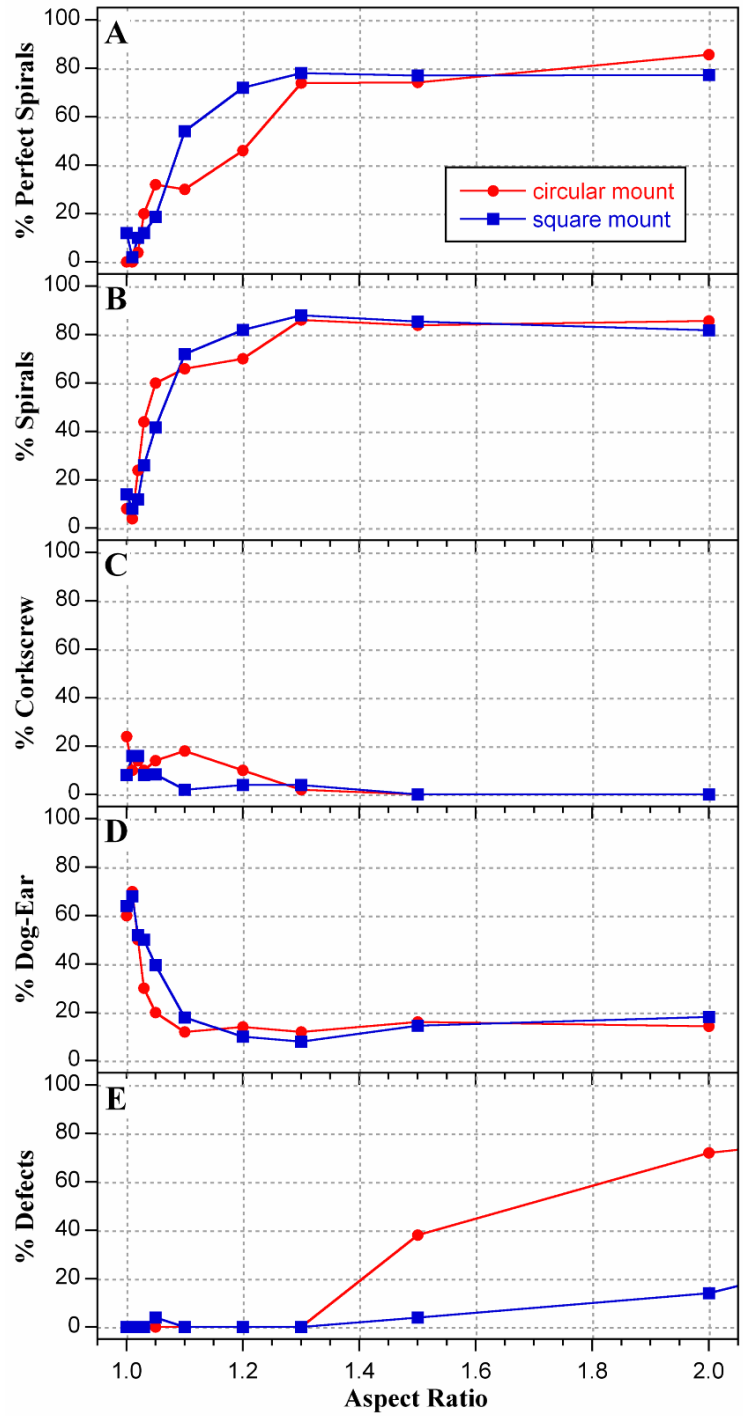
Figure SI - 12. The percentage of bilayers from Sample 4 with circular (red) and square (blue) mounts that curled into perfect spirals or spirals (all spirals, including those slightly tilted), those that curled into corkscrews, those in which at least one corner dog-eared, and bilayers that were defective.

232
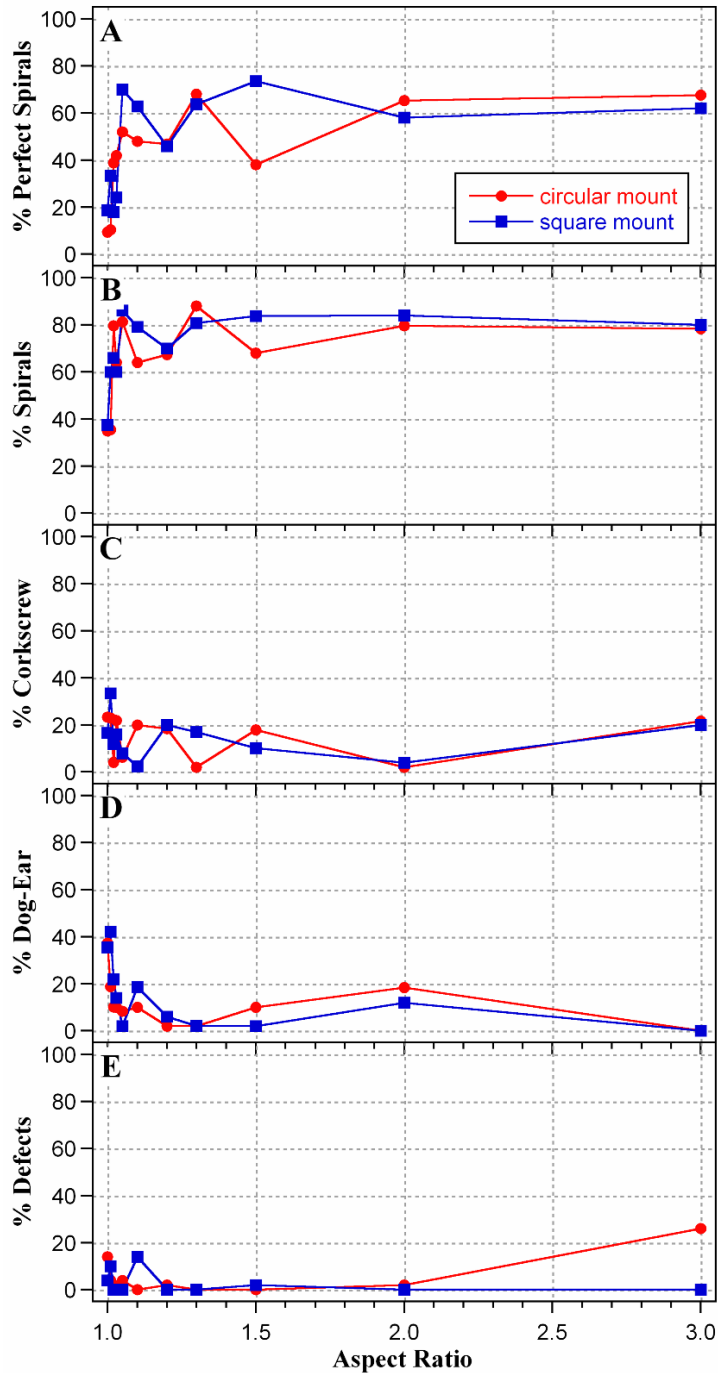
Figure SI - 13. The percentage of bilayers from Sample 5 with circular (red) and square (blue) mounts that curled into perfect spirals or spirals (all spirals, including those slightly tilted), those that curled into corkscrews, those in which at least one corner dog-eared, and bilayers that were defective.

Additional SEM Images\

SEM images of bilayers with increasing aspect ratio are shown in Figure SI - 14, and a schematic of the curling is shown in Figure SI - 15. As the length of the bilayer increases, the only way it can curl into radius R is to form a double spiral. These were also seen in Figure SI - 3 and Figure SI - 4c,d.
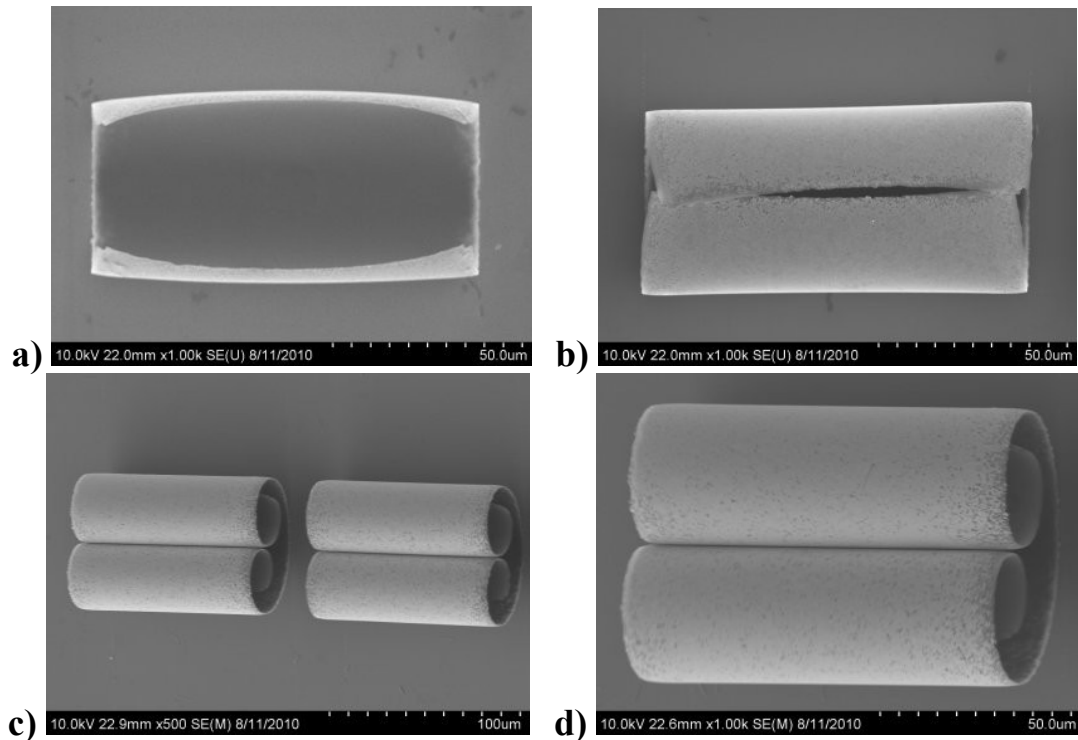
Figure SI - 14. SEM images of bilayers with aspect ratio a) 1.03, b) 1.5, c) 3.0, and d) 3.0.
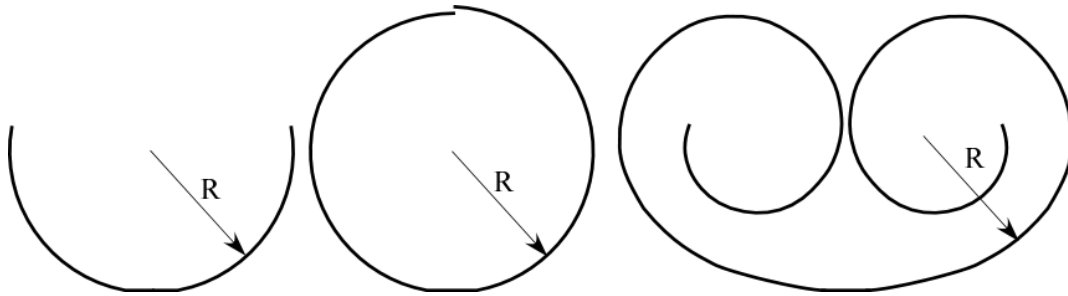
Figure SI - 15. Schematic of bilayer curling with increasing with aspect ratio (length), corresponding approximately to the images in Figure SI - 14.

Dog-Ears

Dog-ears were observed under two scenarios. The first was when the Au adhered slightly to the substrate, so that bilayer bending started at the edges and worked inward. This occurred when the bilayers were made with the differential adhesion method [1,3], as illustrated in Figure SI - 16. For all aspect ratios, the corner curling was seen uniformly over the whole array.
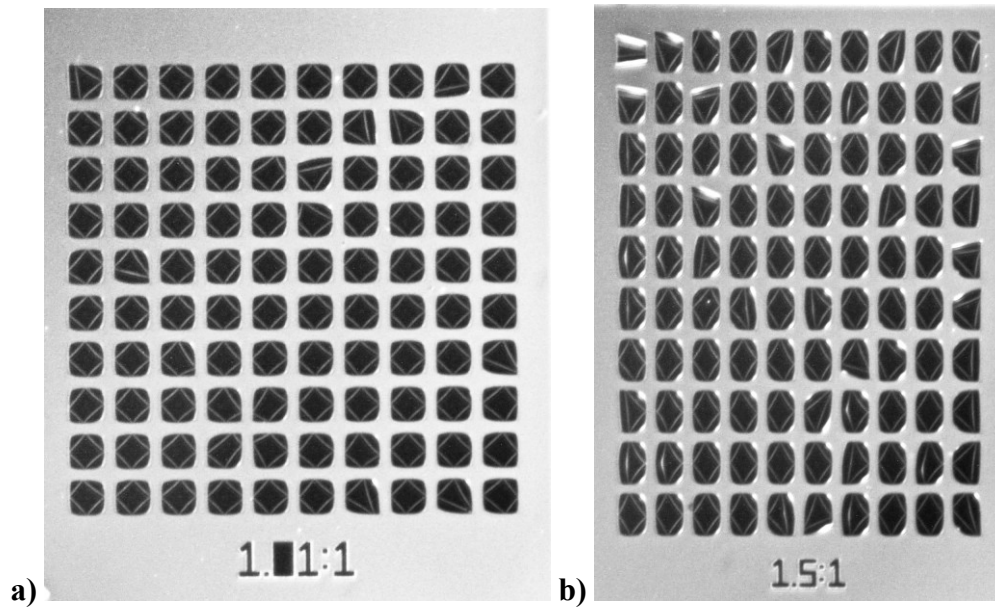
Figure SI - 16. Array of devices with aspect ratio a) $A = 1.01$ and b) $A = 1.5$ fabricated by differential adhesion rather than with a sacrificial layers, so that curling started at the corners and edges.

The second circumstance in which devices curled at an angle was when the connection to the substrate was a small bilayer hinge placed at a corner, rather than a spot in the center, as shown in Figure SI - 17. (We acknowledge Im Deok Jung for fabricating and testing these devices.)
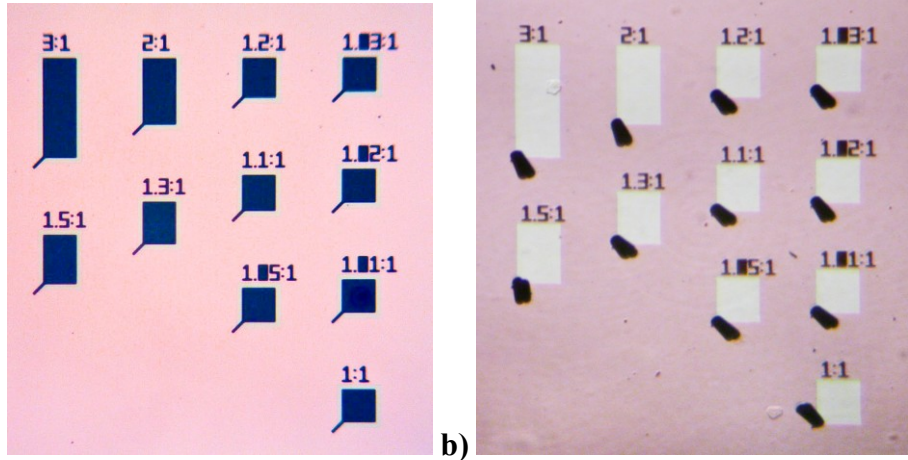
Figure SI - 17. Array of corner-mounted bilayers of varying aspect ratio a) before and b) after actuation.

Bibliography

1. F. Carpi, P. Chiarelli, A. Mazzoldi, and D. De Rossi, "Electromechanical characterisation of dielectric elastomer planar actuators: comparative evaluation of different electrode materials and different counterloads," Sens. Actuator A-Phys., 107 (1)**,** 85-95 (2003).

2. F. Carpi and D. De Rossi, "Contractile folded dielectric elastomer actuators," Smart Structures and Materials 2006: Electroactive Polymer Actuators and Devices (EAPAD), San Diego, California, USA, (SPIE), vol. 6524, edited by Y. Bar-Cohen, p. 65240D (19-22 March 2007, 2007).

3. N. C. Goulbourne, "Cylindrical dielectric elastomer actuators reinforced with inextensible fibers," Smart Structures and Materials 2006: Electroactive Polymer Actuators and Devices (EAPAD), San Diego, CA, USA (SPIE), vol. 6168, edited by Y. Bar-Cohen, p. 61680A (2006).

4. R. Heydt, R. Kornbluh, R. Pelrine, and V. Mason, "Design and performance of an electrostrictive-polymer-film acoustic actuator," J. Sound Vibr., 215 (2)**,** 297-311 (1998).

5. G. Kofod, D. N. Mc Carthy, J. Krissler, G. Lang, and G. Jordan, "Electroelastic optical fiber positioning with submicrometer accuracy: Model and experiment," Appl. Phys. Lett., 94 (20)**,** 3 (2009).

6. R. Kornbluh, R. Pelrine, Q. Pei, R. Heydt, S. Stanford, S. Oh, and J. Eckerle, "Electroelastomers: applications of dielectric elastomer transducers for actuation, generation, and smart structures," Smart Structures and Materials 2002: Industrial and Commercial Applications of Smart Structures Technologies, San Diego, CA, USA (SPIE), vol. 4698, edited by R. M. Anna-Maria, p. 254-270 (2002).

7. B. M. O'Brien, E. P. Calius, T. Inamura, S. Q. Xie, and I. A. Anderson, "Dielectric elastomer switches for smart artificial muscles," Appl. Phys. A-Mater. Sci. Process., 100 (2)**,** 385-389 (2010).

8. R. Pelrine, R. Kornbluh, and J. Joseph, "Electrostriction of polymer dielectrics with compliant electrodes as a means of actuation," Sens. Actuator A-Phys., 64 (1)**,** 77-85 (1998).

9. R. Pelrine, P. Sommer-Larsen, R. Kornbluh, R. Heydt, G. Kofod, Q. Pei, and P. Gravesen, "Applications of dielectric elastomer actuators," Smart Structures and Materials 2001: Electroactive Polymer Actuators and Devices,

Newport Beach, CA, USA (SPIE), vol. 4329, edited by Y. Bar-Cohen, p. 335-349 (2001).

10.   P. Sommer-Larsen and M. Benslimane, "Actuators and sensors from dielectric elastomer with smart compliant electrodes," in <u>Dielectric Elastomers as Electromechanical Transducers: Fundamentals, Materials, Devices, Models and Applications of an Emerging Electroactive Polymer Technology</u>, edited by F. Carpi, D. De Rossi, R. Kornbluh, R. Pelrine, and P. Sommer-Larsen, p. 103-108 (Elsevier Amsterdam, 2008).

11.   Q. Pei, R. Pelrine, M. Rosenthal, S. Stanford, H. Prahlad, and R. Kornbluh, "Recent progress on electroelastomer artificial muscles and their application for biomimetic robots," Smart Structures and Materials 2004: Electroactive Polymer Actuators and Devices (EAPAD), San Diego, CA, USA, (SPIE), vol. 5385, edited by Y. Bar-Cohen, p. 41-50 (2004).

12.   R. Heydt, R. Pelrine, J. Joseph, J. Eckerle, and R. Kornbluh, "Acoustical performance of an electrostrictive polymer film loudspeaker," J. Acoust. Soc. Am., 107 (2)**,** 833-839 (2000).

13.   I. A. Anderson, E. P. Calius, T. Gisby, T. Hale, T. McKay, B. O'Brien, and S. Walbran, "A dielectric elastomer actuator thin membrane rotary motor," Smart Structures and Materials & Nondestructive Evaluation and Health Monitoring 2009: Electroactive Polymer Actuators and Devices (EAPAD) San Diego, CA, USA (SPIE), vol. 7287, edited by Y. Bar-Cohen and T. Wallmersperger, p. 72871H (2009).

14.   R. Pelrine, R. Kornbluh, Q. Pei, and J. Joseph, "High-speed electrically actuated elastomers with strain greater than 100%," Science, 287 (5454)**,** 836-839 (2000).

15.   R. Pelrine, R. Kornbluh, J. Joseph, R. Heydt, Q. B. Pei, and S. Chiba, "High-field deformation of elastomeric dielectrics for actuators," Mater. Sci. Eng. C-Biomimetic Supramol. Syst., 11 (2)**,** 89-100 (2000).

16.   R. Pelrine and R. Kornbluh, "Electromechanical transduction effects in dielectric elastomers: actuation, sensing, stiffness modulation and electric energy generation," in <u>Dielectric Elastomers as Electromechanical Transducers: Fundamentals, Materials, Devices, Models and Applications of an Emerging Electroactive Polymer Technology</u>, edited by F. Carpi, D. De Rossi, R. Kornbluh, R. Pelrine, and P. Sommer-Larsen, p. 3-12 (Elsevier Amsterdam, 2008).

17.   M. Wissler and E. Mazza, "Electromechanical coupling in dielectric elastomer

actuators," Sens. Actuator A-Phys., 138 (2)**,** 384-393 (2007).

18.   G. K. Lau, J. F. L. Goosen, F. v. Keulen, P. J. French, and P. M. Sarro, "Actuated elastomers with rigid vertical electrodes," J. Micromech. Microeng, 16 (6)**,** S35-S44 (2006).

19.   P. Sommer-Larsen, G. Kofod, M. H. Shridhar, M. Benslimane, and P. Gravesen, "Performance of dielectric elastomer actuators and materials," Smart Structures and Materials 2002: Electroactive Polymer Actuators and Devices (EAPAD), San Diego, CA, USA (SPIE), vol. 4695, edited by Y. Bar-Cohen, p. 158-166 (2002).

20.   A. Pimpin, Y. Suzuki, and N. Kasagi, "Microelectrostrictive actuator with large out-of-plane deformation for flow-control application," J. Microelectromech. Syst., 16 (3)**,** 753-764 (2007).

21.   W. D. Callister, <u>Materials Science and Engineering, An Introduction</u>, 6th ed. (John Wiley & Sons, New Jersy, 2003).

22.   F. Carpi, G. Gallone, F. Galantini, and D. De Rossi, "Silicone-poly(hexylthiophene) blends as elastomers with enhanced electromechanical transduction properties," Adv. Funct. Mater., 18 (2)**,** 235-241 (2008).

23.   G. Gallone, F. Carpi, D. De Rossi, G. Levita, and A. Marchetti, "Dielectric constant enhancement in a silicone elastomer filled with lead magnesium niobate-lead titanate," Mater. Sci. Eng. C-Biomimetic Supramol. Syst., 27 (1)**,** 110-116 (2007).

24.   J. P. Szabo, J. A. Hiltz, C. G. Cameron, R. S. Underhill, J. Massey, B. White, and J. Leidner, "Elastomeric composites with high dielectric constant for use in Maxwell stress actuators," Smart Structures and Materials 2003: Electroactive Polymer Actuators and Devices (EAPAD), San Diego, CA, USA (SPIE), vol. 5051, edited by Y. Bar-Cohen, p. 180-190 (2003).

25.   F. Carpi and D. De Rossi, "Improvement of electromechanical actuating performances of a silicone dielectric elastomer by dispersion of titanium dioxide powder," IEEE Trns. Dielectr. Electr. Insul., 12 (4)**,** 835-843 (2005).

26.   C. G. Cameron, R. S. Underhill, M. Rawji, and J. P. Szabo, "Conductive filler-elastomer composites for Maxwell stress actuator applications," Smart Structures and Materials: Electroactive Polymer Actuators and Devices (EAPAD), San Diego, CA, USA (SPIE), vol. 5385, edited by Y. Bar-Cohen, p. 51-59 (2004).

27. Z. Zhang, L. Liu, G. Deng, S. Sun, Y. Liu, and J. Leng, "Silicone dielectric elastomers filled with carbon nanotubes and actuator," Smart Structures and Materials & Nondestructive Evaluation and Health Monitoring 2009: Electroactive Polymer Actuators and Devices (EAPAD), San Diego, CA, USA, (SPIE), vol. 7287, edited by Y. Bar-Cohen and T. Wallmersperger, p. 72871V (2009).

28. M. Kujawski, J. Pearse, and E. Smela, "Graphite/PDMS stretchable electrodes for dielectric elastomer actuators," Electroactive Polymer Actuators and Devices (EAPAD), San Diego, CA, (SPIE), vol. 7642 (9, March, 2010).

29. F. Carpi, A. Migliore, and D. De Rossi, "A new contractile linear actuator made of dielectric elastomers " Smart Structures and Materials 2005: Electroactive Polymer Actuators and Devices (EAPAD), San Diego, CA, USA, (SPIE), vol. 5759, edited by Y. Bar-Cohen, p. 64-74 (2005).

30. S. C. Burgess, C. S. Ling, A. Conn, S. Araromi, J. Wang, and R. Vaidyanathan, "Development of a novel Electro Active Polymer (EAP) actuator for driving the wings of flapping micro air vehicle," WIT Transactions on the Built Environment, Algarve, vol. 106, p. 207-217 (2009).

31. G. Kofod, "The static actuation of dielectric elastomer actuators: how does pre-stretch improve actuation?," J. Phys. D-Appl. Phys., 41 (21)**,** 11 (2008).

32. S. M. Ha, W. Yuan, Q. B. Pei, R. Pelrine, and S. Stanford, "Interpenetrating polymer networks for high-performance electroelastomer artificial muscles," Adv. Mater., 18 (7)**,** 887-891 (2006).

33. S. M. Ha, W. Yuan, Q. Pei, R. Pelrine, and S. Stanford, "Interpenetrating networks of elastomers exhibiting 300% electrically-induced area strain," Smart Mater. Struct., 16 (2)**,** S280-S287 (2007).

34. M. G. Urdaneta, R. Delille, and E. Smela, "Stretchable electrodes with high conductivity and photo-patternability," electrode, 19 (18)**,** 2629-2633 (2007).

35. P. Dubois, S. Rosset, S. Koster, J. Stauffer, S. Mikhailov, M. Dadras, N. F. de Rooij, and H. Shea, "Microactuators based on ion implanted dielectric electroactive polymer (EAP) membranes," Sens. Actuator A-Phys. , 130-131**,** 147-154 (2006).

36. G.-K. Lau, S. C.-K. Goh, and L.-L. Shiau, "Dielectric elastomer unimorph using flexible electrodes of electrolessly deposited (ELD) silver," 169 (1)**,** 234-241 (2011).

37.   E. Biddiss and T. Chau, "Dielectric elastomers as actuators for upper limb prosthetics: Challenges and opportunities," Med. Eng. Phys, 30 (4)**,** 403-418 (2008).

38.   R. Pelrine, R. Kornbluh, and G. Kofod, "High-strain actuator materials based on dielectric elastomers," Adv. Mater., 12 (16)**,** 1223-1225 (2000).

39.   B. O'Brien, E. Calius, S. Xie, and I. Anderson, "An experimentally validated model of a dielectric elastomer bending actuator," Smart Structures and Materials & Nondestructive Evaluation and Health Monitoring: Electroactive Polymer Actuators and Devices (EAPAD), San Diego, California, USA, (SPIE), vol. 6927, p. 69270T-69211 (2008).

40.   F. Carpi, G. Frediani, A. Mannini, and D. DeRossi, "Contractile and buckling actuators based on dielectric elastomers: devices and applications," Adv. Sci.Tech., 61**,** 186-191 (2008).

41.   S. Uma, R. Matusiak, D. L. Hecht, and E. J. Shrader, "Elastomer-based diffractive optical modulator," IEEE J. Sel. Top. Quantum Electron., 10 (3)**,** 435-439 (2004).

42.   N. Galler, H. Ditlbacher, B. Steinberger, A. Hohenau, M. Dansachmüller, F. Camacho-Gonzales, S. Bauer, J. R. Krenn, A. Leitner, and F. R. Aussenegg, "Electrically actuated elastomers for electro-optical modulators," Appl. Phys. B-Lasers Opt., 85 (1)**,** 7-10 (2006).

43.   A. P. Gerratt, B. Balakrisnan, I. Penskiy, and S. Bergbreiter, "Batch microfabricated dielectric elastomer actuators," International Conference on Solid-State Sensors, Actuators, and Microsystem, Beijing, China (June 5-9, 2011).

44.   B. K. Wilson and L. Y. Lin, "Variable wave plate via tunable form-birefringent structures," J. Microelectromech. Syst., 17 (4)**,** 1039-1046 (2008).

45.   T. Maleki, G. Chitnis, A. Panja, and B. Ziaie, "Single-layer elastomeric out-of-plane actuator with asymmetric surface profile," Solid-State Sensors, Actuators, and Microsystems Workshop, Hilton Head Workshop
Hilton Head, South Carolina, (Transducer Research Foundation, Inc.), edited by D. J. M. a. K. L. Turner (June 6 - 10, 2010 2010).

46.   T. Maleki, G. Chitnis, and B. Ziaie, "A batch-fabricated laser-micromachined PDMS actuator with stamped carbon grease electrodes," J. Micromech. Microeng., 21 (2)**,** 8 (2011).

47. J. J. Loverich, I. Kanno, and H. Kotera, "Concepts for a new class of all-polymer micropumps," Lab Chip, 6 (9), 1147-1154 (2006).

48. M. Wissler and E. Mazza, "Modelling of prestrained circular actuators," in <u>Dielectric Elastomers as Electromechanical Transducers: Fundamentals, Materials, Devices, Models and Applications of an Emerging Electroactive Polymer Technology</u>, edited by F. Carpi, D. De Rossi, R. Kornbluh, R. Pelrine, and P. Sommer-Larsen, p. 169-176 (Elsevier Amsterdam, 2008).

49. G. Kofod and P. Sommer-Larsen, "Silicone dielectric elastomer actuators: Finite-elasticity model of actuation," Sens. Actuator A-Phys., 122 (2), 273-283 (2005).

50. G. Kofod and P. Sommer-Larsen, "Finite-elasticity models of actuation," in <u>Dielectric Elastomers as Electromechanical Transducers: Fundamentals, Materials, Devices, Models and Applications of an Emerging Electroactive Polymer Technology</u>, edited by F. Carpi, D. De Rossi, R. Kornbluh, R. Pelrine, and P. Sommer-Larsen, p. 159-168 (Elsevier Amsterdam, 2008).

51. P. Lochmatter and G. Kovacs, "Design and characterization of an active hinge segment based on soft dielectric EAPs," Sens. Actuator A-Phys., 141 (2), 577-587 (2008).

52. P. Lochmatter and G. Kovacs, "Design and characterization of an actively deformable shell structure composed of interlinked active hinge segments driven by soft dielectric EAPs," Sens. Actuator A-Phys., 141 (2), 588-597 (2008).

53. P. Lochmatter, G. Kovacs, and P. Ermanni, "Design and characterization of shell-like actuators based on soft dielectric electroactive polymers," Smart Mater. Struct., 16 (4), 1415-1422 (2007).

54. P. Lochmatter, S. Michel, and G. Kovacs, "Electromechanical model for static and dynamic activation of elementary dielectric elastomer actuators," Smart Structures and Materials 2006: Electroactive Polymer Actuators and Devices (EAPAD), San Diego, CA, USA, (SPIE), vol. 6168, edited by Y. Bar-Cohen, p. 61680F (2006).

55. M. Moscardo, X. H. Zhao, Z. G. Suo, and Y. Lapusta, "On designing dielectric elastomer actuators," J. Appl. Phys., 104 (9), 7 (2008).

56. B. O'Brien, T. McKay, E. Calius, S. N. Xie, and I. Anderson, "Finite element modelling of dielectric elastomer minimum energy structures," Appl. Phys. A-Mater. Sci. Process., 94 (3), 507-514 (2009).

57. J. S. Plante and S. Dubowsky, "On the nature of dielectric elastomer actuators and its implications for their design," Smart Structures and Materials 2006: Electroactive Polymer Actuators and Devices (EAPAD), Activation of dielectric elastomer actuators by means of human electrophysiological signals, (SPIE), vol. 6168, edited by Y. Bar-Cohen, p. 61681J (2006).

58. J. S. Plante and S. Dubowsky, "On the performance mechanisms of dielectric elastomer actuators," Sens. Actuator A-Phys., 137 (1), 96-109 (2007).

59. J. S. Plante and S. Dubowsky, "On the properties of dielectric elastomer actuators and their design implications," Smart Mater. Struct., 16 (2), S227-S236 (2007).

60. V. Racherla, "An electromechanical model for characterizing sensing and actuating performance of unimorphs based on "plain" dielectric polymers," Sens. Actuator A-Phys., 168 (2), 343-350 (2011).

61. C. Kluge, N. Galler, H. Ditlbacher, and M. Gerken, "Modeling of electrically actuated elastomer structures for electro-optical modulation," Appl. Phys. A-Mater. Sci. Process., 102 (2), 407-413 (2011).

62. J. L. Pons, Emerging Actuator Technologies: A Micromechatronic Approach, (John Wiley & Sons Ltd, West Sussex, England, 2005).

63. V. A. Zakrevskiĭ and N. T. Sudar, "Electrical breakdown of thin polymer films," Phys. Solid State, 47 (5), 961-967 (2005).

64. C. Liu, Foundations of MEMS, (Pearson Education Inc., Upper Saddle River, New Jersy, 2006).

65. G. T. A. Kovacs, N. I. Maluf, and K. E. Petersen, "Bulk micromachining of silicon," Proc. IEEE, 86 (8), 1536-1551 (1998).

66. J. M. Bustillo, R. T. Howe, and R. S. Muller, "Surface micromachining for microelectromechanical systems," Proc. IEEE, 86 (8), 1552-1574 (1998).

67. R. Shankar, T. K. Ghosh, and R. J. Spontak, "Electromechanical response of nanostructured polymer systems with no mechanical pre-strain," Macromol. Rapid Commun., 28 (10), 1142-1147 (2007).

68. , Dow Corning, "Photopatternable silicone WL5130 ", http://www.dowcorning.com/applications/search/default.aspx?R=1711EN.

69. C. Liu, "Recent developments in polymer MEMS," Adv. Mater., 19 (22), 3783-3790 (2007).

70. C. Montemayor, personal communication (2009).

71. Y. N. Xia, E. Kim, X. M. Zhao, J. A. Rogers, M. Prentiss, and G. M. Whitesides, "Complex optical surfaces formed by replica molding against elastomeric masters," Science, 273 (5273), 347-349 (1996).

72. J. Garra, T. Long, J. Currie, T. Schneider, R. White, and M. Paranjape, "Dry etching of polydimethylsiloxane for microfluidic systems," 20 (3), 975-982 (2002).

73. H. L. Cong and T. R. Pan, "Photopatternable conductive PDMS materials for microfabrication," Adv. Funct. Mater., 18 (13), 1912-1921 (2008).

74. M. Kujawski, J. D. Pearse, and E. Smela, "Elastomers filled with exfoliated graphite as compliant electrodes," Carbon, In Press, Corrected Proof (2010).

75. D. W. Pashley, "A study of the deformation and fracture of single-crystal gold films of high strength inside an electron microscope," Proc. R. Soc. Lond. A, 255 (1281), 218-231 (1960).

76. R. Kornbluh, R. Pelrine, J. Joseph, R. Heydt, Q. Pei, and S. Chiba, "High-field electrostriction of elastomeric polymer dielectrics for actuation," Smart Structures and Materials 1999: Electroactive Polymer Actuators and Devices, Newport Beach, CA, USA, (SPIE), vol. 3669, edited by Y. Bar-Cohen, p. 149-161 (1999).

77. D. Gray, J. Tien, and C. Chen, "High-conductivity elastomeric electronics," Adv. Mater., 16 (5), 393-397 (2004).

78. T. Li, Z. G. Suo, S. P. Lacour, and S. Wagner, "Compliant thin film patterns of stiff materials as platforms for stretchable electronics," J. Mater. Res., 20 (12), 3274-3277 (2005).

79. D. Brosteaux, F. Axisa, M. Gonzalez, and J. Vanfleteren, "Design and fabrication of elastic interconnections for stretchable electronic circuits," IEEE Electron Device Lett., 28 (7), 552-554 (2007).

80. J. N. Lee, C. Park, and G. M. Whitesides, "Solvent compatibility of poly(dimethylsiloxane)-based microfluidic devices," Anal. Chem., 75 (23), 6544-6554 (2003).

81.   R. Maboudian, W. R. Ashurst, and C. Carraro, "Self-assembled monolayers as anti-stiction coatings for MEMS: characteristics and recent developments," Sens. Actuator A-Phys., 82 (1-3), 219-223 (2000).

82.   J. Y. Kim and C. J. Kim, "Comparative study of various release methods for polysilicon surface micromachining," Tenth Annual International Workshop on Micro Electro Mechanical Systems (MEMS '97), Nagoya, Japan, (IEEE), vol. MEMS '97 Tenth Annual International Workshop on Micro Electro Mechanical System, p. 442-447 (1997).

83.   G. K. Fedder, "Simulation of Microelectromechanical Systems," Electrical Engineering and Computer Sciences, University of California at Berkeley, Berkeley (1994).

84.   P. A. Manoharan and D. Nedumaran, "Modeling-Simulation and analysis of MEMS capacitive millibar pressure sensor," J. Nanotechnol. Eng. Med., 1, 041003-041001 (2010).

85.   M. Lishchynska, C. O'Mahony, O. Slattery, and R. Behan, "Comprehensive spring constant modelling of tethered micromechanical plates," J. Micromech. Microeng., 16 (6), S61-S67 (2006).

86.   Y. L. Loo, T. Someya, K. W. Baldwin, Z. N. Bao, P. Ho, A. Dodabalapur, H. E. Katz, and J. A. Rogers, "Soft, conformable electrical contacts for organic semiconductors: High-resolution plastic circuits by lamination," Proc. Natl. Acad. Sci. U. S. A., 99 (16), 10252-10256 (2002).

87.   S. P. Lacour, J. Jones, S. Wagner, T. Li, and Z. G. Suo, "Stretchable interconnects for elastic electronic surfaces," Proc. IEEE, 93 (8), 1459-1467 (2005).

88.   N. Tiercelin, P. Coquet, R. Sauleau, V. Senez, and H. Fujita, "Polydimethylsiloxane membranes for millimeter-wave planar ultra flexible antennas," J. Micromech. Microeng., 16 (11), 2389-2395 (2006).

89.   T. Li, Z. Y. Huang, Z. Suo, S. P. Lacour, and S. Wagner, "Stretchability of thin metal films on elastomer substrates," Appl. Phys. Lett., 85 (16), 3435-3437 (2004).

90.   S. Wagner, S. P. Lacour, J. Jones, P. H. I. Hsu, J. C. Sturm, T. Li, and Z. G. Suo, "Electronic skin: architecture and components," Physica E, 25 (2-3), 326-334 (2004).

91.   M. Benslimane, P. Gravesen, and P. Sommer-Larsen, "Mechanical properties

of dielectric elastomer actuators with smart metallic compliant electrodes," Smart Structures and Materials 2002: Electroactive Polymer Actuators and Devices (EAPAD), San Diego, CA, USA (SPIE), vol. 4695, edited by Y. Bar-Cohen, p. 150-157 (2002).

92.   N. Bowden, S. Brittain, A. G. Evans, J. W. Hutchinson, and G. M. Whitesides, "Spontaneous formation of ordered structures in thin films of metals supported on an elastomeric polymer," Nature, 393 (6681)**,** 146-149 (1998).

93.   A. Dec and K. Suyama, "Micromachined electro-mechanically tunable capacitors and their applications to RF IC's," IEEE Trans. Microw. Theory Tech., 46 (12)**,** 2587-2596 (1998).

94.   M. Bails, J. A. Martinez, S. P. Levitan, I. Avdeev, M. Lovell, and D. M. Chiarulli, "Computational prototyping of an RF MEMS switch using chatoyant," Nanotech 2004, Boston,MA, vol. 2 (2004).

95.   M. Lishchynska, N. Cordero, and O. Slattery, "Development of behavioural models for mechanically loaded microcantilevers and beams," Analog Integr. Circuits Process., 44 (2)**,** 109-118 (2005).

96.   Handbook on materials selection, edited by M. Kutz (John Wiley & Sons, New York, 2002).

97.   J. M. Gere and S. P. Timoshenko, Mechanics of Materials, 4th ed. (PWS Publishing Company, Boston, 1997).

98.   H.-E. Kiil and M. Y. Benslimane, "Scalable industrial manufacturing of DEAP," Electroactive Polymer Actuators and Devices (EAPAD) 2009, San Diego, (SPIE), edited by Y. Bar-Cohen; and T. Wallmersperger, p. 72870R (2009).

99.   S. P. Lacour, S. Wagner, Z. Y. Huang, and Z. Suo, "Stretchable gold conductors on elastomeric substrates," Appl. Phys. Lett., 82 (15)**,** 2404-2406 (2003).

100.   T. Li and Z. Suo, "Deformability of thin metal films on elastomer substrates," Int. J. Solids Struct., 43 (7-8)**,** 2351-2363 (2006).

101.   S. P. Lacour, D. Chan, S. Wagner, T. Li, and Z. G. Suo, "Mechanisms of reversible stretchability of thin metal films on elastomeric substrates," Appl. Phys. Lett., 88 (20)**,** 3 (2006).

102.   S. P. Lacour, J. Jones, Z. Suo, and S. Wagner, "Design and performance of

thin metal film interconnects for skin-like electronic circuits," IEEE Electron Device Lett., 25 (4)**,** 179-181 (2004).

103. S. P. Lacour, S. Wagner, R. J. Narayan, T. Li, and Z. G. Suo, "Stiff subcircuit islands of diamondlike carbon for stretchable electronics," J. Appl. Phys., 100 (1)**,** 6 (2006).

104. S. P. Lacour, S. Wagner, H. Prahlad, and R. Pelrine, "High voltage photoconductive switches of amorphous silicon for electroactive polymer actuators," J. Non-Cryst. Solids 736-739 (2004).

105. T. Li, Z. Y. Huang, Z. C. Xi, S. P. Lacour, S. Wagner, and Z. Suo, "Delocalizing strain in a thin metal film on a polymer substrate," Mech. Mater. , 37 (2-3)**,** 261-273 (2005).

106. T. Li and Z. Suo, "Ductility of thin metal films on polymer substrates modulated by interfacial adhesion," Int. J. Solids Struct.**,** 1696-1705 (2007).

107. W. C. Young, <u>Roark's Formula for Stress & Strain</u>, 6th ed. (McGraw-Hill Inc, 1989).

108. A. B. Comsol, "COMSOL multiphysics user's guide," (2005).

109. T. A. Davis, <u>UMFPACK version 4.4 user guide</u>, (Department of Computer and Information Science and Engineering, University of Florida, Florida, 2005).

110. F. Carpi, G. Fantoni, and D. DeRossi, "Bubble-like dielectric elastomer actuator with integrated sensor: device and applications," Proceedings of Actuator 2006, Bremen, Germany, edited by H. Borgmann, p. 872-875 (2006).

111. O. A. Araromi, A. T. Conn, C. S. Ling, J. M. Rossiter, R. Vaidyanathan, and S. C. Burgess, "Spray deposited multilayered dielectric elastomer actuators," Sens. Actuator A-Phys., 167 (2)**,** 459-467 (2011).

112. M. Benslimane, P. Gravesen, K. West, S. Skaarup, and P. Sommer-Larsen, "Performance of polymer-based actuators: the three-layer model," Smart Structures and Materials 1999: Electroactive Polymer Actuators and Devices, Newport Beach, CA, USA, (SPIE), vol. 3669, edited by Y. Bar-Cohen, p. 87-97 (1999).

113. D. L. Devoe and A. P. Pisano, "Modeling and optimal design of piezoelectric cantilever microactuators," J. Microelectromech. Syst., 6 (3)**,** 266-270 (1997).

114. R. J. Wood, E. Steltz, and R. S. Fearing, "Optimal energy density piezoelectric bending actuators," Sens. Actuator A-Phys., 119 (2)**,** 476-488 (2005).

115. Q. M. Wang, X. H. Du, B. M. Xu, and L. E. Cross, "Electromechanical coupling and output efficiency of piezoelectric bending actuators," IEEE Trans. Ultrason. Ferroelectr. Freq. Control, 46 (3)**,** 638-646 (1999).

116. M. Sitti, D. Campolo, J. Yan, and R. S. Fearing, "Development of PZT and PZN-PT based unimorph actuators for micromechanical flapping mechanisms," Robotics and Automation, 2001. Proceedings 2001 ICRA. IEEE International Conference on, vol. 4, p. 3839-3846 vol.3834 (2001, 2001).

117. M. S. Weinberg, "Working equations for piezoelectric actuators and sensors," J. Microelectromech. Syst., 8 (4)**,** 529-533 (1999).

118. J. G. Smits and W. Choi, "The constituent equations of piezoelectric heterogeneous bimorphs," IEEE Trans. Ultrason. Ferroelectr. Freq. Control 38 (3)**,** 256-270 (1991).

119. L. F. Campanile, R. Jahne, and A. Hasse, "Exact analysis of the bending of wide beams by a modified elastica approach," Proc. Inst. Mech. Eng. Part C-J. Eng. Mech. Eng. Sci., 225 (C11)**,** 2759-2764 (2011).

120. S. K. Ha and Y. H. Kim, "Analysis of a piezoelectric multimorph in extensional and flexural motions," J. Sound Vibr., 253 (5)**,** 1001-1014 (2002).

121. S. Y. Lee, B. Ko, and W. S. Yang, "Theoretical modeling, experiments and optimization of piezoelectric multimorph," Smart Mater. Struct., 14 (6)**,** 1343-1352 (2005).

122. W. Yang, S. Y. Lee, and B. J. You, "A piezoelectric actuator with a motion-decoupling amplifier for optical disk drives," Smart Mater. Struct., 19 (6)**,** 10 (2010).

123. S. Timoshenko, "Analysis of Bi-metal Thermostats," J. Opt. Soc. Am., 11**,** 223-256 (1925).

124. J. Brugger, G. Beljakovic, M. Despont, H. Biebuyck, N. F. de Rooij, and P. Vettiger, "Low-cast PDMS seal ring for single-side wet etching of MEMS structures," Sens. Actuator A-Phys. , 70 (1-2)**,** 191-194 (1998).

125. A. Mata, A. J. Fleischman, and S. Roy, "Characterization of polydimethylsiloxane (PDMS) properties for biomedical micro/nanosystems," Biomed. Microdevices, 7 (4), 281-293 (2005).

126. Y. N. Xia and G. M. Whitesides, "Soft lithography," Annu. Rev. Mater. Sci., 28, 153-184 (1998).

127. M. A. Eddings and B. K. Gale, "A PDMS-based gas permeation pump for on-chip fluid handling in microfluidic devices," J. Micromech. Microeng., 16 (11), 2396-2402 (2006).

128. B. Xu, F. Arias, and G. M. Whitesides, "Making honeycomb microcomposites by soft lithography," Adv. Mater., 11 (6), 492-496 (1999).

129. E. Kim, Y. N. Xia, X. M. Zhao, and G. M. Whitesides, "Solvent-assisted microcontact molding: A convenient method for fabricating three-dimensional structures on surfaces of polymers," Adv. Mater., 9 (8), 651-654 (1997).

130. S. Takayama, E. Ostuni, X. P. Qian, J. C. McDonald, X. Y. Jiang, P. LeDuc, M. H. Wu, D. E. Ingber, and G. M. Whitesides, "Topographical micropatterning of poly(dimethylsiloxane) using laminar flows of liquids in capillaries," Adv. Mater., 13 (8), 570-574 (2001).

131. A. Plecis and Y. Chen, "Fabrication of microfluidic devices based on glass-PDMS-glass technology," Microelectron. Eng., 84 (5-8), 1265-1269 (2007).

132. N. Lucas, S. Demming, A. Jordan, P. Sichler, and S. Buttgenbach, "An improved method for double-sided moulding of PDMS," J. Micromech. Microeng., 18 (7), 075037_075031 -075035 (2008).

133. D. Szmigiel, K. Domanski, P. Prokaryn, P. Grabiec, and J. W. Sobczak, "The effect of fluorine-based plasma treatment on morphology and chemical surface composition of biocompatible silicone elastomer," Appl. Surf. Sci., 253 (3), 1506-1511 (2006).

134. C. J. Mogab, A. C. Adams, and D. L. Flamm, "Plasma Etching of Si and Sio2 - Effect of Oxygen Additions to Cf4 Plasmas," J. Appl. Phys., 49 (7), 3796-3803 (1978).

135. H. Ahn, K. J. Lee, W. R. Childs, J. A. Rogers, R. G. Nuzzo, and A. Shim, "Micron and submicron patterning of polydimethylsiloxane resists on electronic materials by decal transfer lithography and reactive ion-beam etching: Application to the fabrication of high-mobility, thin-film transistors," J. Appl. Phys., 100 (8), 084907_084901 -084903 (2006).

136. K. W. Meacham, R. J. Giuly, L. Guo, S. Hochman, and S. P. DeWeerth, "A lithographically-patterned, elastic multi-electrode array for surface stimulation of the spinal cord," Biomed. Microdevices, 10 (2)**,** 259-269 (2008).

137. D. Cristea, P. Obreja, M. Kusko, E. Manea, and R. Rebigan, "Polymer micromachining for micro- and nanophotonics," Mater. Sci. Eng. C-Biomimetic Supramol. Syst., 26 (5-7)**,** 1049-1055 (2006).

138. K. L. Mills, X. Y. Zhu, S. C. Takayama, and M. D. Thouless, "The mechanical properties of a surface-modified layer on polydimethylsiloxane," J. Mater. Res., 23 (1)**,** 37-48 (2008).

139. B. Balakrisnan and E. Smela, "Challenges in the microfabrication of dielectric elastomer actuators," Electroactive Polymer Actuators and Devices (EAPAD), San Diego, CA, (SPIE), vol. 7642, edited by Y. Bar-Cohen (9, March, 2010).

140. B. Balakrisnan, S. Patil, and E. Smela, "Patterning PDMS using a combination of wet and dry etching," J. Micromech. Microeng., 19 (4)**,** 7 (2009).

141. R. Maboudian and C. Carraro, "Surface chemistry and tribology of MEMS," Annu. Rev. Phys. Chem., 55**,** 35-54 (2004).

142. S. Bhattacharya, A. Datta, J. M. Berg, and S. Gangopadhyay, "Studies on surface wettability of poly(dimethyl) siloxane (PDMS) and glass under oxygen-plasma treatment and correlation with bond strength," J. Microelectromech. Syst., 14 (3)**,** 590-597 (2005).

143. R. Ghodssi and P. Lin, <u>MEMS materials and processes handbook</u>, (Springer, New York, 2011).

144. B. Qi, G. R. Pickrell, J. C. Xu, P. Zhang, Y. H. Duan, W. Peng, Z. Y. Huang, W. Huo, H. Xiao, R. G. May, and A. Wang, "Novel data processing techniques for dispersive white light interferometer," Opt. Eng., 42 (11)**,** 3165-3171 (2003).

145. B. M. Z. Newby and M. K. Chaudhury, "Friction in adhesion," Langmuir, 14 (17)**,** 4865-4872 (1998).

146. C. Myant, M. Fowell, H. A. Spikes, and J. R. Stokes, "An investigation of lubricant film thickness in sliding compliant contacts," Tribol. Lubr. Technol., 66 (10)**,** 46 (2010).

147. I. S. Chun, A. Challa, B. Derickson, K. J. Hsia, and X. L. Li, "Geometry effect

on the strain-induced self-rolling of semiconductor membranes," 10 (10)**,** 3927-3932 (2010).

148. J. H. Cho, D. Datta, S. Y. Park, V. B. Shenoy, and D. H. Gracias, "Plastic deformation drives wrinkling, saddling, and wedging of annular bilayer nanostructures," 10 (12)**,** 5098-5102 (2010).

149. P. Cendula, S. Kiravittaya, I. Mönch, J. Schumann, and O. G. Schmidt, "Directional roll-up of nanomembranes mediated by wrinkling," 11**,** 236–240 (2011).

150. E. Smela, O. Inganäs, and I. Lundström, "Controlled folding of micrometer-size structures," Science, 268 (23 June)**,** 1735-1738 (1995).

151. G. T. A. Kovacs, <u>Micromachined Transducers Sourcebook</u>, (WCB McGraw-Hill, Boston, 1998).

152. F. T. Cheng, R. Y. Yin, Y. Y. Zhang, C. C. Yen, and Y. L. Yu, "Fully plastic microrobots which manipulate objects using only visible light," Soft Matter, 6 (15)**,** 3447-3449.

153. M. F. Wang, T. Maleki, and B. Ziaie, "Enhanced 3-D folding of silicon microstructures via thermal shrinkage of a composite organic/inorganic bilayer," 17 (4)**,** 882-889 (2008).

154. J. G. Wan, Z. Y. Li, Y. Wang, M. Zeng, G. H. Wang, and J. M. Liu, "Strong flexural resonant magnetoelectric effect in Terfenol-D/epoxy-Pb(Zr,Ti)O$_3$ bilayer," 86 (20) (2005).

155. V. M. Petrov, M. I. Bichurin, V. V. Zibtsev, S. K. Mandal, and G. Srinivasan, "Flexural deformation and bending mode of magnetoelectric nanobilayer," 106 (11) (2009).

156. R. Guerre, U. Drechsler, D. Bhattacharyya, P. Rantakari, R. Stutz, R. V. Wright, Z. D. Milosavljevic, T. Vaha-Heikkila, P. B. Kirby, and M. Despont, "Wafer-level transfer technologies for PZT-based RF MEMS switches," 19 (3)**,** 548-560 (2010).

157. A. B. Vorob'ev and V. Y. Prinz, "Directional rolling of strained heterofilms," 17**,** 614–616 (2002).

158. E. Cerda, S. Chaieb, F. Melo, and L. Mahadevan, "Conical dislocations in crumpling," 401 (6748)**,** 46-49 (1999).

159. A. Lobkovsky, S. Gentges, H. Li, D. Morse, and T. A. Witten, "Scaling properties of stretching ridges in a crumpled elastic sheet," 270 (Dec.)**,** 1482-1485 (1995).

160. E. Smela, O. Inganäs, Q. Pei, and I. Lundström, "Electrochemical muscles: micromachining fingers and corkscrews," Advanced Materials, 5**,** 630-632 (1993).

161. M. T. K. Hou and R. S. Chen, "Effect of width on the stress-induced bending of micromachined bilayer cantilevers," 13 (1)**,** 141-148 (2003).

162. S. Timoshenko, "Analysis of bi-metal thermostats," 11**,** 233-256 (1925).

163. E. Suhir, "Stresses in bimetal thermostats," 53 (3)**,** 657-660 (1986).

164. A. Y. Kuo, "Thermal stresses at the edge of a bimetallic thermostat," 56 (3)**,** 585-589 (1989).

165. J. Zang and F. Liu, "Modified Timoshenko formula for bending of ultrathin strained bilayer films," 92 (2)**,** Article Number 021905 (2008).

166. E. H. Mansfield, "Bending, buckling and curling of a heated thin plate," 265 (1334)**,** 316-327 (1962).

167. E. H. Mansfield, "Bending, buckling and curling of a heated elliptical plate," Proceedings of the Royal Society of London. Series A, Mathematical and Physical Sciences, 288 (1414)**,** 396-417 (1965).

168. L. B. Freund, "Substrate curvature due to thin film mismatch strain in the nonlinear deformation range," 48 (6-7)**,** 1159-1174 (2000).

169. L. D. Landau and E. M. Lifshitz, <u>Theory of Elasticity</u>, Vol. 7 (Butterworth-Heinemann, Oxford, 1960).

170. A. Boudaoud, P. Patricio, Y. Couder, and M. B. Amar, "Dynamics of singularities in a constrained elastic plate," 407 (6805)**,** 718-720 (2000).

171. L. B. Freund and S. Suresh, <u>Thin film materials: stress, defect formation, and surface evolution</u>, (Cambridge University Press, Cambridge 2003).

172. Y. C. Fung and W. H. Wittrick, "A boundary layer phenomenon in the large deflexion of thin plates," 8 (2)**,** 191-210 (1955).

173. E. Smela, "Microfabrication of PPy microactuators and other conjugated

polymer devices," 9**,** 1-18 (1999).

174.   M. Christophersen, B. Shapiro, and E. Smela, "Characterization and modeling of PPy bilayer microactuators. Part 1: Curvature," 115**,** 596-609 (2006).

175.   X. Wang and E. Smela, "Experimental studies of ion transport in PPy(DBS)," 113 (1)**,** 369–381 (2009).

176.   B. Audoly and Y. Pomeau, <u>Elasticity and Geometry: from hair curls to the nonlinear response of shells</u>, (Oxford Univ Pr, 2010).